TECHNISCHE UNIVERSITÄT MÜNCHEN

TUM School of Engineering and Design

A Mixed-Dimensional Multi-Physics Model of a Novel Cardiac Assist Device Coupled to Patient-Specific Cardiovascular Systems

Robert Wohlfarth

Vollständiger Abdruck der von der TUM School of Engineering and Design der Technischen Universität München zur Erlangung des akademischen Grades eines

Doktors der Ingenieurwissenschaften (Dr.-Ing.)

genehmigten Dissertation.

Vorsitz:	Prof. Dr.-Ing. Markus Lienkamp
Prüfer*innen der Dissertation:	
	1. Prof. Dr.-Ing. Michael W. Gee
	2. Prof. Dr. Ulrich Stock

Die Dissertation wurde am 15.04.2021 bei der Technischen Universität München eingereicht und durch die TUM School of Engineering and Design am 17.11.2021 angenommen.

Abstract

Heart failure (HF) is a prevalent disease with profound consequences for society and for the affected patients. Especially for elderly people it is among the main causes for hospitalization and death. Furthermore, it constitutes an enormous burden for health care systems. HF can be described as the inability of the heart to sufficiently pump blood to meet the demand of the organs. Transplantation of suitable donor hearts is the gold standard for patients with end-stage HF. Unfortunately, the amount of patients in need of a heart transplant exceeds the number of available donors by far. Treatment alternatives can be cardiac assist devices, which are already applied in varying designs. However, the existing systems – so-called ventricular assist devices (VAD) – are associated with some distinct disadvantages. The majority of VAD related complications can be ascribed to the permanent blood contact with artificial device surfaces. A novel approach is an extra-vascular and hence blood contact avoiding cardiac assist device. Such a system is being developed by the company AdjuCor GmbH (Munich, Germany). It is a pneumatically driven biventricular assist device (BiVAD) and consists of an extra-corporal drive unit and an implant. Both parts are interconnected by a pneumatic driveline. The implant features three expandable units (EU), which can be inflated with air. Force is exerted on the myocardium during their expansion and work is consequently done on the heart. Specifically, two of the EUs are located on the left ventricular wall (anterior and posterior) and one laterally on the right ventricle. To allow for proper inflation and deflation of these EUs, the drive unit incorporates air-filled reservoirs, valves and a pump. This BiVAD is the subject of the present thesis.

The purpose of the present work is to allow for valid simulations of the periodic states of BiVAD supported patient-specific cardiovascular systems (CVS) in various physiological and pathological conditions. To this end and for the first time, a mixed-dimensional multi-physics computational model of the novel BiVAD is presented and coupled to also mixed-dimensional patient-specific CVS models.

The BiVAD and the driveline are represented by a lumped-parameter model. Thereby, a spatial subdomain of the real system – e.g. the reservoir – is reduced to a single point, the 0-dimensional (0D) node. Its variables represent the state in the entire subdomain of the real system. Per 0D node, at the very least pressure and temperature are computed. Flows can evolve between the nodes in the event of an existing pressure gradient and a free flow path. The flow paths can in turn be changed by altering the opening of control valves. Moreover, pressure compliance of the reservoirs and tubes, hysteretic valve behavior as well as heat transfer between all parts and the environment are considered. The pump output as well as the valve openings are determined by their current control values and by the prevailing thermodynamic conditions. Aside from other components, the pump and valves are electrical consumer loads, which produce heat and warm the BiVAD. After the start of operation, it may take several hours until a constant mean device temperature is reached, which can strongly influence the system behavior. Therefore, a mean temperature prediction (MTP) model for that heated state is additionally presented and coupled to the BiVAD model. It utilizes the results of the preceding supported heart beat to estimate the pump and valve power consumption under the thermodynamic conditions. Thus and in combination with the heat transfer characteristics of the system, the MTP model predicts new mean reservoir temperatures for the next dynamic heart support simulation. This computation sequence iterates until a sufficiently accurate solution is found for the entire system. The functional part

of the implant consists of three 3-dimensional (3D) EUs. The supported 3D heart model is again coupled to a 0D representation of the circulatory system. By utilizing patient-specific heart geometries – obtained from computed tomography (CT) data – and by estimating selected CVS model parameters on the basis of intra-ventricular pressure and volume measurements of the same patient in differing pharmaceutical conditions, individual cases can be analyzed and a BiVAD therapy benefit be assessed. The utilized CT data sets are obtained in animal trials with pigs. They define the HF conditions used within the present work.

Following the modeling step and the depiction of exemplary results, the component models of the BiVAD are validated against experimental data. To account for the volatility of pressure and flow during a supported heart beat, at least one dynamical BiVAD process is experimentally conducted for each component. By varying the boundary and initial conditions in the validating experiments, a large range of the system's working range is covered. All experiments are reproduced in-silico. The mean deviations of the single component models from the respective experimental measurements are around 5 %. The majority of the measured pressure curves in the EUs conform qualitatively with those in the simulations. The validation of the MTP model is performed by estimating selected parameters of the heat transfer model and the drive unit housing, both on the basis of device temperature measurements. The median of the remaining error is below 1 °C and the interquartile range is close to the measurement accuracy of the utilized temperature sensors.

The model parameters and their influence on the system behavior is of importance for the modeling itself, but also for identifying potential improvements regarding the efficacy and efficiency of the BiVAD. Therefore, its parameters are subject to a local sensitivity analysis to quantify their individual influence within the parameter set. The results show that the ambient pressure – as a frequent part of the underlying equations – and the reservoir volumes have essential influence. Likewise, the importance of the MTP model is confirmed, as the predicted mean reservoir temperatures have one of the highest sensitivities. Potential improvements are primarily given by an enlargement of the reservoirs, which would increase both efficacy and efficiency. Altogether, the BiVAD modeling efforts made in the present work are justified.

In the last part of this thesis, the BiVAD model is applied to different patients in varying medical conditions. These patients differ in their heart geometry and in the type of heart failure. Moreover, myocardial infarction, aortic stenosis as well as aortic and mitral valve regurgitation are additionally simulated in these patients. The effects of these medical conditions and their changes on the BiVAD, whose parameters are held constant for the most part, are examined. The results show a strong coupling between CVS and BiVAD. More than the differing patient heart geometries, the generated support work of the BiVAD is co-determined by the prevailing HF condition and additional valvular diseases or infarctions. Concomitant effects are alterations in the efficiency of the BiVAD CVS energy transfer as well as in the efficiency of the support energy provision of the BiVAD itself. The electrical power consumption of the pump varies 20-30 % within the examined cases. Correspondingly, the system temperatures differ by more than 2 °C.

The coupling of the mixed-dimensional multi-physics BiVAD model to the models of the diseased CVS of specific patients allows for fast advancements and improvements of the real BiVAD. Component changes or re-designs can quickly and cost-effectively be assessed in-silico.

Individual treatment options can be tested computationally and prior to surgery, allowing for better risk-benefit analyses. Not least, the fully-coupled model can be used to study the effects of physiological and pathological CVS changes to the BiVAD signals on a larger scale, which may eventually provide a diagnostic capability in future BiVAD versions.

Zusammenfassung

Herzinsuffizienz (englisch heart failure, HF) ist eine stark verbreitete Krankheit mit weitreichenden Folgen für die Gesellschaft und für Betroffene. Sie gehört gerade für ältere Menschen zu den Hauptursachen für Krankenhausaufenthalte und Tod. Darüber hinaus stellt sie eine enorme finanzielle Belastung des Gesundheitssystems dar. HF kann als das Unvermögen des Herzens betrachtet werden, ausreichende Mengen Blut zu pumpen, um den Bedarf des Körpers zu decken. Der Goldstandard für Patienten im Endstadium ist die Transplantation von geeigneten Spenderherzen. Leider übersteigt die Anzahl der Bedürftigen die der Spender bei weitem. Eine Behandlungsalternative stellen Herzunterstützungssysteme dar, die in verschiedenen Formen bereits klinisch Anwendung finden. Die vorhandenen Systeme – sogenannte ventrikuläre Unterstützungssysteme (englisch ventricular assist device, VAD) – bringen aber einige Nachteile mit sich. Ein Großteil der Komplikationen sind auf den permanenten Kontakt von Geräteteilen mit dem Patientenblut zurückzuführen. Ein neuartiger Ansatz ist ein extravaskuläres, also Blutkontakt vermeidendes Herzunterstützungssystem. Ein derartiges System wird von der Firma AdjuCor GmbH (München, Deutschland) entwickelt. Es ist ein pneumatisch betriebenes, biventrikuläres Unterstützungssystem (englisch biventricular assist device, BiVAD). Es besteht aus einer extrakorporalen Antriebseinheit und einem Implantat um das Herz. Beide Teile sind durch eine Implantatszuleitung verbunden. Das Implantat besteht aus drei expandierbaren Einheiten (englisch expandable unit, EU), die kontrolliert mit Luft befüllt werden. Durch die so ausgelöste Expansion kann Kraft auf den Herzmuskel ausgeübt und Arbeit verrichtet werden. Dabei sind zwei der EUs linksventrikulär (anterior und posterior) und eine rechtsventrikulär (lateral) positioniert. Um die In- und Deflation der EUs zu ermöglichen, beinhaltet die Antriebseinheit luftgefüllte Reservoire, Ventile und eine Pumpe. Dieses BiVAD ist Gegenstand der vorliegenden Arbeit.

Der Zweck dieser Arbeit ist die Ermöglichung valider Simulationen von eingeschwungenen Zuständen BiVAD-unterstützter patientenspezifischer Herzkreislaufsysteme zu unterschiedlichen physiologischen und pathologischen Gegebenheiten. Erstmalig wird dazu ein gemischt-dimensionales multiphysikalisches Computermodell des neuartigen BiVADs entwickelt und an vorhandene gemischt-dimensionale und patientenspezifische Herzkreislaufmodelle (englisch cardiovascular system, CVS) gekoppelt.
Das BiVAD-Modell sowie die Implantatszuleitung sind durch ein Netzwerkmodell repräsentiert. Dabei wird ein räumlich ausgedehnter Teilbereich des BiVAD – z.B. das Reservoir – auf einen einzigen Punkt reduziert, den 0-dimensionalen (0D) Netzwerkknoten. Seine Modellvariablen repräsentieren damit den Zustand im gesamten Teilbereich des realen Systems. Pro Netzwerkknoten werden mindestens Druck und Temperatur berechnet. Zwischen ihnen ergeben sich bei Druckdifferenzen und freien Strömungswegen Flüsse. Die Strömungswege werden wiederum durch den Öffnungsgrad der Steuerventile verändert. Des Weiteren werden die Drucknachgiebigkeit der Reservoire und Schläuche berücksichtigt, das Hystereseverhalten der Ventile sowie der Wärmeaustausch aller Teile mit der Umgebung. Die Fördermenge der Pumpe sowie der Öffnungsgrad der Ventile werden durch ihre aktuellen Steuergrößen sowie durch die vorliegenden thermodynamischen Bedingungen bestimmt.
Neben anderen Komponenten sind Pumpe und Ventile elektrische Verbraucher und erzeugen Wärme, die das BiVAD erhitzt. Nach Systemstart kann es in der Realität mehrere Stunden

dauern, bis sich eine konstante mittlere Temperatur im System einstellt, welche starken Einfluss auf das Systemverhalten haben kann. In der vorliegenden Arbeit wird daher ein weiteres Modell zur Schätzung der mittleren Übertemperatur (englisch mean temperature prediction, MTP) eingeführt und an das BiVAD gekoppelt. Es nutzt die Ergebnisse des letzten unterstützten Herzzyklus, um die elektrische Leistungsaufnahme von Pumpe und Ventilen unter den vorliegenden thermodynamischen Bedingungen zu schätzen. Aus diesen und dem Wärmeübertragungsverhalten des BiVAD können neue mittlere Systemtemperaturen geschätzt und für den nächsten unterstützten Herzzyklus bereitgestellt werden. Diese Berechnungsreihenfolge iteriert, bis eine ausreichend genaue Lösung des Gesamtsystems gefunden ist. Der funktionelle Teil des Implantats besteht aus drei 3-dimensionalen (3D) EUs. Das unterstützte 3D Herz ist wiederum mit einem 0D Modell des Blutkreislaufs verbunden. Durch die Verwendung patientenspezifischer Herzgeometrien – gewonnen aus computertomographischen (CT) Daten – sowie der Schätzung ausgewählter CVS-Modellparameter anhand intraventrikulärer Volumen- und Druckmessungen desselben Patienten in verschiedenen medikamentösen Zuständen, können individuelle Fälle analysiert und der Nutzen einer BiVAD-Therapie abgeschätzt werden. Die verwendeten CT- und Hämodynamikdaten stammen aus Tierversuchen mit Schweinen. Sie definieren die Zustände von Herzinsuffizienz, die in dieser Arbeit verwendet werden.

Im Anschluss an die Modellierung und die exemplarische Darstellung möglicher Ergebnisse werden die simulationsfähigen Einzelkomponenten des BiVAD durch den Vergleich zu experimentellen Daten einzeln und/oder kombiniert validiert. Dazu wird für jede Komponente mindestens ein dynamischer Prozess im Versuch abgebildet, um der Volatilität der maßgeblichen Größen wie Druck oder Fluss während eines Herzschlags gerecht zu werden. Durch Variation der Rand- und Anfangsbedingungen in den validierenden Versuchen wird ein breiter Bereich des möglichen Arbeitsraums des Systems abgedeckt. Die Versuche werden alle in-silico reproduziert. Die mittleren Abweichungen der einzelnen Validierungsmodelle von den experimentellen Daten liegen um die $5\ \%$. Die Druckverläufe in den EUs stimmen qualitativ mehrheitlich mit der Simulation überein. Die Validierung des MTP-Modells geht mit der Kalibrierung von Parametern der Wärmeübertragung und der Gehäusegeometrie anhand von Langzeittemperaturmessungen einher. Der Median des verbleibenden Fehlers ist kleiner als $1\ ^\circ\mathrm{C}$ und der Interquartilsabstand liegt nahe an der Messgenauigkeit der verwendeten Temperatursensoren.

Um Verbesserungspotential hinsichtlich der Systemeffektivität und -effizienz aufzudecken sowie zur Modellierung selbst, sind die Systemparameter und ihr Einfluss auf das Systemverhalten von Bedeutung. Die Parameter der BiVAD-Teilmodelle werden daher einer lokalen Sensitivitätsanalyse unterzogen, um diesen Einfluss innerhalb der Parametermenge zu quantifizieren. Aus ihr geht hervor, dass der Umgebungsluftdruck als häufiger Bestandteil der verwendeten Formeln sowie die Reservoirvolumina entscheidenden Einfluss haben. Ebenso bestätigt die Sensitivitätsanalyse die Bedeutung des MTP-Modells. Verbesserungspotential liegt vor allem in einer Vergrößerung der Reservoire, was sowohl die Effektivität als auch die Effizienz steigert. Insgesamt rechtfertigen die Ergebnisse den Modellierungsaufwand des BiVADs.

Im letzten Teil dieser Arbeit wird das BiVAD-Modell in verschiedenen Patienten in unterschiedlichen medizinischen Zuständen angewandt. Die Patienten unterscheiden sich in der Geometrie des Herzens und im Typ der Herzinsuffizienz. Darüber hinaus werden zusätzlich Myokardinfarkt, Aortenstenose sowie Mitral- und Aortenklappeninsuffizienz in diesen Patienten simuliert.

Es werden die Effekte der medizinischen Zustände und ihrer Änderung auf das BiVAD untersucht, dessen Parameter während dieser Untersuchung weitestgehend konstant gehalten werden. Es zeigt sich eine starke Koppelung zwischen den Systemen. Mehr als die Patientengeometrie beeinflusst der Patientenzustand in Form der vorliegenden HF und/oder zusätzlicher Krankheiten die vom BiVAD geleistete Unterstützungsarbeit. Damit einhergehend zeigen sich Veränderungen im Wirkungsgrad der Energieübertragung von BiVAD auf CVS sowie in der pneumatischen Energiebereitstellung innerhalb des BiVADs. Die Spanne der elektrischen Leistungsaufnahme der Pumpe innerhalb der betrachteten Fälle kann 20 bis 30 % ihrer eigentlichen Leistungswerte ausmachen. Entsprechend unterscheiden sich die Systemtemperaturen um mehr als 2 °C.

Die Koppelung des gemischt-dimensionalen multiphysikalischen BiVAD-Modells an die Modelle erkrankter CVSs spezifischer Patienten ermöglicht eine schnelle Weiterentwicklung und Verbesserung des BiVADs. In-silico kann ein Austausch von Komponenten sowie eine geometrische Veränderung schnell und kostengünstig auf Vorteilhaftigkeit geprüft werden. Die individuellen Therapiemöglichkeiten für einen Patienten können im Vorfeld simulativ untersucht werden und erlauben eine verbesserte Risiko-Nutzen-Abschätzung vor dem chirurgischen Eingriff. Nicht zuletzt eröffnet sich die Möglichkeit, im BiVAD messbare physiologische und pathologische CVS-Veränderungen im großen Stil zu untersuchen und dem Herzuntersützungssystem damit eine diagnostische Fähigkeit zu verleihen.

Danksagung

Die vorliegende Arbeit entstand in der Zeit zwischen 2015 und 2021. Während dieser Zeit war ich als externer Doktorand sowohl mit der Anfertigung meiner Doktorarbeit am Fachgebiet Mechanik auf Höchstleistungsrechnern der TUM beschäftigt als auch in der Firma AdjuCor GmbH als Ingenieur tätig. Ich habe in dieser Zeit meine Frau Kathrin kennengelernt und unser Sohn Gustav wurde geboren. Ich möchte mich an dieser Stelle herzlich bei den Menschen bedanken, ohne deren Unterstützung die vorliegende Arbeit nicht möglich gewesen wäre.

Meinem Doktorvater Prof. Dr.-Ing. Michael Gee möchte ich für das entgegengebrachte Vertrauen und die Unterstützung während meiner Zeit am Fachgebiet danken. Sein stets offenes Ohr und die fachlichen sowie privaten Ratschläge haben mir sehr geholfen und mich motiviert. In gleichem Maße gilt mein Dank Prof. Dr. Stephen Wildhirt, der mich nach Anfertigung meiner Diplomarbeit in seiner Firma AdjuCor GmbH als Doktorand bei Prof. Gee vorgeschlagen und damit erst den Impuls zur Promotion gegeben hat. Er hat mir großes Vertrauen entgegengebracht und mich vielfältig persönlich und beruflich gefördert. Ebenso möchte ich mich bei Dr. Andreas Maier bedanken, der sich von Anfang an für meine Promotion eingesetzt hat und mir immer wohlwollend mit Rat und Tat zur Seite stand. Mein Dank gilt allen genannten auch für ihren höflichen und respektvollen Umgang miteinander, was für den Ausgleich zwischen Firmen- und Promotionsinteressen sehr wichtig war.

Meinen Kollegen am Fachgebiet danke ich für die angenehme und hilfsbereite Atmosphäre. Ohne die unzähligen kleineren und größeren Hilfeleistungen wäre ich schlicht verzweifelt gewesen. Insbesondere möchte ich mich bei Dr. Marc Hirschvogel bedanken sowohl als Kollege für die geduldige fachliche Unterstützung als auch als Tauchlehrer für die fundierte Ausbildung unter Wasser. Dr. André Hemmler hat mir in vielen motivierenden Telefonaten entscheidende Ratschlägen zur Auflösung von Simulationsproblemen gegeben. Mein Dank gilt auch Willem Schüttler und Thomas Egger, die für mich besondere Stützen während meiner Promotionszeit waren. Dazu gehört auch das Korrekturlesen der kompletten Arbeit. Wertvolle Korrekturarbeit haben darüber hinaus Alexander Schein, Lukas Bruder, Dr. Andreas Maier und Dr. Hamman de Vaal geleistet.

Schließlich möchte ich mich bei meiner Familie für die fortwährende Unterstützung bedanken. Insbesondere gilt mein Dank meiner Frau Kathrin, die vieles auf sich nehmen musste und ohne deren Rückhalt der Abschluss dieser Arbeit unmöglich gewesen wäre.

Saarbrücken, im Februar 2022 Robert Wohlfarth

Contents

1. Introduction **1**
1.1. Motivation . . . 1
1.2. The cardiovascular system . . . 2
1.3. Heart failure . . . 6
1.4. Heart transplantation . . . 7
1.5. Assist technology . . . 8
1.5.1. Clinically applied systems . . . 8
1.5.2. Shortcomings of clinically applied systems . . . 11
1.5.3. Direct cardiac compression devices . . . 12
1.5.4. A novel biventricular assist device (BiVAD) . . . 14
1.6. Computational models of cardiac assist technology . . . 16
1.7. Research objectives . . . 17
1.8. Outline . . . 18

2. Physical fundamentals **19**
2.1. Thermodynamics . . . 19
2.1.1. The ideal gas law . . . 20
2.1.2. The principle of energy conservation . . . 21
2.1.3. Polytropic processes . . . 22
2.1.4. Heat transfer . . . 23
2.2. Mechanics . . . 25
2.2.1. Fluid mechanics . . . 25
2.2.1.1. The medium air . . . 25
2.2.1.2. Mass conservation . . . 26
2.2.1.3. Balance of linear momentum . . . 26
2.2.1.4. One-dimensional flow . . . 27
2.2.1.5. Flow patterns in a pipe . . . 28
2.2.2. Solid mechanics . . . 28
2.2.2.1. Kinematics . . . 29
2.2.2.2. Constitutive laws . . . 30
2.2.2.3. Balance equations . . . 31
2.2.2.4. Contact mechanics . . . 31
2.2.2.5. Principle of virtual work . . . 32
2.3. Discretization and solution . . . 32
2.3.1. Spatial discretization . . . 32
2.3.2. Temporal discretization . . . 33
2.3.3. Linearization . . . 33

3. Modeling **35**
3.1. 0D-3D biventricular assist device (BiVAD) . . . 35
3.1.1. Assumptions . . . 37
3.1.2. Reservoirs . . . 38
3.1.3. Pump . . . 41
3.1.4. Valves . . . 43
3.1.5. Tubing and connectors . . . 46
3.1.6. The implant's expandable units (EUs) . . . 51
3.1.7. Control . . . 53
3.1.7.1. Pump control . . . 53
3.1.7.2. Valve control . . . 53
3.1.8. Model parameters . . . 55
3.2. 0D mean temperature prediction model (MTP) . . . 55
3.2.1. General approach . . . 57
3.2.2. Electrical power . . . 58
3.2.3. Pneumatic power . . . 60
3.2.4. Heat exchange power . . . 60
3.3. 0D-3D-3D-0D supported cardiovascular model (SCVS) . . . 62
3.3.1. Materials . . . 64
3.3.2. Coupling conditions . . . 65
3.3.3. Prestressing . . . 65
3.3.4. Discretization and solution . . . 66
3.3.4.1. SCVS model . . . 66
3.3.4.2. MTP model . . . 70
3.4. Convergence study . . . 71
3.4.1. Methods . . . 71
3.4.1.1. Temporal discretization . . . 71
3.4.1.2. Spatial discretization . . . 72
3.4.2. Results . . . 73
3.4.3. Discussion . . . 74
3.5. Exemplary results . . . 75
3.6. Discussion . . . 80
3.7. Limitations . . . 85
3.8. Summary . . . 86

4. Validation **89**
4.1. Methods . . . 89
4.1.1. Reservoirs and pump . . . 91
4.1.2. Reservoirs and valve . . . 91
4.1.3. Tubes and connector . . . 91
4.1.4. Expandable units . . . 92
4.1.5. MTP model . . . 93
4.2. Results . . . 94
4.2.1. Reservoirs and pump . . . 94
4.2.2. Reservoirs and valve . . . 94

4.2.3. Tubes and connector . . . 96
4.2.4. Expandable units . . . 99
4.2.5. MTP model . . . 99
4.3. Discussion . . . 100
4.4. Summary . . . 107

5. Sensitivity analysis **109**
5.1. Methods . . . 109
5.2. Results . . . 110
5.2.1. SCVS model . . . 110
5.2.2. MTP model . . . 110
5.3. Discussion . . . 110
5.4. Summary . . . 113

6. Application **117**
6.1. Methods . . . 117
6.1.1. Medical cases . . . 117
6.1.1.1. Specific patients . . . 117
6.1.1.2. Heart failure conditions . . . 118
6.1.1.3. Myocardial infarction . . . 119
6.1.1.4. Valvular heart diseases . . . 120
6.1.2. Computation process . . . 120
6.1.3. Case study . . . 123
6.2. Results . . . 126
6.2.1. Specific HF patients . . . 126
6.2.2. Mitral valve regurgitation . . . 127
6.2.3. Other diseases . . . 131
6.3. Discussion . . . 131
6.3.1. Specific HF patients . . . 142
6.3.2. Mitral valve regurgitation . . . 144
6.3.3. Other diseases . . . 145
6.4. Summary . . . 146

7. Summary and outlook **149**
7.1. Summary . . . 149
7.2. Outlook . . . 150
7.2.1. Model improvements and extensions . . . 151
7.2.2. Model usages . . . 152

A. Appendix **153**
A.I. Bench tests . . . 153
A.I.1. Volume and compliance . . . 153
A.I.2. Heat transmittance . . . 153
A.I.3. Flow coefficient . . . 154
A.I.4. Equipment . . . 154

A.II. Supporting documents 155
A.II.1. Neglecting kinetic energy 155
A.II.2. Model parameter 156
A.II.3. Robin boundary conditions 156
A.II.4. Material parameter 158
A.II.5. Pump power curve 158
A.II.6. The BiVAD model stiffness matrix 158

Bibliography **165**

Nomenclature

Abbreviations

0D	Zero-dimensional
1D	One-dimensional
3D	Three-dimensional
ACCF/AHA	American College of Cardiology Foundation/American Heart Association
AD	Assist device
AR	Aortic regurgitation
AS	Aortic stenosis
AV	Atrioventricular
BiVAD	Biventricular assist device
bpm	Beats per minute
BTD	Bridge-to-decision
BTR	Bridge-to-recovery
BTT	Bridge-to-transplant
CAD	Computer-aided design
CCD	Cardiac compression device
CF	Continuous flow
CO	Cardiac output
CT	Computer tomography
CVS	Cardiovascular system
DCC	Direct cardiac compression
DCCD	Direct cardiac compression device
DCM	Dilated cardiomyopathy
DMM	Digital multimeter
DOF	Degree of freedom
DT	Destination therapy
ECG	Electrocardiogram
EDP	End-diastolic pressure
EDV	End-diastolic volume
EF	Ejection fraction
ESP	End-systolic pressure
ESV	End-systolic volume
EU	Expandable unit
FE	Finite element
FS	Flow sensor
GMRES	Generalized minimal residual method

HCM	Hypertrophic cardiomyopathy
HF	Heart failure
HFpEF	Heart failure with preserved ejection fraction
HFrEF	Heart failure with reduced ejection fraction
HA-HF	High-afterload heart failure
HMII	Heart Mate II™
HMIII	Heart Mate III™
HPR	High pressure reservoir
HR	Heart rate
IMACS	International Registry for Mechanically Assisted Circulatory Support
INTERMACS	Interagency Registry for Mechanically Assisted Circulatory Support
KKT	Karush-Kuhn-Tucker
LA	Left atrium
LA-HF	Low-afterload heart failure
LPR	Low pressure reservoir
LV	Left ventricle
LVAD	Left ventricular assist device
MI	Myocardial infarction
MR	Mitral regurgitation
MS	Mitral stenosis
MULF	Modified Updated Lagrangian Formulation
MTP	Mean temperature prediction
NO-HF	No heart failure
NYHA	New York Heart Association
ODE	Ordinary differential equation
PS	Pressure sensor
PWM	Pulse with modulated (signal)
RA	Right atrium
RR	Time between two R-waves in the ECG = Time of heart beat
RV	Right ventricle
RVAD	Right ventricular assist device
SCVS	Supported cardiovascular system
SIMPLE	Semi-Implicit Method for Pressure-Linked Equations
SV	Stroke volume
TAH	Total artificial heart
TS	Temperature sensor
VAD	Ventricular assist device
VHD	Valvular heart disease

Main notations and symbols

t	Time
m	Mass
$\mathcal{B}_{\text{sys}}$	Extensive system property
β	Intensive system property ($= \mathcal{B}_{\text{sys}}/m$)
ρ	Density
V, v	Volume, specific volume
A	Area/Surface area
$\mathrm{d}A/\mathrm{d}V$	Infinitesimal surface/volume element in either reference or current configuration
z	Altitude
g	Gravitational acceleration
$\mathcal{U}$	Electrical voltage
$\mathcal{I}$	Electrical current
$\mathcal{R}$	Electrical resistance
H, $\bar{\mathrm{H}}$	Hysteresis
f	Auxiliary function
E	Error measure
$\hat{\mathrm{E}}$	Absolute unsigned error measure
$\hat{\mathrm{e}}$	Relative unsigned error measure
$\tilde{\mathrm{S}}$	Signal
$\mathcal{S}$	Sensitivity

Fluid mechanics

$\dot{m}, g$	Mass flow rate
$\dot{V}, q$	Volumetric flow rate
v	Average velocity (scalar)
Ma	Mach number
$\tilde{c}$	Speed of sound
η	Dynamic viscosity
ν	Kinematic viscosity
λ	Darcy friction factor
ζ	Loss coefficient
$a_{\lambda/\zeta}$, $b_{\lambda/\zeta}$	Friction model parameter
Re	Reynolds number
L	Length
L_{c}	Characteristic length scale
D	Diameter
s	Streamline

Thermodynamics

p	Pressure
T	Temperature
U, u	Internal energy, specific internal energy
H, h	Enthalpy, specific enthalpy
S	Entropy
R	Specific gas constant
E, e	Energy, specific energy
Q	Heat
W	Work
P	Power
C_{th}, c_{th}	Heat capacity, specific heat capacity
c_p, c_{v}	Specific heat capacity at constant pressure, volume
κ	Isentropic exponent/Heat capacity ratio
n	Polytropic exponent
$\dot{\mathbf{q}}(\boldsymbol{x}, t)$	Heat flux vector field
$T(\boldsymbol{x}, t)$	Temperature field
λ_{th}	Thermal conductivity
Λ_{th}	Thermal conductance
d_{W}	Wall thickness
α	Heat transfer coefficient
k_{th}	Thermal transmittance
τ	Rate of change of temperature $\frac{\mathrm{d}T}{\mathrm{d}t}$
$\boldsymbol{T}$	Temperature vector

Control and timing

t_0	Initial time of transient computation
T	Total computation time
t_{ec}	End of cardiac cycle
t_{es}	End of systole/Beginning of cardiac relaxation/T-wave in ECG
t_{ed}	End of diastole/Beginning of cardiac contraction/R-wave in ECG
$t_{\text{in,1}}$	Beginning of inflation phase 1 $= t_{\text{ed}}$
$t_{\text{in,2}}$	Beginning of inflation phase 2
t_{out}	Beginning of deflation phase $= t_{\text{es}}$
Δt_{c}	Time needed to reach a set valve opening
y	Actuator control value
$y_{\text{inlet,1}}$	Inlet valve control value during inflation phase 1
$y_{\text{inlet,2}}$	Inlet valve control value during inflation phase 2
y_{outlet}	Outlet valve control value during deflation

Domains

Ω_0, Ω	Reference (material), current (spatial) domain
$\Gamma_0^{\mathrm{D}}, \Gamma^{\mathrm{D}}$	Reference (material), current (spatial) Dirichlet boundary
$\Gamma_0^{\mathrm{N}}, \Gamma^{\mathrm{N}}$	Reference (material), current (spatial) Neumann boundary
Γ_0^{R}	Reference (material) Robin boundary
$\Gamma_{0,\mathrm{H}}^{\mathrm{R},b}$	Reference (material) Robin boundary at heart basis
$\Gamma_{0,\mathrm{H}}^{\mathrm{R},e}$	Reference (material) Robin boundary at heart epicardium
$\Gamma_{0,\mathrm{H}}^{\mathrm{lids}}$	Reference (material) endocardial lids boundary (closure for ventricles)
Γ_0^{c}	Reference (material) contact boundary
Γ_0^{AD}	Reference (material) coupling boundary to 0D assist device
Γ_0^{CS}	Reference (material) coupling boundary to 0D circulatory system

Solid mechanics

$\boldsymbol{X}, \boldsymbol{x}$	Position vector in reference, current configuration
$\boldsymbol{e}_1, \boldsymbol{e}_2, \boldsymbol{e}_3$	Basis vectors of Cartesian coordinate system
$\boldsymbol{\varphi}_t$	Mapping between reference and current configuration
$\boldsymbol{u}$	Displacement
$\hat{\boldsymbol{u}}$	Prediscribed displacement
$\boldsymbol{a}$	Acceleration vector
$\boldsymbol{F}$	Deformation gradient
J	Determinant of deformation gradient
$\boldsymbol{v}$	Velocity vector
$\boldsymbol{n}$	Surface normal
$\mathbf{F}$	Force
$\boldsymbol{C}, \boldsymbol{b}$	Right/Left Cauchy-Green deformation tensor
$\boldsymbol{E}, \boldsymbol{e}$	Green-Lagrange, Euler-Almansi strain tensor
$\hat{\boldsymbol{b}}_0, \hat{\boldsymbol{b}}$	Body force vector in reference, current configuration
$\boldsymbol{t}_0, \boldsymbol{t}$	Traction vector in reference, current configuration
$\boldsymbol{\sigma}$	Cauchy stress
$\boldsymbol{P}, \boldsymbol{S}$	First, second Piola-Kirchhoff stress tensor
Ψ	Strain energy function
$\bar{\Psi}, \Psi_{\mathrm{vol}}$	Isochoric, volumetric part of strain energy function
I_C, II_C, III_C	Principal invariants of right (left) Cauchy-Green deformation tensor
$\overline{I}_C, \overline{II}_C, \overline{III}_C$	Modified principal invariants of right (left) Cauchy-Green deformation tensor
$\boldsymbol{f}_0$, $\boldsymbol{s}_0$	Cardiac muscle fibers directions in material configuration
μ	Shear modulus
ν	Poisson's ratio

κ	Bulk modulus
g_n	Gap function
p_n	Contact stress in normal direction
$\boldsymbol{t}_t$	Tangential traction vector in contact interface
$\delta\mathcal{W}$	Virtual work

Discretization and solution

n_{el}	Number of finite elements
$\Omega_0^{(e)}$	Finite element subdomain
$\boldsymbol{N}^{(e)}$	Shape function
$\boldsymbol{d}^{(e)}$	Nodal displacement
$\boldsymbol{u}^{(e)}$	Displacement of the finite element
$\boldsymbol{X}^{(e)}$	Position of the finite element
$\bar{\boldsymbol{X}}^{(e)}$	Nodal position of the finite element
$\boldsymbol{r}$	Residual
$\boldsymbol{K}$	Stiffness matrix
$\boldsymbol{M}$	Mass matrix
$\boldsymbol{D}$	Rayleigh damping matrix
α_M	Rayleigh damping contribution of mass matrix
β_K	Rayleigh damping contribution of stiffness matrix
$\boldsymbol{d}$	Global nodal displacement vector
$\mathbf{v/a}$	Global nodal velocity/acceleration vector
$\mathbf{F}_{\text{int}}$	Internal force
$\mathbf{F}_{\text{ext}}$	External force
$\boldsymbol{p}$	Vector of 0D state variables
$\alpha_m, \alpha_f, \beta, \gamma$	Parameters of the Generalized-α time discretization method
θ	Parameter of the One-Step-θ time discretization method
ϵ	Tolerance of stop criterion
k_{PTC}	Pseudo-transient continuation parameter
Δt	Time step size
Δt_{fine}	Fine time step size
Δt_{coarse}	Coarse time step size
$f_{\Delta t}$	Time step factor
n_{DOF}	Number of degrees of freedom
$\boldsymbol{\xi}$	Vector of parameters to be estimated
$t_{\text{c,out,e}}$	End of coarse time step use in deflation phase
$t_{\text{f,in,s}}$	Beginning of fine time step use in inflation phase ($= t_{\text{yin,1}} = t_{\text{contr}}$)
$t_{\text{f,in,e}}$	End of fine time step use in inflation phase
$t_{\text{c,in,s}}$	Beginning of coarse time step use in inflation phase
$t_{\text{c,in,e}}$	End of coarse time step use in inflation phase

$t_{\text{f,out,s}}$	Beginning of fine time step use in deflation phase ($= t_{\text{yout}} = t_{\text{contr}}$)
$t_{\text{f,out,e}}$	End of fine time step use in deflation phase
$t_{\text{c,out,s}}$	Beginning of coarse time step use in deflation phase

Super- and subscripts

$(\bullet)^{\text{AD}}$, $(\bullet)_{\text{AD}}$	Relating to assist device model
$(\bullet)^{\text{CVS}}$	Relating to cardiovascular system model
$(\bullet)^{\text{MTP}}$	Relating to mean temperature prediction model
$(\bullet)^{\text{S}}$	Relating to a 3D structural model
$(\bullet)^{\text{0D}}$	Relating to a 0D model
$(\bullet)_{\text{EU}}$	Relating to the implant's expandable units
$(\bullet)_{\text{TE}}$	Relating to the tube ends near the EUs
$(\bullet)_{\text{V}}$	Relating to the valves (node between valves and tube)
$(\bullet)_{\text{V,in}}$	Relating to the inlet valves
$(\bullet)_{\text{V,out}}$	Relating to the outlet valves
$(\bullet)_{\text{T}}$	Relating to the tubes (tube center point)
$(\bullet)_{\text{Res}}$	Relating to a assist device's reservoir
$(\bullet)_{\text{HPR}}$	Relating to the high pressure reservoir
$(\bullet)_{\text{LPR}}$	Relating to the low pressure reservoir
$(\bullet)_{\text{PP}}$	Relating to the pump
$(\bullet)^{k}$	Relating to the k-th EU, tube or valve
$(\bullet)_{\infty}$	Environmental value
$(\bullet)_{\text{W}}$	Relating to the reservoir septum wall
$(\bullet)_{\text{body}}$	Relating to patient body
$(\bullet)_{\text{H}}$	Relating to heart model
$(\bullet)^{\ell}$	Relating to the left ventricle
$(\bullet)^{r}$	Relating to the right ventricle
$(\bullet)_{\text{v}}$	Relating to the ventricle
$(\bullet)^{\text{sys}}$	Relating to the systemic circulatory system
$(\bullet)^{\text{pul}}$	Relating to the pulmonary circulatory system
$(\bullet)_{\text{at}}$	Relating to atria
$(\bullet)_{\text{ar}}$	Relating to arteries
$(\bullet)_{\text{ven}}$	Relating to veins
$(\bullet)^{\text{c}}$	Contact mechanics quantity
$(\bullet)_{\text{int}}$	Internal
$(\bullet)_{\text{ext}}$	External
$(\bullet)_{\text{kin}}$	Kinetic
$(\bullet)_{\text{pot}}$	Potential
$(\bullet)_{\text{min}}$	Minimum
$(\bullet)_{\text{max}}$	Maximum
$(\bullet)_{\text{syst}}$	Relating to a defined system

$(\bullet)_{\text{norm}}$	Quantity at normal conditions
$(\bullet)_{\text{std}}$	Quantity at standard conditions
$(\bullet)_{\text{trans}}$	Transition
$(\bullet)_{\text{crit}}$	Critical
$(\bullet)_{\text{incr}}$	Increment
$(\bullet)_{\text{res}}$	Residual
$(\bullet)_{\text{exp}}$	Experimental
$(\bullet)_{\text{sim}}$	Simulated
$(\bullet)_{\lambda}$	Relating to the Darcy friction model
$(\bullet)_{\zeta}$	Relating to the loss coefficient model
$(\bullet)_{z}$	Relating to the z-th heart beat
$(\bullet)_{n}$	Previous time step/Portion of property in normal direction
$(\bullet)_{n+1}$	Current time step
$(\bullet)^{i}$	Previous Newton iteration step
$(\bullet)^{i+1}$	Current Newton iteration step
$(\overline{\bullet})$	Modified value

Operands

$(\bullet)^{-1}$	Inverse
$(\bullet)^{T}$	Transpose
$(\bullet)^{-T}$	Transpose of inverse
$\dot{(\bullet)}$	First time derivative
$\ddot{(\bullet)}$	Second time derivative
$\frac{\partial}{\partial(\bullet)}$	Partial derivative with respect to $(\bullet)$
$\mathrm{d}(\bullet)$	Infinitesimal quantity
$\delta(\bullet)$	Differential of process quantity or virtual quantity
$\Delta(\bullet)$	Difference of quantity
$\lvert(\bullet)\rvert$	Absolute value
$\lvert\lvert(\bullet)\rvert\rvert_2$	2-norm
$\wedge$	And
$\boldsymbol{\nabla}$	Nabla operator
$\boldsymbol{\nabla}_{\boldsymbol{x}}(\bullet)$	Gradient with respect to $\boldsymbol{x}$
$\mathbb{R}$	Space of real numbers
$\otimes$	Outer product
det	Determinant
Lin	Linearization operator
tr	Trace operator
ln	Natural logarithm
sgn	Sign function

1. Introduction

This work is concerned with the design and control of a novel cardiac assist device. In the following chapter, the reader is introduced to the current state of heart failure and its impact on society, to the physiology and pathology of the human heart, to standard treatment strategies of heart failure and to the state of the art of cardiac assist technology. Furthermore, shortcomings of existing systems are discussed to motivate the novel approach of the system under investigation. The introduction concludes with the research objectives and an outline of this work.

1.1. Motivation

Heart failure (HF) affects more than 26 million people worldwide [83]. In developed countries 1 to 2 % of the adult population are estimated to suffer from HF [38]. In the USA roughly 6.5 million people are affected and a total of 960000 new diagnoses are reported yearly [9], with over 50 % of all patients being 75 years or older [123]. In 2015, 47,414 deaths due to HF were recorded in Germany, making it the third most common cause of death [108]. HF can be described as the inability of the heart to supply all organs of the body with a sufficient amount of oxygenated blood. Symptoms include shortness of breath, fatigue and swelling of legs and ankles. The condition is ultimately lethal [98], [115]. In most developed countries, where the majority of HF related statistics originate, prevalence has been increasing, while incidence appears to have stabilized or even slightly decreased in the recent years [123]. The increase in prevalence is mainly driven by an aging society [109], [84]. A projection for the US estimates an increase of 46% to about 8 million affected patients in 2030 [9]. This trend can be adopted for all aging societies worldewide. In contrast, enhanced prevention, diagnosis and therapy strategies are responsible for stagnating or even dropping incidence numbers [98],[38]. HF is the number one cause of hospitalization in the United States and Europe, accounting for roughly 2 % of all admissions [3]. It is therefore a burden for health care systems. Most european countries spend more than 2 % of their health care budget on HF related treatments, whereof 70 % are consumed for hospitalization alone.

The burden of HF is devastating and it is important to tackle this global problem from all sides. One promising approach are technical apparatuses, such as cardiac assist devices, which intend to improve the quality of life of patients, bridge the time to heart transplantation or even fully replace the diseased heart. However, the development of such an apparatus is complicated since the wide range of patient-individual needs has to be met. Furthermore, developing and launching such systems requires adherence to normative requirements. Thus, there is a need to allow for fast engineering iterations and patient-specific treatment planning.

In recent years, many such systems have been developed and their clinical importance has been growing. In the fight against HF, AdjuCor GmbH (Munich, Germany) has been pursuing the development of a novel cardiac assist device. Our research group has been collaborating for many years with AdjuCor by developing prototypes and computational models to predict physiological and pathological cardiac mechanics [54], [44], [45]. This thesis is part of that collaboration. It partly builds on previous work but rather focuses on the technical aspects and hence on the cardiac assist device, than on the medical part. But ultimately, technical and medical characteristics are strongly coupled and only if mutually considered, can the developed system successfully contribute in the fight against HF.

1.2. The cardiovascular system

The heart is the central organ of the circulatory system. It is a muscular organ which pumps blood through the blood vessels of the entire body. Figure 1.1 depicts a schematic of the heart and a simple representation of the connected blood vessel networks. The heart consists of four compartments, namely two atria and two ventricles. Oxygen depleted blood, as venous return from the body, gathers in the right atrium (RA), from which it is sucked into the right ventricle (RV). It is then ejected into the pulmonary artery through the pulmonary valve and oxygenated in the alveoli of the lung. The oxygen rich blood, which gathers in the left atrium (LA), is sucked into the left ventricle (LV) through the mitral valve and ejected into the systemic circulatory system through the aortic valve. The blood flow is separated right after the aortic valve, where a part supplies the heart muscle through the coronary arteries. The flow is further split in the aortic bow, supplying brain, arms and the lower body. The blood is pumped through arteries, arterioles and capillaries where the exchange of gas and nutrients eventually takes place. Their diameter are variable and define the systemic resistance. Once the blood has passed the fine capillaries, it must be pumped back to the heart through the venous vessel network and usually against gravity. Veins are compressed by neighboring skeleton or arterial muscle contraction and venous valves prevent blood to flow back. Thereby, an unidirectional flow is established and the blood is transported back to the heart, where it reenters the RA. The entire blood vessel system of a human has an impressive length of approximately 96000 km.

The cardiac contraction is, under normal conditions, triggered by a spontaneous depolarization at the sinus node, located in the right atrium. The right atrium is connected to the sinus node through a direct connection. However, this electrical stimulus spatially propagates from the right atrium over the atrioventricular node (AV node), through the bundles of His in the septum down towards apex and from the bundle branches to the respective Purkinje fibers in both ventricles. These fibers excite the ventricles from apex to valvular plane, causing their contraction. The repolarization process restores the initial state and propagates from apex to base. This cycle repeats and the number of cycles per time defines the heart frequency or heart rate (HR). Typical resting pulse rates are 50-80 beats per minute (bpm) [109]. The described propagation can technically be measured and is known as an electrocardiogram (ECG), which is widely used by clinicians for many purposes and its use during surgery is standard.

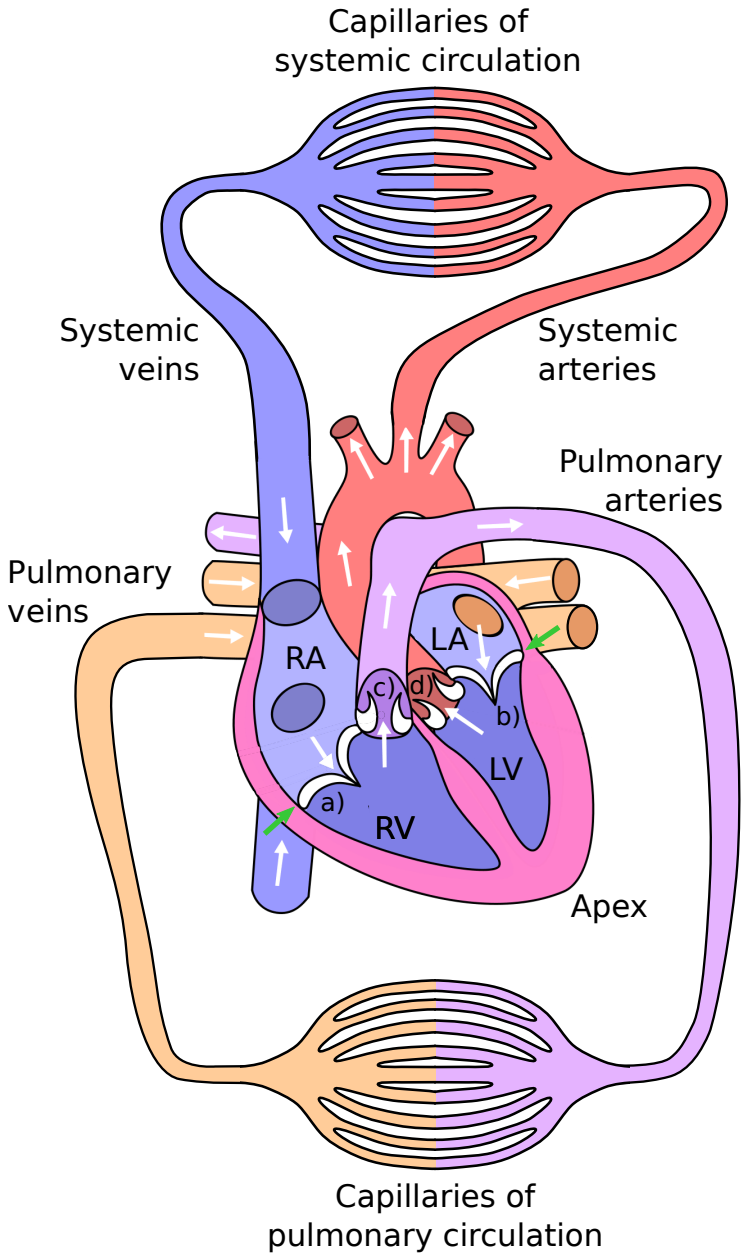

Figure 1.1.: Schematic of the circulatory system: Upper vessels represent the larger systemic circulation system, including most organs, muscles and other body parts. The lower vessels indicate the pulmonary circulation system, which transports blood back and forth from heart to lung for gas exchange. The two right chambers, i.e. right atrium (RA) and right ventricle (RV), are separated by the atrioventricular valve a), also called tricuspid valve. The pulmonary valve is marked with c). Left atrium (LA) and left ventricle (LV) are separated by the atrioventricular or mitral valve b) and d) is the aortic valve. All white arrows indicate flow directions. The tip of the heart is referred to as apex and the two green arrows indicate the valvular plane.

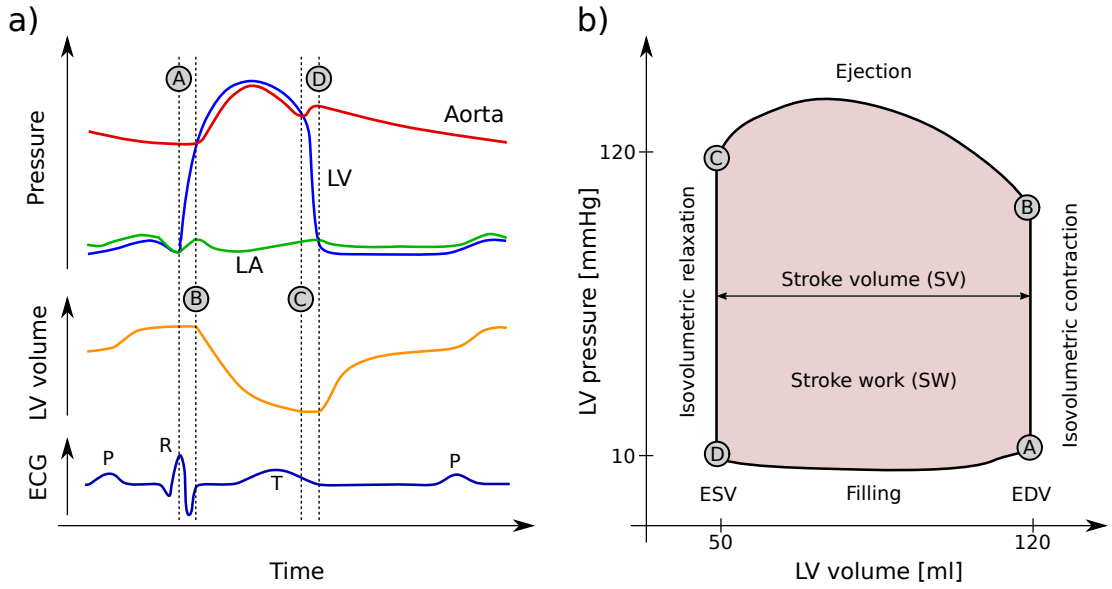

Figure 1.2.: Generic pressure, volume and ECG curves during one heart beat in a) as well as the pressure-volume (pV) loop of the left ventricle (LV) in b). At the end of the diastole (A), the ventricles are filled with blood and the mitral valve closes. The R-wave peak in the ECG signal marks the beginning of the heart muscle contraction, which is isovolumetric between (A) and (B). When the aortic pressure is built up in (B), the aortic valve opens and the blood is ejected between (B) and (C) into the aorta, before the aortic valve closes at point (C). This end point of contraction is characterized by the end of the T-wave in the ECG signal. During the subsequent isovolumetric relaxation phase, the LV pressure drops below the left atrium pressure, provoking the mitral valve to open at point (D). The cardiac cycle ends by the filling phase between (D) and (A), with the atrial contraction visible in the ECG as the P-wave. In b), the cardiac stroke volume (SV) is indicated as well as the cardiac stroke work (SW), which is the enclosed area of the pV loop.

The cardiac cycle is often described as a pressure-volume (pV) loop, as depicted in figure 1.2 b). By the time of the spontaneous depolarization at the sinus node, the heart is at the end of the previous heart cycle and atria and ventricles are filled with blood. Since the stimulus reaches the atria first, they contract and are responsible for approximately 20-30 % of the total ventricular filling [109]. Typical end-diastolic volumes (EDV) are around 120 ml for an average 70 kg man [21]. The first phase of ventricular contraction is called isovolumetric contraction phase, since the pressure has to build up to the respective systemic pressures first, before pulmonary and aortic semilunar valves open and blood is ejected into pulmonary artery and aorta, respectively. As long as the systolic pressures of the pulmonary and systemic system can be maintained by the contracting heart, blood is further ejected. Meanwhile, the two atrioventricular valves (right: tricuspid; left: mitral) remain closed, preventing backflow into the atria. The end of the contraction, when the semilunar valves close is called the end-systolic point and the remaining end-systolic volume (ESV) is about 50 ml, again for an average 70 kg man [21]. The phase hereafter is called isovolumetric relaxation, since all valves remain closed. Once the ventricular pressure drops be-

Quantity	Value	Unit
Heart rate (HR)	70	bpm
Total blood volume	5	l
End diastolic volume (EDV)	120	ml
End systolic volume (ESV)	50	ml
Stroke Volume (SV)	70	ml
Cardiac output (CO)	4,9	l/min
Ejection fraction (EF)	58	%
End-systolic pressure (ESP)	120	mmHg
End-diastolic pressure (EDP)	80	mmHg

Table 1.1.: Normal cardiovascular conditions for a healthy human male weighting 70 kg [3].

low the atrial pressure, both atrioventricular valves open and blood flows into the ventricles. The underlying suction effect arises from a valvular plane displacement throughout the cardiac cycle [109]. The following medical parameters are widely used by clinicians to assess the cardiovascular status and its change during treatment. The difference between end-diastolic and end-systolic volume is called the stroke volume (SV). It is mostly given in units of milliliters [ml] or liters [l] and defined by:

$$\mathrm{SV} = \mathrm{EDV} - \mathrm{ESV}. \tag{1.1}$$

The cardiac output (CO) relates stroke volume and time. It is given in units of liters per minute [min^{-1}]:

$$\mathrm{CO} = \mathrm{HR} \cdot \mathrm{SV}. \tag{1.2}$$

The ratio of SV to EDV is called the ejection fraction (EF) and is a standard parameter to assess the severity of HF. It is given in percent by:

$$\mathrm{EF} = \frac{\mathrm{SV}}{\mathrm{EDV}}. \tag{1.3}$$

Low end-diastolic pressure (EDP) creates higher perfusion gradients, resulting in an enhanced blood supply to the myocardium. End-systolic pressure (ESP) is always equal to the aortic pressure and thus to systemic blood pressure. Therefore it is closely related to high blood pressure (hypertension) diseases. Table 1.1 lists typical values for a healthy human male. Note that ranges for biological parameters vary strongly without necessarily being pathological.

A slight discrepancy of the SV of both ventricles for an extended period of time can lead to severe diseases, like e.g. pulmonary edema. To prevent such cases, the heart can adapt to small and temporary variations of a so-called pre- and afterload. The former is the amount of stretch of cardiac muscle cells due to ventricular blood filling, whereas the latter is the resistance the contracting LV experiences when ejecting blood against the systemic blood pressure [51]. The ability to adapt to changes in pre- and afterload, for the purpose of alleviating SV imbalances, is known as *Frank-Starling-Mechanism*. An increased preload, e.g. due to a currently higher volume in the pulmonary system, overstretches cardiac muscle cells and enables the generation of higher pressures, which increases the SV. On the other hand, a greater afterload would result in an increased EDV in a first step, before normal SV is restored due to the augmented ventricular filling.

1.3. Heart failure

Many different definitions for HF can be found in literature [111]. A very common one defines HF as a complex clinical syndrome, characterized by the inability of the heart to sufficiently pump blood or to completely fill with blood (or even both). It normally develops from either structural or functional changes or both. The disease is progressive and ultimately terminal [98], [115].

In essence, two underlying mechanisms lead to HF, namely systolic and diastolic dysfunction. The latter is also referred to as HF with preserved EF (HFpEF) or backward-failure. In this case, EF is normal (>50%) even though clinical signs of HF are present. It is characterized by a reduced ventricular filling, which, due to the Frank-Starling-Mechanism, results in a decreased SV. The impaired filling may have various causes, but is often related to a myocardial thickening or stiffening, mainly due to remodeling processes to compensate for chronic hypertension or myocardial damage, e.g. after myocardial infarction (MI). The typical thickening of the ventricular wall is also referred to as *concentric ventricular hypertrophy* and a *hypertrophic cardiomyopathy* (HCM). In contrast to the remodeling of wall thicknesses, an underlying systolic dysfunction is associated with myocardial dilation as a response to the elevated myocardial stretching. Thereby, wall strain is reduced, but so is the systolic performance. This pattern is referred to as *eccentric ventricular hyperthrophy* and a *dilated cardiomyopathy* (DCM) [64]. Systolic dysfunction frequently implicates diastolic dysfunction [115]. Figure 1.3 summarizes the presented concepts.

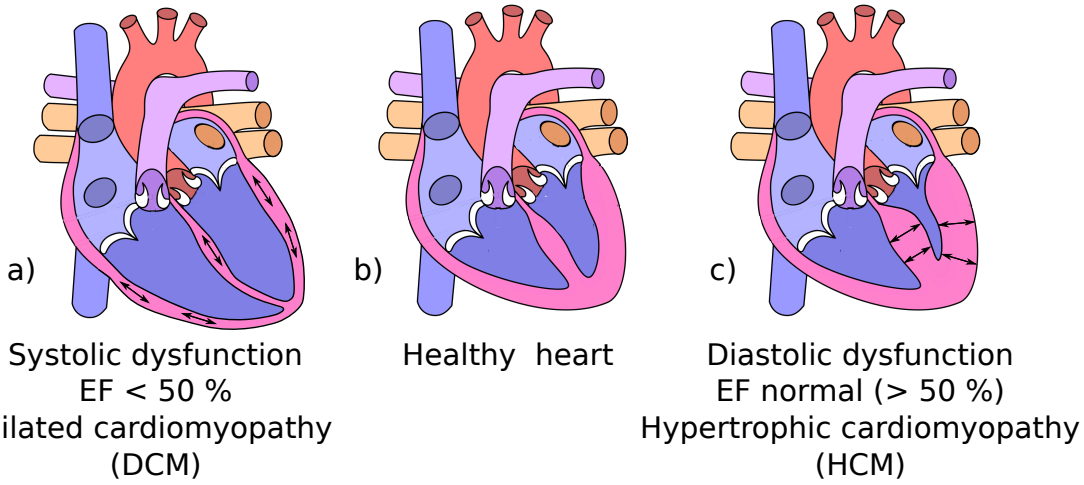

Figure 1.3.: Cardiac remodeling in systolic dysfunction due to ventricular overfilling is based on eccentric growth and characterized by dilated ventricles as can be seen in a). It is also referred to as heart failure with reduced ejection fraction (HFrEF). In contrast, EF is preserved (HFpEF) in the case of diastolic dysfunction, which is driven by concentric growth as indicated in c). b) shows a healthy heart for comparison.

Two-thirds of all HF cases can be associated with ischaemic heart disease, chronic obstructive pulmonary disease, hypertensive heart disease and rheumatic heart disease. In addition, cardiomyopathy and myocarditis are known to be HF related diseases. The dominance of one or

NYHA class	Description	1-year survival[%][115]
I	patients without limitations of physical activities (but with cardiac disease)	95
II	patients with slight limitations of physical activities	80-90
III	patients with marked limitations of physical activities	55
IV	patients with symptoms present at rest	5-15

Table 1.2.: Classification scheme of the *New York Heart Association* (NYHA). Another classification by the *American College of Cardiology Foundation/American Heart Association* (ACCF/AHA) uses stages A to D, where A defines normal heart conditions, B corresponds to NYHA I, C to the NYHA classes II and III and D to NYHA IV [51].

more of these trigger diseases depends on the patient population [123]. Valvular dysfunction, in which blood can flow back, is referred to as *regurgitation* and can lead to HF [51].

A person is diagnosed with HF when typical symptoms arise and evidence of cardial dysfunction is present [84]. The latter can be realized by EF measurements in the case of HFrEF or by measurements of flow through mitral or pulmonary valve in case of HFpEF. The cardinal symptom of HF is subjective shortness of breath in addition to other typical signs like fatigue or lower limp swelling [115]. Patients are classified by the severity of their symptoms in a scheme introduced by the *New York Heart Association* (NYHA). Table 1.2 describes NYHA classes I-IV.

By the time the patient is classified NYHA class IV, the course of HF has almost reached its fatal conclusion. Those patients have normally been advancing through all previous classes during a time span of years or even decades. Once diagnosed, approximately 50 % of all patients die within 4 to 5 years [84], [9] and suffer a poor quality of life [98]. However, the potentially long course and the knowledge of risk factors such as age, obesity, diabetes, smoking, activity level and genetic predisposition allow some early control of the likelihood of occurrence and progression pace. Note that these risk factors are mutual for hypertension, which is considered a main driver of HF.

1.4. Heart transplantation

The best treatment strategy is always prevention. Many of the risk factors for HF are controllable and their consideration should be the basis of any holistic treatment concept. However, HF will continue to be one of the most resource intensive diseases in the coming decades simply because of aging societies. Preceding diseases are treated according to their specific guidelines. They may include, among many others, pharmacological therapy, revascularization surgeries, cardiac valve replacement surgery, implantation of an internal cardiac defibrilator or resynchronization therapy. That said, all therapies will fail at one point for end-stage patients. The gold standard is heart transplantation with high 1-year and 5-year survival rates of 84,5 % and 72,5 % respectively[1]. After 20 years 21 % of all patients undergone heart transplantation are still alive [117]. Reported median post-transplant survival times have reached 11 to 12 years [49], [74]. However,

[1]For comparison: 1 and 5-year survival rates in the 1980s where 76,9 % and 62,7 %, respectively [117].

donor hearts are very limited compared to the demand, which, correlating with the prevalence of HF, is increasing. A total of 1123 patients were on the waiting list for transplantation in Germany in 2017, while only 257 underwent surgery. Since 2012, new listings as well as actual transplantations have decreased 29.7 % and 25.7 %, repectively [88]. The discrepancy between demand and supply can similarly be observed in the United States [49], [36]. Also, the waiting time for an appropriate donor heart ranges from a few days to over two years, depending on urgency and availability [41], [101]. This time is precarious as the mortality while on the waiting list is between 15 to 30 % per year [11]. Cardiac assist systems are continuously growing in importance as alternative therapies for end-stage patients awaiting donor hearts.

1.5. Assist technology

Mechanical cardiac assist systems were first investigated in the 1960s, but it was not until after the turn of the millenium that these systems started to play a central role in long term therapy. Today, they are the only option for end-stage HF patients awaiting or not eligible for heart transplantation. The number of potential candidates for such therapy is estimated 125000 - 250000 in the United States alone [74].

1.5.1. Clinically applied systems

The review in this section will present applied systems for long-term use only. For short-term support, other products are commercially available and in clinical use. A good overview for those systems can be found in [11].

Various registries worldwide were created to faciliate reporting of ventricular assist device (VAD)[2] treatments. The Interagency Registry for Mechanically Assisted Circulatory Support (INTERMACS) includes over 25000 patients from the United States and has contributed since 2016 to the International Registry for Mechanically Assisted Circulatory Support (IMACS) with over 14000 patients from 35 countries [65], [61]. In the US, the number of primary LVAD annual volume has peaked in 2019 with 3198 implantations [75]. In Germany, implantations have recently reached approximately 1000 VADs and 30 *total artificial hearts* (TAH) surgeries per year [11]. The many kinds of VADs can be categorized by indication, type of support or type of flow generation as well as pump technology.

Appropriate indication is essential to ensure a successful VAD therapy. Table 1.3 lists the indications for which VADs must be approved prior to clinical usage. The indications *bridge-to-decision* (BTD) and *bridge-to-recovery* (BTR) play a minor role as they account for only 2 % of all IMACS patients. The device strategy *bridge-to-transplant* (BTT) was selected for 57 % as they were either actively listed or candidates for heart transplantation. For 41 % of all patients,

[2] Various notations for mechanical cardiovascular assist devices exist, e.g. Mechanically Assisted Circulatory Support Systems (MACSS), Mechanically Circulatory Support Systems (MCSS) or Mechanical Cardiac Assist Device (MCAD). VAD is the most common notation and will be used as umbrella term in this work.

Indication	Description
Bridge-to-decision (BTD)	Urgent cases; decision regarding therapy often not certain at the time of implantation.
Bridge-to-recovery (BTR)	Therapy until heart performance has recovered. This may be after heart surgery or for patients suffering from myocarditis.
Bridge-to-transplantation (BTT)	Patient is in need of support, but no appropriate donor heart is available at the moment.
Destination therapy (DT)	End-stage patients not eligible for heart transplantation.

Table 1.3.: Indications for VAD implantation. Indication for BTT or DT is about to be changed as to whether temporary or chronic use is necessary. Indications may also change during therapy [11].

destination therapy (DT) remained the only option [61]. ACCF/AHA define the indication for VAD support when EF drops below 25 % for advanced systolic dysfunction.

The type of support refers to the assisted part of the cardiovascular system. VADs can be designed or applied to support both ventricles or exclusively the right or left ventricle, referred to as BiVAD, RVAD or LVAD, respectively. The latter is the most common type of support, accounting for 93 % of all IMACS registered devices. Biventricular support was used in 5 % of all cases, meaning the combined use of two VADs, one for each ventricle. Due to the rarity of isolated RV failure, no durable RVAD systems are available. However, LVADs may be used contrary to their specified purpose for RV support [42]. A quite radical type of cardiac assist devices are TAHs, which are used for patients with biventricular dysfunctions with no chances of recovery, e.g. severe myocardial damage after MI. They fully replace the patient heart and are mainly used as BTT. The only BTT approved biventricvular support systems on the market are the SynCardia TAH (SynCardia Systems, LLC, Tucson, AZ, USA) and the Carmat C-TAH (Carmat SA, Vélizy-Villacoublay, France). The latter received CE certification in December 2020. TAHs are applied in approximately 2 % of all registered cases [65], [61].

Pump technology is generally assigned to a certain device generation. First generation VADs generated pulsatile blood flows to mimic physiological conditions, but their size and weight were considerable and their durability poor. Pumps usually failed within the first two years [74] and pulsatile VADs have ultimately vanished from clinical practice. Relevant systems were, among others, HeartMate XVE™, Thoratec IVAD™(both former Thoratec Inc., now Abbott Laboratories, Lake Bluff, IL, USA) or BerlinHeart®(Berlin, Germany). The second device generation built on this experience and led to continuous flow VADs, usually designed as axial-flow devices, e.g. the widely used HeartMate II™(Abbot) or the Jarvik 2000®(Jarvik Heart Inc., New York, NY, USA). Continuous flow (CF) devices account for 95 % and 92 % of all devices in the INTERMACS and IMACS registry, respectively [60], [61]. The third generation is characterized by magnetically levitated impeller systems to reduce blood trauma, e.g. hemolysis and most systems use centrifugal pump technology. Important models are the HeartWare

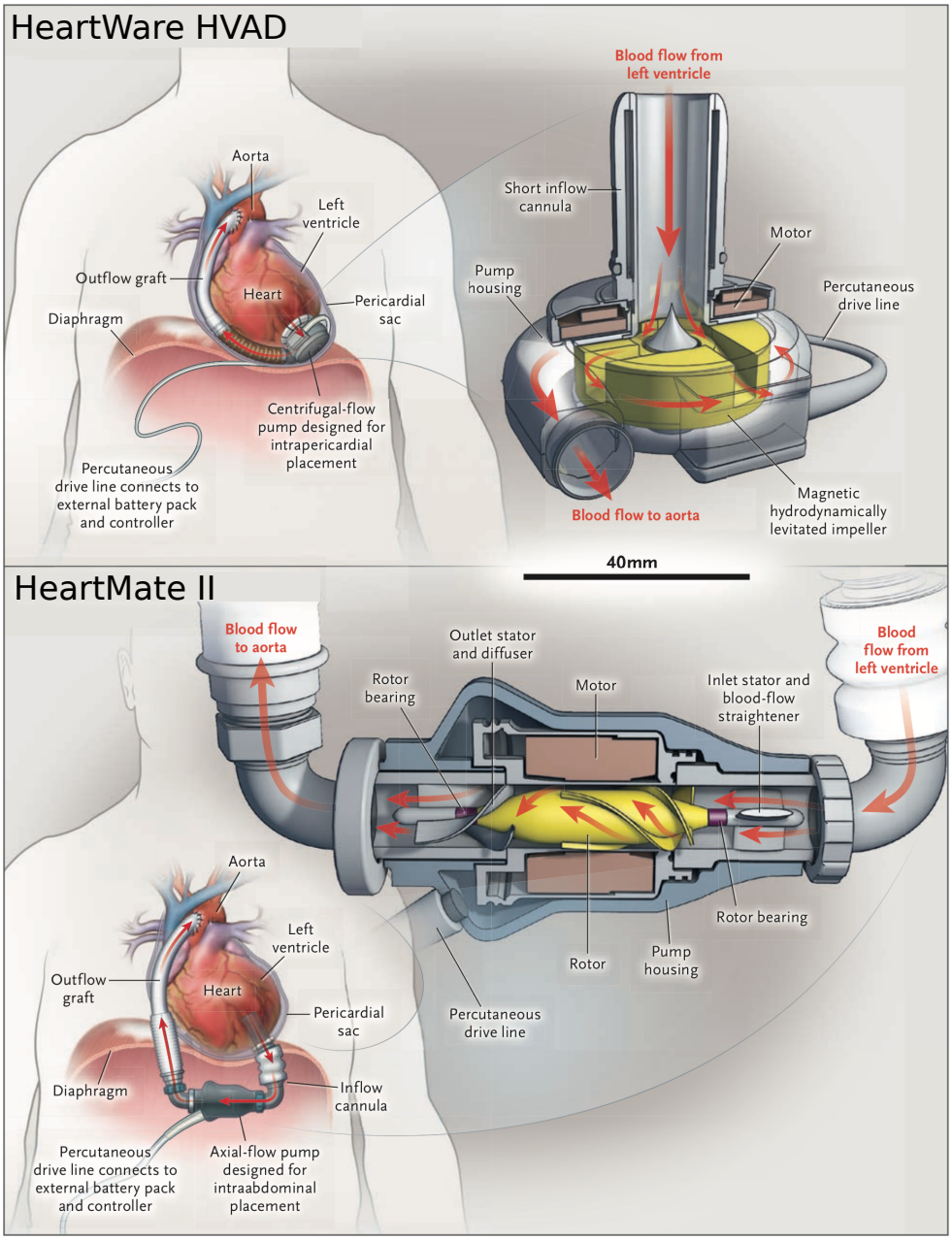

Figure 1.4.: Centrifugal-flow intrapericadal VAD HeartWare HVAD®and axial-flow VAD HeartMate II™. Reproduced with permission from [93], Copyright Massachusetts Medical Society.

HVAD®(Medtronic, Dublin, Irland) and Abbot's HeartMate III™(HMIII) [11]. These last two, together with HeartMate II™(HMII), are the most widely reported systems in clinical trials. Figure 1.4 depicts the application of HeartWare HVAD®and HeartMate II™as well as some technical details. They both have an inflow and outflow cannula, a pump, a percutaneous driveline and an electrical controller. The inflow cannula is inserted into the ventricle at the apex and sewed to the epimyocardium. The outflow cannula normally enters the ascending aorta. The

supported ventricle is then unloaded by pumping the blood parallel to the natural flow path. The mentioned systems HMII, HMIII and HVAD can generate flows up to 10 l/min. Systems of the latest generation reach these flows at maximum pump speeds between 4000 and 5500 revolutions per minute (rpm) [102]. The HMIII features wider flow channels to further reduce shear-stress induced adverse effects on the blood cells, e.g. hemolysis. All blood contacting surfaces are textured with sintered titanium microspheres with the intention of providing a less thrombogenic tissue interface to the surrounding blood. Pump speed variations allow pump washouts and further contribute to a minimization of thrombogenesis.

The outcome of VAD therapy has significantly improved in the recent years. This is due to a multitude of technical innovations, but also due to improved patient selection, training and emergency management. The 1- and 2-year survival rates in the years from 2015-2019 are 82 % and 73 %, respectively [75]. Isolate biventricular and TAH 1-year survival reach 53 % and 48 % [61]. DT patients have lower survival rates due to higher comorbidities. The impact of VAD therapy on the patient's quality of life (QoL) is usually reported to be favorable [60], [68]. However, LVAD support may also create new physical impairments or shift patient anxieties to device related failures, as reported by Adam and Wrightson [1], who have reviewed 19 QoL studies concerning LVAD therapy. Nonetheless, these recent advancements are increasing user confidence and work towards treating a larger number of end-stage HF patients in the future.

1.5.2. Shortcomings of clinically applied systems

Despite the previously mentioned achievements, VAD patients remain at high risk for fatal events. In the final report of a large study, conducted with HMII and HMIII, 201 of 1020 patients died in the first two years [73]. The dominant causes of death were in 28 % due to RV failure, 21 % were adjudicated to stroke, 14 % to infections and 4.5 % due to pump thrombosis. The remaining causes were each less than 3 %. The IMACS statistics paint a similar picture, where multiorgan failure (21 %), right heart failure (20 %) and stroke (19 %) are the preponderant causes of death [61]. Nonlethal adverse events are predominately bleeding and infections followed by thrombotic events, cardiac arrhythmia, respiratory failure and renal dysfunction [60], [61], [67]. The treatment of complications puts patients at additional risk when they again have to undergo surgery. Pump replacement was needed in 7-10 % of patients enrolled in recent studies whereof 81 % were due to pump thrombosis. In 9-13 % post-implantation RV failure was treated by RVAD implantation [93], [73]. Immediate biventricular support can drastically reduce postoperative mortality and related events, e.g. renal failure [59]. In the general case of pump stoppage the patients heart may maintain organ perfusion without the support system, but a restart of the system is generally only recommended within the first hour after occurrence. Restarts thereafter pose a great risk for thrombotic events and VAD specialists are required [67].

The conventional surgery procedure is a complete median sternotomy with the generally narcotized patient being connected to a heart-lung machine for two to three hours. Recent device developments allow for minimally invasive implantation procedures [72], [37], but heart-lung machine interaction remains traumatic [62].

After discharge, up to 50 % of patients return to the emergency department within the first month and on average around 7 times per year [67]. Pump events are responsible for the longest hospital

stays with a median of 9 days, hence accounting for most of the direct hospital costs, followed by events directly related to the heart (arrythmias, HF, MI), stroke and bleeding with median stays of 7, 5 and 3 days, respectively [2].
The shortcomings of existing systems mainly stem from blood contacting surfaces, blood thinning and the absence of biventricular support. Even if further improvements of applied systems are promising, fundamentally new concepts might be necessary to shift clinical outcome of cardiac assist devices towards those of heart transplantation.

1.5.3. Direct cardiac compression devices

Some systems are briefly presented here to provide an overview of different previously pursued approaches. A detailed summary of those systems is provided in the work of Naveed et al. [79] and those of Jagschies [54], [53]. Direct cardiac compression devices (DCCD) have been investigated for over 50 years. The first system in this field is the Anstadt cup from 1966 [5], which has extensively been studied over the years. A more recent version can be seen in figure 1.5 a). It consists of a rigid cup with an inlaid diaphragm and is connected to a pneumatic drive unit. The implant sticks to the heart by suction. Applied pressures for heart support ranged between -135 to 160 mmHg. The Heart Booster (ABIOMED Inc., Danvers, MS, USA) was intended for chronic use and is shown in figure 1.5 b). It consists of multiple inflatable, radially connected tube-like chambers, forming a bowl, which are put over the ventricles and adhere to the epicardial surface using biocompatible glue. The implant with initially flat chambers fits the end-diastolic heart geometry. When hydraulically filled during systole, the chambers become sleeves, reducing the inner diameter up to 60 % and eventually compressing the heart [66]. The Heart Patch, in contrast, consists of two separate, inflatable pads to allow for independent left and right ventricular support. The adhesion was based on biointegration which required about two weeks of time prior to the start of therapy [71]. Figure 1.5 c) depicts the concept.

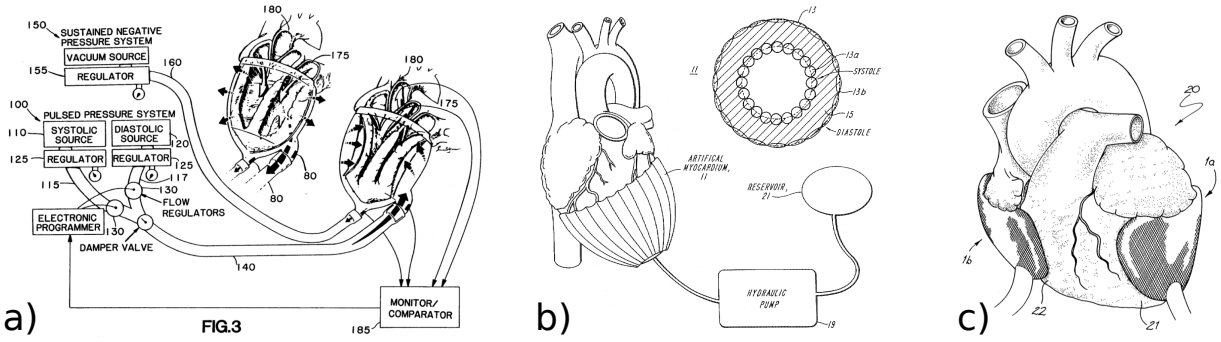

Figure 1.5.: Patent figures of cardiac compression devices (CCD): A more recent version of the Anstadt cup in a) [6], the Heart Booster in b) [95] and the HeartPatch in c) [50])

More recent attempts to develop DCCDs are depicted in figure 1.6, where a) shows a so-called soft robotic sleeve approach. It aims to compress the heart while the natural cardiac twisting motion is mimicked in order to assist diastolic ventricular filling. Therefore, soft pneumatic artificial muscles are integrated circumferentially and in myocardial fiber orientation in a multilayer design [90], [91]. The muscles are silicon coated and embedded in a thin silicon layer,

giving the implant a similar elasticity as myocardial material and aiming to fit the patient's heart geometry. All muscles are separately activatable, allowing for a great variety of motion patterns. In an acute drug induced porcine HF model (n=6, β-blockade), reducing the CO to 45 %, device support could almost fully restore the CO to 97 % of initial conditions. The natural twisting motion had almost vanished in the acute HF model and could be restored by the twisting properties of the system [91]. A similar approach using pneumatic artificial muscles is followed by Payne et. al. [81].

The CorInnova (CorInnova, Inc., Houston, TX, USA) heart assist device is inserted within the pericardium and encloses the ventricles from apex to base, as can be seen in figure 1.6 b). An inner thin polyurethane bladder can be filled with fluid to adapt to the patient-specific heart geometry. Arranged behind, a second bladder can be inflated with air, triggered by the patient's ECG. Both bladders are attached to a nitinol structure, allowing easy self expansion during the minimal-invasive implantation procedure. The CorInnova assist device design is a further improvement of the work previously presented by Moreno et. al. in 2011 [76], [77]. At the moment, the device is intended for acute, short-term support and surfaces are designed to minimize adhesion to the epimyocardium, but Hord et. al. mention their intention for long-term use in the future. In a drug induced, porcine HF model (n=4) the device could increase CO by 1 l/min and systolic blood pressure as well as peak left ventricular pressure by 16 mmHg, when a mean systolic assist pressure of 17 mmHg (peak 25 mmHg) was applied [48].

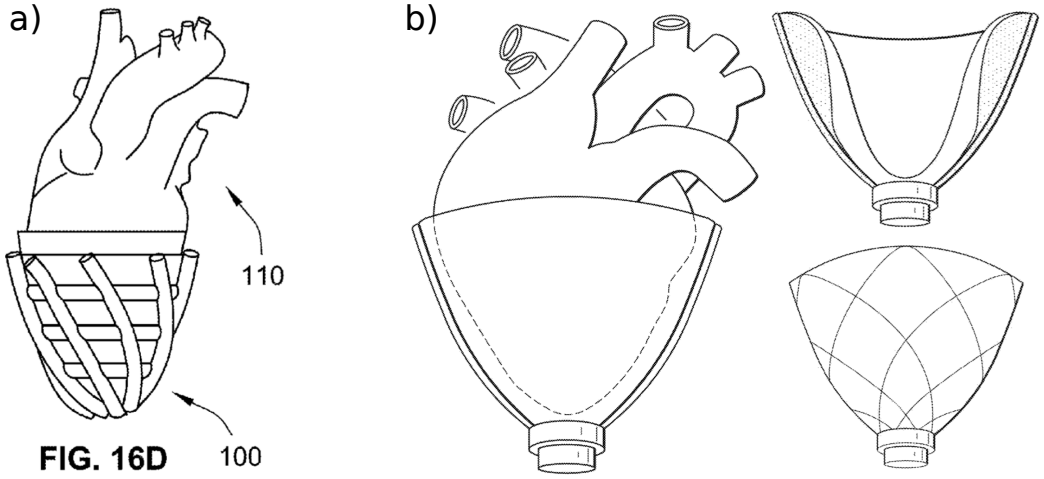

Figure 1.6.: Soft robotic sleeve approach with the intention of mimicking both, cardiac contraction and twist, by means of pneumatic artificial muscles in a) [92], CorInnova heart assist device in b) [18].

Many DCCD approaches have been investigated, some of them even in humans, but none of the systems are currently in clinical use or have ever been approved for long-term support. Multiple reasons can account for this. Adverse immunological reactions to artificial surfaces have probably been limiting long-term application so far. An implant has to deal with the heart's beating motion, comply with epimyocardial and pericadial tissue needs, should be implantable in a minimally-invasive procedure and must eventually support the weakened cardiovascular system. Due to a lack of data, little is known about long-term effects of direct cardiac compression (DCC) and thus serious efforts to develop and approve such systems implicate a great entrepreneurial

risk. So far, present DCCDs have failed to fully overcome the bio-technical hurdles of long-term treatment and concurrent improvements in the outcome of VAD therapy have drawn the focus further away from DCCD development, despite their intrinsic advantages. Of the previously mentioned DCCDs, only the CorInnova heart assist device is being professionally developed, aiming for a sophisticated, clinically used product. In the next section, a promising heart assist device of the company AdjuCor GmbH (Munich, Germany) is presented.

1.5.4. A novel biventricular assist device (BiVAD)

A novel biventricular assist device (BiVAD) for long-term HF therapy has been developed by the company AdjuCor GmbH (Munich, Germany). It consists of a patient-specific, yet soft implant, which is placed in the pericardial space, covering the heart from apex to base. Computer tomography (CT) data is used to obtain the epicardial geometry, which is the starting point of the manufacturing process. Together with a structured implant surface, long-term adhesion and effective energy transfer to the heart is ensured. The implant features electrodes to record the patient ECG, which is the source signal for any support control. The ECG is analyzed in a cascade of sophisticated algorithms to precisely detect R- and T-waves, thereby ensuring a safe, heart-synchronous inflation and deflation [100]. Three built-in bladders, referred to as expandable units (EU), are inflated and deflated according to the output of the ECG algorithm. Two are located on the anterior and posterior walls of the LV and one laterally on the RV. Their pressure-volume relationships are highly individual and depend, among others, on the patient heart size, disease course (e.g. infarct regions) and spatial particularities, e.g. due to previous heart surgeries or available space. The EUs are individually connected over a skin-penetrating driveline to an extra-corporal, pneumatic drive unit. This drive unit periodically establishes a pressure potential and releases air into and out of the EUs. Figure 1.7 shows a depiction of drive unit, driveline, implant and patient.

The implantation can be performed in a minimally-invasive procedure, avoiding lengthy general anesthesia, open chest surgery and traumatic heart-lung machine usage. Thus the patient can be discharged from hospital early after surgery, improving quality of life and drastically reducing hospitalization related costs. The system is designed to avoid post-operative adverse events, especially major shortcomings due to blood-contacting surfaces and exclusive left ventricular support as it was outlined in section 1.5.2. The system works in support of the heart's native functioning and an impairment of blood delivery of the unassisted heart is minimized by the implant design. Pressure setpoints can individually be chosen by the treating clinician for each EU to tune the amount of LV and RV support.

As outlined, AdjuCor's BiVAD introduces many advantages over state-of-the-art support devices and may help to provide a suitable therapy for patients awaiting a donor heart or for those not eligible for heart transplantation. However, during device development, numerous questions of a technical and medical nature need to be answered. They mainly stem from the wide variety of patients and their conditions prior to therapy. In particular, the individual disease course, heart size, medication and systemic condition impede a straight-forward formulation of requirements. Furthermore, any validation of implemented features can be time and cost intensive due to long lasting preparatory and evaluation work during animal trials, not to mention the lengthy device

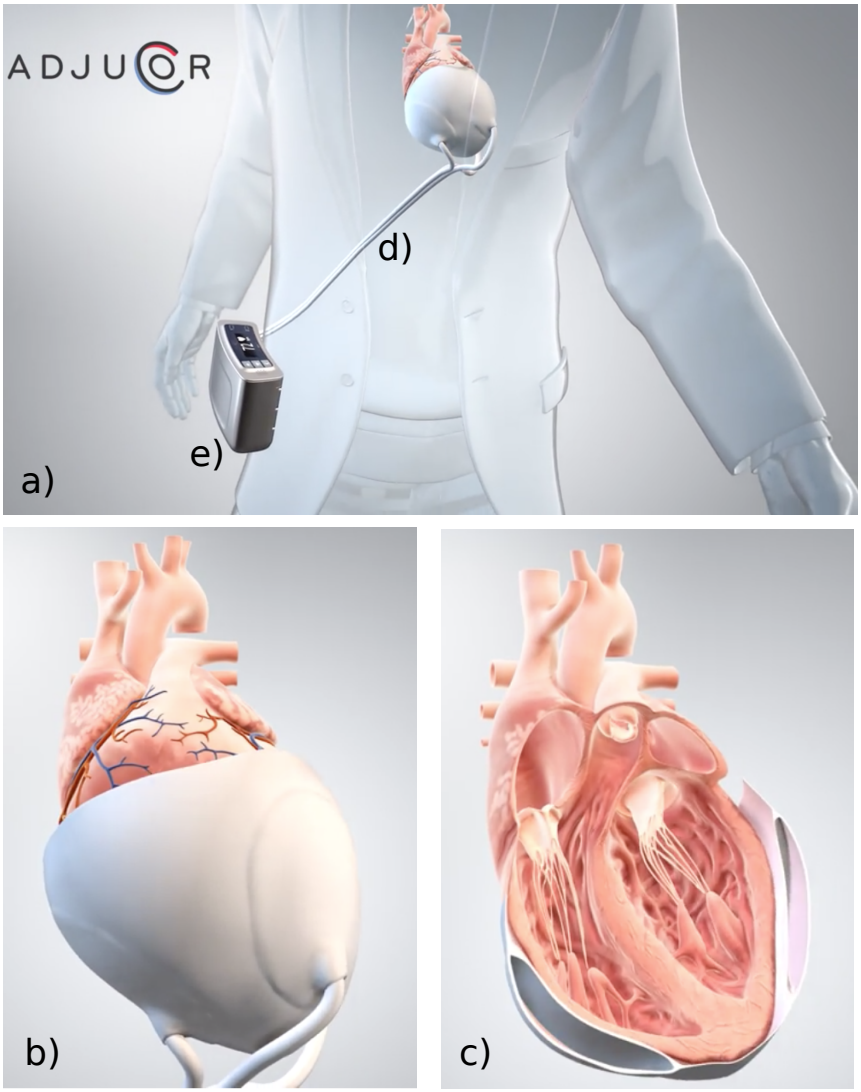

Figure 1.7.: AdjuCor's system (AdjuCor GmbH, Munich, Germany): a) shows the entire system, consisting of implant around the patient heart, driveline d) and drive unit e). A close-up of the implant can be seen in b) and a section in c), showing inflated units supporting the heart.

approval process. This alone motivates the pursuit of computational tools to accelerate engineering and validation processes, as earlier availability of AdjuCor's BiVAD may save lives. The following aspects emphasize the need for computational models in the development process: Firstly, engineering iterations can be accelerated by assessing the specification compliance of a changing component or an alternative design before prototyping. Also, the fulfillment of normative requirements as e.g. temperature development can be simulated beforehand. Secondly, the number of animal experiments can be reduced. The development of a safe system to be used in humans is paramount and animal trials may therefore be unavoidable. However, some animal sacrifice may be obviated if the questions to be answered can be analyzed in-silico. Thirdly, the individual support efficacy can be estimated prior to implantation and hence prior to the risk of

a surgery. Device parameters can further be tuned beforehand to optimize the individual therapy outcome. Finally and as a consequence of the before mentioned aspects, in-silico analyzes help to reduce costs.

1.6. Computational models of cardiac assist technology

Cardiac assist devices have been developed for many years and various aspects have deeply been investigated by researchers, with the main focus on hemodynamic effects. Especially computational models to predict support effects are of interest, as they allow to reduce time and resource intensive clinical studies and animal sacrifices. Therefore, many researchers have developed lumped-parameter cardiovascular models. Purely 0-dimensional (0D) cardiovascular models under cardiac assist are easy to find, e.g. with focus on device control [40], [34], on hemodynamic effects or both [121], [78], [82]. Herein, the assist devices are simply modeled as additional blood flows or supportive pressures. More complex models of pneumatic drive units are rare. While the assist device controller in the work of Cordeiro et al. [16] is at least represented by a resistor capacitor circuit, the work of Sievert et al. [103], [104], [105] models valve and tube flow as well as the pump performance for the EXCOR support system (Berlin Heart GmbH, Germany), which is coupled to a cardiovascular system, both as a lumped-parameter model. However, the drive unit representation is somewhat rudimentary, since no temperature evolution nor any pressure losses are modeled. These models are unsuitable for providing reliable answers in assist device engineering. The limited number of published research on pneumatic heart assist systems can be explained by the commercial success of continuous flow systems and the accompanied shift of research interest towards these systems. In contrast to a wide range of purely lumped models, only a small number of multi-dimensional cardiovascular models has been published so far. Here, the works of Kerckhoffs et al. [58], Jagschies [54] and especially Hirschvogel et al. [43] - [45] are to be mentioned. While all couple a 0D circulatory system to patient-specific 3-dimensional (3D) finite element heart models, only the works of Jagschies and Hirschvogel et al. comprise heart support, namely a pneumatic cardiac assist device. It is utilized to investigate the effects of varying support pressures on medical parameters as listed in table 1.1. The coupled model presented by Jagschies is a pseudo two-dimensional model of generic ventricles which extends in the third dimension and with inflatable support device wrapped around. In contrast, the work of Hirschvogel is a patient-specific representation of either the ventricles or the entire heart, including left and right atria. It allows for the simulation of gas transport and dissociation, growth and remodeling, infarct and valvular cardiac diseases. Furthermore, a model of the AdjuCor implant can be placed around it and the inflatable units can be pressurized. However, neither of these works include a model of the assist device drive unit and hence, support pressures within the inflatable units of the implant are artificially prescribed. This may be enlightening in the analysis of VAD effects on the cardiovascular system but leaves technical feasibility and engineering challenges unconsidered. A multi-physics model of AdjuCors's drive unit was developed in the thesis of [119]. However it does not include patient-specific cardiac mechanics nor circulatory systems.

1.7. Research objectives

This thesis is intended to provide essential computational tools to develop and apply a novel BiVAD in HF treatment. Accelerating market approval and clinical acceptance as well as reliable patient-specific risk-benefit predictions prior to the implantation surgery can save the lives of many end-stage HF patients. Validated computational models are required, which accurately describe the present system and allow for the verification of medical, normative and technical requirement compliance. They may further allow for identifying valuable potential for improvements when analyzed. Therefore and in contrast to available models, the BiVAD must be reproduced in-silico as a multi-physics stand-alone device, featuring all relevant components and the functionality of the real counterpart. This includes highly dynamic physics, e.g. the abrupt filling of the implant's expandable units, but also long-term heating phenomena. The BiVAD model must further be applicable in a clinically meaningful context. Consequently, it must be coupleable to patient-specific cardiovascular models, which allow for mimicking the current patient condition and other potential disease progressions, e.g. additional myocardial infarctions or valvular heart diseases. Both the stand-alone BiVAD model and the BiVAD-supported, patient-specific cardiovascular system model are crucial for fast engineering iterations to rapidly approve the promising system and to allow for reliable risk-benefit predictions. Based on this, the concrete objectives of this thesis are listed in the following:

- **Development of a mixed-dimensional multi-physics BiVAD model**
  Other than the available models, the BiVAD model in the present work must be built from specific and exchangeable components, e.g. pump and valves. All actuators must be controllable based on the patient-specific ECG-signal, which must trigger inflation and deflation of the implant. The actuators consume electrical power which depletes the device battery, reduces the operation time and heats the device. Hence, long-term heating processes due to non-ideal actuators and circuitry must also be considered. Furthermore, atmospheric conditions must be considered to test for normative requirement compliance. Finally, steady system state calculation must be allowed by enabling the dynamic simulation of single and of consecutive support cycles.

- **Validation of the BiVAD model**
  The basis of every reliable simulation is a valid model. In spite of necessary simplifications made during the modeling process, the BiVAD model must accurately predict ECG-synchronous inflation and deflation dynamics, which pressurize the implant and eventually enable cardiac support. An acceptable accuracy within the system operating range must be proven using adequate validation methods.

- **Coupling of the BiVAD model to existing cardiovascular models**
  Valid and versatile in-silico cardiovascular models have been introduced by Hirschvogel et al. [43]-[45]. They consist of an actively beating 3D heart and a 0D circulatory system, which are both patient-specific. The BiVAD model must robustly be coupled to these models, allowing for patient-specific cardiovascular system support with a technically complete assist device.

- **Device application and improvement**
  Analyses and application of the BiVAD model to clinically relevant cases may identify

valuable potential for improvements. The introduced models can be used to perform suitable simulations, which may result in concrete design or therapy recommendations. The goal is to increase support efficacy and hence beneficial effects on the cardiovascular system as well as to enhance device efficiency, thereby reducing power consumption and device heating. Therefore, the system should be analyzed as a stand-alone device from a purely technical perspective and as an actual assist device, supporting patients in specific conditions. The latter configuration should further be used to assess the assist device's response to differing, clinically relevant medical cases.

1.8. Outline

The remainder of this work is structured as follows: Chapter 2 will describe the relevant fundamentals of all physical domains that are used within this work. Here, the reader is introduced to important thermodynamic concepts, heat transfer basics and mechanical theory, which delves into fluid and solid mechanics. The chapter concludes with a presentation of the numerical solution process. In Chapter 3, a holistic mixed-dimensional, multi-physics and strongly coupled model is introduced, consisting of a 0D model of the drive unit with supply tubes, a 3D model of the implant and heart and again a 0D model of the cardiovascular system. It is complemented with a model to predict the mean, steady drive unit temperature after device heating. The introduced models are validated in chapter 4 and a sensitivity analysis is performed in chapter 5. Thereafter, the model is applied in a case study in chapter 6, including several patients, HF conditions and other diseases. Finally, an overall summary of this work is given in chapter 7, including an outlook for future work.

2. Physical fundamentals

In this chapter, the underlying physical concepts are introduced by presenting the governing equations of the models derived in this work. Most physical analyses are limited to a region of interest, a so-called control volume. Within the present work, any interaction between the surroundings and the control volume over its boundaries is described by the laws of mechanics and thermodynamics. This chapter starts off with the *Reynolds*[1] *transport theorem*, a concept to convert a system description from a control volume moving in space, to a spatially fixed control volume. This is useful for proper pneumatic system modeling. The theorem permits to relate a system property, e.g. mass or energy, to the rate of change of that property within a distinct control volume. It states

$$\frac{\mathrm{d}}{\mathrm{d}t}\mathcal{B}_{\text{syst}} = \int_{\Omega} \frac{\partial}{\partial t}(\beta\rho)\,\mathrm{d}V + \int_{\Gamma} \beta\rho\,\boldsymbol{v}\cdot\boldsymbol{n}\,\mathrm{d}A. \tag{2.1}$$

Here, $\mathcal{B}_{\text{syst}}$ is any extensive system property, like mass, momentum or energy and β is the corresponding intensive (cf. section 2.1) quantity, i.e. the amount of $\mathcal{B}_{\text{syst}}$ per unit mass in a volume element $\mathrm{d}V$. The instantaneous change of $\mathcal{B}_{\text{syst}}$ in the system is equal to the sum of change within the volume plus flows thereof over the control volume surface, denoted with A. The notations Ω and Γ refer to the control volume and control surface, respectively. In the present work, $\mathrm{d}V$ and $\mathrm{d}A$ are used as generic infinitesimal volume and surface elements for both the reference and current configuration, depending on the integration domain.

2.1. Thermodynamics

Conversion of energy within a defined system and energy exchange with its environment are the main topics of thermodynamics. This section introduces basic concepts, which are important for the models derived in the present work. More detailed descriptions of thermodynamics can be found in [33] and [99].
Two sets of state variables permit the identification of the state of a system. These are referred to as *thermal state variables* and *caloric state variables*, as listed in table 2.1. In contrast to caloric state variables, thermal state variables can directly be measured. Pressure and temperature are intensive variables, meaning that they are independent of the system size. All other state variables are extensive and do change with the size of the system. Therefore, *specific state variables* can be introduced, by dividing extensive quantities by the system mass.

[1] Osborne Reynolds, British physicist (1842-1912)

Thermal variable	SI-unit	Caloric variable	SI-unit
Pressure p	Pascal [Pa]	Internal energy U	Joule [J]
Temperature T	Kelvin [K]	Enthalpy H	Joule [J]
Volume V	Cubic meters [m^3]	Entropy S	Joule per Kelvin $\left[\frac{J}{K}\right]$

Table 2.1.: Thermal and caloric state variables.

According to the Gibbs' phase rule[2], two state variables define the state of a pure substance, single phase system unequivocally. In the present work, pressure and temperature are typically used. The theoretical value range for pressure is [0,∞[, but can also be given relatively to the ambient pressure p_∞, resulting in a modified range of $[-p_\infty,\infty[$. However, most equations require absolute values. Also, various units for pressure exist and a helpful conversion is given in equation (2.2). As shown in table 2.1, temperatures are given in Kelvin, but for temperature differences, Kelvin and Celsius can be used interchangeably.

$$0.001 \text{ bar} = 100 \text{ Pa} = 1 \text{ hPa} = 0.1 \text{ kPa} = 1 \text{ mbar} \approx 0.75 \text{ mmHg} \tag{2.2}$$

2.1.1. The ideal gas law

The ideal gas law can be derived by combining two empirical laws, namely the observation by the french physicist Gay-Lussac[3] concerning the change of volume due to temperature change at constant pressure and those of Boyle[4] and Mariotte[5], which state that the product of pressure and volume remains constant for a constant temperature. The ideal gas law states

$$pV = mRT, \tag{2.3}$$

where R [J/(kgK)] is the specific gas constant and m the mass of gas.[6] An equation for the density can be formulated from the expression (2.3):

$$\rho = \frac{p}{RT}. \tag{2.4}$$

For an ideal gas, the following caloric relations hold:

$$R = c_p - c_\mathrm{v}, \tag{2.5}$$

$$\kappa = \frac{c_p}{c_\mathrm{v}}, \tag{2.6}$$

$$u = c_\mathrm{v} T \quad \text{and} \tag{2.7}$$

$$h = c_p T. \tag{2.8}$$

[2]Josiah Willard Gibbs, American physicist (1839-1903)
[3]Joseph Louis Gay-Lussac, French chemist and physicist (1778-1850)
[4]Robert Boyle, english chemist (1627 - 1691)
[5]Edme Mariotte, french physicist (1620 - 1684)
[6]The ideal gas law can also be formulated using the universal gas constant and the amount of substance of a system. However, this notation is not used within the present work.

Equations (2.5) to (2.8) represent the specific gas constant R, isentropic exponent κ, specific internal energy u and specific enthalpy h, respectively. The isentropic exponent (2.6) refers to an adiabatic and reversible change of state, thus without heat exchange nor friction. It is a theoretical model, but shows good results for nearly adiabatic systems. The specific gas capacities differ for the case of constant pressure (c_p) and for the case of constant volume (c_v). However, both quantify the stored energy per unit mass and per unit temperature by the gas and are given in [J/(kgK)].

2.1.2. The principle of energy conservation

The principle of energy conservation, as applied to thermodynamic processes, is also known as the first law of thermodynamics. For a closed system, it states that the change in internal energy U equals the energy transferred to or from the system across its boundaries, namely heat and work, and the change in energy of the system itself. By convention, all energy entering the system adds to its total energy, whereas leaving energy is subtracted. The extensive notation between the two states $\in \{1, 2\}$ reads

$$U_2 - U_1 = \Delta Q_{12} + \Delta W_{12} + \Delta E_\mathrm{pot} + \Delta E_\mathrm{kin}. \tag{2.9}$$

If the potential and kinetic energy of the entire system are unaltered, ΔE_pot and ΔE_kin vanish. Q_{12} is the exchanged heat and W_{12} can be mechanical, electrical or volume work. Other forms of energy exist, but are not of interest here, e.g. chemical or nuclear energy. For modeling purposes, it can be of use to start with the first law in differential notation. For a system at rest it obeys:

$$\mathrm{d}E = \delta Q + \delta W. \tag{2.10}$$

Here, differentials of process values are denoted with δ, whereas differentials of state values are denoted by d.

For an open system with fixed boundaries, the Reynolds transport theorem (2.1) can be used to derive the energy balance from the first law of thermodynamics. The property of interest is energy with $\mathcal{B}_\mathrm{syst} = E$ and $\beta = \frac{E}{m} = e$ and thus the theorem yields

$$\frac{\mathrm{d}Q}{\mathrm{d}t} + \frac{\mathrm{d}W}{\mathrm{d}t} = \frac{\mathrm{d}E}{\mathrm{d}t} = \int_\Omega \frac{\partial}{\partial t}(e\rho)\,\mathrm{d}V + \int_\Gamma e\rho\,(\boldsymbol{v}\cdot\boldsymbol{n})\,\mathrm{d}A. \tag{2.11}$$

Here, the specific energy is composed of internal, kinetic and potential energy $e = e_\mathrm{int} + e_\mathrm{kin} + e_\mathrm{pot} = u + \frac{v^2}{2} + \mathrm{g}z$, with g being the gravitational acceleration, u the specific internal energy and z the altitude. Work fluxes can be $\dot{W} = \dot{W}_\mathrm{pressure} + \dot{W}_\mathrm{viscous} + \dot{W}_\mathrm{shaft} + \dot{W}_\mathrm{electrical}$. Pressure work flux is defined as

$$\dot{W}_\mathrm{pressure} = \int_\Gamma p(\boldsymbol{v}\cdot\boldsymbol{n})\,\mathrm{d}A \tag{2.12}$$

and can be combined with the surface integral in (2.11). Several heat or work flows can be summed, yielding

$$\sum \dot{Q} + \sum \dot{W} = \int_\Omega \frac{\partial}{\partial t}\left[\left(u + \frac{v^2}{2} + \mathrm{g}z\right)\rho\right]\mathrm{d}V + \int_\Gamma \left(h + \frac{v^2}{2} + \mathrm{g}z\right)\,(\boldsymbol{v}\cdot\boldsymbol{n})\,\rho\,\mathrm{d}A, \tag{2.13}$$

where h is the specific enthalpy, defined as $h = u + p\mathrm{v}$, with v being the specific volume $V/m = 1/\rho$. Now, (2.13) can be further simplified, e.g. for steady conditions or for the one-dimensional (1D) case. For this 1D case, the second integral converts to a sum of in- and outflows (cf. (2.14)) and the first integral can - in case of homogeneity - be rewritten as the total change of energy of the control volume $\frac{\mathrm{d}E_{\mathrm{CV}}}{\mathrm{d}t}$ (cf. (2.15)):

$$\frac{\mathrm{d}E_{\mathrm{CV}}}{\mathrm{d}t} = \sum \dot{Q} + \sum \dot{W} + \sum \dot{m}_{\text{in/out}} \left(h_{\text{in/out}} + \frac{v^2_{\text{in/out}}}{2} + \mathrm{g}z_{\text{in/out}} \right), \tag{2.14}$$

$$\frac{\mathrm{d}E_{\mathrm{CV}}}{\mathrm{d}t} = \frac{\mathrm{d}U_{\mathrm{CV}}}{\mathrm{d}t} + \frac{\mathrm{d}E_{\text{kin,CV}}}{\mathrm{d}t} + \frac{\mathrm{d}E_{\text{pot,CV}}}{\mathrm{d}t}. \tag{2.15}$$

In equation (2.14) all energy flows that enter or exit through the system boundaries are considered. Heat exchange with the environment is represented by $\dot{Q}$ and work by $\dot{W}$. The terms $\dot{m}\left(h + \frac{v^2}{2} + \mathrm{g}z\right)$ represent exchanged energy with incoming or outgoing mass flows. They include thermal and displacement work as well as kinetic and potential work. Depending on the application, one or several contributions may be neglected.
Equation (2.15) adds all energy changes of the control volume itself: $\frac{\mathrm{d}U_{\mathrm{CV}}}{\mathrm{d}t}$ is the change of internal energy and $\frac{\mathrm{d}E_{\text{kin,CV}}}{\mathrm{d}t} + \frac{\mathrm{d}E_{\text{pot,CV}}}{\mathrm{d}t}$ are the terms for kinetic and potential energy changes, respectively.

2.1.3. Polytropic processes

Another important concept is that of the polytropic process. It is described by the equation

$$pV^n = \text{constant} \tag{2.16}$$

and can be rewritten to $p_1 V_1^n = p_2 V_2^n$ between two states $\in \{1, 2\}$. Equation (2.16) can also be formulated with the specific volume v, leading to the differential form

$$\frac{\mathrm{d}p}{p} = n\frac{\mathrm{d}\rho}{\rho}. \tag{2.17}$$

The exponent n can theoretically have any real value. Equation (2.16) is typically evaluated for $n = 1$, which corresponds to an isothermal change of state, with temperatures before and afterwards being the same, $T_1 = T_2$, or for $n = 1.4$, representing an isentropic change of state. Other typical values often mentioned in literature are $n = 0$ for isobaric and $n = \infty$ for isochoric processes. Figure (2.1) depicts typical values of n. For an expansion, i.e. an increase in specific volume, temperature drops for values of $n > 1$, which is the space below and to the right of the curves $n = 1$ and $n = \infty$ (blue dashed lines). In reverse, temperature rises during compression with $n > 1$, covered by the space above and to the left of the same curves (red dashed lines). Red and blue spaces indicate heat inflow and outflow, respectively. Polytropic processes are widely used to model density or temperature as a function of pressure. After some rearrangements, equations for density or temperature can be derived:

$$\rho_2 = \rho_1 \left(\frac{p_2}{p_1} \right)^{\frac{1}{n}}, \tag{2.18}$$

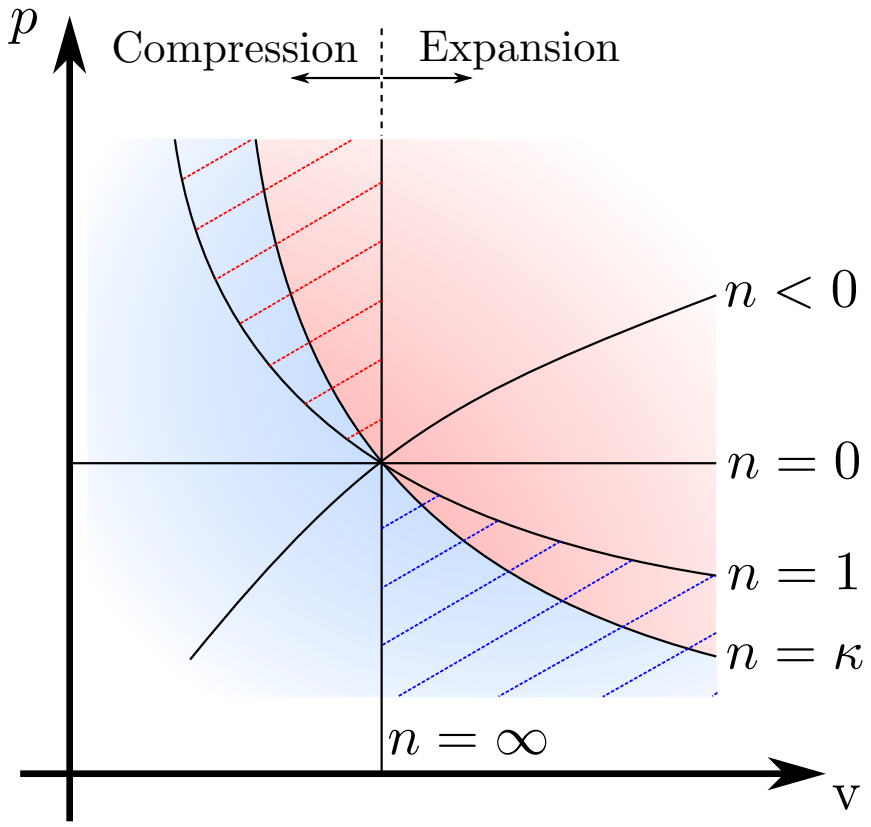

Figure 2.1.: Schematic of a reversible polytropic processes in a pressure-volume diagram. Red and blue spaces indicate heat inflow and outflow, while red and blue dash lines indicate the ranges that are accompanied by a temperature increase or decrease.

$$T_2 = T_1 \left(\frac{p_2}{p_1} \right)^{\frac{n-1}{n}} . \tag{2.19}$$

2.1.4. Heat transfer

Heat transfer in the present work is understood to be energy transferred across the system boundaries, driven by an existing temperature gradient. Two types of heat transfer can be described[7], namely heat conduction and heat radiation. Heat conduction, with and without convection, requires matter to be in direct contacting thermal communication whereas heat radiation is transferred by electro-magnetic waves. For a more detailed description of heat transfer, the reader is referred to the textbook of Baehr and Stephan [7].

Heat transfer is driven by a temperature gradient. Starting from a temperature field $T(\boldsymbol{x}, t)$, the density of transferred energy is described by a vector field named heat flux $\dot{\mathbf{q}}(\boldsymbol{x}, t)$, which is the

[7] Sometimes literature differs three basic heat transfer types, but the physical principles for heat conduction and heat convection are similar.

heat flow per area. It can be expressed as the gradient of the temperature field

$$\begin{aligned} \dot{\mathbf{q}} &= -\lambda_{\text{th}} \nabla T, \\ \dot{Q} &= -\lambda_{\text{th}} \nabla T \boldsymbol{n} \mathrm{d}A. \end{aligned} \tag{2.20}$$

The coefficient of proportionality λ_{th} is called thermal conductivity. The sign accounts for the second law of thermodynamics, stating that heat flows from high to low temperatures.

Figure 2.2 depicts the heat transfer from one fluid to another across a separating wall element. In this 1D case and for the heat conduction through the wall element only, equation (2.20) can be solved, yielding

$$\dot{Q} = \lambda_{\text{th}} \frac{A_{\text{W}}}{d_{\text{W}}} (T_{\text{W2}} - T_{\text{W1}}), \tag{2.21}$$

with d_{W} being the wall thickness and A_{W} the surface area of the wall element. The quotient $\Lambda_{\text{th}} = \frac{\lambda_{\text{th}} A_{\text{W}}}{d_{\text{W}}}$ and its inverse can be understood as thermal conductance $[\frac{\text{W}}{\text{K}}]$ and thermal resistance $[\frac{\text{K}}{\text{W}}]$, respectively. Convective heat transfer is the superposition of heat conduction and macroscopic

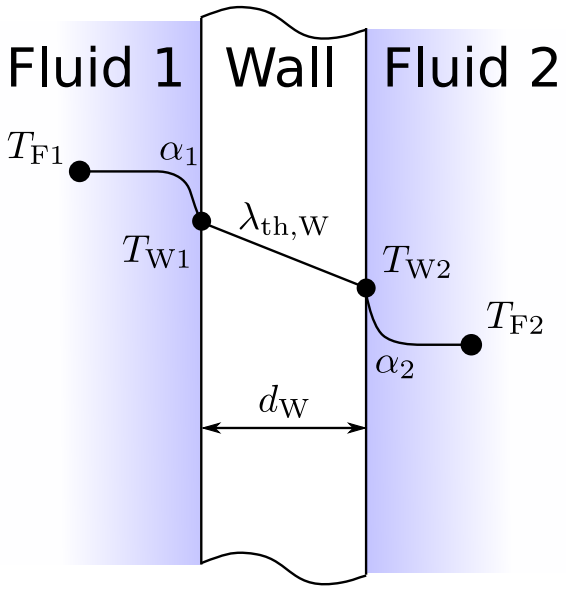

Figure 2.2.: Model of heat transfer from one fluid to another across a separating wall element in 1D: Convective heat transfer from a point T_{F1} to T_{W1} with heat transfer coefficient α_1, followed by heat conduction from T_{W1} to T_{W2} with $\lambda_{\text{th,W}}$ and again convective heat transfer from T_{W2} to T_{F2} with heat transfer coefficient α_2.

movement of fluid particles. The boundary layer theory of Prandtl[8] states, that in case of fluid flow along a solid, e.g. a tube wall, the velocity component parallel to that wall increases rapidly from zero at the wall to the free stream velocity of the core flow in some distance to the wall. Also, the temperature changes mainly in this layer. For the 1D case in figure 2.2, convection fluid-structure heat transfer obeys

$$\dot{Q} = \alpha A_{\text{W}} (T_{\text{F1}} - T_{\text{W1}}), \tag{2.22}$$

[8]Ludwig Prandtl, German physicist (1875-1953)

with the coefficient of proportionality α, which is called the heat transfer coefficient with units $[\frac{\mathrm{W}}{\mathrm{m^2K}}]$. An everyday technical problem concerns the heat transfer through a wall, e.g. cooling a heated container. This is the case between the temperatures T_{F1} and T_{F2} in the example in figure 2.2. It is equivalent to convection heat transfer from the fluid to the casing wall, heat conduction through this wall and again convection heat transfer from the outer wall surface to the surrounding fluid. For such a heat transfer cascade, the coefficients can be merged to the so-called thermal transmittance k_{th}, which is calculated by

$$\frac{1}{k_{\mathrm{th}}} = \frac{1}{\alpha_1} + \frac{d_{\mathrm{W}}}{\lambda_{\mathrm{th}}} + \frac{1}{\alpha_2}. \tag{2.23}$$

2.2. Mechanics

2.2.1. Fluid mechanics

In this section, the relevant equations of fluid mechanics used in the models within the present work are derived. A more detailed review can be found in the textbooks of *White* [116] or *Sigloch* [106].

Mass flow rate $\dot{m}$, volumetric flow rate $\dot{V}$ and average velocity v are related by flow area and density as stated in equation (2.24). The respective SI units are $[\frac{\mathrm{kg}}{\mathrm{s}}]$, $[\frac{\mathrm{m^3}}{\mathrm{s}}]$, $[\frac{\mathrm{m}}{\mathrm{s}}]$.

$$\dot{m} = \rho v A = \rho \dot{V} \tag{2.24}$$

2.2.1.1. The medium air

Air is used in all models of the present work. It is a viscous and compressible fluid. However, compressibility may play a negligible role under certain conditions. The Mach[9] number is a dimensionless quantity, relating the average flow velocity v to the local speed of sound $\tilde{c}$, with

$$\tilde{c} = \sqrt{\kappa R T} \quad \text{and} \tag{2.25}$$

$$Ma = \frac{v}{\tilde{c}}. \tag{2.26}$$

Under the assumptions that κ and R are constant (cf. section 3.1.1), the speed of sound and the Mach number depend exclusively on the temperature. The Mach number allows the relative density change to be related to the average flow velocity. It can be used to assess if a gas flow can be treated as incompressible, which is typically assumed for flows with Mach numbers $\leq$ 0.3 [106], [12], [116]. This threshold corresponds to a 5 % change in density:

$$\frac{\Delta\rho}{\rho} = \frac{1}{2} Ma^2 \approx 0.05 \qquad \text{for} \quad Ma = \frac{1}{3}. \tag{2.27}$$

This is equivalent to near ambient air flows with average velocities up to 110-120 $\frac{\mathrm{m}}{\mathrm{s}}$, depending on the prevailing conditions, which can consequently be treated as incompressible. By using

[9] Ernst Mach, Austrian physicist and philosopher (1838-1916)

equation (2.24), this threshold can be verified for mass flows. For air as a newtonian fluid, viscosity depends only on the temperature. The equation of Sutherland[10] is an approximation of the dynamic viscosity

$$\eta(T) = \frac{1.4747 \cdot 10^{-6} T^{1.5}}{T + 113} \qquad [\mathrm{Pa} \cdot \mathrm{s}]. \tag{2.28}$$

Another definition of viscosity, namely the kinematic viscosity, as the ratio of η to the density ρ, is given by $\nu = \eta/\rho$ [m^2/s].

2.2.1.2. Mass conservation

Mass conservation must apply for any system:

$$\frac{\mathrm{d}m_{\text{syst}}}{\mathrm{d}t} = \frac{\mathrm{d}}{\mathrm{d}t} \int_\Omega \rho \, \mathrm{d}V = 0. \tag{2.29}$$

Using the Reynolds transport theorem (2.1) with $\mathcal{B}_{\text{syst}} = m$, $\beta = 1$, (2.29) can be converted into the mass change within Ω plus the mass flow across the boundary Γ:

$$\int_\Omega \frac{\partial}{\partial t} \rho \, \mathrm{d}V + \int_\Gamma \rho \boldsymbol{v} \cdot \boldsymbol{n} \, \mathrm{d}A = 0. \tag{2.30}$$

In a 1D case, equation (2.30) can be rewritten to

$$\int_\Omega \frac{\partial}{\partial t} \rho \, \mathrm{d}V + \dot{m}_{\text{in/out}} = 0. \tag{2.31}$$

2.2.1.3. Balance of linear momentum

Balance of momentum equations are based on Newton's first and second law of motion, stating, that any change in linear momentum equals the sum of forces acting on the system. The rate of change of linear momentum is equal to the sum of applied forces:

$$\frac{\mathrm{d}}{\mathrm{d}t} \int_\Omega \rho \boldsymbol{v} \, \mathrm{d}V = \sum \mathbf{F}. \tag{2.32}$$

It can be formulated for a control volume using the Reynolds transport theorem (2.1) with $\mathcal{B}_{\text{syst}} = \int_\Omega \rho \boldsymbol{v} \, \mathrm{d}V$, $\beta = \boldsymbol{v}$ to

$$\int_\Omega \frac{\partial}{\partial t} (\boldsymbol{v}\rho) \, \mathrm{d}V + \int_\Gamma \boldsymbol{v}\rho \, (\boldsymbol{v} \cdot \boldsymbol{n}) \, \mathrm{d}A = \sum \mathbf{F}. \tag{2.33}$$

Note that $\sum \mathbf{F}$ is a vector sum and $\boldsymbol{v}$ is an inertial-frame velocity. Otherwise additional relative acceleration terms must be included, which are omitted here.

[10] William Sutherland, Australian physicist (1859-1911)

2.2.1.4. One-dimensional flow

0D models can be gained by further simplifying the above equations. They are then referred to as Bernoulli[11] equations. Friction due to shear forces on the wall and due to viscous particle interactions is neglected. Changing equation (2.30) to treat 1D flow along a streamline s for a small volume element gives

$$\frac{\partial \rho}{\partial t}\mathrm{d}V + \mathrm{d}\dot{m} = 0. \tag{2.34}$$

Using $\mathrm{d}V = A\mathrm{d}s$, it becomes

$$\mathrm{d}\dot{m} = -\frac{\partial \rho}{\partial t}A\mathrm{d}s. \tag{2.35}$$

Similarly, the balance of linear momentum (2.33) along the streamline for an elemental control volume results in

$$\sum \mathrm{d}\mathbf{F} = \frac{\partial}{\partial t}(\rho v)A\ \mathrm{d}s + \mathrm{d}(\dot{m}v) = \frac{\partial \rho}{\partial t}vA\ \mathrm{d}s + \frac{\partial v}{\partial t}\rho A\ \mathrm{d}s + \dot{m}\mathrm{d}v + \mathrm{d}\dot{m}v \tag{2.36}$$

with gravity and pressure forces being $\mathrm{d}F_\mathrm{g} = -\rho \mathrm{g} A \mathrm{d}z$ and $\mathrm{d}F_p = -A\mathrm{d}p$, respectively. Inserting the relation obtained from mass conservation (2.35) into (2.36) cancels out the first and last term on the right side. Dividing by ρA, yields the inviscid Bernoulli equation in differential form $\frac{\partial v}{\partial t}\mathrm{d}s + \frac{\mathrm{d}p}{\rho} + v\mathrm{d}v + \mathrm{g}\mathrm{d}z = 0$, which can be integrated between two points along a streamline:

$$\int_1^2 \frac{\partial v}{\partial t}\mathrm{d}s + \int_1^2 \frac{\mathrm{d}p}{\rho} + \frac{1}{2}(v_1^2 - v_2^2) + \mathrm{g}(z_1 - z_2) = 0. \tag{2.37}$$

Finally, for steady, incompressible flow and neglecting gravitational effects, equation (2.37) becomes

$$\frac{\Delta p_{12}}{\rho} + \frac{1}{2}(v_1^2 - v_2^2) = 0. \tag{2.38}$$

Viscous pipe flows between two points result in a pressure drop along the flow path. The resistance force $\mathrm{F_R}$ acting on a volume parcel in a pipe is proportional to the wetted pipe surface πDL, the kinetic energy $\frac{v^2}{2}$ and the fluid density ρ. With the coefficient Φ, the resistance force reads $\mathrm{F_R} = \Phi \pi DL \frac{v^2}{2}\rho$. In addition, $\mathrm{F_R} = (p_1 - p_2)A$ holds. Equating both expressions for $\mathrm{F_R}$ and using $\lambda = 4\Phi$ the Darcy-Weisbach[12] equation can be obtained

$$\Delta p_{12} = \lambda \frac{L}{D}\rho \frac{v^2}{2}, \tag{2.39}$$

with λ being the dimensionless Darcy friction factor. From the Hagen[13]-Poiseuille[14] law, describing the laminar flow through a pipe, the friction factor can be derived from $\lambda = 64/Re$, with Re being the Reynolds number. For turbulent flow, several standard equations can be found in literature describing the Darcy friction factor as a function of the pipe diameter, the surface roughness and the Reynolds number of the flow, e.g. the empirical equations of Haaland [39], Prandtl or Blasius [116].

[11] Daniel Bernoulli, Swiss mathematician and physicist (1700-1782)

[12] Henry Darcy, French engineer (1803-1858) and Julius Weisbach, German mathematician and engineer (1806-1871)

[13] Gotthilf Hagen, German engineer (1797-1884)

[14] Jean Léonard Marie Poiseuille, French physicist and physiologist (1797-1869)

2.2.1.5. Flow patterns in a pipe

The current flow regime in the actual pipe flow has to be identified, namely *laminar* or *turbulent* flow. Laminar flow is typically observed for flows below a critical Reynolds number and is characterized by fluid particles flowing along smooth paths in layers, with each layer flowing past the neighbor layer without or with little mixing. In turbulent flows, the bulk flow is superimposed by cross and lengthwise flows. This chaotic pattern generally occurs in flows above a critical Reynolds number. The onset of one of the two can be predicted by the Reynolds number, but may also depend on the flow path geometry and flow dynamics, as these influence the amount of distortion of the particle flow layers. The dimensionless Reynolds number can be calculated by

$$Re = \frac{vL_c}{\nu} = \frac{\rho v L_c}{\eta} = \frac{\dot{m} L_c}{\eta A} \tag{2.40}$$

with L_c being the characteristic length scale [m]. For pipe flow, the pipe diameter is commonly used. The critical Reynolds number, hence the value where the flow pattern spontaneously changes from laminar to turbulent or vice versa, may depend on the conditions of the flow path (e.g. geometry), but is usually reported in literature to occur around $Re \approx 2300$ [116].

2.2.2. Solid mechanics

Here, basic equations for finite deformation solid mechanics problem formulations are provided, consisting of kinematic, constitutive and balance equations. For more details, the reader is referred to the textbook of Holzapfel [46].

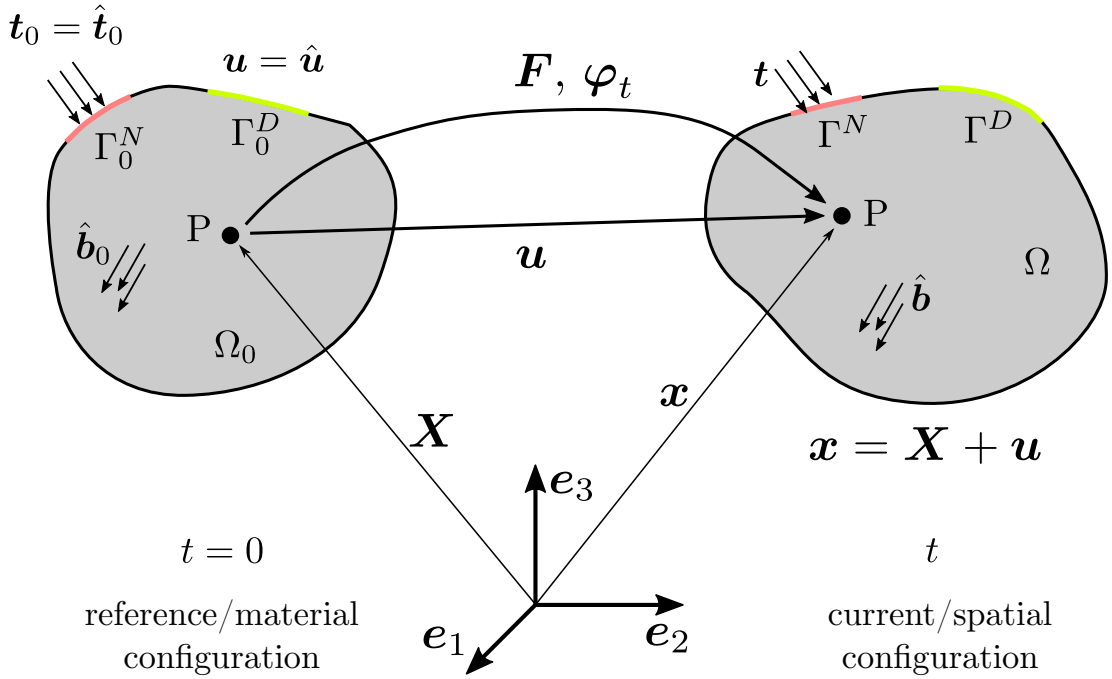

Figure 2.3.: The general setting in solid mechanics: A body is deformed from the material configuration to the spatial configuration.

Figure 2.3 shows a general depiction of a body at two distinct time points undergoing a deformation described by the deformation map $\boldsymbol{\varphi}_t$. The reference or material configuration is indicated by $\Omega_0 \subset \mathbb{R}^3$, containing all material points $\boldsymbol{X}$. On the right side, the deformed body, referred to as the spatial or current configuration, is depicted and denoted as $\Omega \subset \mathbb{R}^3$. It is the domain occupied by the points $\boldsymbol{x}$ at times $t \geq 0$. So-called body forces $\hat{\boldsymbol{b}}_0$ are applied per unit undeformed volume. The body is subject to boundary conditions, namely external tractions $\hat{\boldsymbol{t}}_0$ on the Neumann boundary Γ_0^N and Dirichlet conditions $\boldsymbol{u} = \hat{\boldsymbol{u}}$ applied to Γ_0^D, with $\Gamma_0^D \cap \Gamma_0^N = \emptyset$.

2.2.2.1. Kinematics

The mapping function $\boldsymbol{\varphi}_t$ maps points from the material to the spatial configuration and the displacement $\boldsymbol{u}$ is the difference between the points $\boldsymbol{X}$ and $\boldsymbol{x}$:

$$\boldsymbol{x} = \boldsymbol{\varphi}_t(\boldsymbol{X}, t), \qquad \boldsymbol{X} = \boldsymbol{\varphi}_t^{-1}(\boldsymbol{x}, t) \tag{2.41}$$

$$\boldsymbol{u}(\boldsymbol{X}, t) = \boldsymbol{x}(\boldsymbol{X}, t) - \boldsymbol{X}. \tag{2.42}$$

Velocity and acceleration are given by their first and second derivative with respect to time

$$\boldsymbol{v}(\boldsymbol{X}, t) = \frac{\partial \boldsymbol{u}(\boldsymbol{X}, t)}{\partial t} = \dot{\boldsymbol{u}}(\boldsymbol{X}, t), \tag{2.43}$$

$$\boldsymbol{a}(\boldsymbol{X}, t) = \frac{\partial^2 \boldsymbol{u}(\boldsymbol{X}, t)}{\partial t^2} = \ddot{\boldsymbol{u}}(\boldsymbol{X}, t). \tag{2.44}$$

The deformation gradient maps an infinitesimal line element to its counterpart in the other configuration either as a *push-forward* (material $\mapsto$ spatial) or as a *pull-back* (spatial $\mapsto$ material) operation. The fundamental kinematic variable and its inverse are defined as

$$\boldsymbol{F} = \frac{\mathrm{d}\boldsymbol{x}}{\mathrm{d}\boldsymbol{X}}, \tag{2.45}$$

$$\boldsymbol{F}^{-1} = \frac{\mathrm{d}\boldsymbol{X}}{\mathrm{d}\boldsymbol{x}}. \tag{2.46}$$

The mapping operands for area and volume elements are $J\boldsymbol{F}^{-T}$ and J, respectively, with $J = \det(\boldsymbol{F})$. Commonly used deformation measures can be obtained from the deformation gradient tensor, namely the material *right Cauchy-Green deformation tensor*

$$\boldsymbol{C} = \boldsymbol{F}^T \boldsymbol{F} \tag{2.47}$$

and the spatial *left Cauchy-Green deformation tensor*

$$\boldsymbol{b} = \boldsymbol{F}\boldsymbol{F}^T. \tag{2.48}$$

Commonly used strain measures are the material *Green-Lagrange strain tensor* (2.49) and the spatial *Euler-Almansi strain tensor* (2.50)

$$\boldsymbol{E} = \frac{1}{2}(\boldsymbol{C} - \boldsymbol{1}), \tag{2.49}$$

$$\boldsymbol{e} = \frac{1}{2}(\boldsymbol{1} - \boldsymbol{b}^{-1}). \tag{2.50}$$

2.2.2.2. Constitutive laws

Constitutive laws relate strains, emerging from kinematic equations, to the response in the material, i.e. stress. Common stress measures are the spatial *Cauchy stress* $\boldsymbol{\sigma}$, relating the Cauchy traction $\boldsymbol{t}$ to the unit outward normal $\boldsymbol{n}$, the *first Piola-Kirchhoff stress* $\boldsymbol{P}$, relating the first Piola-Kirchhoff traction $\boldsymbol{t}_0$ to the normal $\boldsymbol{n}_0$ in material configuration and the *second Piola-Kirchhoff stress* $\boldsymbol{S}$, a pure material stress field. $\boldsymbol{P}$ is a tensor with bases in both configurations.

$$\boldsymbol{t} = \boldsymbol{\sigma}\boldsymbol{n}, \tag{2.51}$$

$$\boldsymbol{P} = J\boldsymbol{\sigma}\boldsymbol{F}^{-T}, \tag{2.52}$$

$$\boldsymbol{S} = \boldsymbol{F}^{-1}\boldsymbol{P} = J\boldsymbol{F}^{-1}\boldsymbol{\sigma}\boldsymbol{F}^{-T}. \tag{2.53}$$

Nonlinear hyperelastic material behavior is often defined by the existence of an *energy density function* Ψ, which expresses the stored energy in the material when undergoing a deformation. It is a scalar-valued function, which must satisfy important properties, e.g. that an infinite amount of expansion or compression of the body requires infinite energy. Other requirements can be found in [46]. The differentiation of Ψ allows one to express the stress state of a body. For the first and second Piola-Kirchhoff stress, the following constitutive relations hold

$$\boldsymbol{P} = \frac{\partial \Psi}{\partial \boldsymbol{F}}, \qquad \boldsymbol{S} = 2\frac{\partial \Psi}{\partial \boldsymbol{C}} = \frac{\partial \Psi}{\partial \boldsymbol{E}}. \tag{2.54}$$

Ψ can be represented by the principal invariants, for example of the right Cauchy-Green deformation tensor $\boldsymbol{C}$, $\Psi = \Psi(I_C, II_C, III_C)$, with

$$\begin{aligned} I_C &= \text{tr}[\boldsymbol{C}], \\ II_C &= \tfrac{1}{2}\left((\text{tr}[\boldsymbol{C}])^2 - \text{tr}[\boldsymbol{C}^2]\right), \\ III_C &= \det(\boldsymbol{C}) = J^2. \end{aligned} \tag{2.55}$$

For compressible material behavior, the deformation may be split into an isochoric and a volumetric part:

$$\begin{aligned} \Psi(\boldsymbol{C}) &= \bar{\Psi}(\bar{\boldsymbol{C}}) + \Psi_{\text{vol}}(J), \\ \Psi(I_C, II_C, III_C) &= \bar{\Psi}(\bar{I}_C, \bar{II}_C) + \Psi_{vol}(J), \\ \text{where } \overline{I}_C &= J^{-2/3} I_C, \overline{II}_C = J^{-4/3} II_C \text{ and } \overline{III}_C = 1. \end{aligned} \tag{2.56}$$

Here, $\overline{I}_C$,$\overline{II}_C$ and $\overline{III}_C$ are the modified isochoric invariants [43] and $\boldsymbol{C} = J^{2/3}\bar{\boldsymbol{C}}$. Equation (2.56) can be seen as a penalty-like approach to model nearly incompressible material behavior through large Ψ_{vol}.

2.2.2.3. Balance equations

Balance equations were previously introduced in section 2.2.1. However, mass and linear momentum conservation are briefly given in their local forms. Also, the balance of energy does not provide additional information in purely structural problems and is omitted.
Using Gauss' divergence theorem and dismissing the integrals over arbitrary volumes in equation (2.30), the local forms of mass conservation in the current and reference configuration yield

$$\dot{\rho} + \rho \boldsymbol{\nabla} \cdot \boldsymbol{v} = 0 \qquad \text{and} \qquad \dot{\rho}_0 = 0. \tag{2.57}$$

Similarly for conservation of linear momentum, the local forms can be obtained from equation (2.33), including body forces and surface tractions. This is called *Cauchy's first law of motion* and obeys in the current and reference configuration

$$\rho \dot{\boldsymbol{v}} = \boldsymbol{\nabla} \cdot \boldsymbol{\sigma} + \hat{\boldsymbol{b}} \qquad \text{and} \qquad \rho_0 \dot{\boldsymbol{v}} = \boldsymbol{\nabla}_0 \cdot (\boldsymbol{F}\boldsymbol{S}) + \hat{\boldsymbol{b}}_0. \tag{2.58}$$

Here, $\boldsymbol{\nabla}_0$ and $\boldsymbol{\nabla}$ are the Nabla operators with respect to the reference and current configuration, respectively.

Note that both the Cauchy stress and the second Piola-Kirchhoff stress are symmetric, i.e. $\boldsymbol{\sigma} = \boldsymbol{\sigma}^{\mathrm{T}}$ and $\boldsymbol{S} = \boldsymbol{S}^{\mathrm{T}}$. This property is equivalent to local conservation of angular momentum, which is not further detailed here.

2.2.2.4. Contact mechanics

Below, a brief introduction to contact mechanics is given. Details can be found in the textbook of Wriggers [120]. The methods used in this thesis can be found in the works of Popp et al. [86, 87] and in Popp's thesis [85]. The defined contact boundaries of two bodies Γ_1^{c} and Γ_2^{c} will eventually touch at the respective points $\boldsymbol{x}_1^{\mathrm{c}}$ and $\boldsymbol{x}_2^{\mathrm{c}}$, which are to be determined during the solution process. A so-called *gap function* is defined as

$$g_n = -\boldsymbol{n}^{\mathrm{c}} \cdot (\boldsymbol{x}_1^{\mathrm{c}} - \boldsymbol{x}_2^{\mathrm{c}}), \tag{2.59}$$

which quantifies the distance between the contact partners. The resulting contact traction can be split into a normal and a tangential component,

$$\boldsymbol{t} = p_n \boldsymbol{n}^{\mathrm{c}} + \boldsymbol{t}_t, \tag{2.60}$$

with $p_n \leq 0$ being the stress in normal direction and $\boldsymbol{t}_t$ the tangential component, which is set to zero throughout this thesis. It is then known as frictionless contact. The contact constraints are formulated as Karush-Kuhn-Tucker (KKT) conditions:

$$g_n(\boldsymbol{x}, t) \geq 0, \tag{2.61}$$

$$p_n(\boldsymbol{x}, t) \leq 0 \text{ and} \tag{2.62}$$

$$p_n(\boldsymbol{x}, t) g_n(\boldsymbol{x}, t) = 0. \tag{2.63}$$

These guarantee no penetration (2.61), negative or zero contact pressure (2.62) and traction only when the bodies are in contact (2.63), hence when the gap function is zero.

2.2.2.5. Principle of virtual work

The initial boundary value problem may be presented in its weak form in the reference configuration. This is advantageous for problems being solved with the finite element (FE) method, since the solutions for weighted integrals are searched for and only first-order spatial derivatives remain. The principle of virtual work is given by:

$$\delta\mathcal{W} = \int_{\Omega_0} \rho_0 \ddot{\boldsymbol{u}} \cdot \delta\boldsymbol{u} \mathrm{d}V + \int_{\Omega_0} \boldsymbol{S} : \delta\boldsymbol{E} \mathrm{d}V - \int_{\Omega_0} \hat{\boldsymbol{b}}_0 \cdot \delta\boldsymbol{u} \mathrm{d}V - \int_{\Gamma_0} \hat{\boldsymbol{t}}_0 \cdot \delta\boldsymbol{u} \mathrm{d}A = 0, \quad \forall \delta\boldsymbol{u}. \tag{2.64}$$

2.3. Discretization and solution

A brief introduction to the discretization methods used in this work follows. Later sections build on the equations derived here. More information can be found in the textbook of Zienkiewicz [124]. Models in the present work are either mixed-dimensional 0D-3D as in the sections 3.1 and 3.3 or purely 0D as in section 3.2.

2.3.1. Spatial discretization

All 3D models are discretized for use with the *finite element* method. Its basics can be found in [124]. Therefore, the entire real domain Ω_0 is split into n_{el} non-overlapping subdomains $\Omega_0^{(e)}$. These subdomains are referred to as finite elements:

$$\Omega_0 \approx \sum_{e=1}^{n_{el}} \Omega_0^{(e)}. \tag{2.65}$$

The element displacement field $\boldsymbol{u}^{(e)}$ is a linear combination of position dependent shape functions $\boldsymbol{N}^{(e)}(\boldsymbol{X})$ and time dependent nodal displacements $\boldsymbol{d}^{(e)}(t)$ yielding

$$\boldsymbol{u}^{(e)}(\boldsymbol{X}, t) = \boldsymbol{N}^{(e)}(\boldsymbol{X}) \boldsymbol{d}^{(e)}(t). \tag{2.66}$$

The nodal coordinates $\bar{\boldsymbol{X}}^{(e)}$ are mapped to the physical domain by the same shape functions, i.e. $\boldsymbol{X}^{(e)} = \boldsymbol{N}^{(e)} \bar{\boldsymbol{X}}^{(e)}$. Since a *Bubnov-Galerkin approach* is utilized, the weight functions or virtual displacements are approximated in the same manner:

$$\delta\boldsymbol{u}^{(e)}(\boldsymbol{X}) = \boldsymbol{N}^{(e)}(\boldsymbol{X}) \delta\boldsymbol{d}^{(e)}. \tag{2.67}$$

Using (2.66) and (2.67), the semi-discrete global balance equation yields

$$\boldsymbol{M}\ddot{\boldsymbol{d}} + \mathbf{F}_{\text{int}}(\boldsymbol{d}) = \mathbf{F}_{\text{ext}}. \tag{2.68}$$

Here, $\boldsymbol{M}$ is the mass matrix and $\boldsymbol{d}$ the global displacement vector. $\mathbf{F}_{\text{ext}}$ incorporates all external forces, namely all body and traction forces. When considering follower loads, the external force vector is dependent upon the displacement $\mathbf{F}_{\text{ext}} = \mathbf{F}_{\text{ext}}(\boldsymbol{d})$. Every material has damping properties, which have not been dealt with so far. To avoid rather complicated formulations in

the constitutive laws, it is a common approach in engineering to model damping as a linear combination of mass and stiffness properties, referred to as *Rayleigh damping*. It utilizes the coefficients α_M [1/s] and β_K [s] to create the damping matrix $\boldsymbol{D}$

$$\boldsymbol{D} = \alpha_M \boldsymbol{M} + \beta_K \boldsymbol{K}_{T,0}, \tag{2.69}$$

where $\boldsymbol{K}_{T,0}$ is the initial tangent stiffness matrix. The discretized global system of equations then reads

$$\boldsymbol{M}\ddot{\boldsymbol{d}} + \boldsymbol{D}\dot{\boldsymbol{d}} + \mathbf{F}_{\text{int}}(\boldsymbol{d}) - \mathbf{F}_{\text{ext}}(\boldsymbol{d}) = \mathbf{0}. \tag{2.70}$$

2.3.2. Temporal discretization

Finite difference methods are used to discretize all models in time. The Generalized-α method [15] is used for second-order differential equations of structural mechanics (cf. 2.70). It is based on Newmark's method [80], which assumes a linear progression of the acceleration over the time step. In the following, $(\bullet)_{n+1}$ denotes values of the current time step whereas $(\bullet)_n$ represents values of the previous time step. With $\mathbf{a} = \ddot{d}$ and $\mathbf{v} = \dot{d}$, velocity and acceleration are approximated by

$$\begin{aligned} \mathbf{v}_{n+1} &= \tfrac{\gamma}{\beta\Delta t}(\boldsymbol{d}_{n+1} - \boldsymbol{d}_n) - \tfrac{\gamma-\beta}{\beta}\mathbf{v}_n - \tfrac{\gamma-2\beta}{2\beta}\Delta t\, \mathbf{a}_n \text{ and} \\ \mathbf{a}_{n+1} &= \tfrac{1}{\beta\Delta t^2}(\boldsymbol{d}_{n+1} - \boldsymbol{d}_n) - \tfrac{1}{\beta\Delta t}\mathbf{v}_n - \tfrac{1-2\beta}{2\beta}\mathbf{a}_n, \end{aligned} \tag{2.71}$$

with parameters $\beta \in$ [0,0.5] and $\gamma \in$ [0,1] at the time step t_{n+1}. The structural residual (2.70) is then

$$\boldsymbol{r}^{\text{S}} = \boldsymbol{M}\ddot{\boldsymbol{d}}_{n+1-\alpha_m} + \boldsymbol{D}\dot{\boldsymbol{d}}_{n+1-\alpha_f} + \mathbf{F}_{\text{int},n+1-\alpha_f} - \mathbf{F}_{\text{ext},n+1-\alpha_f} = \mathbf{0}, \tag{2.72}$$

with

$$(\bullet)_{n+1-\alpha_{[\circ]}} = (1-\alpha_{[\circ]})(\bullet)_{n+1} + \alpha_{[\circ]}(\bullet)_n. \tag{2.73}$$

Here, α_m, $\alpha_f \in$ [0,1]. The parameters $\{\alpha_m, \alpha_f, \beta, \gamma\}$ can be chosen to control numerical dissipation.

For 0D models, the *One-Step-θ method* is used [8]. Depending on the choice of $\theta \in$ [0,1] it represents the mid-point as a weighted linear combination of the function evaluated at the previous and the current time step. It reads

$$\frac{(\bullet)_{n+1} - (\bullet)_n}{\Delta t} = \theta f[(\bullet)_{n+1}] + (1-\theta) f[(\bullet)_n]. \tag{2.74}$$

The values $\theta \in \{0, 1\}$ represent the *Forward-Euler* and *Backward-Euler* method, respectively.

2.3.3. Linearization

Newton's method is used to solve the system of nonlinear equations (2.72). The method searches for the root of the discrete residual $\boldsymbol{r}^S(\boldsymbol{d}_{n+1})$ for the time step $n+1$. Note that also non solid

mechanics problems are solved in such a manner within the present work. The method requires the linearized residual to vanish, Lin $\boldsymbol{r}^{\mathrm{S}}(\boldsymbol{d}_{n+1}^{i}) \stackrel{!}{=} \boldsymbol{0}$, with

$$\text{Lin } \boldsymbol{r}^{\mathrm{S}}(\boldsymbol{d}_{n+1}^{i}) = \boldsymbol{r}^{\mathrm{S}}(\boldsymbol{d}_{n+1}^{i}) + \left.\frac{\partial \boldsymbol{r}^{\mathrm{S}}(\boldsymbol{d}_{n+1})}{\partial \boldsymbol{d}_{n+1}}\right|^{i} \Delta\boldsymbol{d}_{n+1}^{i+1} = \boldsymbol{r}^{\mathrm{S}}(\boldsymbol{d}_{n+1}^{i}) + \boldsymbol{K}(\boldsymbol{d}_{n+1}^{i})\Delta\boldsymbol{d}_{n+1}^{i+1}. \tag{2.75}$$

Therefore, in each Newton iteration, the incremental update $\Delta\boldsymbol{d}_{n+1}^{i+1}$ must be solved for in

$$\boldsymbol{K}(\boldsymbol{d}_{n+1}^{i})\Delta\boldsymbol{d}_{n+1}^{i+1} = -\boldsymbol{r}^{\mathrm{S}}(\boldsymbol{d}_{n+1}^{i}). \tag{2.76}$$

The solution of (2.76) updates the displacement of the current time step

$$\boldsymbol{d}_{n+1}^{i+1} = \boldsymbol{d}_{n+1}^{i} + \Delta\boldsymbol{d}_{n+1}^{i+1}, \tag{2.77}$$

until a convergence criterion is met. In the present work, the iterative solution process is stopped when the 2-norm of the residual and of the solution increment are below their respective tolerances. For monolithic solution processes in multiphysics modeling, the vector of unknowns may be clustered for a convergence check to allow for meaningful tolerances for different physical units for the problem at hand.

3. Modeling

In this chapter, a mixed-dimensional multi-physics model of a BiVAD-supported patient is presented. Its purpose is to provide answers to overarching questions concerning the interaction between the technical and the biological system, but also to serve as a tool during assist device design iterations. The chapter structures as follows: First, the BiVAD model is introduced, followed by the model to predict the mean steady state temperatures of the heated drive unit. Thereafter, the BiVAD is coupled to an existing cardiovascular model. Finally, exemplary results are shown and discussed.

In order to simulate a supported cardiovascular system, several submodels have to be built and coupled, namely the biventricular assist device, the heart and the circulatory system. First, the drive unit model, with the equations for all functional components, such as pump, valves, tubes and reservoirs as well as those for valve control, is introduced. It allows for pressure, flow and temperature signal computation at designated points of the drive unit during the dynamic simulation of a supported heart beat. In contrast, device heating may take hours before the mean temperature eventually reaches a steady state. In order to start the dynamic simulation from such a steady mean temperature, a heating model is introduced in a second step. The drive unit is mainly described as a 0D model, but eventually couples to a 3D structure, the implant, which itself interacts with the patient heart, also represented in three dimensions. The heart model is further coupled to a patient-specific 0D circulatory system. The reader will briefly be introduced to both, the heart and circulatory model, which were developed by Hirschvogel [44], [45], [43].

3.1. 0D-3D biventricular assist device (BiVAD)

The mixed-dimensional multi-physics BiVAD model is presented in this section. The real system is introduced in section 1.5.4. A photograph of the real system is given in figure 3.1. It depicts the drive unit with connected driveline and implant.

The BiVAD functioning will be explained in more detail here, using the schematic in figure 3.2. It consists of the drive unit which provides pressurized air to cyclically inflate the EUs. Therefore, the drive unit consists of two pressure reservoirs, which are interconnected by a pump. The pump continuously supplies air to the high pressure reservoir (HPR), such that its pressure is permanently above ambient level. Consequently, the pressure in the low pressure reservoir (LPR) always remains below ambient pressure. The inlet valves connect the HPR and EUs over the supply tubes. Their opening can be controlled to adequately inflate the EUs during cardiac contraction. Likewise, the outlet valves connect EUs and LPR to allow for deflation during the

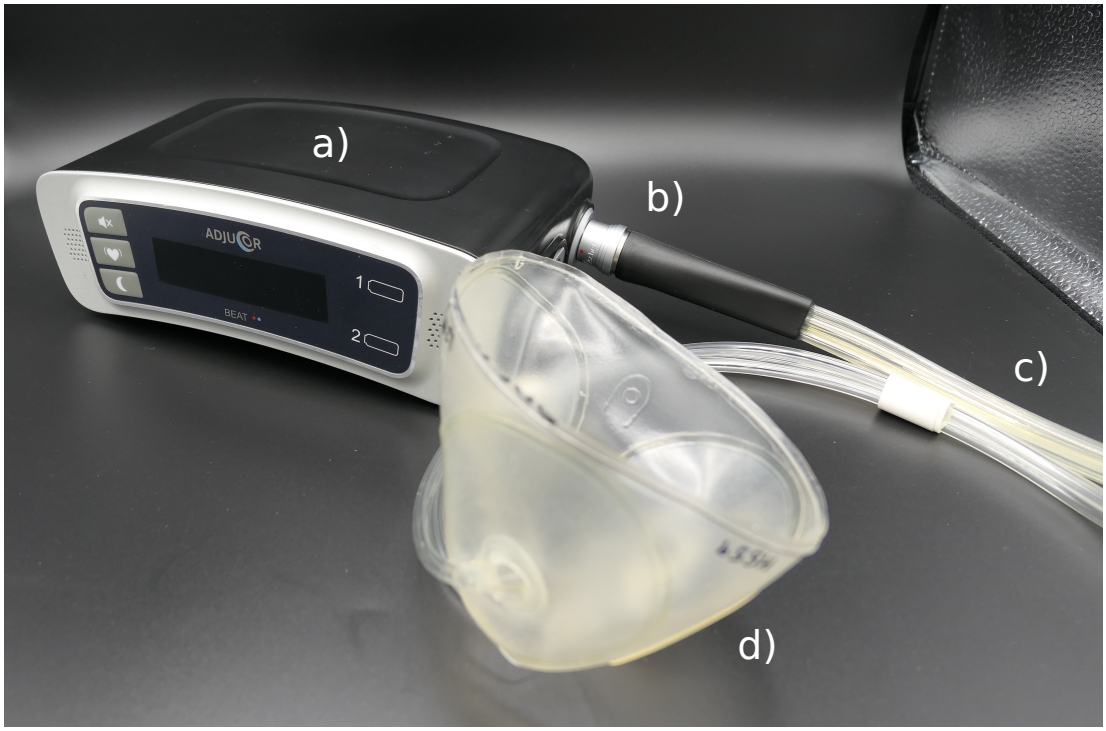

Figure 3.1.: Photograph of AdjuCor's BiVAD, consisting of the drive unit a), the driveline connector b), the driveline tubes c) and the embedded EUs d). The drive unit features a user interface to display information, e.g. the current heart rate, and to allow for parameter setting.

cardiac relaxation. The supply tubes are plugged into the drive unit by a connector, which both represent a pneumatic flow restriction. The implant with EUs and roughly one third of the supply tubes are located in the body. The tubes exit the body at a certain point in the lower, lateral abdominal area.

The given introduction illustrates that thermodynamics and fluid mechanics formulations prevail in the model. In addition, some control and auxiliary equations are needed. As described in section 2.1, two state variables suffice to unequivocally describe the state of air at a particular point. The drive unit of the BiVAD is represented by a lumped-parameter model, where a subdomain of the real system is reduced to a node. These nodes are connected as depicted in figure 3.2 and at least two equations are assigned to each node: one for pressure and one for temperature. Consequently, flows within the system result from pressure differences between these points. The reservoirs and the pump are only present once, while, due to the existence of three EUs, three inlet and outlet valves as well as three tubes are installed. As can be seen in figure 3.2, the blue nodes are consistently located before and after each component. The drive unit model consists of ordinary differential equations (ODE) and algebraic equations. Within this work, the rates of change of mass, volume and temperature are substituted according to

$$\dot{m} = g, \qquad \dot{V} = q \quad \text{and} \quad \dot{T} = \tau. \tag{3.1}$$

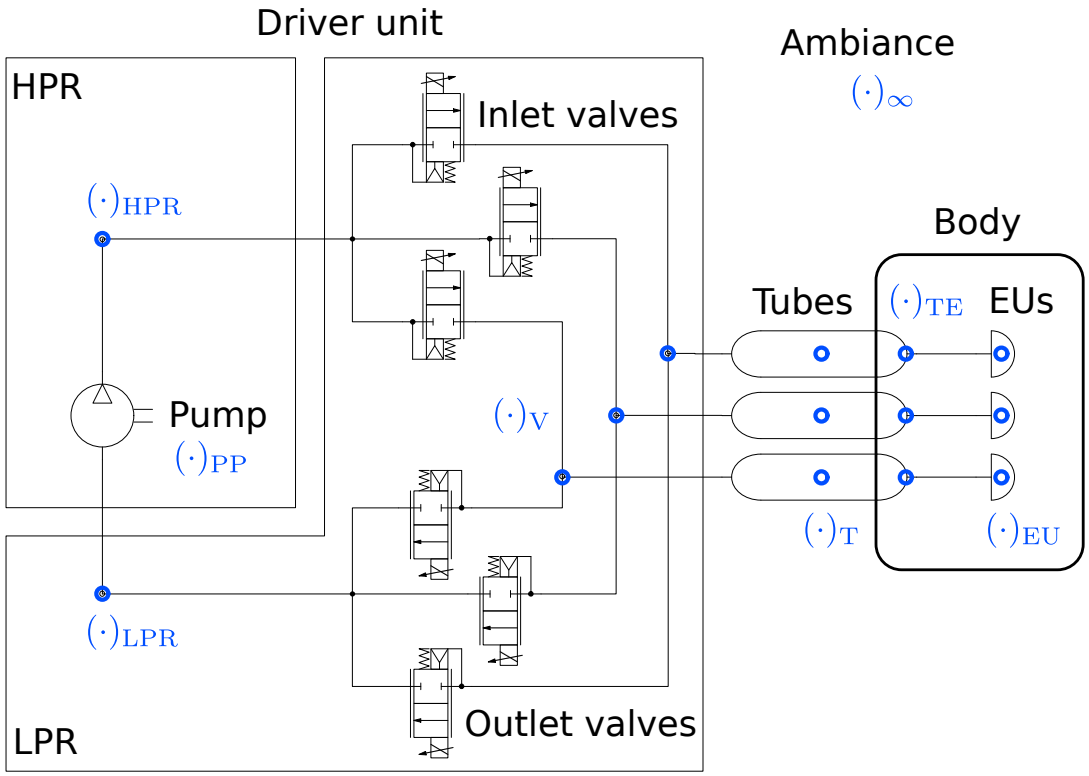

Figure 3.2.: Schematic of the pneumatic system of the BiVAD with the lumped nodes of the model and their corresponding index notation in blue. The three expandable units (EU) are individually supplied by a tube, an inlet and outlet valve. They share the reservoirs HPR and LPR and the pump, which cyclically restores the needed pneumatic energy.

3.1.1. Assumptions

The following assumptions regarding thermodynamic modeling are applied:

- Air is modeled as an ideal gas. The difference in specific volume to real measurements is below 1 % for the wide range of pressures until $2 \cdot 10^3$ kPa and temperatures between 0°C and 800°C [33]. Pressures and temperatures of the underlying BiVAD range between [-50,50] kPa and [10,50]°C. A thermodynamically ideal gas is characterized by a constant material parameter, namely the specific gas constant $R = 287\ [\frac{\mathrm{J}}{\mathrm{Kg\ K}}]$ and the dimensionless ratio between the constant specific heat coefficients $\kappa = \frac{c_p}{c_v} = 1.4$ [106].
- Air within the system is modeled as a homogeneous, single phase fluid.
- Gravitational effects are neglected within the system volumes: The density of air is relatively low and no significant altitude differences apply.
- Pressure and temperature are homogeneous within the system volumes. This assumption is valid when flow velocities are below the speed of sound, since pressure waves travel at that specific velocity. Hence, $v < \tilde{c}$ must agree, with v being the average flow velocity and $\tilde{c}$ the speed of sound (cf. section 2.2.1.1).

3.1.2. Reservoirs

The system at hand features two reservoirs, which are referred to as the low pressure reservoir (LPR) and the high pressure reservoir (HPR). Their purpose is to store pneumatic energy, created by the system's pump and cyclically consumed by the load, the patient's implant. To describe the pressure evolution, the total derivative of the ideal gas law (2.3) is utilized

$$\frac{\mathrm{d}p}{\mathrm{d}t}V + p\frac{\mathrm{d}V}{\mathrm{d}t} = \frac{\mathrm{d}m}{\mathrm{d}t}RT + mR\frac{\mathrm{d}T}{\mathrm{d}t}. \tag{3.2}$$

The reservoirs are made of polyoxymethylene (POM) and undergo deformation when pressurized. Therefore, the reservoirs are modeled as compliant containers. The left side of equation (3.2) is transformed to

$$\frac{\mathrm{d}p}{\mathrm{d}t}V + p\frac{\mathrm{d}V}{\mathrm{d}p}\frac{\mathrm{d}p}{\mathrm{d}t} = \frac{\mathrm{d}p}{\mathrm{d}t}V + pC_{\mathrm{Res}}\frac{\mathrm{d}p}{\mathrm{d}t} = \frac{\mathrm{d}p}{\mathrm{d}t}\left(V + pC_{\mathrm{Res}}\right), \tag{3.3}$$

where the reservoir compliance $C_{\mathrm{Res}} = \frac{\mathrm{d}V}{\mathrm{d}p}$ is introduced. The first term on the right side of equation (3.2) is converted into the sum of inflows and outflows. After rearranging and substituting according to (3.1), the pressure equation for the reservoir yields

$$\frac{\mathrm{d}p}{\mathrm{d}t} = \frac{RT\sum g + \frac{pV}{T}\tau}{V + pC_{\mathrm{Res}}}. \tag{3.4}$$

The sum of in- and outflows differs for HPR and LPR. Air is released from the HPR over the inlet valves into the k-th tube and EU, resulting in the mass flows $g^k_{\mathrm{V,in}}$. In contrast, air mass flows into the LPR over the outlet valves, described by $g^k_{\mathrm{V,out}}$. Both reservoirs are related by the pump's generated flow g_{PP}, which leaves the LPR and enters the HPR. The two pressure equations finally read

$$\frac{\mathrm{d}p_{\mathrm{HPR}}}{\mathrm{d}t} = \frac{RT_{\mathrm{HPR}}\left(g_{\mathrm{PP}} - \sum_{k=1}^{3} g^k_{\mathrm{V,in}}\right) + \frac{p_{\mathrm{HPR}}V_{\mathrm{HPR}}}{T_{\mathrm{HPR}}}\tau_{\mathrm{HPR}}}{V_{\mathrm{HPR}} + p_{\mathrm{HPR}}C_{\mathrm{HPR}}}, \tag{3.5}$$

$$\frac{\mathrm{d}p_{\mathrm{LPR}}}{\mathrm{d}t} = \frac{RT_{\mathrm{LPR}}\left(\sum_{k=1}^{3} g^k_{\mathrm{V,out}} - g_{\mathrm{PP}}\right) + \frac{p_{\mathrm{LPR}}V_{\mathrm{LPR}}}{T_{\mathrm{LPR}}}\tau_{\mathrm{LPR}}}{V_{\mathrm{LPR}} + p_{\mathrm{LPR}}C_{\mathrm{LPR}}}, \tag{3.6}$$

with $k \in \{1, 2, 3\}$ representing the individual EU with supply line.

After power-on and start of cardiac support, the system is subject to a long-term heating process. The reservoir temperatures eventually become periodic and their mean values remain constant. The heating process is governed by the input electrical power and is addressed in section 3.2, but the results thereof are used as an input to the dynamic model of this section. Once the periodic state is reached, the reservoir temperature depends on the entering and leaving mass-stored thermal energy and the heat exchange with the environment. The first law of thermodynamics (2.9) is used to model the temperature in the reservoirs. The rate of change of internal energy equals heat and enthalpy transfers across the reservoir boundaries. Kinetic energy is approximately four orders of magnitude smaller than thermal energy contributions and is neglected here. A more detailed explanation can be found in the appendix A.II.1. Replacing $U = c_{\mathrm{v}}mT$ and $H = c_pmT$, the power balance for a reservoir reads

$$c_{\mathrm{v}}\left(\frac{\mathrm{d}m}{\mathrm{d}t}T + \frac{pV}{RT}\frac{\mathrm{d}T}{\mathrm{d}t}\right) = \dot{Q} + \dot{W} + c_pT_{\mathrm{in}}g_{\mathrm{in}} - c_pT_{\mathrm{out}}g_{\mathrm{out}}, \tag{3.7}$$

with $(\bullet)_{\text{in}}$, $(\bullet)_{\text{out}}$ being quantities entering or leaving the system, respectively. Heat exchange is modeled according to equation (2.22) with the heat transmittance k_{th}, introduced in (2.23). It is split into heat transfer with the environment $(\bullet)_\infty$ and through the reservoir septum wall $(\bullet)_{\text{W}}$ with the neighbor reservoir:

$$\dot{Q}_{\text{Res}} = \dot{Q}_\infty + \dot{Q}_{\text{W}} = k_{\text{th,Res}} A_{\text{Res}} (\tilde{T}_\infty - T_{\text{Res}}) + k_{\text{th,W}} A_{\text{W}} (T_{\text{Neighbor}} - T_{\text{Res}}). \tag{3.8}$$

Since the system is considered to have reached a constant mean reservoir temperature prior to the transient simulation, any work done on the system is zero, $\dot{W} = 0$, and the pseudo-ambient temperature $\tilde{T}_\infty$ is set to the respective mean reservoir temperature $\Delta\hat{T}_{\text{HPR}}$ or $\Delta\hat{T}_{\text{LPR}}$, respectively. The latter are the result of the mean temperature prediction model (MTP) in section 3.2 and the heat transfer $\dot{Q}_{\text{Res}}$ becomes

$$\dot{Q}_{\text{HPR}} = k_{\text{th,HPR}} A_{\text{HPR}} \left((T_\infty + \Delta\hat{T}_{\text{HPR}}) - T_{\text{HPR}} \right) + k_{\text{th,W}} A_{\text{W}} (T_{\text{LPR}} - T_{\text{HPR}}) \quad \text{and} \tag{3.9}$$

$$\dot{Q}_{\text{LPR}} = k_{\text{th,LPR}} A_{\text{LPR}} \left((T_\infty + \Delta\hat{T}_{\text{LPR}}) - T_{\text{LPR}} \right) + k_{\text{th,W}} A_{\text{W}} (T_{\text{HPR}} - T_{\text{LPR}}). \tag{3.10}$$

Hence, heat exchange with the environment only occurs when the momentary reservoir temperatures T_{HPR} and T_{LPR} differ from $T_\infty + \Delta\hat{T}_{\text{HPR}}$ and $T_\infty + \Delta\hat{T}_{\text{LPR}}$, respectively. Thus the following equations add to the reservoir model:

$$\frac{V_{\text{HPR}}}{R} \frac{\mathrm{d}T_{\text{HPR}}}{\mathrm{d}t} = \left[\dot{Q}_{\text{HPR}} \frac{\kappa - 1}{R} - \kappa T_{\text{HPR}} \sum_{k=1}^{3} g_{\text{V,in}}^k + \kappa g_{\text{PP}} T_{\text{PP}} - \left(g_{\text{PP}} - \sum_{k=1}^{3} g_{\text{V,in}}^k \right) T_{\text{HPR}} \right] \frac{T_{\text{HPR}}}{p_{\text{HPR}}}, \tag{3.11}$$

$$\frac{\mathrm{d}T_{\text{HPR}}}{\mathrm{d}t} = \tau_{\text{HPR}}, \tag{3.12}$$

$$\frac{V_{\text{LPR}}}{R} \frac{\mathrm{d}T_{\text{LPR}}}{\mathrm{d}t} = \left[\dot{Q}_{\text{LPR}} \frac{\kappa - 1}{R} + \kappa T_{\text{V}} \sum_{k=1}^{3} g_{\text{V,out}}^k - \kappa g_{\text{PP}} T_{\text{LPR}} - \left(\sum_{k=1}^{3} g_{\text{V,out}}^k - g_{\text{PP}} \right) T_{\text{LPR}} \right] \frac{T_{\text{LPR}}}{p_{\text{LPR}}}, \tag{3.13}$$

$$\frac{\mathrm{d}T_{\text{LPR}}}{\mathrm{d}t} = \tau_{\text{LPR}}. \tag{3.14}$$

Modeling temperature in a pneumatic chamber as in (3.11) and (3.13) can also be found in other works [13], [29]. In (3.11), the temperature of the air entering the HPR through the pump is modeled as a general polytropic change of state with the exponent n_{PP}, as introduced in (2.19). It reads

$$T_{\text{PP}} = T_{\text{LPR}} \left(\frac{p_{\text{HPR}}}{p_{\text{LPR}}} \right)^{\frac{n_{\text{PP}} - 1}{n_{\text{PP}}}}. \tag{3.15}$$

The reservoir model parameters $V_{\text{HPR}}, V_{\text{LPR}}, C_{\text{HPR}}$ and C_{LPR} where determined experimentally. Therefore, a validated test bench was designed and built, which uses the general law (2.16) with $n = 1$ to describe an isothermal process. In short, an air-charged container with a known, fixed volume at a known pressure is pneumatically connected to the volume to be measured. After the pressure and temperature equilibrium is reached, the unknown volume can be determined with high accuracy [89]. A more detailed documentation of this procedure can be found

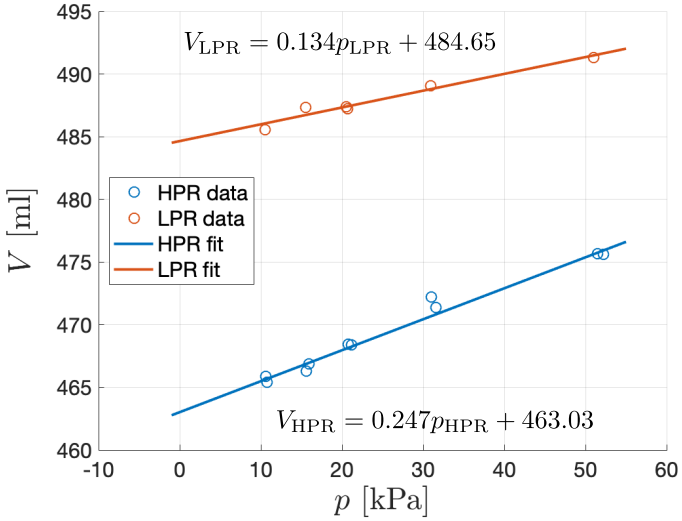

Figure 3.3.: Compliance and volume of the reservoirs as the result of volumetric measurements. The upper line represents the LPR, whereas the HPR is described by the lower curve. The intersection with the volume axis is used as unloaded reservoir volume and the slope as reservoir compliance.

in the appendix A.I.1. Therewith, the volumes and the compliances of both reservoirs could be determined by varying the equilibrium pressure, yielding a linear relation between pressure and volume, with the slope being the compliance and the intersection with the volume axis at zero pressure being the unloaded volume, as can be seen in figure 3.3. The identified values are listed in table 3.1. This process is also known as *metering in liters*. The heat transmittances $k_{\mathrm{th,HPR}}$, $k_{\mathrm{th,LPR}}$, $k_{\mathrm{th,W}}$ are estimated in section 3.2 and heat exchange surface areas of the reservoirs A_{HPR}, A_{LPR}, A_{W} are obtained from CAD data.

Parameter [Unit]	Value
V_{HPR} [mm^3]	$4.63 \cdot 10^5$
C_{HPR} [$\frac{\mathrm{mm}^3}{\mathrm{kPa}}$]	247.0
V_{LPR} [mm^3]	$4.84 \cdot 10^5$
C_{LPR} [$\frac{\mathrm{mm}^3}{\mathrm{kPa}}$]	134.0

Table 3.1.: Parameters of the reservoir model.

In summary, the reservoir is modeled by the pressure equations (3.5) and (3.6) as well as the temperature related equations (3.11) to (3.14).

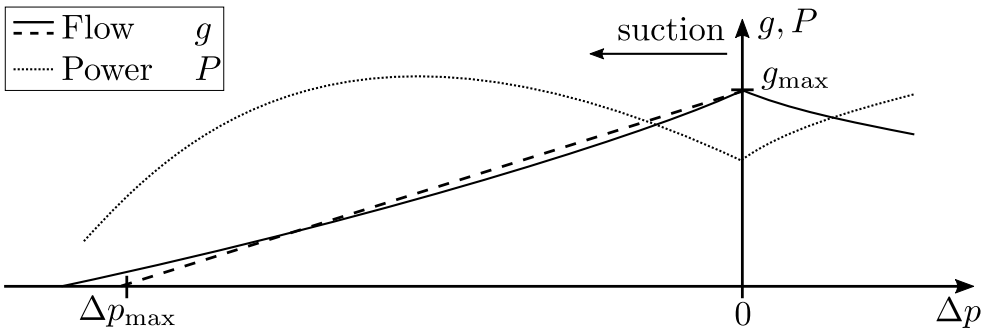

Figure 3.4.: Schematic reproduction of the pump data sheet graph, with the solid line being the specified flow and the dotted line the electrical power consumption, both as function of the pressure load. The dashed line indicates the linear basis of the pump flow model, connecting the distinct *free flow* point ($\Delta p = 0$) with the *zero flow* point ($g = 0$). This model is only the basis and is adapted to the specific conditions of the pump within the BiVAD.

3.1.3. Pump

The electrically driven diaphragm pump converts electrical energy into pneumatic energy and heat. The pump is located in the HPR, drawing in air from the LPR and pumping it into its environment, the HPR. The generated flow depends upon the pressure load as well as on the control and supply voltage. The flow and power consumption are given in the manufacturer's data sheet as curves over the pressure load and are reproduced schematically in figure 3.4.

A linear model is used, as indicated by the dashed line in figure 3.4, to connect the distinctive points of maximum flow at zero load, also called the *free flow*, $g(\Delta p = 0) = g_{\max}$ and *zero flow* at maximum load $g(\Delta p = \Delta p_{\max}) = 0$. When this notation is adapted to the system at hand, with any pump related property denoted by $(\bullet)_{\text{PP}}$, the basic equation reads

$$g_{\text{PP}} = g_{\text{PP,max}} \left(1 - \frac{\Delta p_{\text{Res}}}{\Delta p_{\text{Res,max}}} \right) = g_{\text{PP,max}} \left(1 - \frac{p_{\text{HPR}} - p_{\text{LPR}}}{\Delta p_{\text{Res,max}}} \right). \tag{3.16}$$

However, the zero flow bound $\Delta p_{\text{Res,max}}$ is not constant and depends on the prevailing pressure condition itself. The diaphragm pump can be treated similar to a piston pump, with two distinctive phases: compression (expansion) and expulsion (suction) of air during piston upstroke (downstroke). Now, the pump reaches its zero flow bound $\Delta p_{\text{Res,max}}$ exactly when the full piston stroke is needed for compression (expansion) and hence none is left for expelling (suction). The maximum and minimum volumes of the pump's cylinders are constant, $V_{\text{min}},\ V_{\text{max}} = \text{constant}$, as they result from the rigid internal geometry. The polytropic law (2.16) allows to express this boundary condition as

$$\frac{p_{\text{HPR}}}{p_{\text{LPR}}} = \left(\frac{V_{\text{max}}}{V_{\text{min}}} \right)^n = (\text{constant})^n = \text{constant} =: C_{\text{PP}}. \tag{3.17}$$

Assuming a constant polytropic exponent n, the pressure ratio C_{PP} can be introduced, which is a pump specific parameter and characterizes the zero flow $\Delta p_{\max}$ point in figure 3.4. This relation can be inserted into the denominator of (3.16), when $\Delta p_{\text{Res}} = p_{\text{HPR}} - p_{\text{LPR}}$ is rearranged to

$\frac{\Delta p_{\text{Res}}}{p_{\text{LPR}}} = \frac{p_{\text{HPR}}}{p_{\text{LPR}}} - 1$. By inserting the pressure ratio (3.17), Δp_{Res} passes over to $\Delta p_{\text{Res,max}}$, making it the reservoir pressure difference at this zero flow point:

$$\Delta p_{\text{Res,max}} = p_{\text{LPR}}(C_{\text{PP}} - 1). \tag{3.18}$$

The pump speed is primarily dependent upon two input properties. Firstly, the rotational speed can be tuned by altering the control voltage, e.g. by changing the duty cycle of a pulse-width modulated (PWM) signal. The duty cycle is the time percentage during which the supply voltage is fed to the pump motor and it is introduced in this model as the pump control signal $y_{\text{PP}} \in [0, 1]$. It scales the output flow of the pump model. Secondly, the revolution speed depends upon the prevailing supply voltage $\mathcal{U}_{\text{supply}}$ itself, which is provided by the system battery. It may decline over time as the battery discharges during operation. The supply voltage $\mathcal{U}_{\text{supply}}$ co-determines the maximum speed and hence the maximum free flow $g_{\text{PP,max}}$.

The manufacturer's data sheet curve was taken at normal conditions, meaning at $T_{\text{norm}} = 20\ °\text{C}$ and $p_{\text{norm}} = 101.325$ kPa, defining the normal density condition by (2.4). The generated flow has hence to be scaled to the actual density condition prevailing on the suction side by $\rho_{\text{LPR}}/\rho_{\text{norm}}$. The specific gas constant in (2.4) cancels out and the quotient $\frac{T_{\text{norm}}}{T_{\text{LPR}}} \frac{p_{\text{LPR}}}{p_{\text{norm}}}$ remains. Inserting (3.18) into (3.16) as well as adding the introduced density adjustments, the final pump flow model is derived:

$$g_{\text{PP}} = g_{\text{PP,max}} y_{\text{PP}} \frac{T_{\text{norm}}}{T_{\text{LPR}}} \frac{p_{\text{LPR}}}{p_{\text{norm}}} \left(1 - \frac{p_{\text{HPR}} - p_{\text{LPR}}}{p_{\text{LPR}}(C_{\text{PP}} - 1)}\right). \tag{3.19}$$

The free flow $g_{\text{PP,max}}$ in the range of possible supply voltages $\mathcal{U}_{\text{supply}} \in [12, 17]$ V was determined experimentally for $y_{\text{PP}} = 1$ by measuring the generated free flow. The measured data points and the linear regression curve utilized can be found in figure 3.5 b) and the linear function in table 3.2. The pump specific compression ratio C_{PP} was determined experimentally by letting the pump run within the drive unit until the zero flow point was reached and pressures in both reservoirs remained constant. This was reproduced for three different supply voltages, three different control signals and two different drive units, giving a sample size $3 \times 3 \times 2 = 18$. Figure 3.5 shows the evaluation of the obtained data. The median of the full data set, denoted as *all* in the graph a), is 4.76, those of the individual drive units are 4.73 and 4.87, respectively. Since the compression ratio C_{PP} is not significantly altered with the changed conditions, the median of the complete data set is utilized in this model, $C_{\text{PP}} = 4.76$. A summary of the pump model parameters can be found in table 3.2.

Parameter [Unit]	Value
$g_{\text{PP,max}}\ \left[\frac{\text{mg}}{\text{ms}}\right]$	$1.827 \cdot 10^{-3}\mathcal{U}_{\text{supply}} + 0.204$
C_{PP} [/]	4.76

Table 3.2.: Parameters of the pump model.

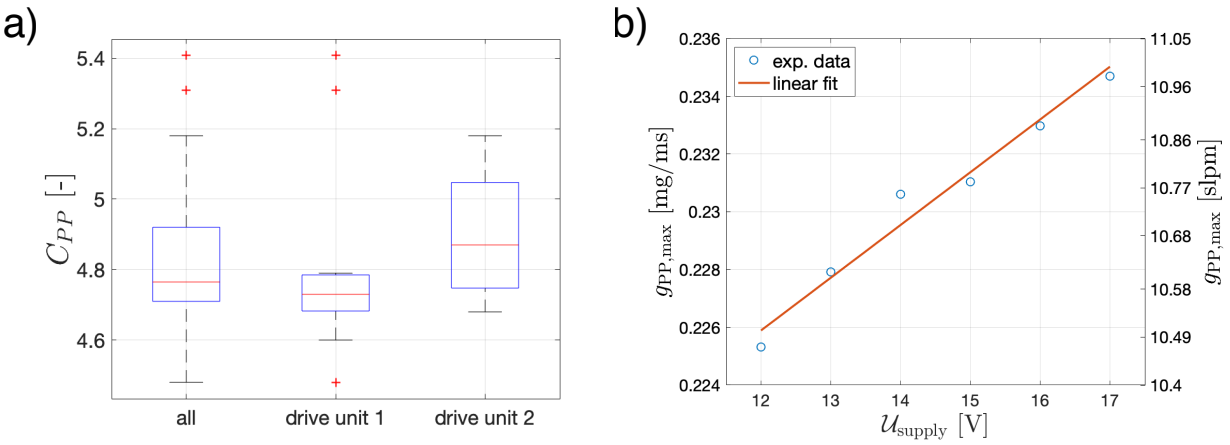

Figure 3.5.: Experimental data to determine the pump specific compression ratio C_{PP} in a). A total of 18 measurements were taken from two different drive units at three different supply voltages and three different control signals. The boxplots in a) depict the distributions for all samples and for the two drive units individually. The right graph b) shows the experimentally derived linear relation between supply voltage $\mathcal{U}_{supply}$ and free flow $g_{PP,max}$ at $y_{PP} = 1.0$.

3.1.4. Valves

Valves are essential in a drive unit of a pneumatic cardiac assist device, as the connection between reservoirs and implant has to be cleared and closed at particular time instances. After the detection of a R-wave in the ECG-signal, inlet valves of all three supply lines are opened to inflate the respective EU. Similarly, after detection of a T-wave, the EUs are deflated across the opened outlet valves. In the following, the flow and temperature equations are described. Furthermore, hysteretic effects are modeled. Valve control, however, is described in section 3.1.7.

Valve flow The proportional solenoid valve converts electrical energy first into magnetic energy, which exerts force on the movable part of the valve, the so-called plunger, performing work while it is moved. Once the plunger has stabilized, all energy is dissipated into heat. The adjective *proportional* refers to a continuous lift of the plunger, depending on the solenoid's current. Between the fully closed and fully opened condition, any position of the plunger is tunable, leading to variable flow through the valve.

The valve, installed in a valve block, represents a flow resistance, which, in case of a proportional valve, is variable. In order to model flow generation as a result of the pressure difference, the Bernoulli equation (2.38) is utilized. For low pressure ranges, as is the case in the system at hand, relatively slow velocities develop, with Mach-numbers below 0.3 (cf. section 2.2.1.1) and the density of the flow through the restriction can be modeled as the mean density between two potential points, $\hat{\rho} = 0.5(\rho_1 + \rho_2)$ [125]. Also, the mean air velocity in the reservoir is assumed to be zero and only the velocity at the valve remains. Inserting (2.24) into (2.38) yields

$$\frac{\Delta p}{\hat{\rho}} + \frac{1}{2}\frac{\dot{m}^2}{\hat{\rho}^2 A^2} = 0, \tag{3.20}$$

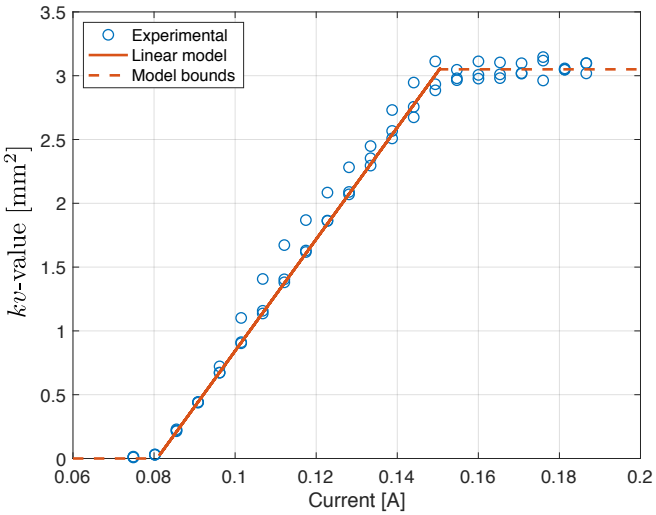

Figure 3.6.: Bounded linear model of the kv-value as function of the coil current. The dashed lines indicate the kv bounds resulting from the electro-mechanical valve design.

with A being the geometric flow area of the valve orifice. After rearranging, the equation reads

$$g = \dot{m} = \sqrt{2}A\sqrt{(p_1 - p_2)\frac{1}{2}(\rho_1 + \rho_2)}. \tag{3.21}$$

Now, the flow at the valve's orifice is subject to jet constriction and turbulences, which reduce the geometric flow area to an effective flow area $\bar{A} = C_{\text{jet}} \cdot C_{\text{turb}} \cdot A$. Further explanations of the coefficients $C_{\text{jet}}, C_{\text{turb}}$ are omitted as an integral approach is chosen. Fluid mechanics textbooks, e.g [106], [35], [125], can be consulted for more detailed information. The described effects are simultaneously modeled using the so-called kv-value, which can be understood as the corrected orifice area. Throughout this thesis it is defined as

$$kv = \sqrt{2}\ \bar{A}. \tag{3.22}$$

Figure 3.6 plots the experimental kv data over the applied current, together with the used linear model and its bounds. The exact curve and bounds result, among others, from spring and solenoid coil design as well as from the used materials. The experimental procedure to derive the data is described in appendix A.I.3. Using equation (3.22) and explicitly formulating the flow between HPR and inlet valves as well as between outlet valves and LPR and using the density formulation (2.4), the valve flow equations per supply tube $k \in \{1, 2, 3\}$ become

$$g^k_{\text{V,in}} = \text{sgn}(p_{\text{HPR}} - p^k_{\text{V}})kv^k_{\text{V,in}}\sqrt{\left|p_{\text{HPR}} - p^k_{\text{V}}\right|\frac{1}{2R}\left(\frac{p_{\text{HPR}}}{T_{\text{HPR}}} + \frac{p^k_{\text{V}}}{T^k_{\text{V}}}\right)}, \tag{3.23}$$

$$g^k_{\text{V,out}} = \text{sgn}(p^k_{\text{V}} - p_{\text{LPR}})kv^k_{\text{V,out}}\sqrt{\left|p^k_{\text{V}} - p_{\text{LPR}}\right|\frac{1}{2R}\left(\frac{p^k_{\text{V}}}{T^k_{\text{V}}} + \frac{p_{\text{LPR}}}{T_{\text{LPR}}}\right)}. \tag{3.24}$$

Here, $(\bullet)_{\text{V}}$ refers to the *valve* node, which is downstream of the inlet valves and upstream of the outlet valves. Since the flow along a streamline is unidirectional by default, the unsigned value

of the pressure potential is inserted and its sign is added outside of the square root to allow for bidirectional flow. The temperature equations for the valves use the polytropic change of state, introduced in (2.16). They read

$$T_{\mathrm{V}}^{k} = T_{\mathrm{HPR}} \left(\frac{p_{\mathrm{V}}^{k}}{p_{\mathrm{HPR}}} \right)^{\frac{n_{\mathrm{V}}-1}{n_{\mathrm{V}}}} \qquad \text{for } g_{\mathrm{EU}}^{k} \geq 0 \text{ (inflation)}, \tag{3.25}$$

$$T_{\mathrm{V}}^{k} = T_{\mathrm{EU}}^{k} \left(\frac{p_{\mathrm{V}}^{k}}{p_{\mathrm{EU}}^{k}} \right)^{\frac{n_{\mathrm{V}}-1}{n_{\mathrm{V}}}} \qquad \text{for } g_{\mathrm{EU}}^{k} < 0 \text{ (deflation)}. \tag{3.26}$$

As explained in the previous section, the valve's opening and hence its kv-value depends on the applied current. The current is the result of the applied control voltage and the ohmic resistance of the coil, which itself is dependent on the coil temperature, which again is heated up by the current going through it. This reciprocal dependency is simplified for the dynamic model by directly controlling the opening, namely the kv-value. However, the interdependence of current, coil temperature and resistance is used to predict the mean temperatures of the reservoirs (cf. section 3.2).

The kv-value can be modeled to be linearly dependent on the applied current, contingent upon the actual valve type to be modeled. The ones mimicked here show no significant deviations from a linear fit within the variance of the measurements. Owing to this observation, the kv-value for each valve k is modeled as a linear function between zero and a maximum value $kv_{\mathrm{V,max}}$

$$kv_{\mathrm{V,in/out}}^{k} = kv_{\mathrm{V,max}} \cdot y_{\mathrm{V,in/out}}^{k}, \tag{3.27}$$

with $y_{\mathrm{V,in/out}}^{k} \in [0, 1]$ as the valve opening control signal.

Hysteresis Hysteretic behavior occurs when the current state of a variable depends on its preceding values. Several hysteresis models exist, e.g. the Jiles-Atherton [55], Bouc-Wen [52] models or those of Vaiana et al.[113]. In this thesis, a solely condition-based approach is chosen, where the degree of hysteresis is proportional to the maximal degree of previous magnetization, thus to the valve's individual maximal control value during that energizing period z. It is represented as a percentage value $\mathrm{H_V}$, which is defined as

$$\mathrm{H_V} = \begin{cases} 0 & \text{for } \mathrm{d}y_{\mathrm{V,in/out}}^{k} \geq 0, \\ \bar{\mathrm{H}}_{\mathrm{V}} & \text{for } \mathrm{d}y_{\mathrm{V,in/out}}^{k} < 0. \end{cases} \tag{3.28}$$

Whenever the control value $y_{\mathrm{V,in/out}}^{k}$ is increased, the hysteresis equals zero $\mathrm{H_V} = 0$. When the opposite is the case, meaning a decrease in the respective control value, the hysteresis adopts the value input to the model, $\mathrm{H_V} = \bar{\mathrm{H}}_{\mathrm{V}}$. The hysteretic kv-values are then computed by the following equations which replace (3.27)

$$kv_{\mathrm{V,in/out}}^{k} = kv_{\mathrm{max}} \left(y_{\mathrm{V,in/out}}^{k} + \mathrm{H_V} y_{\mathrm{V,in/out,max},z}^{k} \right), \tag{3.29}$$

for the supply lines $k \in \{1, 2, 3\}$. $y_{\mathrm{V,in/out,max},z}^{k}$ is the maximum magnetization during the current energizing cycle z of valve k. The modification of the control value due to hysteresis cannot

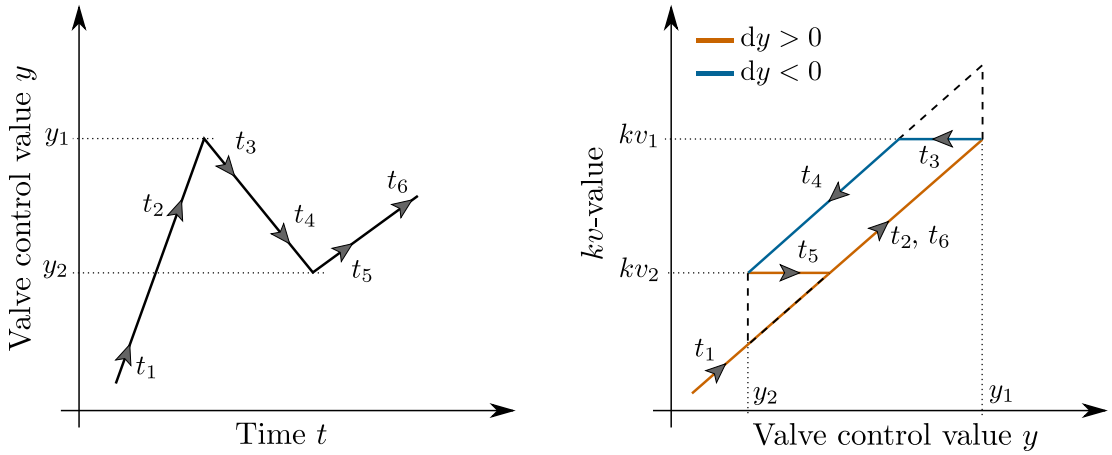

Figure 3.7.: Schematic of the valve hysteresis model: The time dependent control signal y in the left graph translates to the hysteretic valve opening in the right graph, represented by its kv-value. Here, the change in the input y is colored in orange for a control value increase and in blue for a decrease. The arrows in both graphs indicate the same time instances. The dashed lines represent the restrictions to prevent greater (or lower) kv-values than in the previous time instant for a control value decrease (or increase).

result in a greater (or lower) value than in the previous time instant. It is restricted to these historic limits during a control value decrease (or increase), hence

$$kv^k_{\mathrm{V,in/out}}(t) = kv^k_{\mathrm{V,in/out}}(t-\mathrm{d}t) \qquad \text{for} \quad \begin{cases} \mathrm{d}y^k_{\mathrm{V,in/out}} < 0 \wedge \mathrm{d}kv^k_{\mathrm{V,in/out}} > 0, \\ \mathrm{d}y^k_{\mathrm{V,in/out}} > 0 \wedge \mathrm{d}kv^k_{\mathrm{V,in/out}} < 0. \end{cases} \tag{3.30}$$

The model is visualized in figure 3.7, showing the translation from a generic time dependent control value y in the left graph to a corresponding valve opening in the right graph. Here, the blue and orange curves represent the possible values of the hysteresis $\mathrm{H_V}$ as described in (3.28) and how they translate y into the opening kv through (3.29). Note that without the operations in (3.30), the hysteresis curve would be given by the dashed black lines.

To derive a valve type specific hysteresis value, two different valves where taken and kv-values were determined while the valve was stepwise opened and closed; in a first cycle up to the maximum possible opening and in a second run to an arbitrary value below the maximum. For both valves and runs, the detected hysteresis was related to the previous maximum current and averaged. Note that the offset of 0.08 A (cf. figure 3.6) was subtracted from that maximum current in order to adapt the hysteresis value to the linear model (3.27). The resulting model parameter for hysteresis is $\bar{\mathrm{H}}_\mathrm{V} = 4.3\ \%$.

3.1.5. Tubing and connectors

The driveline of the BiVAD connects the cardiac implant to the drive unit and allows for inflation and deflation of the EUs. The main technical characteristics are tube length and tube inner

diameter and the specifications thereof are dictated by medical framework conditions.
Fluid, passing through a tube or duct, experiences internal (viscous) and external (wall) friction. Kinetic energy is transformed to heat. The result is a decrease in pressure along the tube, which leads to a further expansion of the medium. Consequently, the fluid speed increases and thus, the pressure drops disproportionately. In adiabatic models, the heat contributes again to the energy of the fluid, but at a lower temperature, hence the entropy increases. In isothermal models, the change of density depends only on changes in pressure. For short lines and quick flows, the adiabatic assumption is typically used, whereas for longer uninsulated lines the isothermal approach is known to better approximate the physics. It is common practice to test for both values [56], [57], [30], [24]. Inserting equation (2.24) into (2.39) yields the general Darcy-Weisbach equation for duct flow

$$\Delta p_{12} = \lambda \frac{L_\mathrm{T}}{D_\mathrm{T}} \frac{1}{2\rho_\mathrm{T}} \frac{\dot{m}^2}{A_\mathrm{T}^2}, \tag{3.31}$$

where λ is the Darcy friction factor. It depends, among others, on the flow pattern (cf. section 2.2.1.5). Approximations of λ by Prandtl, Blasius and Haaland (cf. section 2.2.1.4) are widely referenced in literature when pure tube flows are modeled, but it has been shown to be insufficient within the present system. Possible reasons can be the wider definition range of the above equations, yielding larger local errors and a non-circular geometry of additional components within the flow path. Also, typical Reynolds numbers, where the flow regime switches from laminar to turbulent and vice versa, have shown to differ significantly. Therefore, a data-based model was developed. To enable separate changes in internal and external design, the model contains a tube term and a so-called connector term, representing primarily the connection interface between tube and drive unit. Equation (3.31) is extended by the loss coefficient ζ [116], accounting for these additional restrictions:

$$\Delta p = \left(\lambda \frac{L_\mathrm{T}}{D_\mathrm{T}} + \zeta \right) \frac{1}{2\rho_\mathrm{T}} \frac{g^2}{A_\mathrm{T}^2}. \tag{3.32}$$

As the friction factors λ and ζ are functions of the Reynolds number, the following model was chosen to be fit to experimental data

$$\gamma(Re) = \frac{a_\gamma}{Re} + b_\gamma \qquad \text{with } \gamma \in \{\lambda, \zeta\}, \tag{3.33}$$

with distinct parameters $a_\lambda,\ a_\zeta,\ b_\lambda$ and b_ζ for each flow regime. Replacing Re in (3.33) by (2.40) and inserting the friction factor models into (3.32) yields

$$\Delta p = \left[\left(a_\lambda \frac{\eta A_\mathrm{T}}{g D_\mathrm{T}} + b_\lambda \right) \frac{L_\mathrm{T}}{D_\mathrm{T}} + a_\zeta \frac{\eta A}{g D_\mathrm{T}} + b_\zeta \right] \frac{1}{2\rho} \frac{g^2}{A_\mathrm{T}^2}, \tag{3.34}$$

with a_λ, b_λ and a_ζ, b_ζ being the parameters of λ and ζ in (3.33). When valves are abruptly opened or closed, the inertance of the gas may play a role as it opposes the flow. Starting with the balance of linear momentum (2.33), $\mathrm{d}(mv)/\mathrm{d}t = \sum \mathrm{F}$, with the force acting on the fluid in the tube being $\Delta p A_\mathrm{T}$ and replacing $m = \rho L A$ as well as with (2.24), the additional pressure drop due to inertance is given by [56]

$$\Delta p = \frac{L_\mathrm{T}}{A_\mathrm{T}} \ddot{m} = \frac{L_\mathrm{T}}{A_\mathrm{T}} \dot{g}. \tag{3.35}$$

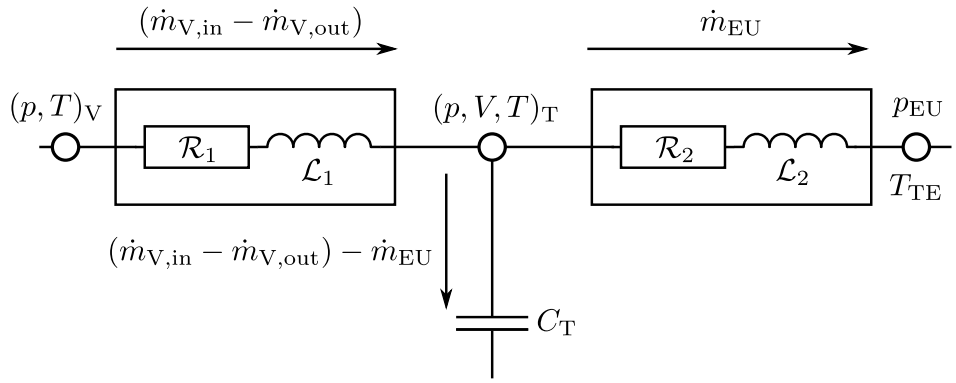

Figure 3.8.: Schematic of the tube model, consisting of two resistor-inductor elements ($\mathcal{RL}$) and a capacitance, accounting for tube compliance and air compressibility.

After sorting and expanding (3.34) by multiplication with $(g/A_{\mathrm{T}})^2$, inserting a mean density and adding the inertance term (3.35), the problem specific equations read

$$\begin{aligned} p_{\mathrm{V}}^k - p_{\mathrm{T}}^k = & \left[\mathrm{f}_{\mathrm{T},1}\left(g_{\mathrm{V,in}}^k - g_{\mathrm{V,out}}^k\right) + \mathrm{f}_{\mathrm{T},2}\left(g_{\mathrm{V,in}}^k - g_{\mathrm{V,out}}^k\right)^2\right]\mathrm{f}_{\mathrm{T},3} + \\ & + \frac{L_{\mathrm{T}}}{2A_{\mathrm{T}}}\frac{\mathrm{d}}{\mathrm{d}t}\left(g_{\mathrm{V,in}}^k - g_{\mathrm{V,out}}^k\right), \end{aligned} \tag{3.36}$$

$$p_{\mathrm{T}}^k - p_{\mathrm{EU}}^k = \left[\mathrm{f}_{\mathrm{T},4} g_{\mathrm{EU}}^k + \mathrm{f}_{\mathrm{T},5} g_{\mathrm{EU}}^{k2}\right]\mathrm{f}_{\mathrm{T},6} + \frac{L_{\mathrm{T}}}{2A_{\mathrm{T}}}\frac{\mathrm{d}}{\mathrm{d}t}\left(g_{\mathrm{EU}}^k\right). \tag{3.37}$$

Friction and density related terms are substituted for readability and listed below:

$$\mathrm{f}_{\mathrm{T},1} = \left(a_\lambda \frac{L_{\mathrm{T}}}{2D_{\mathrm{T}}} + a_\zeta\right)\frac{\eta}{D_{\mathrm{T}}A_{\mathrm{T}}}, \tag{3.38}$$

$$\mathrm{f}_{\mathrm{T},2} = \left(b_\lambda \frac{L_{\mathrm{T}}}{2D_{\mathrm{T}}} + b_\zeta\right)\frac{1}{A_{\mathrm{T}}^2}, \tag{3.39}$$

$$\mathrm{f}_{\mathrm{T},3} = \frac{R}{\frac{p_{\mathrm{V}}^k}{T_{\mathrm{V}}^k} + \frac{p_{\mathrm{T}}^k}{T_{\mathrm{T}}^k}}, \tag{3.40}$$

$$\mathrm{f}_{\mathrm{T},4} = a_\lambda \frac{L_{\mathrm{T}}}{2D_{\mathrm{T}}}\frac{\eta}{D_{\mathrm{T}}A_{\mathrm{T}}}, \tag{3.41}$$

$$\mathrm{f}_{\mathrm{T},5} = b_\lambda \frac{L_{\mathrm{T}}}{2D_{\mathrm{T}}}\frac{1}{A_{\mathrm{T}}^2}, \tag{3.42}$$

$$\mathrm{f}_{\mathrm{T},6} = \frac{R}{\frac{p_{\mathrm{T}}^k}{T_{\mathrm{T}}^k} + \frac{p_{\mathrm{EU}}^k}{T_{\mathrm{TE}}^k}}. \tag{3.43}$$

Figure 3.8 depicts the schematic of the tube model, with two resitor-inductor elements and a capacitance, accounting for tube compliance and air compressibility. Based on the conservation of mass $\frac{\mathrm{d}m}{\mathrm{d}t} = \frac{\mathrm{d}(\rho V)}{\mathrm{d}t} = \sum g$, an equation to describe the tube pressure p_{T} can be derived. Two terms arise after applying the chain rule, whereof the first is transformed into an expression of tube capacitance as it was done for the reservoirs, $\rho\frac{\mathrm{d}V}{\mathrm{d}t} = \frac{\mathrm{d}p}{\mathrm{d}t}\frac{pC}{RT}$. Using the polytropic equation

in differential form (2.17) allows to transform the second term, $V\frac{\mathrm{d}\rho}{\mathrm{d}t} = \frac{\mathrm{d}p}{\mathrm{d}t}\frac{V}{nRT}$, into the final tube pressure relation [56]

$$\frac{\mathrm{d}p_{\mathrm{T}}^k}{\mathrm{d}t} = \frac{\left(g_{\mathrm{EU}}^k - g_{\mathrm{V,in}}^k + g_{\mathrm{V,out}}^k\right) RT_{\mathrm{T}}^k}{p_{\mathrm{T}}^k C_{\mathrm{T}} + \frac{V_{\mathrm{T}}}{n_{\mathrm{T}}}}, \tag{3.44}$$

with C_{T} being the compliance, V_{T} the tube volume and n_{T} the polytropic exponent. Each resistive element in figure 3.8 accounts for half of the tube, but only the first element features the additional resistance expressed by ζ, since the connector is located at the interface between driveline and drive unit. The temperature T_{T} is simply modeled as the mean temperature between both extreme ends of the tube

$$T_{\mathrm{T}}^k = \frac{1}{2}\left(T_{\mathrm{V}}^k + T_{\mathrm{TE}}^k\right), \tag{3.45}$$

with the temperature at the end of the tube T_{TE}

$$\begin{aligned} T_{\mathrm{TE}}^k &= T_{\mathrm{V}}^k \left(\frac{p_{\mathrm{EU}}^k}{p_{\mathrm{V}}^k}\right)^{\frac{n_{\mathrm{T}}-1}{n_{\mathrm{T}}}} && \text{for } g_{\mathrm{EU}}^k \geq 0 \text{ (inflation)}, \\ T_{\mathrm{TE}}^k &= T_{\mathrm{EU}}^k && \text{for } g_{\mathrm{EU}}^k < 0 \text{ (deflation)}. \end{aligned} \tag{3.46}$$

Parameter estimation The previously introduced equations to model tube and connector contain parameters, which are problem specific and need to be determined, specifically the friction factor parameters a_λ, b_λ and a_ζ, b_ζ as well as the tube compliance C_{T}. Therefore, a tube of length $L_{\mathrm{T}} = 1.3$ m and inner diameter $D_{\mathrm{T}} = 0.003$ m was connected in series to a pneumatic low pass filter and a pump. The pump was used to set three different flows and the pressure drop over the tube was measured. The same procedure was utilized to analyze the connector. Refer to figure 4.1 d) for a detailed schematic of the setup. The Darcy-Weisbach equation, (3.31), rearranged such that λ or ζ could be determined as the function value and the Reynolds number, (2.40), was used to compute the function input. When plotted in figure 3.9 a) and c) the flow pattern transition between laminar and turbulent flow is clearly visible. Since many data sets were used, the transition occurs within a range. Therefore, a transition between both patterns was introduced to adapt to the width of such transition and to avoid unsteady behavior. The model function (3.33) was fitted to the so-obtained data for both flow patterns and is depicted, together with the transition functions, in figure 3.9. The identified critical Reynolds numbers and their transition ranges are listed in table 3.3. The transition range is defined by the critical Reynolds numbers $Re_{\mathrm{crit},\lambda} = 2900$, $Re_{\mathrm{crit},\zeta} = 700$ and the laminar-turbulent transition intervals $\Delta Re_{\mathrm{trans},\lambda} = 500$, $\Delta Re_{\mathrm{trans},\zeta} = 200$, respectively, by

$$\text{Transition range} := \left(Re_{\mathrm{crit}} - \frac{1}{2}\Delta Re_{\mathrm{trans}}\right) \leq Re \leq \left(Re_{\mathrm{crit}} + \frac{1}{2}\Delta Re_{\mathrm{trans}}\right). \tag{3.47}$$

The compliance was derived as described before for the reservoirs in section 3.1.2. Refer to appendix A.I.1 for a more detailed description of the compliance identification. Figure 3.10 shows the volume data for different pressures of the tube and the fitted linear function.

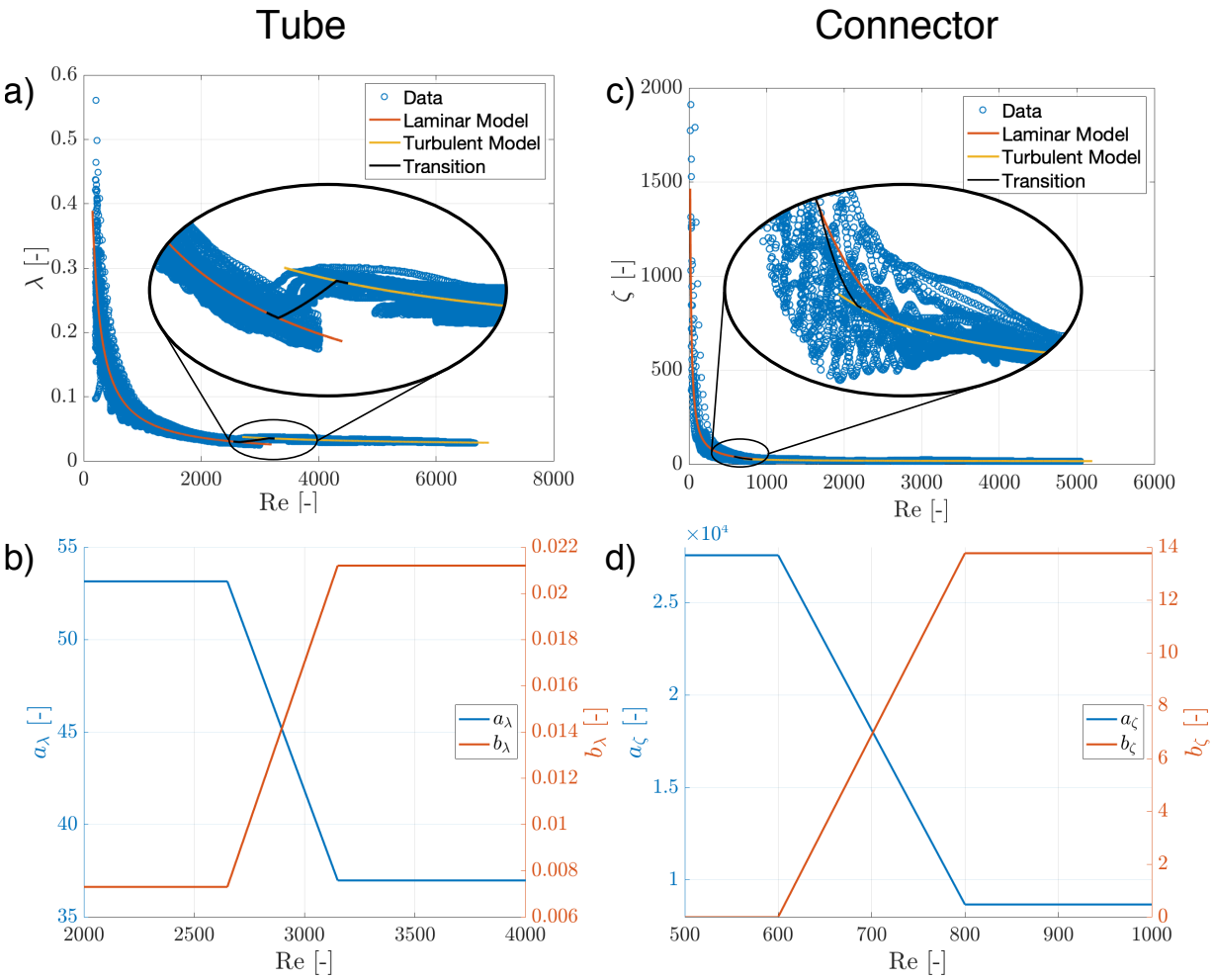

Figure 3.9.: Friction parameter for the tube a) and the connector c) and their respective transition functions in b), d) between both flow patterns.

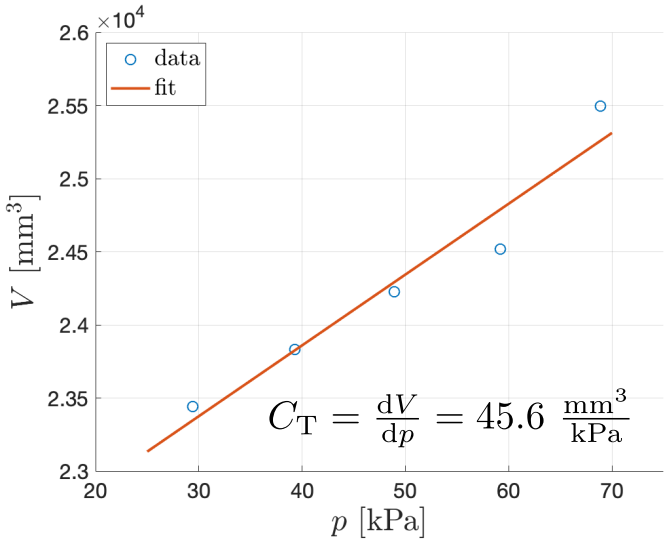

Figure 3.10.: Compliance data and respective linear regression with five points.

	Parameter	Laminar	Turbulent
Tube	Slope a_λ	53.1495	36.9768
	Offset b_λ	0.0073	0.0212
	Re	< 2650.0	> 3150.0
	C_T $[\frac{\text{mm}^3}{\text{kPa}}]$	45.6	
Connector	Slope a_ζ	27560.0	8675.5
	Offset b_ζ	0.0	13.77
	Re	< 600.0	> 800.0

Table 3.3.: Parameters for the tube and connector model. All parameters, except for the compliance, are dimensionless.

3.1.6. The implant's expandable units (EUs)

The cardiac implant with inflatable EUs represents the bio-technical interface. Here, work is done on the heart and the cardiovascular system is supported. The EUs are mixed-dimensional models, combining the EU's 0D nodal point with a continuum model. Connecting a 3D implant model allows for supporting 3D heart models, which is addressed in section 3.3. The implant with its EUs can technically be treated similarly to a pneumatic cylinder of varying volume. Consequently, besides equations for pressure and temperature evolution, relations to determine the EUs' volumes are needed, which can be obtained from the geometry of the 3D implant. As in section 3.1.2, the ideal gas law (2.3) is differentiated with respect to time, leading to equation (3.2). The resulting equation is transferred to a system of ODEs using the substitutions in (3.1). Replacing the air mass by $pV/(RT)$, the system of ODEs reads

$$\frac{\mathrm{d}p}{\mathrm{d}t} = \frac{1}{V}\left(gRT - pq\right) + \frac{p}{T}\tau, \tag{3.48}$$

$$\frac{\mathrm{d}V(\boldsymbol{u})}{\mathrm{d}t} = q, \tag{3.49}$$

$$\frac{\mathrm{d}T}{\mathrm{d}t} = \tau. \tag{3.50}$$

Here, the volume is a function of the displacement field $\boldsymbol{u}$ of the EU's continuum model. The temperature is modeled similar to the reservoir temperature. Therefore, the energy balance equation (2.14) is used. The kinetic energy contributions of the gas and the control volume itself in (2.14) and (2.15), respectively, are approximately four orders of magnitude smaller than thermal and potential contributions h, $\frac{\mathrm{d}E_{\text{pot}}}{\mathrm{d}t}$ and are neglected (cf. appendix A.II.1). Also, the potential energy of the gas in (2.14) is neglected. Now, the equation reads

$$\frac{\mathrm{d}U}{\mathrm{d}t} + \frac{\mathrm{d}E_{\text{pot}}}{\mathrm{d}t} = \dot{Q} + \dot{W} + gh. \tag{3.51}$$

The heat flow rate $\dot{Q}$ is replaced by the relations introduced in section 2.1.4 and the rate of change of pressure-volume work by $\dot{W} = -pq$, with $q = \frac{\mathrm{d}V}{\mathrm{d}t}$ and the negative sign accounting

for energy leaving the system. Furthermore, the internal energy U and the specific enthalpy h are substituted by the equations (2.7) and (2.8), respectively, yielding

$$c_{\mathrm{v}} \frac{\mathrm{d}(mT)}{\mathrm{d}t} + \frac{\mathrm{d}E_{\mathrm{pot}}}{\mathrm{d}t} = k_{\mathrm{th}} A(T_\infty - T) - pq + gc_p T. \tag{3.52}$$

Using equations (2.5) and (2.6), the specific heat capacities of air can be expressed by

$$c_{\mathrm{v}} = \frac{1}{\kappa - 1} R \qquad \text{and} \qquad c_p = \frac{\kappa}{\kappa - 1} R. \tag{3.53}$$

The rate of change of potential energy stems from the energy stored in the deformed elastic material and can be expressed as

$$\frac{\mathrm{d}E_{\mathrm{pot}}}{\mathrm{d}t} = \frac{\mathrm{d}W_{\mathrm{int}}(\boldsymbol{u})}{\mathrm{d}t}. \tag{3.54}$$

The enthalpy flow in (3.52) can be split into in- and outflow, where the respective temperatures differ. Whereas during outflow it is the EU temperature, during inflow it is the temperature of the air at the end of the tube (3.46). The final system of equations per EU k, including the derived energy equation, then reads

$$\frac{\mathrm{d}p^k_{\mathrm{EU}}}{\mathrm{d}t} = \frac{1}{V^k_{\mathrm{EU}}} \left(g^k_{\mathrm{EU}} R T^k_{\mathrm{EU}} - p^k_{\mathrm{EU}} q^k_{\mathrm{EU}} \right) + \frac{p^k_{\mathrm{EU}}}{T^k_{\mathrm{EU}}} \tau^k_{\mathrm{EU}}, \tag{3.55}$$

$$\frac{\mathrm{d}V^k_{\mathrm{EU}}(\boldsymbol{u})}{\mathrm{d}t} = q^k_{\mathrm{EU}}, \tag{3.56}$$

$$\frac{\mathrm{d}T^k_{\mathrm{EU}}}{\mathrm{d}t} = \tau^k_{\mathrm{EU}}, \tag{3.57}$$

$$\begin{aligned} \frac{\mathrm{d}W^k_{\mathrm{EU,int}}(\boldsymbol{u})}{\mathrm{d}t} = {} & k_{\mathrm{th,EU}} A_{\mathrm{EU}} (T_{\mathrm{Body}} - T^k_{\mathrm{EU}}) - p^k_{\mathrm{EU}} q^k_{\mathrm{EU}} - \frac{p^k_{\mathrm{EU}} V^k_{\mathrm{EU}}}{T^k_{\mathrm{EU}}(\kappa - 1)} \tau^k_{\mathrm{EU}} + \\ & + g^k_{\mathrm{EU,in}} \left(\frac{\kappa}{\kappa - 1} R T^k_{\mathrm{TE}} - \frac{R}{\kappa - 1} T^k_{\mathrm{EU}} \right) + \\ & + g^k_{\mathrm{EU,out}} R T^k_{\mathrm{EU}}. \end{aligned} \tag{3.58}$$

For the EU flows $g^k_{\mathrm{EU,in}}$ and $g^k_{\mathrm{EU,out}}$ the following holds:

$$\begin{aligned} g^k_{\mathrm{EU,in}} &= g^k_{\mathrm{EU}} && \text{for } g^k_{\mathrm{EU}} \geq 0 \text{ (inflation)}, \\ g^k_{\mathrm{EU,in}} &= 0 && \text{for } g^k_{\mathrm{EU}} < 0 \text{ (deflation)}, \\ g^k_{\mathrm{EU,out}} &= 0 && \text{for } g^k_{\mathrm{EU}} \geq 0 \text{ (inflation) and} \\ g^k_{\mathrm{EU,out}} &= g^k_{\mathrm{EU}} && \text{for } g^k_{\mathrm{EU}} < 0 \text{ (deflation).} \end{aligned} \tag{3.59}$$

The thermal transmittance k_{th} was derived using a method that was extended to pneumatic cylinders by Carneiro and Almeida [14]. In brief, the thermal time constant of the cylinder, here the EU, is derived by measuring the pressure decrease due to heat exchange. See appendix A.I.2 for a more detailed description of the method. Eight different EUs were tested and the obtained values averaged, yielding $k_{\mathrm{th}} = 4.47 \, \frac{\mathrm{W}}{\mathrm{m^2 K}}$.

3.1.7. Control

In accordance with the real system, the BiVAD model is controlled by setting the pump speed and the valve openings.

3.1.7.1. Pump control

Pump speed and thereby the amount of air per time delivered at the prevailing thermodynamic conditions is set by the control value y_{PP}. It is held constant during the heart cycle. The reason for this lies in the user experience: Fast and frequent changing motor speeds alter vibration and sound of the drive unit in the same manner and can lead to strong discomfort for the patient. Consequently, the motor control signal remains at a fixed level $y_{\text{PP}} = \text{constant}$ during one heart cycle within this model. It may be subject to change between two heart beats.

3.1.7.2. Valve control

The valves can be controlled dynamically. Opening and closing – fully or partly – do not result in any audible clicking sounds. Therefore the control values for inlet valves $y^k_{\text{EU,in}}$ and outlet valves $y^k_{\text{EU,out}}$, with $k \in \{1, 2, 3\}$, are allowed to vary during systole and diastole, respectively. This work presents an open-loop valve control strategy.

In open-loop control, the actuation variables, here the valve control signals, are not dependent upon the process variable, which are the EUs' pressures. Here, prescribed valve control signals set a time dependent curve $y^k_{\text{V,in/out}}(t)$ individually for all inlet and outlet valves. A parameterized signal is utilized and its values can be set in each heart cycle. The curve can be seen in figure 3.11. In general, the opening time point of the inlet valves triggers simultaneously the closing of the outlet valves and vice versa. The intention is to avoid any direct flow from the HPR to the LPR without filling the EUs due to open inlet and outlet valves at the same time. Such flow does not contribute to the heart support but decreases the energy stored in the reservoirs. It is called waste flow. The openings $\{y^k_{\text{inlet,1}}, y^k_{\text{inlet,2}}, y^k_{\text{outlet}}\}$ can be set individually for inlet and outlet valve of each EU. The primary control time points $\{t_{\text{yin,1}}, t_{\text{yin,2}}, t_{\text{yout}}\}$ are common for all valves, as well as the transition time span Δt_{c}, which represents the time needed to change between two control values. It is set to

$$\Delta t_{\text{c}} = 0.02 \text{ s} \approx 5\, \tau_{\text{V}}, \tag{3.60}$$

where $\tau_{\text{V}} \approx 4.35$ ms is the valve's time constant for opening (and closing) processes as specified in the manufacturer's data sheet[1] [28].

[1] It is indirectly given by the times to reach 90 % (10 %) of the input signal during opening (closing), which is specified with 10 ms. 90 % of change, expressed in a time constant value, correspond to approximately 2.3 $\times \tau_{\text{V}}$, such that τ_{V} adopts 4.35 ms.

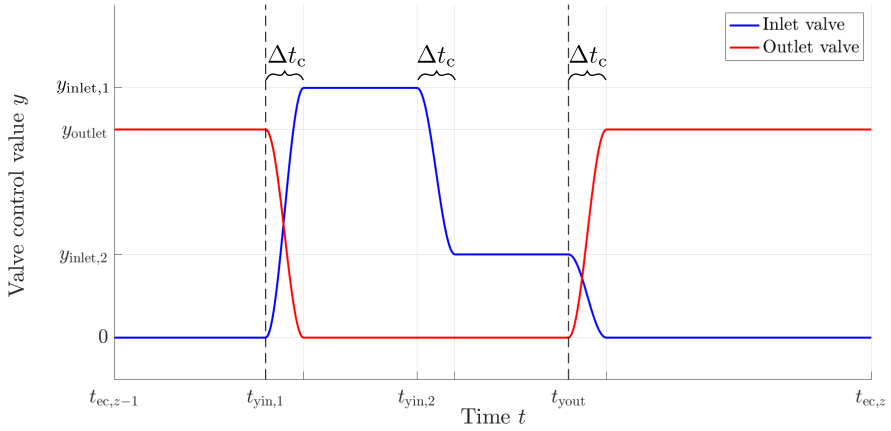

Figure 3.11.: Parameterized valve control signals for open-loop control. The left vertical dashed line at $t_{\text{yin},1}$ represents the end-diastolic time point of the heart beat. The end-systolic time point is marked by the right vertical dashed line at t_{yout}. For the inflation process, two inlet valve openings, $y_{\text{inlet},1}$ and $y_{\text{inlet},2}$, can be set to values in the range [0,1]. The deflation process is only governed by one valve opening value, namely y_{outlet}, also $\in$ [0,1]. Δt_c is the transient time span and hence the time needed to reach a prescribed value level. Note that for visibility, the spacing on the x-axis is not to scale.

The exact definition of the inlet and outlet valve opening control signals is given by

$$
\begin{aligned}
y^k_{\text{V,in}} &= 0 \\
y^k_{\text{V,out}} &= y_{\text{outlet}} && \text{for } 0 < t \leq t_{\text{yin},1} \\
y^k_{\text{V,in}} &= \tfrac{1}{2} y_{\text{inlet},1} \left(1 - \cos(\pi (t - t_{\text{yin},1}) / \Delta t_c)\right) \\
y^k_{\text{V,out}} &= \tfrac{1}{2} y_{\text{outlet}} \left(1 - \cos(\pi (t - t_{\text{yin},1} - \Delta t_c) / \Delta t_c)\right) && \text{for } t_{\text{yin},1} < t \leq t_{\text{yin},1} + \Delta t_c, \\
y^k_{\text{V,in}} &= y_{\text{inlet},1} \\
y^k_{\text{V,out}} &= 0 && \text{for } 0 < t_{\text{yin},1} + \Delta t_c \leq t_{\text{yin},2}, \\
y^k_{\text{V,in}} &= \tfrac{1}{2} (y_{\text{inlet},1} - y_{\text{inlet},2}) \left(1 - \cos(\pi (t - t_{\text{yin},2} - \Delta t_c) / \Delta t_c) + y_{\text{inlet},2}\right) \\
y^k_{\text{V,out}} &= 0 && \text{for } t_{\text{yin},2} < t \leq t_{\text{yin},2} + \Delta t_c, \\
y^k_{\text{V,in}} &= y_{\text{inlet},2} \\
y^k_{\text{V,out}} &= 0 && \text{for } 0 < t_{\text{yin},2} + \Delta t_c \leq t_{\text{yout}}, \\
y^k_{\text{V,in}} &= \tfrac{1}{2} y_{\text{inlet},2} \left(1 - \cos(\pi (t - t_{\text{yin},1} - \Delta t_c) / \Delta t_c)\right) \\
y^k_{\text{V,out}} &= \tfrac{1}{2} y_{\text{outlet}} \left(1 - \cos(\pi (t - t_{\text{yout}}) / \Delta t_c)\right) && \text{for } t_{\text{yout}} < t \leq t_{\text{yout}} + \Delta t_c, \\
y^k_{\text{V,in}} &= 0 \\
y^k_{\text{V,out}} &= y_{\text{outlet}} && \text{for } 0 < t_{\text{yout}} + \Delta t_c \leq t_{\text{ec}}.
\end{aligned}
\tag{3.61}
$$

Parameter	Explanation	Default
$t_{\text{yin,1}}$	Start point of first inflation phase with inlet valve opening $y_{\text{inlet,1}}$ and end of previous deflation with outlet valve opening y_{outlet} End of diastole and beginning of systole	0.2 s
$t_{\text{yin,2}}$	Start point of second inflation phase with inlet valve opening $y_{\text{inlet,2}}$.	0.3 s
t_{yout}	Start point of deflation phase with outlet valve opening y_{outlet} and end of second inflation phase with $y_{\text{inlet,2}}$ End of systole and beginning of diastole	0.52 s
Δt_{c}	Transition time span to reach applied valve opening	0.02 s
t_{ec}	End of cardiac cycle (approx. 80 % of time between two R-waves)	1 s
$y_{\text{inlet,1}}$	Inlet valve relative opening during first inflation phase	0.7
$y_{\text{inlet,2}}$	Inlet valve relative opening during second inflation phase	0.3
y_{outlet}	Outlet valve relative opening during deflation	0.5

Table 3.4.: Valve control parameters with explanation and default values. Note that the default values are exemplary, as they are patient-specific.

During inflation, the first shorter phase with a major opening is intended to allow for fast pressure build-up in the EUs, while the longer second phase, with typically minor opening, aims to hold the reached pressure by supplying an adequate inflow during heart contraction. However, any value in the range [0,1] is possible. The time span for the first inflation phase $t_{\text{yin,2}} - t_{\text{yin,1}}$ is set to 0.1 s, thus co-defining the time span for the second inflation phase.

3.1.8. Model parameters

For traceability reasons, BiVAD model parameters are summarized in table 3.5. They are only altered in the context of the sensitivity analysis in section 5 but remain fixed for all other purposes. Control-related parameters are not listed.

3.2. 0D mean temperature prediction model (MTP)

The temperature of the drive unit changes over a longer period of time after support start, before eventually reaching a periodic level, with a constant mean temperature. This period may take hours, depending on the initial conditions and cannot be simulated on the same time scale as the previously presented dynamic BiVAD model, as it would be computationally too expensive. Hence, a different approach is required. The objective of the MTP model is to predict the steady mean operating temperature based on the currently prevailing BiVAD model conditions. The preceding lengthy transient temperature phase is not of interest, as the periodic solution is needed for further analysis. Obviously, a BiVAD model forward simulation may alter the prevailing conditions in the BiVAD and thereby change the input to the MTP model. Hence, a repeated execution is likely necessary to update the predicted steady mean operating temperature after each BiVAD model run until its variation is sufficiently small. The BiVAD features various electro-pneumatic converters, such as the pump and the valves. The latter convert almost all

Parameter		Unit	Value
Ambient pressure	p_∞	kPa	100.0
Body temperature	T_{body}	K	310.0
Specific gas constant	R	μJ/mgK	287.0
Heat transmittance	k_{th}	mW/mm^{2}K	4.47
Tube length	L_{T}	mm	1300.0
Tube diameter	D_{T}	mm	3.0
Tube friction model slope laminar/turbulent	a_λ	-	53.1495 / 36.9768
Tube friction model offset laminar/turbulent	b_λ	-	0.0073 / 0.0212
Tube critical Reynolds number	$Re_{\text{crit},\lambda}$	-	2900.0
Tube laminar-turbulent transition interval	$\Delta Re_{\text{trans},\lambda}$	-	500.0
Connector friction model slope laminar/turbulent	a_λ	-	27560.0 / 8675.5
Connector friction model offset laminar/turbulent	b_λ	-	0.0 / 13.77
Connector critical Reynolds number	$Re_{\text{crit},\zeta}$	-	700.0
Connector laminar-turbulent transition interval	$\Delta Re_{\text{trans},\zeta}$	-	200.0
Tube polytropic exponent	n_{T}	-	1.4
Tube compliance	C_{T}	mm^3/kPa	45.6
Supply voltage	$\mathcal{U}_{\text{supply}}$	V	15
Valve polytropic exponent	$n_{\text{V,in/out}}$	-	1.4
Maximum valve flow coefficient	kv_{max}	mm^2	3.1
Valve hysteresis	$\bar{H}_{\text{V}}$	%	4.3
Reservoir volumes HPR / LPR	$V_{\text{HPR/LPR}}$	mm^3	$4.63{\cdot}10^5$ / $4.84{\cdot}10^5$
Reservoir compliances HPR / LPR	$C_{\text{HPR/LPR}}$	mm^3/kPa	247.0 / 134.0
Reservoir initial pressures HPR / LPR	$p_{\text{HPR/LPR},0}$	kPa	15.0 / -10.0
Reservoir mean temperatures(*) HPR / LPR	$\Delta\hat{T}_{\text{HPR/LPR}}$	°C	30.0 / 30.0
Pump free flow	g_{max}	mg/ms	$f(\mathcal{U}_{\text{supply}})$ (table 3.2)
Pump compression ratio	C_{PP}	-	4.76
Pump polytropic exponent	n_{PP}	-	1.0

Table 3.5.: Fixed parameters of BiVAD model. (*) Reservoir mean temperatures are predicted by the MTP model 3.2 and updated every heart cycle.

electrical energy into heat, since the work done on the plunger is very small. Their nominal power consumption is around 2.5 W per unit when fully energized [28]. The pump nominal power consumption reaches values up to 9 W when supplied by 12 V [63], depending on the instantaneous working point. However, both are the main sources for heat development. An efficient approach to predict the final heated state of the drive unit is introduced here, to provide meaningful initial mean reservoir temperatures to the dynamic BiVAD model.

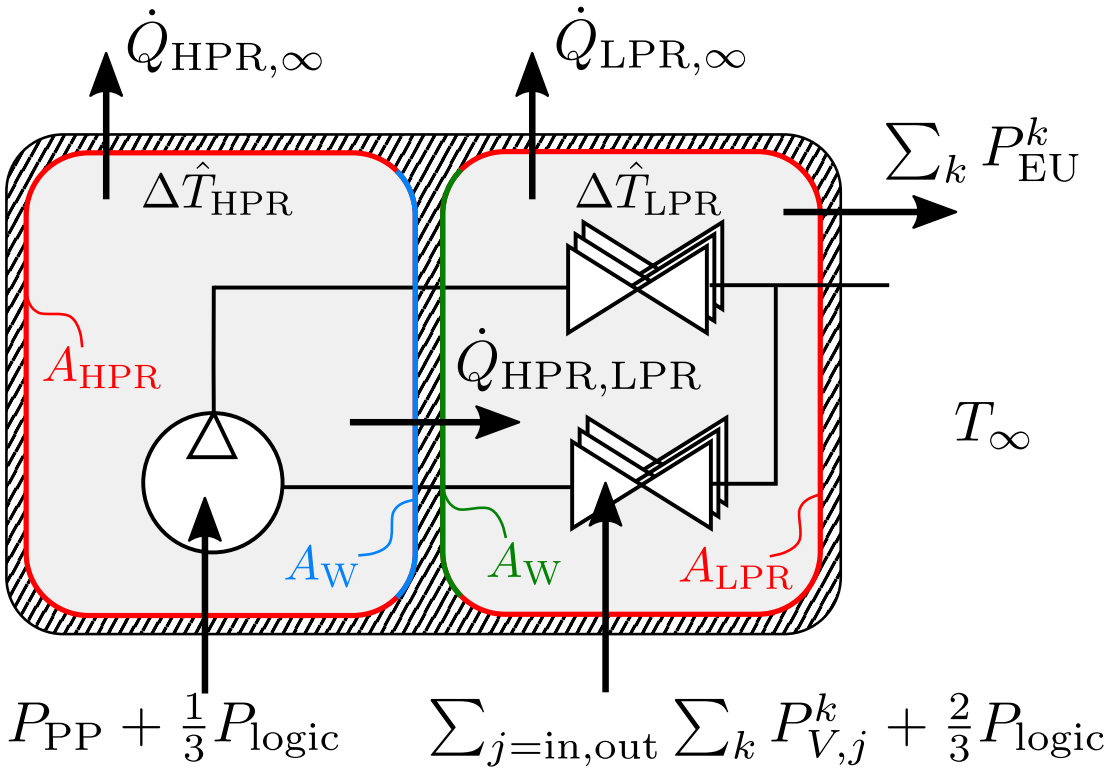

Figure 3.12.: Schematic of the mean temperature prediction (MTP) model with all included powers. The HPR (left) and LPR (right) are separated by the reservoir septum wall. The HPR includes the pump, while all inlet and outlet valves are installed inside the LPR. The power consumption of the logical unit and other electrical parts is distributed according to the surface area of the circuit boards within the reservoirs, splitting P_{logic} into 1/3 and 2/3 for HPR and LPR, respectively.

3.2.1. General approach

The first law of thermodynamics in its differential form (2.10) can be used balance work contributions which eventually heat the system. With the only systemic energy being the internal energy, $\mathrm{d}E = \mathrm{d}U = c_{\mathrm{v}} m \, \mathrm{d}\Delta T$ and splitting $\mathrm{d}W$ into work done on and by the system $\mathrm{d}W_{\mathrm{in}}$, $\mathrm{d}W_{\mathrm{out}}$, (2.10) can be rewritten to

$$\mathrm{d}W_{\mathrm{in}} = c_{\mathrm{v}} m \, \mathrm{d}\Delta T + \mathrm{d}W_{\mathrm{out}}, \tag{3.62}$$

with ΔT as temperature relative to ambient conditions. Relating everything to time results in the power balance, which is depicted in figure 3.12. The power balance is formulated for each reservoir:

$$P_{\text{HPR,in}} = c_{\text{v}} m_{\text{HPR}} \Delta\dot{T}_{\text{HPR}} + P_{\text{HPR,out}} \qquad \text{with} \tag{3.63}$$

$$P_{\text{HPR,in}} = P_{\text{PP}} + \frac{1}{3} P_{\text{logic}}, \tag{3.64}$$

$$P_{\text{HPR,out}} = \dot{Q}_{\text{HPR},\infty} + \dot{Q}_{\text{HPR,LPR}} + \sum_{k=1}^{3} P_{\text{EU}}^{k} \qquad \text{and} \tag{3.65}$$

$$P_{\text{LPR,in}} = c_{\text{v}} m_{\text{LPR}} \Delta\dot{T}_{\text{LPR}} + P_{\text{LPR,out}} \qquad \text{with} \tag{3.66}$$

$$P_{\text{LPR,in}} = \sum_{k=1}^{3} P_{\text{V,in}}^{k} + \sum_{k=1}^{3} P_{\text{V,out}}^{k} + \frac{2}{3} P_{\text{logic}} + \dot{Q}_{\text{HPR,LPR}}, \tag{3.67}$$

$$P_{\text{LPR,out}} = \dot{Q}_{\text{LPR},\infty}. \tag{3.68}$$

Here, P_{PP} is the electrical pump power, $P_{\text{V,in}}^{k}$ and $P_{\text{V,out}}^{k}$ the electrical power of inlet and outlet valves and P_{EU}^{k} the pneumatic power delivered to the heart by the EUs. P_{logic} is the constant electrical power needed by the micro-controller and other electrical components. The latter is split according to the ratio of circuit board surface area within and adjacent to the respective reservoirs. It is estimated to be $\frac{1}{3}$ and $\frac{2}{3}$ for HPR and LPR, respectively. $\dot{Q}_{\text{HPR},\infty}$ and $\dot{Q}_{\text{LPR},\infty}$ are the heat flow rates to the environment and $\dot{Q}_{\text{HPR,LPR}}$ the heat flow rate between both reservoirs. The transient terms vanish when a steady state is reached and can be canceled in (3.63) and (3.66). Inserting $\dot{Q} = k_{\text{th}} A \Delta\hat{T}$ for the respective heat flow rates and rearranging yields the final equations

$$\Delta\hat{T}_{\text{HPR}} = \frac{\frac{1}{3} P_{\text{logic}} + P_{\text{PP}} - \sum_{k=1}^{3} P_{\text{EU}}^{k} + k_{\text{th,W}} A_{\text{W}} \Delta\hat{T}_{\text{LPR}}}{k_{\text{th,HPR}} A_{\text{HPR}} + k_{\text{th,W}} A_{\text{W}}} \qquad \text{and} \tag{3.69}$$

$$\Delta\hat{T}_{\text{LPR}} = \frac{\frac{2}{3} P_{\text{logic}} + \sum_{j=\text{in,out}} \sum_{k=1}^{3} P_{\text{V},j}^{k} + k_{\text{th,W}} A_{\text{W}} \Delta\hat{T}_{\text{HPR}}}{k_{\text{th,LPR}} A_{\text{LPR}} + k_{\text{th,W}} A_{\text{W}}}. \tag{3.70}$$

The individual equations for electrical, pneumatic and heat exchange power are presented in the following sections.

3.2.2. Electrical power

The pump power consumption depends on the momentary pressure load and hence on the difference between both reservoir pressures. A lookup table was created from the nonlinear function of power consumption over this pressure difference, found in the manufacturer data sheet [63]. The given curve represents the power consumption at the maximum control signal y_{PP}. For lower control values, it is linearly interpolated to this value. The momentary pump power consumption $P_{\text{PP,m}}$ thus is

$$P_{\text{PP,m}} = P\left(p_{\text{HPR}} - p_{\text{LPR}}\right) y_{\text{PP}}, \tag{3.71}$$

with $P\left(p_{\text{HPR}} - p_{\text{LPR}}\right)$ being the power function indicated in figure 3.4 and explicitly depicted in the appendix A.II.5. The effective power value to be used in equation (3.69) is computed by

$$P_{\text{PP}} = \frac{1}{t_{\text{ec},z-1} - t_{\text{ec},z}} \int_{t_{\text{ec},z-1}}^{t_{\text{ec},z}} P_{\text{PP,m}} \, \mathrm{d}t, \tag{3.72}$$

with $t_{\text{ec},z-1} - t_{\text{ec},z}$ being the time period of the current heart beat. To estimate the electrical power consumption of a valve, its mean solenoid temperature $\Delta\hat{T}^k_{\text{spool},j}$ has to be predicted, because its resistance depends linearly on it. The resistance itself is needed to calculate the power. The electrical properties voltage, ohmic resistance and direct current $\mathcal{U}, \mathcal{R}$ and $\mathcal{I}$, respectively, are introduced. The electrical power consumed by the solenoid of the valve is derived by expressing the direct current in $P = \mathcal{U}\mathcal{I}$ with the ohmic law, such that $P = \frac{\mathcal{U}^2}{\mathcal{R}}$. The resistance of the solenoid is a linear function of its temperature, with the parameters $a_{\mathcal{R}}$, $b_{\mathcal{R}}$. They were fitted to resistance measurements of valves being placed in water at different constant temperatures. The equation for $\Delta\hat{T}^k_{\text{spool},j}$ is derived from the first law of thermodynamics, similarly to (3.63) and (3.66). This time however, only the electrical valve power and the heat flow rate from the valve solenoid to the surrounding LPR need to be considered. Due to a lack of knowledge of surface area and thermal conductivity, the valve heat transfer is modeled using the thermal conductance $\Lambda_{\text{th,V}}$ (cf. section 2.1.4). The system of equations used to compute the valve power consumption $P^k_{\text{V},j}$ is

$$P^k_{\text{V},j} = \frac{\mathcal{U}^{k^2}_{\text{V},j}}{\mathcal{R}^k_{\text{V},j}}, \tag{3.73}$$

$$\mathcal{R}^k_{\text{V},j} = a_{\mathcal{R}} \cdot \Delta\hat{T}^k_{\text{spool},j} + b_{\mathcal{R}} \quad \text{and} \tag{3.74}$$

$$\Delta T^k_{\text{spool},j} = \frac{P^k_{\text{V},j}}{\Lambda_{\text{th,V}}} + \Delta\hat{T}_{\text{LPR}}, \tag{3.75}$$

with $j \in \{\text{in}, \text{out}\}$ and $k \in \{1, 2, 3\}$. The valve heat conductance $\Lambda_{\text{th,V}}$ is derived from experimental data: Valves were energized at a constant power and the resistances were measured when steady conditions were reached. With knowledge of the resistance-temperature relation (3.74), $\Lambda_{\text{th,V}}$ could be determined by a rearranged equation (3.75). The valve's squared voltage is

$$\mathcal{U}^{k^2}_{\text{V},j} = \frac{\mathcal{U}^2_{\text{supply}}}{t_{\text{ec},z-1} - t_{\text{ec},z}} \int_{t_{\text{ec},z-1}}^{t_{\text{ec},z}} y^k_{\text{V},j} \, \mathrm{d}t. \tag{3.76}$$

The valve voltage is calculated from the supply voltage times the control signal, given as pulse width modulated (PWM) signal, $\mathcal{U}^k_{\text{V},j} = \mathcal{U}_{\text{supply}} y^k_{\text{V},j}$.[2] The parameters of the model are summarized in table 3.6.

[2]Note that the power of a PWM signal is calculated by $P = \frac{\mathcal{U}^2_{\text{supply}}}{R} y$ and **not** by $P = \frac{(\mathcal{U}_{\text{supply}} y)^2}{R}$

3.2.3. Pneumatic power

Pressure volume power, leaving the system during the supported heart beat z over the k-th EU, is calculated according to

$$P_{\mathrm{EU}}^{k} = \frac{1}{t_{\mathrm{ec},z-1} - t_{\mathrm{ec},z}} \int_{V_{\mathrm{EU}}^{k}(t_{\mathrm{ec},z-1})}^{V_{\mathrm{EU}}^{k}(t_{\mathrm{ec},z})} p_{\mathrm{EU}}^{k} \mathrm{d}V, \tag{3.77}$$

with $V_{\mathrm{EU}}^{k}(t_{\mathrm{ec},z-1})$ and $V_{\mathrm{EU}}^{k}(t_{\mathrm{ec},z})$ being the EU volumes at the beginning and the end of the heart cycle, respectively.

3.2.4. Heat exchange power

As derived in the heat transfer section 2.1.4, the heat flow rates can be expressed as $\dot{Q} = k_{\mathrm{th}} A \Delta T$. According to equation (2.23), the heat transmittances $k_{\mathrm{th,HPR/LPR}}$ are composed of the heat coefficients $\alpha_{\mathrm{HPR/LPR}}$ and α_{∞} as well as the material thicknesses, the thermal conductivity of the material λ_{th} and the respective areas. The surface areas are determined from CAD data and are listed in table 3.6. The thermal conductivity of the housing material is obtained from the data sheet [27] and listed in the same table. The heat transfer coefficients $\alpha_{\mathrm{HPR/LPR}}$ and α_{∞} however, as well as a mean material thickness $\hat{d}_{\mathrm{HPR/LPR}}$ are unknown and estimated in 4.1.5. The heat transmittances $k_{\mathrm{th,HPR}}$, $k_{\mathrm{th,LPR}}$ in the equations (3.69) and (3.70) read

$$k_{\mathrm{th,HPR}} A_{\mathrm{HPR}} = \frac{A_{\mathrm{HPR}}}{\frac{1}{\alpha_{\mathrm{HPR}}} + \frac{\hat{d}_{\mathrm{HPR}}}{\lambda_{\mathrm{th}}} + \frac{1}{\alpha_{\infty}}}, \tag{3.78}$$

$$k_{\mathrm{th,LPR}} A_{\mathrm{LPR}} = \frac{A_{\mathrm{LPR}}}{\frac{1}{\alpha_{\mathrm{LPR}}} + \frac{\hat{d}_{\mathrm{LPR}}}{\lambda_{\mathrm{th}}} + \frac{1}{\alpha_{\infty}}}. \tag{3.79}$$

The system of equations, defining the MTP model and comprising equations (3.69) to (3.79) is implemented and solved in MATLAB (The MathWorks Inc. Natick, Massachusetts, USA). The principal 24 unknowns of the MTP model are

$$\boldsymbol{p}^{\mathrm{MTP}} = \begin{bmatrix} \Delta\hat{T}_{\mathrm{HPR}} & \Delta\hat{T}_{\mathrm{LPR}} & P_{\mathrm{PP}} & P_{\mathrm{EU}}^{k} & P_{\mathrm{V},j}^{k} & \mathcal{R}_{\mathrm{V},j}^{k} & \Delta T_{\mathrm{spool},j}^{k} \end{bmatrix}^{T}, \tag{3.80}$$

with $j \in \{\mathrm{in}, \mathrm{out}\}$ and $k \in \{1, 2, 3\}$. The obtained values for $\Delta\hat{T}_{\mathrm{HPR}}$ and $\Delta\hat{T}_{\mathrm{LPR}}$ are used in the supported cardiovascular system (SCVS) model for the dynamic heart beat simulation.

Parameter		Unit	Value	Source
Resistance model slope	$a_{\mathcal{R}}$	°C/Ω	0.222	Experimental
Resistance model offset	$b_{\mathcal{R}}$	°C	52.39	Experimental
Valve thermal conductance	$\Lambda_{\text{th,V}}$	W/K	0.0272	Experimental
Reservoir area HPR	A_{HPR}	m^2	$386.347 \cdot 10^{-3}$	CAD data
Reservoir area LPR	A_{LPR}	m^2	$384.764 \cdot 10^{-3}$	CAD data
Reservoir (mean) septum wall area	A_{W}	m^2	$0.0305 \cdot 10^{-3}$	CAD data
Reservoir thermal conductance	λ_{th}	W/mK	0.39	Data sheet [27]
Reservoir heat transmittances	$k_{\text{th,HPR/LPR/W}}$	$\text{W/m}^2\text{K}$	cf. section 4.1.5	Estimated
Load-free power consumption	P_{logic}	W	1.544	Experimental
Supply voltage	$\mathcal{U}_{\text{supply}}$	V	15	Exemplary
Ambient temperature	T_{∞}	°C	25	Exemplary

Table 3.6.: Parameters of the mean temperature prediction (MTP) model with standard values and their sources.

3.3. 0D-3D-3D-0D supported cardiovascular model (SCVS)

The mixed-dimensional BiVAD model of the previous section 3.1 is a stand-alone computational replica of the real assist device and can be run independently. This may be useful for engineering purposes but leaves individual patient conditions unconsidered. Therefore, it is placed around a 3D solid mechanics heart model, which is further coupled to a 0D model of the circulatory system, both recently presented by Hirschvogel [43]. Figure 3.13 depicts the complete system. To date, no combination of technically complete direct cardiac compression device, patient-specific heart and circulatory system was presented. Hirschvogel et al. [45],[43] have introduced a supported 3D heart with attached 0D circulatory system, but assist pressures have been prescribed and no representation of the technical drive unit has been included. This section will formulate the coupled problem. For the sake of brevity, BiVAD associated domains, boundaries, variables or parameters are marked with the abbreviation for assist device, AD. The equations of the coupled system in their strong form are listed in the following, with $i \in \{\ell, r\}$ and $k \in \{1, 2, 3\}$. Note that none of the 0D drive unit nor 0D circulatory model equations are included in this list.

$$\boldsymbol{\nabla}_0 \cdot (\boldsymbol{F}\boldsymbol{S}) = \rho_0 \ddot{\boldsymbol{u}} \qquad \text{in } \Omega_{0,\mathrm{H}} \times [t_0, \mathrm{T}], \tag{3.81}$$

$$\boldsymbol{t}_0 = -(\boldsymbol{n}_0 \otimes \boldsymbol{n}_0)(\alpha_e \boldsymbol{u} + \beta_e \dot{\boldsymbol{u}}) \qquad \text{on } \Gamma^{\mathrm{R},e}_{0,\mathrm{H}} \times [t_0, \mathrm{T}], \tag{3.82}$$

$$\boldsymbol{t}_0 = -\alpha_b \boldsymbol{u} - \beta_b \dot{\boldsymbol{u}} - (\boldsymbol{n}_0 \otimes \boldsymbol{n}_0)(\alpha_{b,\perp} \boldsymbol{u} + \beta_{e,\perp} \dot{\boldsymbol{u}}) \qquad \text{on } \Gamma^{\mathrm{R},b}_{0,\mathrm{H}} \times [t_0, \mathrm{T}], \tag{3.83}$$

$$\boldsymbol{t}_0 = \boldsymbol{P}\boldsymbol{n}_0 = -p^i_{\mathrm{v}} J \boldsymbol{F}^{-T} \boldsymbol{n}_0 \qquad \text{on } \Gamma^{\mathrm{CS},i}_{0,\mathrm{H}} \times [t_0, \mathrm{T}], \tag{3.84}$$

$$\boldsymbol{\nabla}_0 \cdot (\boldsymbol{F}\boldsymbol{S}) = \rho_0 \ddot{\boldsymbol{u}} \qquad \text{in } \Omega^k_{0,\mathrm{EU}} \times [t_0, \mathrm{T}], \tag{3.85}$$

$$\boldsymbol{t}_0 = -(\boldsymbol{n}_0 \otimes \boldsymbol{n}_0)(\alpha_p \boldsymbol{u} + \beta_p \dot{\boldsymbol{u}}) \qquad \text{on } \Gamma^{\mathrm{R},k}_{0,\mathrm{EU}} \times [t_0, \mathrm{T}], \tag{3.86}$$

$$\boldsymbol{t}_0 = \boldsymbol{P}\boldsymbol{n}_0 = -p^k_{\mathrm{EU}} J \boldsymbol{F}^{-T} \boldsymbol{n}_0 \qquad \text{on } \Gamma^{\mathrm{AD},k}_{0,\mathrm{EU}} \times [t_0, \mathrm{T}]. \tag{3.87}$$

The dynamic simulation of a supported heart beat takes place during $[t_0, \mathrm{T}]$, while the heart is prestressed [32] to the initial geometry during $[0, t_0]$, presented in section 3.3.3. Contact constraints are enforced between heart and the EUs of the implant on $\Gamma^{\mathrm{c},k}_{0,\mathrm{EU}}$ and $\Gamma^{\mathrm{c}}_{0,\mathrm{H}}$ as well as between the EU's inner surfaces on $\Gamma^{\mathrm{c,AD},k}_{0,\mathrm{EU}}$ for $k \in \{1, 2, 3\}$:

$$g_n \geq 0, \quad p_n \leq 0, \quad p_n g_n = 0 \qquad \text{on } \Gamma^{\mathrm{c},k}_{0,\mathrm{EU}}, \Gamma^{\mathrm{c}}_{0,\mathrm{H}} \text{ and } \Gamma^{\mathrm{c,AD},k}_{0,\mathrm{EU}} \times [t_0, \mathrm{T}]. \tag{3.88}$$

Here, (3.81) and (3.85) are the partial differential equations of the local linear balance of momentum of heart and implant model, respectively. The material density is given by ρ_0 and differs for $\Omega_{0,\mathrm{H}}$ and $\Omega^k_{0,\mathrm{EU}}$. They are subject to a set of Neumann boundary conditions. 0D-3D coupling conditions of heart and circulatory system (3.84) are the left and right ventricular pressures p^i_{v} with $i \in \{\ell, r\}$. Likewise, the coupling of the 0D drive unit and the 3D implant (3.87) is represented by the EU pressures p^k_{EU} with $k \in \{1, 2, 3\}$. Furthermore, Robin boundary conditions, (3.82), (3.83) and (3.86), hold the structural models in place, mimicking their embedding within the surrounding tissue. Here, α denotes the spring stiffness and β the dashpot damping coefficient. Owing to the absence of the atria and attached vessels, the stiffness acting on the basal cut plane is assumed to be higher in the normal direction. Therefore, the spring-dashpot condition

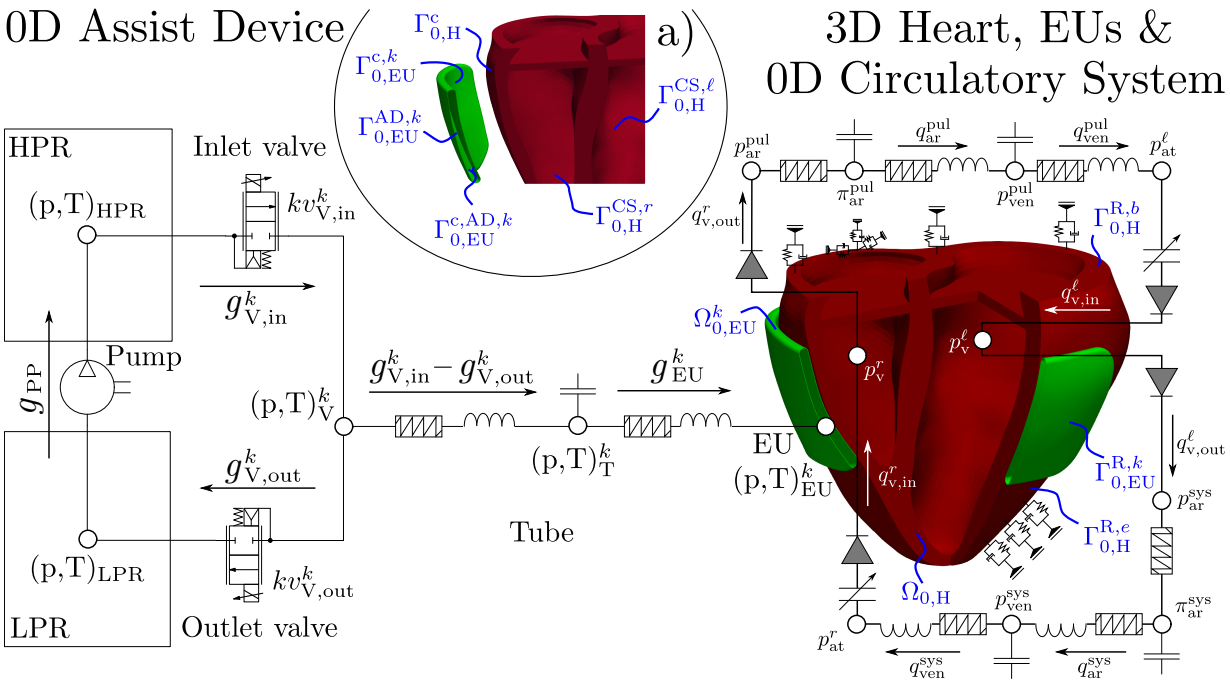

Figure 3.13.: Schematic of the coupled 0D-3D-3D-0D model of a supported cardiovascular system, including the 0D drive unit, the 3D implant (consisting of three EUs, green), the 3D heart and the 0D circulation model. Domains and boundaries are indicated in blue script. The heart and implant are held in place by Robin boundary conditions, indicated with spring-dashpot symbols, at the heart base $\Gamma^{\mathrm{R},b}_{0,\mathrm{H}}$, the heart epicardium $\Gamma^{\mathrm{R},e}_{0,\mathrm{H}}$ and the implant's EU back faces $\Gamma^{\mathrm{R},k}_{0,\mathrm{EU}}$, for $k \in \{1,2,3\}$. The view a) depicts the interface boundaries between 0D assist device (AD) and 3D EUs, namely the coupling boundary $\Gamma^{\mathrm{AD},k}_{0,\mathrm{EU}}$ and the contact boundaries between the implant's EU and heart $\Gamma^{\mathrm{c},k}_{0,\mathrm{EU}}$, $\Gamma^{\mathrm{c}}_{0,\mathrm{H}}$. It further shows the internal EU contact $\Gamma^{\mathrm{c,AD},k}_{0,\mathrm{EU}}$, for $k \in \{1,2,3\}$, and the 3D-0D boundaries of heart and circulatory system $\Gamma^{\mathrm{CS},r}_{0,\mathrm{H}}$ and $\Gamma^{\mathrm{CS},\ell}_{0,\mathrm{H}}$. The figure depicts all 0D degrees of freedom.

is composed of a purely perpendicular (indexed $(\cdot)_{b_\perp}$) and an omnidirectional part (indexed $(\cdot)_b$) [43]. All material and Robin parameter values are listed in table A.2 in the appendix.

3.3.1. Materials

The heart model geometry is obtained from segmented CT data. In order to mimic myocardial contraction, muscle fibers $\boldsymbol{f}_0$ are embedded into the cardiac walls, following a cardiac fiber angle from $-60°$ at the epicardium to $60°$ at the endocardium with respect to the circumference [110]. In order to exhibit orthotropic material behavior, an additional sheet layer $\boldsymbol{s}_0$ is included, rotated $90°$ to the fibers. A detailed description of the geometry building process as well as fiber and sheet directions, can be found in [43]. The myocardial material is a hybrid material, consisting of a passive and an active part, where the latter is referred to as *active stress*. The constitutive equation for the second Piola-Kirchhoff stress reads

$$\boldsymbol{S} = 2\frac{\partial \Psi_{\mathrm{H}}}{\partial \boldsymbol{C}} + \tau_a(t)\boldsymbol{f}_0 \otimes \boldsymbol{f}_0, \tag{3.89}$$

with the hyperelastic strain energy function Ψ_{H}. It is adapted from Holzapfel and Ogden [47] and reads

$$\Psi_{\mathrm{H}} = \frac{a_0}{2b_0}\left(e^{b(\bar{I}_C-3)}-1\right) + \sum_{i=f,s}\frac{a_i}{2b_i}\left(e^{b_i(IV_i-1)^2-1}\right) + \frac{a_{fs}}{2b_{fs}}\left(e^{b_{fs}VIII_{fs}^2}-1\right) + \frac{\kappa_{\mathrm{H}}}{2}(J-1)^2, \tag{3.90}$$

with the isotropic modified invariant $\bar{I}_C$ in (2.56), the squared stretches along fiber and sheet direction IV_i, with $i = f, s$, and the shear coupling invariant between both layers $VIII_{fs} = \boldsymbol{f}_0 \cdot \boldsymbol{C}\boldsymbol{s}_0$. The bulk modulus κ_{H} can be chosen to model nearly-incompressible behavior in the volumetric part, which is the last term of (3.90). The active stress τ_a along the fibers $\boldsymbol{f}_0$ is given by the ODE [10]

$$\dot{\tau}_a = -|\mathsf{u}|\tau_a + \sigma_0 \mathrm{max}(0, \mathsf{u}), \tag{3.91}$$

with the scaled activation function u with tunable rise and fall rates [44]. The cardiac cycle is characterized by the end-diastolic time point t_{ed}, which is also the starting point of contraction and coincides with the R-wave in the ECG signal (cf. section 3.1.7). Likewise, the end-systolic time point t_{es} is simultaneously the starting point of cardiac relaxation, which becomes noticeable as a T-wave in the same signal. As the BiVAD uses the patient's ECG to control the timing, t_{ed} and t_{es} similarly trigger the beginnings of inflation and deflation. The passive material parameters are listed in table A.3 in the appendix. Generic parameters of the active stress can be found in [43].

The implant material is purely passive and is also modeled as a hyperelastic material, with the second Piola-Kirchhoff stress being

$$\boldsymbol{S} = 2\frac{\partial \Psi_{\mathrm{EU}}}{\partial \boldsymbol{C}}. \tag{3.92}$$

It consists of a isochoric Neo-Hookean and an Ogden-type volumetric part:

$$\Psi_{\mathrm{EU}} = \frac{\mu_{\mathrm{EU}}}{2}\left(\bar{I}_{C,\mathrm{EU}} - 3\right) + \frac{\kappa_{\mathrm{EU}}}{4}\left(J^2 - 2\ln J - 1\right), \tag{3.93}$$

with shear and bulk modulus μ_{EU}, κ_{EU}, respectively. The former was derived in an uniaxial tensile test to $\mu_{\text{EU}} = 9346$ kPa [45] and

$$\kappa = \frac{\mu}{1 - 2\nu} \tag{3.94}$$

is used to derive $\kappa_{\text{EU}} = 233.65 \cdot 10^3$ kPa, with the Poisson's ratio $\nu_{\text{EU}} = 0.48$ [69]. The density is set to $\rho_{0,\text{EU}}$ =1.2·10^{-6} kg/mm^3 [17]. The parameters are also summarized in table A.4.

3.3.2. Coupling conditions

Equation (3.87) represents the boundary traction on the inner EU surfaces $\Gamma_{0,\text{EU}}^{\text{AD},k}$, caused by the coupling variables of the 0D drive unit model, namely p_{EU}^k. In order to compute these EU pressures, the 0D drive unit model requires information about the EU volume and internal energy (cf. section 3.1.6) and hence is dependent upon the displacement field $\boldsymbol{u}$ of the solid mechanics problem. The volume of one EU is computed as the boundary integral over its inner surface

$$V_{\text{EU}}^k(\boldsymbol{u}) = -\frac{1}{3} \int_{\Gamma_{0,\text{EU}}^{\text{AD},k}} (\boldsymbol{u} + \boldsymbol{X}) \cdot J \boldsymbol{F}^{-T} \boldsymbol{n}_0 \, \mathrm{d}A. \tag{3.95}$$

The second piece of information needed is the internal energy, which can be expressed as

$$W_{\text{int,EU}}^k(\boldsymbol{u}) = \int_{\Omega_{0,\text{EU}}^k} \Psi_{\text{EU}} \, \mathrm{d}V, \tag{3.96}$$

with $k \in \{1, 2, 3\}$ for both terms. Likewise, the circulatory model requires the rate of change of volume to compute the ventricular pressures $p_{\text{v}}^{\ell,r}$, which are, in return, needed by the heart as boundary traction. Consequently, the ventricular volume information is calculated according to

$$V_{\text{v}}^i(\boldsymbol{u}) = -\frac{1}{3} \int_{\Gamma_{0,\text{H}}^{\text{CS},i} \cup \Gamma_{0,\text{H}}^{\text{lids},i}} (\boldsymbol{u} + \boldsymbol{X}) \cdot J \boldsymbol{F}^{-T} \boldsymbol{n}_0 \, \mathrm{d}A, \tag{3.97}$$

with $i \in \{\ell, r\}$. Note that the artificial basal lids $\Gamma_{0,\text{H}}^{\text{lids},i}$ are simplified representations of the valvular plane, ensuring an enclosed volume, which is needed for the volume calculation according to (3.97). However, the ventricular pressure is not exerted on this boundary [43].

3.3.3. Prestressing

The ventricles are subject to the respective ventricular blood pressure during CT imaging to obtain the patient-specific heart geometry. Hence, the geometry is in deformed state, which has to be considered during later simulation. Here, the so-called Modified Updated Lagrangian Formulation (MULF), presented by Gee et al. [32], is utilized to prestress the heart geometry to the initial ventricular pressures and fiber active stresses, which were present at the time of CT imaging. This process is performed prior to any dynamic simulation during the time $t \in [0, t_0]$:

$$\boldsymbol{\nabla_0} \cdot (\boldsymbol{F}\boldsymbol{S}) = \boldsymbol{0} \qquad \text{in } \Omega_{0,\mathrm{H}} \times [0, t_0], \tag{3.98}$$

$$\boldsymbol{t}_0 = -(\boldsymbol{n}_0 \otimes \boldsymbol{n}_0)(\alpha_e \boldsymbol{u}) \qquad \text{on } \Gamma^{\mathrm{R},e}_{0,\mathrm{H}} \times [0, t_0], \tag{3.99}$$

$$\boldsymbol{t}_0 = -\alpha_b \boldsymbol{u} - (\boldsymbol{n}_0 \otimes \boldsymbol{n}_0)(\alpha_{b,\perp} \boldsymbol{u}) \qquad \text{on } \Gamma^{\mathrm{R},b}_{0,\mathrm{H}} \times [0, t_0]. \tag{3.100}$$

In addition, ventricular pressures p_{v}^i, with $i \in \{\ell, r\}$, are set to the initial values of the subsequent dynamic simulation. The prestressed state is used as a starting point for the dynamic simulation. To do so, the deformation gradient and the deflection of the Robin boundary springs of the prestressed state are stored. Both are further used in the subsequent transient simulation. While the displacement starts at $\boldsymbol{u}(t_0) = \boldsymbol{0}$, the combined deformation gradient $\boldsymbol{F}\boldsymbol{F}_{\text{prestressed}}$ is utilized instead of $\boldsymbol{F}$ alone. Likewise for the Robin boundaries, $(\boldsymbol{u} + \boldsymbol{u}_{\text{prestressed}})$ describes the current spring deflections.

3.3.4. Discretization and solution

The presented models of BiVAD, MTP and SCVS are discretized with respect to their spatial and temporal resolution and the applied solution strategies are specifically described in the following sections. Properties of the assist device are identified with the superscript $(\bullet)^{\mathrm{AD}}$ and those of the cardiovascular system are marked with $(\bullet)^{\mathrm{CVS}}$.

3.3.4.1. SCVS model

The coupled mixed-dimensional SCVS model is spatially discretized using the FE method. A formulation of the specific discretized principle of virtual work is omitted here. Also, the system of equations of the 0D cardiovascular system is not explicitly noted, but can be retrieved in [44], [45] and [43]. However, figure 3.13 depicts all degrees of freedom for both 0D systems at the discrete time step $n + 1$, which are

$$\begin{aligned} \boldsymbol{p}^{\mathrm{CVS}}_{n+1} = [&p^{\ell}_{\mathrm{at}} \quad q^{\ell}_{\mathrm{v,in}} \quad q^{\ell}_{\mathrm{v,out}} \quad p^{\ell}_{\mathrm{v}} \quad p^{\mathrm{sys}}_{\mathrm{ar}} \quad q^{\mathrm{sys}}_{\mathrm{ar}} \quad p^{\mathrm{sys}}_{\mathrm{ven}} \quad q^{\mathrm{sys}}_{\mathrm{ven}} \\ &p^{r}_{\mathrm{at}} \quad q^{r}_{\mathrm{v,in}} \quad q^{r}_{\mathrm{v,out}} \quad p^{r}_{\mathrm{v}} \quad p^{\mathrm{pul}}_{\mathrm{ar}} \quad q^{\mathrm{pul}}_{\mathrm{ar}} \quad p^{\mathrm{pul}}_{\mathrm{ven}} \quad q^{\mathrm{pul}}_{\mathrm{ven}}]^T, \end{aligned} \tag{3.101}$$

$$\begin{aligned} \boldsymbol{p}^{\mathrm{AD}}_{n+1} = [&p^{k}_{\mathrm{EU}} \quad q^{k}_{\mathrm{EU}} \quad \tau^{k}_{\mathrm{EU}} \quad T^{k}_{\mathrm{EU}} \quad T^{k}_{\mathrm{TE}} \quad p^{k}_{\mathrm{V}} \quad T^{k}_{\mathrm{V}} \quad g^{k}_{\mathrm{EU}} \quad g^{k}_{\mathrm{V,in}} \quad g^{k}_{\mathrm{V,out}} \\ &p^{k}_{\mathrm{T}} \quad T^{k}_{\mathrm{T}} \quad p_{\mathrm{HPR}} \quad T_{\mathrm{HPR}} \quad p_{\mathrm{LPR}} \quad T_{\mathrm{LPR}} \quad g_{\mathrm{PP}} \quad \tau_{\mathrm{HPR}} \quad \tau_{\mathrm{LPR}}]^T, \end{aligned} \tag{3.102}$$

with $k \in \{1, 2, 3\}$. Their sizes are $n^{\mathrm{CVS}}_{\mathrm{DOF}} = 16$ and $n^{\mathrm{AD}}_{\mathrm{DOF}} = 3 \cdot 12 + 7 = 43$. The BiVAD model is discretized in time using the One-step-θ method, cf. section 2.3.2. Thereby, the discretized residual $\boldsymbol{r}^{\mathrm{AD}}$ can be delineated as follows: The implant's EU equations (3.55) to (3.58) transform to the first four entries in (3.103). The next four entries stem from the tube model equations (3.46), (3.36), (3.25) and (3.44), respectively. They are followed by the valve flow and control equations (3.23) and (3.24). The entry 11 and 12 in (3.103) result from the pressure drop over the second tube element (3.37) and the tube temperature (3.45). The reservoir equations (3.5), (3.6) and (3.11) to (3.14) as well as the pump model (3.19) are given in the last seven entries.

$$
\boldsymbol{r}^{\mathrm{AD}} = \begin{bmatrix}
\frac{p^k_{\mathrm{EU},n+1}-p^k_{\mathrm{EU},n}}{\Delta t} - \left\{ \frac{1}{V^k_{\mathrm{EU}}} \left(g^k_{\mathrm{EU}} R T^k_{\mathrm{EU}} - p^k_{\mathrm{EU}} q^k_{\mathrm{EU}} \right) + \frac{p^k_{\mathrm{EU}}}{T^k_{\mathrm{EU}}} \tau^k_{\mathrm{EU}} \right\}_{n+\theta} \\
\frac{V^k_{\mathrm{EU},n+1}(\boldsymbol{d}_{n+1})-V^k_{\mathrm{EU},n}(\boldsymbol{d}_n)}{\Delta t} - q^k_{\mathrm{EU}n+\theta} \\
\frac{T^k_{\mathrm{EU},n+1}-T^k_{\mathrm{EU},n}}{\Delta t} - \tau^k_{\mathrm{EU},n+\theta} \\
\frac{W^k_{\mathrm{EU,int},n+1}(\boldsymbol{d}_{n+1})-W^k_{\mathrm{EU,int},n}(\boldsymbol{d}_n)}{\Delta t} + \Big\{ p^k_{\mathrm{EU}} q^k_{\mathrm{EU}} - \mathrm{k}_{\mathrm{th,EU}} A^k_{\mathrm{EU}} (T_{\mathrm{body}} - T^k_{\mathrm{EU}}) + \tau^k_{\mathrm{EU}} \frac{p^k_{\mathrm{EU}} V^k_{\mathrm{EU}}}{T^k_{\mathrm{EU}}(\kappa-1)} - \dots \\
\dots - g^k_{\mathrm{EU,in}} \frac{R}{\kappa - 1} (\kappa T^k_{\mathrm{TE}} - T^k_{\mathrm{EU}}) - g^k_{\mathrm{EU,out}} R T^k_{\mathrm{EU}} \Big\}_{n+\theta} \\
\left\{ T^k_{\mathrm{TE}} - T^k_{\mathrm{V}} \left(\frac{p^k_{\mathrm{EU}}}{p^k_{\mathrm{V}}} \right)^{\frac{n_{\mathrm{T}}-1}{n_{\mathrm{T}}}} \right\}_{n+\theta} \\
\frac{L_{\mathrm{T}}}{2A_{\mathrm{T}}} \left(\frac{g^k_{\mathrm{V,in},n+1}-g^k_{\mathrm{V,in},n}}{\Delta t} - \frac{g^k_{\mathrm{V,out},n+1}-g^k_{\mathrm{V,out},n}}{\Delta t} \right) \dots - \\
\dots - \left\{ p^k_{\mathrm{V}} - p^k_{\mathrm{T}} - \left(\mathrm{f}_{\mathrm{T},1} (g^k_{\mathrm{V,in}} - g^k_{\mathrm{V,out}}) + \mathrm{f}_{\mathrm{T},2} (g^k_{\mathrm{V,in}} - g^k_{\mathrm{V,out}})^2 \right) \mathrm{f}_{\mathrm{T},3} \right\}_{n+\theta} \\
\left\{ T^k_{\mathrm{V}} - T_{\mathrm{HPR}} \left(\frac{p^k_{\mathrm{V}}}{p_{\mathrm{HPR}}} \right)^{\frac{n_{\mathrm{V}}-1}{n_{\mathrm{V}}}} \right\}_{n+\theta} \\
\frac{p^k_{\mathrm{T},n+1}-p^k_{\mathrm{T},n}}{\Delta t} - \left\{ \frac{\left(g^k_{\mathrm{V,in}} - g^k_{\mathrm{V,out}} - g^k_{\mathrm{EU}} \right) R T^k_{\mathrm{T}}}{p^k_{\mathrm{T}} C_{\mathrm{T}} + \frac{V_{\mathrm{T}}}{n_{\mathrm{T}}}} \right\}_{n+\theta} \\
\left\{ g^k_{\mathrm{V,in}} \sqrt{2 T^k_{\mathrm{HPR}} T^k_{\mathrm{V}} R} - k v^k_{\mathrm{V,in}} \sqrt{\left(p^k_{\mathrm{HPR}} - p^k_{\mathrm{V}} \right) \left(p^k_{\mathrm{HPR}} T^k_{\mathrm{V}} + p^k_{\mathrm{V}} T^k_{\mathrm{HPR}} \right)} \right\}_{n+\theta} \\
\left\{ g^k_{\mathrm{V,out}} \sqrt{2 T^k_{\mathrm{LPR}} T^k_{\mathrm{V}} R} - k v^k_{\mathrm{V,out}} \sqrt{\left(p^k_{\mathrm{V}} - p^k_{\mathrm{LPR}} \right) \left(p^k_{\mathrm{LPR}} T^k_{\mathrm{V}} + p^k_{\mathrm{V}} T^k_{\mathrm{LPR}} \right)} \right\}_{n+\theta} \\
\frac{L_{\mathrm{T}}}{2A_{\mathrm{T}}} \frac{g^k_{\mathrm{EU},n+1}-g^k_{\mathrm{EU},n}}{\Delta t} - \left\{ p^k_{\mathrm{T}} - p^k_{\mathrm{EU}} - \left(\mathrm{f}_{\mathrm{T},4} g^k_{\mathrm{EU}} + \mathrm{f}_{\mathrm{T},5} (g^k_{\mathrm{EU}})^2 \right) \mathrm{f}_{\mathrm{T},6} \right\}_{n+\theta} \\
\left\{ T^k_{\mathrm{T}} - \frac{T^k_{\mathrm{V}} + T^k_{\mathrm{TE}}}{2} \right\}_{n+\theta} \\
\frac{p_{\mathrm{HPR},n+1}-p_{\mathrm{HPR},n}}{\Delta t} - \left\{ \frac{R T_{\mathrm{HPR}} \left(g_{\mathrm{PP}} - \sum_k^3 g^k_{\mathrm{V,in}} \right) - \frac{p_{\mathrm{HPR}} V_{\mathrm{HPR}}}{T_{\mathrm{HPR}}} \tau_{\mathrm{HPR}}}{V_{\mathrm{HPR}} + p_{\mathrm{HPR}} C_{\mathrm{HPR}}} \right\}_{n+\theta} \\
\frac{V_{\mathrm{HPR}}}{R} \frac{T_{\mathrm{HPR},n+1}-T_{\mathrm{HPR},n}}{\Delta t} - \left\{ \left[\Upsilon_{\mathrm{HPR}} \frac{\kappa-1}{R} + T_{\mathrm{HPR}} \sum_k^3 g^k_{\mathrm{V,in}} (1-\kappa) + g_{\mathrm{PP}} (\kappa T_{\mathrm{LPR}} T_{\mathrm{PP}} - T_{\mathrm{HPR}}) \right] \frac{T_{\mathrm{HPR}}}{p_{\mathrm{HPR}}} \right\}_{n+\theta} \\
\frac{p_{\mathrm{LPR},n+1}-p_{\mathrm{LPR},n}}{\Delta t} - \left\{ \frac{R T_{\mathrm{LPR}} \left(\sum_k^3 g^k_{\mathrm{V,out}} - g_{\mathrm{PP}} \right) - \frac{p_{\mathrm{LPR}} V_{\mathrm{LPR}}}{T_{\mathrm{LPR}}} \tau_{\mathrm{LPR}}}{V_{\mathrm{LPR}} + p_{\mathrm{LPR}} C_{\mathrm{LPR}}} \right\}_{n+\theta} \\
\frac{V_{\mathrm{LPR}}}{R} \frac{T_{\mathrm{LPR},n+1}-T_{\mathrm{LPR},n}}{\Delta t} - \left\{ \left[\Upsilon_{\mathrm{LPR}} \frac{\kappa-1}{R} + \sum_k^3 g^k_{\mathrm{V,out}} (\kappa T_{\mathrm{V}} - T_{\mathrm{LPR}}) + g_{\mathrm{PP}} T_{\mathrm{LPR}} (1-\kappa) \right] \frac{T_{\mathrm{LPR}}}{p_{\mathrm{LPR}}} \right\}_{n+\theta} \\
\left\{ g_{\mathrm{PP}} T_{\mathrm{LPR}} p_{\mathrm{norm}} - g_{\mathrm{PP,max}} y_{\mathrm{PP}} T_{\mathrm{norm}} p_{\mathrm{LPR}} \left(1 - \frac{p_{\mathrm{HPR}} - p_{\mathrm{LPR}}}{p_{\mathrm{LPR}} (C_{\mathrm{PP}} - 1.0)} \right) \right\}_{n+\theta} \\
\frac{T_{\mathrm{HPR},n+1}-T_{\mathrm{HPR},n}}{\Delta t} - \tau_{\mathrm{HPR},n+\theta} \\
\frac{T_{\mathrm{LPR},n+1}-T_{\mathrm{LPR},n}}{\Delta t} - \tau_{\mathrm{LPR},n+\theta}
\end{bmatrix}, \tag{3.103}
$$

with $k \in \{1,2,3\}$. $\Upsilon_{\text{HPR/LPR}}$ takes the place of $\dot{Q}_{\text{HPR/LPR}}$, which can be extended as in (3.8). All expressions, except for reservoir and pump equations and hence all but the last seven in (3.103), represent the connection to one EU only. They consist of inlet and outlet valve, tube and EU. It coincides with the visualization in figure 3.13. The two additional sets, initially depicted in 3.2, are omitted here for the sake of brevity. Every expressions of the type $\{\bullet\}_{n+\theta}$, can further be extended to $\{\bullet\}_{n+\theta} = \theta\{\bullet\}_{n+1} + (1-\theta)\{\bullet\}_{n}$, representing the respective property at the time point $t_{n+\theta}$. Now, the 0D residuals of CVS and BiVAD, $\boldsymbol{r}^{\text{CVS}}$ and $\boldsymbol{r}^{\text{AD}}$, are merged into one 0D residual, formulated with respect to their corresponding state variables

$$\boldsymbol{r}^{\text{0D}}(\boldsymbol{d}, \boldsymbol{p}^{\text{0D}}) = \begin{bmatrix} \boldsymbol{r}^{\text{CVS}}(\boldsymbol{d}, \boldsymbol{p}^{\text{CVS}}) \\ \boldsymbol{r}^{\text{AD}}(\boldsymbol{d}, \boldsymbol{p}^{\text{AD}}) \end{bmatrix}_{n+1}, \tag{3.104}$$

with the combined vector of 0D degrees of freedom $\boldsymbol{p}^{\text{0D}}$. A global residual, $\boldsymbol{r}^{\text{S-0D}}(\boldsymbol{d}, \boldsymbol{p}^{\text{CVS}}, \boldsymbol{p}^{\text{AD}})$, is built from the 0D and the 3D residual, which was formulated in (2.72). This global residual, $\boldsymbol{r}^{\text{S-0D}}(\boldsymbol{d}, \boldsymbol{p}^{\text{CVS}}, \boldsymbol{p}^{\text{AD}})_{n+1}$, must vanish at every time step $n+1$. It can be written as the linearized monolithic system of equations

$$\begin{bmatrix} \boldsymbol{K}^{\text{S}} & \boldsymbol{K}^{\text{S,0D}} \\ \boldsymbol{K}^{\text{0D,S}} & \boldsymbol{K}^{\text{0D}} \end{bmatrix}_{n+1}^{i} \begin{bmatrix} \Delta\boldsymbol{d} \\ \Delta\boldsymbol{p}^{\text{0D}} \end{bmatrix}_{n+1}^{i+1} = - \begin{bmatrix} \boldsymbol{r}^{\text{S}} \\ \boldsymbol{r}^{\text{0D}} \end{bmatrix}_{n+1}^{i}, \tag{3.105}$$

which is solved for $\Delta\boldsymbol{d}_{n+1}^{i+1}$ and $\Delta(\boldsymbol{p}^{\text{0D}})_{n+1}^{i+1}$ prior to updating the solution

$$\boldsymbol{d}_{n+1}^{i+1} = \boldsymbol{d}_{n+1}^{i} + \Delta\boldsymbol{d}_{n+1}^{i+1}, \tag{3.106}$$

$$\boldsymbol{p}_{n+1}^{\text{CVS},i+1} = \boldsymbol{p}_{n+1}^{\text{CVS},i} + \Delta\boldsymbol{p}_{n+1}^{\text{CVS},i+1} \quad \text{and} \tag{3.107}$$

$$\boldsymbol{p}_{n+1}^{\text{AD},i+1} = \boldsymbol{p}_{n+1}^{\text{AD},i} + \Delta\boldsymbol{p}_{n+1}^{\text{AD},i+1}, \tag{3.108}$$

in each Newton iteration i, until all of the following convergence criteria are met:

$$||\boldsymbol{r}^{\text{S}}(\boldsymbol{d}_{n+1}^{i}, \boldsymbol{p}_{n+1}^{\text{CVS},i}, \boldsymbol{p}_{n+1}^{\text{AD},i})||_2 \leq \epsilon_{\text{res}}^{\text{S}} \quad \text{and} \quad ||\Delta\boldsymbol{d}_{n+1}^{i+1}||_2 \leq \epsilon_{\text{incr}}^{\text{S}}, \tag{3.109}$$

$$||\boldsymbol{r}^{\text{CVS}}(\boldsymbol{d}_{n+1}^{i}, \boldsymbol{p}_{n+1}^{\text{CVS},i})||_2 \leq \epsilon_{\text{res}}^{\text{CVS}} \quad \text{and} \quad ||\Delta\boldsymbol{p}_{n+1}^{\text{CVS},i+1}||_2 \leq \epsilon_{\text{incr}}^{\text{CVS}}, \tag{3.110}$$

$$||\boldsymbol{r}^{\text{AD}}(\boldsymbol{d}_{n+1}^{i}, \boldsymbol{p}_{n+1}^{\text{AD},i})||_2 \leq \epsilon_{\text{res}}^{\text{AD}} \quad \text{and} \quad ||\Delta\boldsymbol{p}_{n+1}^{\text{AD},i+1}||_2 \leq \epsilon_{\text{incr}}^{\text{AD}}. \tag{3.111}$$

The structural stiffness block $\boldsymbol{K}^{\text{S}} \in \mathbb{R}^{n_{\text{DOF}}^{\text{S}} \times n_{\text{DOF}}^{\text{S}}}$ is described by

$$\begin{aligned} \boldsymbol{K}^{\text{S}} \,|_{n+1}^{i} \quad &= \frac{\partial \boldsymbol{r}^{\text{S}}}{\partial \boldsymbol{d}} \,|_{n+1}^{i} = \\ &= \frac{1-\alpha_m}{\beta\Delta t^2}\boldsymbol{M} + \frac{(1-\alpha_f)\gamma}{\beta\Delta t}\boldsymbol{D} + (1-\alpha_f)\frac{\partial \mathbf{F}_{\text{int}}(\boldsymbol{d})}{\partial \boldsymbol{d}} \,|_{n+1}^{i} - (1-\alpha_f)\frac{\partial \mathbf{F}_{\text{ext}}(\boldsymbol{d})}{\partial \boldsymbol{d}} \,|_{n+1}^{i}. \end{aligned} \tag{3.112}$$

The off-diagonal coupling block $\boldsymbol{K}^{\text{S,0D}} \in \mathbb{R}^{n_{\text{DOF}}^{\text{S}} \times n_{\text{DOF}}^{\text{OD}}}$ accounts for the 0D pressure load on the boundary surfaces of the structure, namely $\Gamma_{\text{0,H}}^{\text{CS},i}$ with $i \in \{\ell, r\}$ and $\Gamma_{\text{0,EU}}^{\text{AD},k}$ for $k \in \{1,2,3\}$. Utilizing the Generalized-α parameter description (2.73) in (2.72), the residual can be differentiated

with respect to the 0D state variable vectors, yielding

$$\boldsymbol{K}^{\mathrm{S,0D}}\big|_{n+1}^{i} = \left.\frac{\partial \boldsymbol{r}^{\mathrm{S}}}{\partial \boldsymbol{p}^{\mathrm{0D}}}\right|_{n+1}^{i} = -(1-\alpha_f)\left.\frac{\partial \mathbf{F}_{\mathrm{ext}}(\boldsymbol{d},\boldsymbol{p}^{\mathrm{0D}})}{\partial \boldsymbol{p}^{\mathrm{0D}}}\right|_{n+1}^{i}. \tag{3.113}$$

Similarly, the 0D systems are dependent on the structural displacement $\boldsymbol{d}_{n+1}^{i}$. Consequently, the matrix $\boldsymbol{K}^{\mathrm{0D,S}} \in \mathbb{R}^{n_{\mathrm{DOF}}^{\mathrm{0D}} \times n_{\mathrm{DOF}}^{\mathrm{S}}}$ accounts for the changes in volume of the heart's ventricles and the implant's EUs, as well as for the internal energy of the latter. The (1,0)-block reads

$$\boldsymbol{K}^{\mathrm{0D,S}} = \left.\frac{\partial \boldsymbol{r}^{\mathrm{0D}}}{\partial \boldsymbol{d}}\right|_{n+1}^{i} = \begin{bmatrix} \boldsymbol{K}^{\mathrm{0D^{CVS},S}} \\ \boldsymbol{K}^{\mathrm{0D^{AD},S}} \end{bmatrix}, \tag{3.114}$$

with

$$\boldsymbol{K}^{\mathrm{0D^{CVS},S}} = \left[\mathbf{0} \quad \mathbf{0} \quad \frac{1}{\Delta t}\frac{\partial V_{\mathrm{v}}^{\ell}(\boldsymbol{d})}{\partial \boldsymbol{d}}^{T} \quad \dots \quad \mathbf{0} \quad \mathbf{0} \quad \frac{1}{\Delta t}\frac{\partial V_{\mathrm{v}}^{r}(\boldsymbol{d})}{\partial \boldsymbol{d}}^{T} \quad \dots \right]_{n+1}^{i\,T} \tag{3.115}$$

$$\begin{aligned} \boldsymbol{K}^{\mathrm{0D^{AD},S}} = \Bigg[& \theta \frac{p_{\mathrm{EU}}^{k} q_{\mathrm{EU}}^{k} - R T_{\mathrm{EU}}^{k} g_{\mathrm{EU}}^{k}}{(V_{\mathrm{EU}}^{k})^2} \frac{\partial V_{\mathrm{EU}}^{k}(\boldsymbol{d})}{\partial \boldsymbol{d}}^{T} \quad \frac{1}{\Delta t}\frac{\partial V_{\mathrm{EU}}^{k}(\boldsymbol{d})}{\partial \boldsymbol{d}}^{T} \quad \mathbf{0} \\ & \frac{1}{\Delta t}\frac{\partial W_{\mathrm{EU,int}}^{k}(\boldsymbol{d})}{\partial \boldsymbol{d}}^{T} + \theta \frac{\tau_{\mathrm{EU}}^{k} p_{\mathrm{EU}}^{k}}{T_{\mathrm{EU}}^{k}(\kappa - 1)} \frac{\partial V_{\mathrm{EU}}^{k}(\boldsymbol{d})}{\partial \boldsymbol{d}}^{T} \quad \dots \Bigg]_{n+1}^{i\,T}, \end{aligned} \tag{3.116}$$

with the contributions from the circulatory (3.115) and assist device model (3.116) with $k \in \{1,2,3\}$. $\mathbf{F}_{\mathrm{EU,int}}^{k}$ was used to replace the partial derivative $\partial W_{\mathrm{EU,int}}^{k}(\boldsymbol{d})/\partial \boldsymbol{d}$. The 0D stiffness matrix can be further written as

$$\boldsymbol{K}^{\mathrm{0D}} = \begin{bmatrix} \boldsymbol{K}^{\mathrm{CVS}} & \mathbf{0} \\ \mathbf{0} & \boldsymbol{K}^{\mathrm{AD}} \end{bmatrix}, \tag{3.117}$$

showing that the two 0D models are not directly coupled. The explicit presentation of $\boldsymbol{K}^{\mathrm{CVS}}$ is omitted here. Its derivation from the residual $\boldsymbol{r}^{\mathrm{CVS}}$ can be found in [43], [44] and the vector of the degrees of freedom $\boldsymbol{p}^{\mathrm{CVS}}$, written out in (3.101), is straightforward due to its mainly linear character. For the BiVAD model, however, the stiffness matrix is not trivial and is presented in full in the appendix section A.II.6.

The described monolithic 0D-3D-3D-0D system, (3.105), is implemented in the in-house multi-physics finite element software. A 2×2 block SIMPLE[3]-like preconditioner [26] is used, together with a GMRES[4] [97] solver, which is implemented in Trilinos [118].

The problem at hand must deal with thin-walled structures, the EUs, and sudden contact phenomena (i.e. EU-heart and EU-EU), which may cause the failure of the Newton linearization

[3] Semi-Implicit Method for Pressure-Linked Equations
[4] Generalized Minimal Residual Method

θ^{CVS}	0.5	CVS model One-step-θ time integration parameter [-]
θ^{AD}	1.0	BiVAD model One-step-θ time integration parameter [-]
α_M	0.0	Mass matrix proportionality factor of Rayleigh damping [s^{-1}]
α_K	10^{-5}	Stiffness matrix proportionality factor of Rayleigh damping [s]
$\epsilon^{\text{S}}_{\text{res}}$	10^{-5}	Solid mechanics residual tolerance of Newton's method [mN]
$\epsilon^{\text{S}}_{\text{incr}}$	10^{-6}	Solid mechanics increment tolerance of Newton's method [mm]
$\epsilon^{\text{CVS}}_{\text{res}}$	10^{-6}	CVS model residual tolerance of Newton's method (*)
$\epsilon^{\text{CVS}}_{\text{incr}}$	10^{-6}	CVS model increment tolerance of Newton's method (*)
$\epsilon^{\text{AD}}_{\text{res}}$	10^{-5}	BiVAD model residual tolerance of Newton's method (*)
$\epsilon^{\text{AD}}_{\text{incr}}$	10^{-6}	BiVAD model increment tolerance of Newton's method (*)

Table 3.7.: Base algorithmic parameters of coupled SCVS model. Note that the tolerances marked with (*) are given without unit as they apply to all dimensions in $\boldsymbol{p}^{\text{CVS}}$ and $\boldsymbol{p}^{\text{AD}}$.

procedure. Besides time step reducing methods, as e.g. using the half step size in case of non-convergence and automatically restoring the initial step size after eventual convergence, pseudo-transient continuation (PTC) [31] is used. This procedure adds the value k^i_{PTC} to the diagonal entries of the structural stiffness matrix at the i-th Newton iteration, according to $\boldsymbol{K}^{\text{S}} + k_{\text{PTC}}\mathbf{1}\,|^i_{n+1}$. The value of k_{PTC} is initially chosen and adapted up to ten times in case of consecutive non-convergence before a calculation is ultimately stopped. Within a time step, the k^i_{PTC} is continuously altered in every Newton iteration i, obeying

$$k^i_{\text{PTC}} = k^{i-1}_{\text{PTC}} \frac{||\boldsymbol{r}^{\text{S}}||^i_2}{||\boldsymbol{r}^{\text{S}}||^{i-1}_2} \tag{3.118}$$

and eventually vanishes conjointly with the residual. Table 3.7 lists the algorithmic parameters for time integration, Rayleigh damping and the tolerances of the Newton's method.

3.3.4.2. MTP model

The MTP model is a purely 0D representation and utilizes the results of the SCVS model to compute new mean temperature predictions for the reservoirs. In order to compute pump and EU power in (3.76) and (3.77), respectively, the trapezoidal numerical integration rule for a non-uniform grid is used. Its general form for the function $f(x)$ in the interval $[a, b]$ reads

$$\int_a^b f(x)\,\mathrm{d}x \approx \sum_{n=1}^{N} \frac{f(x_n) + f(x_{n+1})}{2} \Delta x_{n+1}, \tag{3.119}$$

with Δx_{n+1} being the $(n+1)$th sub-interval $\Delta x_{n+1} = x_{n+1} - x_n$, and $a = x_1$, $b = x_{N+1}$. As the MTP model is implemented in MATLAB (The MathWorks Inc. Natick, Massachusetts, USA), the integration is performed with the built-in function *trapz*.

Parameter	Explanation	Default [s]
$t_{\text{c,out,e}}$	End of coarse time step in deflation phase	0.19
$t_{\text{f,in,s}}$	Start of fine time step in inflation phase Equal to $t_{\text{yin,1}}$ and to end of diastole/beginning of systole	0.2
$t_{\text{f,in,e}}$	End of fine time step in inflation phase Not necessarily equal to $t_{\text{yin,2}}$	0.4
$t_{\text{c,in,s}}$	Begin of coarse time step use in inflation phase	0.41
$t_{\text{c,in,e}}$	End of coarse time step use in inflation phase	0.52
$t_{\text{f,out,s}}$	Begin of fine time step use in deflation phase Equal to t_{yout} and end of systole/beginning of diastole	0.53
$t_{\text{f,out,e}}$	End of fine time step use in deflation phase	0.73
$t_{\text{c,out,s}}$	Begin of coarse time step use in deflation phase	0.74
t_{ec}	End of cardiac cycle (approx. 80 % of time between two R-waves)	1.0
Δt_{fine}	Fine time step size	e.g. 0.001
Δt_{coarse}	Coarse time step size	e.g. 0.004

Table 3.8.: Time step adaptation parameters with explanation and default values. They are adapted in case of patient-specific analyses.

3.4. Convergence study

3.4.1. Methods

3.4.1.1. Temporal discretization

A temporal discretization analysis for the heart model has previously been performed by Hirschvogel [43], resulting in a suggested resolution of 100 or more time steps per heart cycle, which yields a minimum time step size of $\Delta t = 10$ ms at a heart rate of 60 beats per minute. Here, the temporal discretization is assessed for the 3D implant and 0D drive unit. Therefore, a convergence study with respect to the temporal discretization is conducted. The rate of change of the solution is fast during two periods of the heart cycle, namely during the initial phases of inflation and deflation. Here, the high rate of EU volume change requires small time step sizes. This is especially necessary during deflation, since the thin-walled EU stiffness decreases while it is depressurized, which is likely to result in numerical difficulties. During the rest of the heart beat, time step sizes may be larger, reducing the overall computational costs. Therefore, the time step size is prescribed as a function of time. It is shown in figure 3.14. With the beginnings of inflation and deflation, indicated by the left and right vertical dashed lines, respectively, the time step size is set to Δt_{fine}. For the rest of the heart cycle, the time step size is set to a coarse value, defined by the factor $f_{\Delta t}$ to

$$\Delta t_{\text{coarse}} = f_{\Delta t} \cdot \Delta t_{\text{fine}}. \tag{3.120}$$

Linear interpolation is utilized to derive transition values between fine and coarse time step levels. Table 3.8 describes the time instances of figure 3.14. The output to assess convergence was chosen to be the pressure-volume (pV) curve of the EU. Since it is the coupling point, this

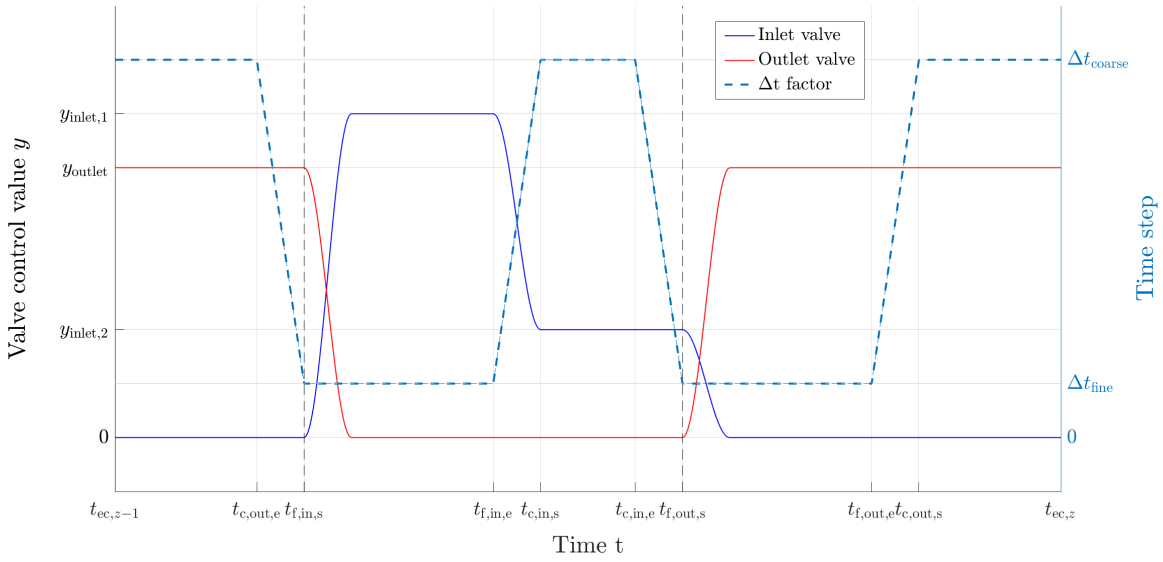

Figure 3.14.: Prescribed time step sizes over one heart beat with valve inlet and outlet control signal as the underlying cause of rapid EU volume changes. Explanation of parameters can be found in table 3.8.

EU	Valve opening [-]		
	$y_{\text{inlet},1}$	$y_{\text{inlet},2}$	y_{outlet}
1	0.9	0.3	0.6
2	0.8	0.2	0.6
3	0.5	0.2	0.4

Table 3.9.: Utilized valve control values in temporal discretization study.

measure unites information of both dimensions and models. The pV work is obtained by

$$W_{\text{EU}}^{k} = \int_{V_{\text{EU}}^{k}(t_{\text{ec},z-1})}^{V_{\text{EU}}^{k}(t_{\text{ec},z})} p_{\text{EU}}^{k} \mathrm{d}V, \tag{3.121}$$

with $V_{\text{EU}}^{k}(t_{\text{ec},z-1})$ and $V_{\text{EU}}^{k}(t_{\text{ec},z})$ being the EU volumes at the beginning and the end of the heart cycle, respectively. The pV-work is computed for fine time step sizes $\Delta t_{\text{fine}} \in \{0.1, 0.5, 1.0, 1.5, 2.0\}$ ms and for time step factors $f_{\Delta t} \in \{1.0, 2.0, 5.0, 10.0\}$, resulting in a tested time step size range $\Delta t \in [0.1, 20]$ ms. Time step sizes above these values have occasionally provoked non-convergence. The utilized valve control values are summarized in table 3.9.

3.4.1.2. Spatial discretization

Spatial convergence analysis for the 3D heart and implant has previously been performed by Hirschvogel [43]. Here, the heart model is discretized using tetrahedral finite elements and an approximate edge length of 2 mm is considered suitable. Hexahedral finite elements are used for

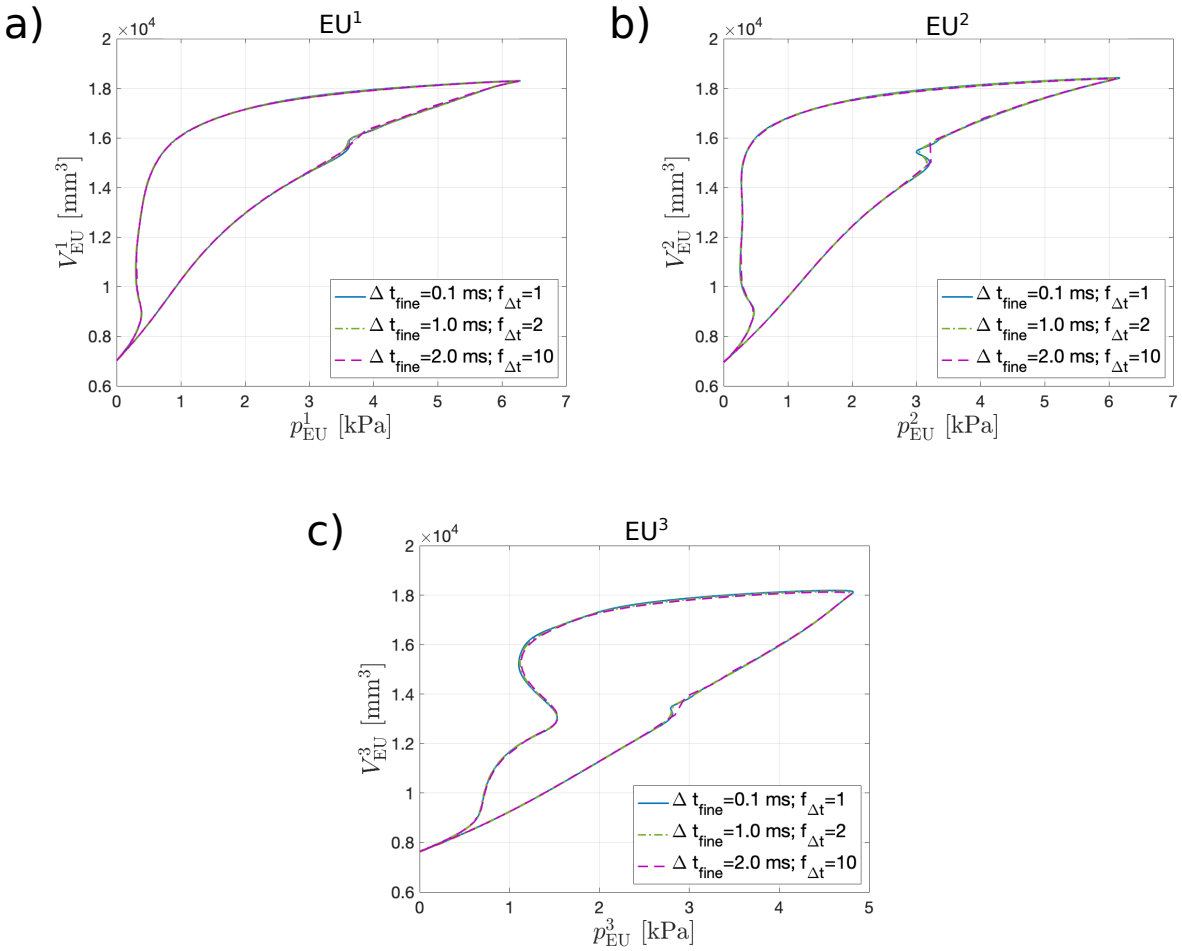

Figure 3.15.: Results of the temporal discretization study plotted as pV curves for each of the EU. Note that only three of 20 results are visualized for readability reasons: the finest reference discretization of $t_{\text{fine}} = 0.1$ ms, $f_{\Delta t} = 1.0$, the coarsest combination $t_{\text{fine}} = 2.0$ ms, $f_{\Delta t} = 10.0$ and a central value combination of $t_{\text{fine}} = 1.0$ ms, $f_{\Delta t} = 2.0$.

the implant's EUs and the solution was previously found to be unchanged for in-plane element edge lengths of approximately 1 mm, which is the element size used within this work.

3.4.2. Results

The visualized pV curves of the temporal dicretization analysis can be found figure 3.15, with the pV relations of the individual EUs in a) to c). The resulting integral measure pV work can be found in table 3.10.

EU[1] - Relative deviation [%]

$f_{\Delta t}$	Δt_{fine}				
	0.1	0.5	1.0	1.5	2.0
1.0	0.0	0.36	0.94	1.47	1.99
2.0	-0.14	0.37	0.96	1.54	2.04
5.0	-0.13	0.41	1.04	1.64	2.17
10.0	-0.11	0.48	1.16	1.68	2.31

EU[2] - Relative deviation [%]

$f_{\Delta t}$	Δt_{fine}				
	0.1	0.5	1.0	1.5	2.0
1.0	0.0	0.45	1.01	1.54	2.01
2.0	-0.02	0.45	1.01	1.54	2.01
5.0	-0.02	0.45	1.00	1.53	2.00
10.0	-0.01	0.46	1.01	1.40	2.11

EU[3] - Relative deviation [%]

$f_{\Delta t}$	Δt_{fine}				
	0.1	0.5	1.0	1.5	2.0
1.0	0.0	0.64	1.24	1.80	2.35
2.0	0.15	0.65	1.25	1.82	2.40
5.0	0.16	0.68	1.32	1.91	2.53
10.0	0.17	0.74	1.42	1.86	2.75

Table 3.10.: Relative deviation of the pV work from the finest temporal resolution with $\Delta t_{\text{fine}} = 0.1$ ms and $f_{\Delta t} = 1.0$ (grey).

3.4.3. Discussion

The pV work differs very little over the tested time step intervals $[0.1\ 20.0]$ ms. The only noticeable deviations from the finest temporal resolution with $\Delta t_{\text{fine}} = 0.1$ ms and $f_{\Delta t} = 1.0$ can be observed in the kink at roughly 3 kPa in figure 3.15 b) and c). In combination with an almost identical curve for the rest of the pV loop, these deviations can result in greater pV work for coarser time step sizes, which can mathematically manifest itself as a negative relative deviation in table 3.10. However, their values are far below 1 %. Likewise small are the deviations at the coarsest temporal discretization, which differ by less than 3 %. Consequently, any of the investigated combinations can be used for reliable analyses. Here, $\Delta t_{\text{fine}} = 1.0$ ms and $f_{\Delta t} = 4.0$, where chosen as standard values.

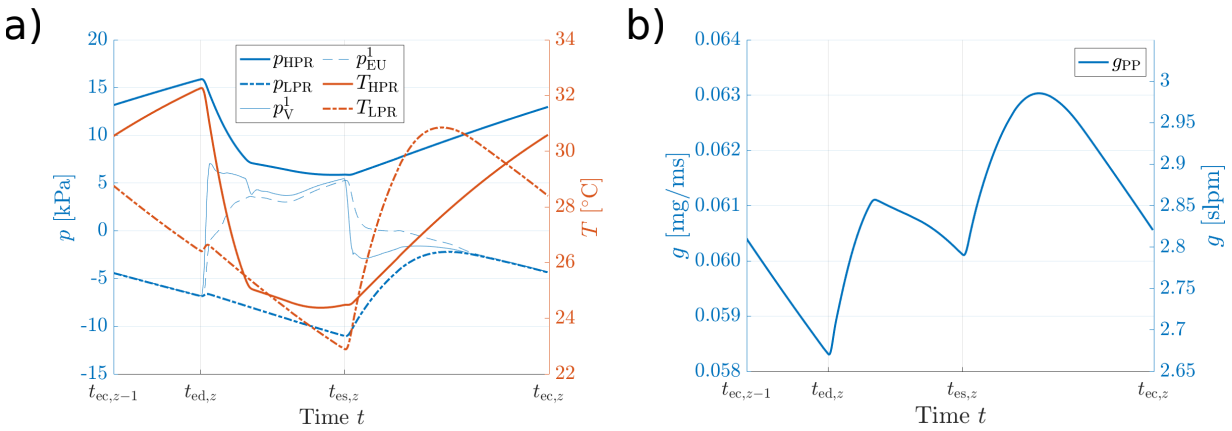

Figure 3.16.: Exemplary results for the reservoir pressures and temperatures in a) as well as for the generated pump flow in b). Valve and EU pressures have been included in a) for a better understanding. The pump flow is also given in standard liters per minute (slpm).

3.5. Exemplary results

The coupled SCVS model allows for analyzing the results of up to 83 0D unknowns: 16 DOF in $\boldsymbol{p}^{\mathrm{CVS}}$ (3.101), 43 DOF in $\boldsymbol{p}^{\mathrm{AD}}$ (3.102) and 24 DOF in $\boldsymbol{p}^{\mathrm{MTP}}$ (3.80). However, MTP model solutions are of interest primarily due to their effects on the SCVS. In addition, insights in 3D solid mechanics solutions can be gained. In the following, a selection of the principal solutions is given in order to provide an overview to the reader. All presented solutions have reached periodicity. If not otherwise stated, the given examples stem from the same simulation and are obtained using standard parameters listed in table 3.5.

Reservoir HPR and LPR pressures and temperatures with auxiliary EU pressures are depicted in 3.16 a) and the concurrently generated pump flow with $y_{\mathrm{PP}} = 0.33$ in b). Pump flow is further given in standard liters per minute to provide a more intuitive flow unit. *Standard* refers to standard conditions with $T_{\mathrm{std}} = 273.15\ \mathrm{K} = 0\ °\mathrm{C}$ and $p_{\mathrm{std}} = 101.325\ \mathrm{kPa}$ [22], resulting in the standard density $\rho_{\mathrm{std}} = 1.2925 \cdot 10^{-3}\ \frac{\mathrm{mg}}{\mathrm{mm}^3}$.

Valve Figure 3.17 a) depicts the flow coefficients for one inlet and outlet valve $kv^1_{\mathrm{V,in/out}}$, which result from the prescribed open-loop valve control signals $y^1_{\mathrm{V,in}}$ and $y^1_{\mathrm{V,out}}$. The valve flow coefficients and the prevailing pressure differences $p_{\mathrm{HPR}} - p^1_{\mathrm{V}}$ and $p^1_{\mathrm{V}} - p_{\mathrm{LPR}}$ (cf. figure 3.16 a) provoke the valve flows during inflation $g^1_{\mathrm{V,in}}$ and deflation $g^1_{\mathrm{V,out}}$, shown in b). The collateral hysteresis occurring in both valves is plotted explicitly in figure 3.17 c).

Tube and connector Pressures and temperatures at the three distinctive connector-tube points are visualized in figure 3.18 a). Here, the indices $(p,T)_{\mathrm{V}}$ and $(p,T)_{\mathrm{T}}$ refer to the beginning and the middle of the tube, as it is modeled according to figure 3.2. While the tube end temperature T_{TE} is explicitly computed in (3.46) to derive the enthalpy flow into the EUs, its

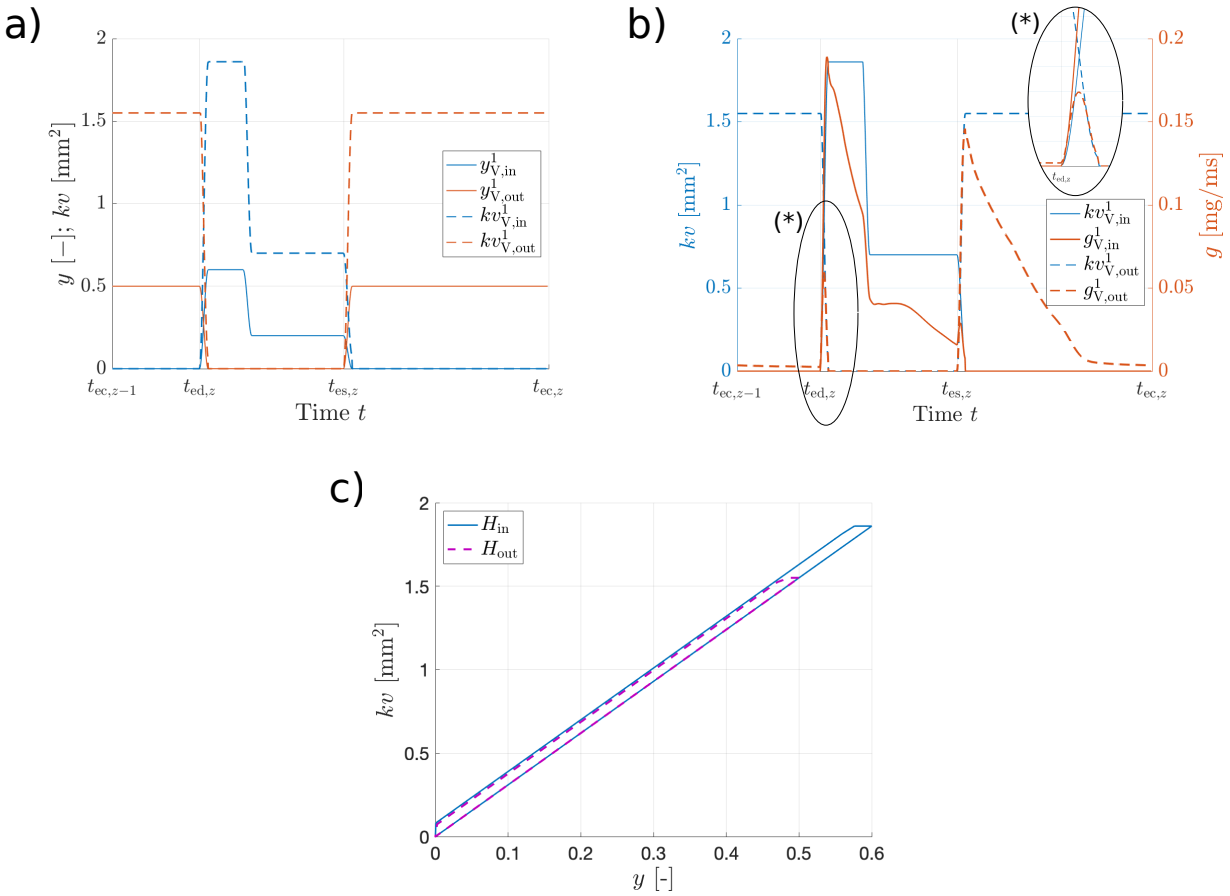

Figure 3.17.: Exemplary results for valve flow coefficients kv as results of the valve control signal y in a). The kv values are proportional to the evolving flow, shown in b). Here, a close-up (*) is given to distinguish the signals at the beginning of EU inflation. During inflation in $t \in [t_{\mathrm{ed}}, t_{\mathrm{es}}]$, the hysteresis alters the falling edge and the second plateau of $kv^1_{\mathrm{V,in}}$ while only the falling edge is delayed near t_{ed} during deflation. The latter results in a greater waste flow directly from HPR to LPR. It is detailed in 3.17 b)(*). The effect of valve hysteresis is depicted in c).

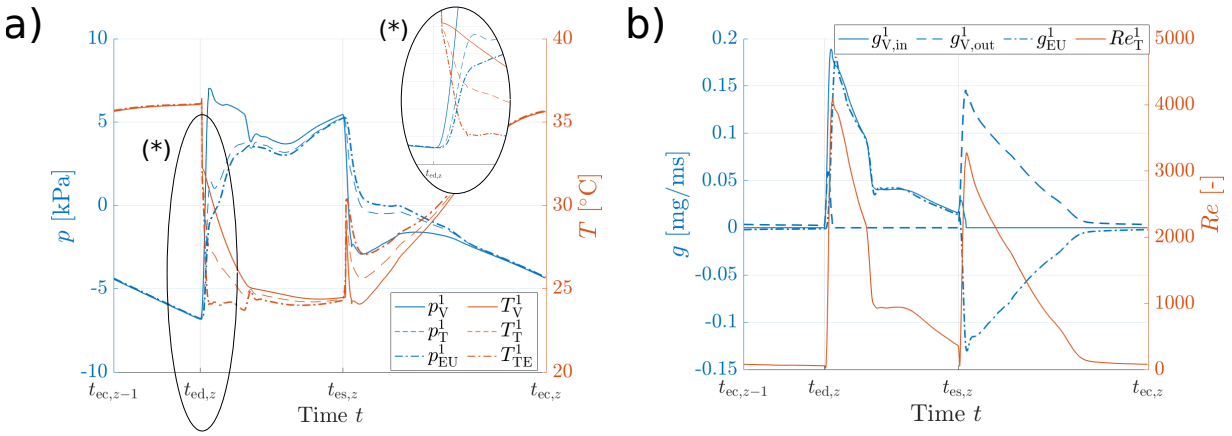

Figure 3.18.: Exemplary results for tube pressures and temperatures in a) as well as corresponding flows and Reynolds number in b). A close-up (*) is again given in a) to distinguish the signals near inflation start $t = t_{ed,z}$. Both valve flows and EU flow govern the pressure and temperature curves. While the definition of the valve flow directions results predominately in positive values, the EU flow adopts a negative sign during deflation. According to (3.47), the critical Reynolds numbers are 700 and 2900 for connector and tube flow, respectively.

pressure is defined the same as in the EUs. The flows passing through the tube are mutually plotted in b). Furthermore, the Reynolds number is sketched, indicating whether the laminar or turbulent flow regime is dominant.

Expandable units The EU pressure and temperature curves are plotted together with the EU flow in figure 3.19 a). In addition, EU volume and internal energy (3.96) are depicted in b). The latter approaches zero when the EU adopts values close to the unloaded initial volume.

BiVAD-CVS coupling Another way to display EU behavior is to plot its pV curve and it stands to reason to compare it to the corresponding cardiac pV loops. Figure 3.20 a) visualizes EU and ventricular pV curves, without and with BiVAD support. The mechanical work done on the heart by the BiVAD is the area under the EU pV curve.

Contact conditions Contacting inner EU surfaces ensure a proper deflation of the EUs during diastole and the corresponding volumes can approach zero. Figure 3.21 a) visualizes the active contacting elements at the end of diastole and b) depicts the corresponding displacement of the 3D bodies at that time point. Interaction between the implant EUs and the heart stems exclusively from mechanical contact, which is depicted in figure 3.21 c) at the end of the inflation process. Here, the contacting elements are again colored in red. The corresponding displacement is shown in d).

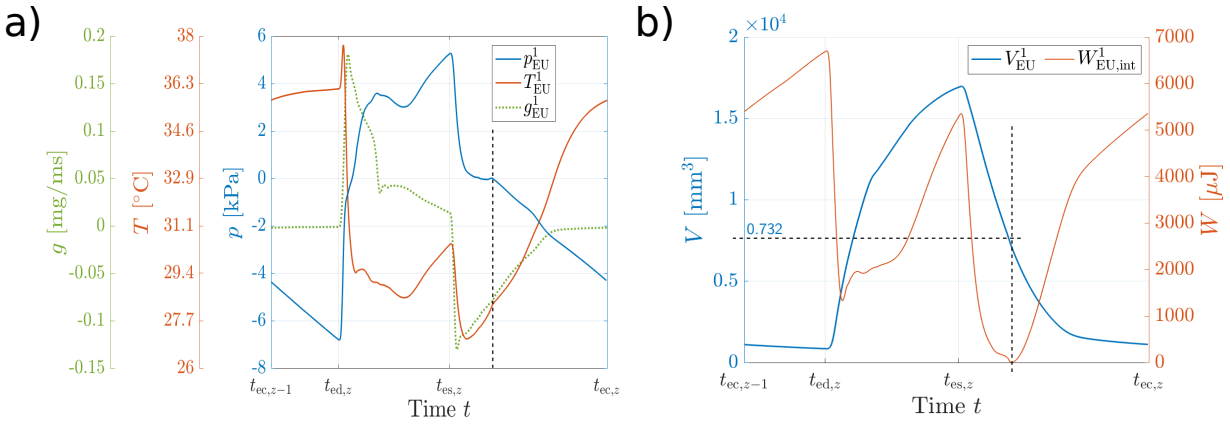

Figure 3.19.: Exemplary results for the EU pressure, temperature and flow in a) as well as corresponding volume and internal energy signals in b).

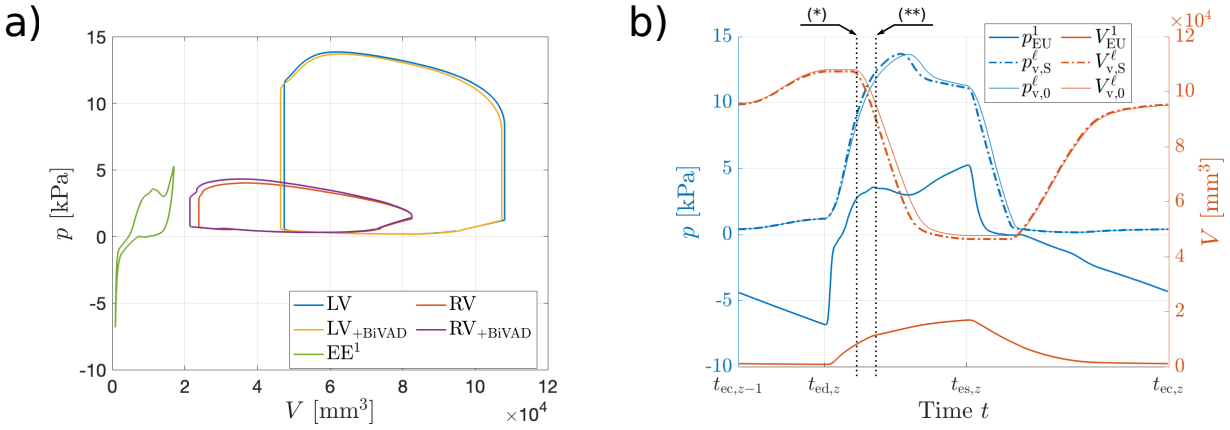

Figure 3.20.: Exemplary results for the cardiac and implant pressure-volume curves in a). Only the pV curve of EU^1 is given, consistent to the other results depicted in this section. The total work delivered to the heart is the pV area sum of all three EUs, $\sum_{k=1}^{3} pV_{\mathrm{EU}}^{k}$. The ventricular pV curves of the unsupported heart are compared to those with BiVAD support (+BiVAD). In b) LV and EU^1 pressure and volume signals under support $(\bullet)_{\mathrm{S}}$ are plotted over time. RV signals are left out to facilitate signal inspection. The first dotted line (*) indicates the aortic valve opening, hence the start of blood ejection and concomitant cardiac volume reduction. The second line (**) points the beginning of the second, lower valve control value $y_{\mathrm{inlet},2}$. Pressure and volume are also plotted without BiVAD support, indicated by $(\bullet)_0$

.

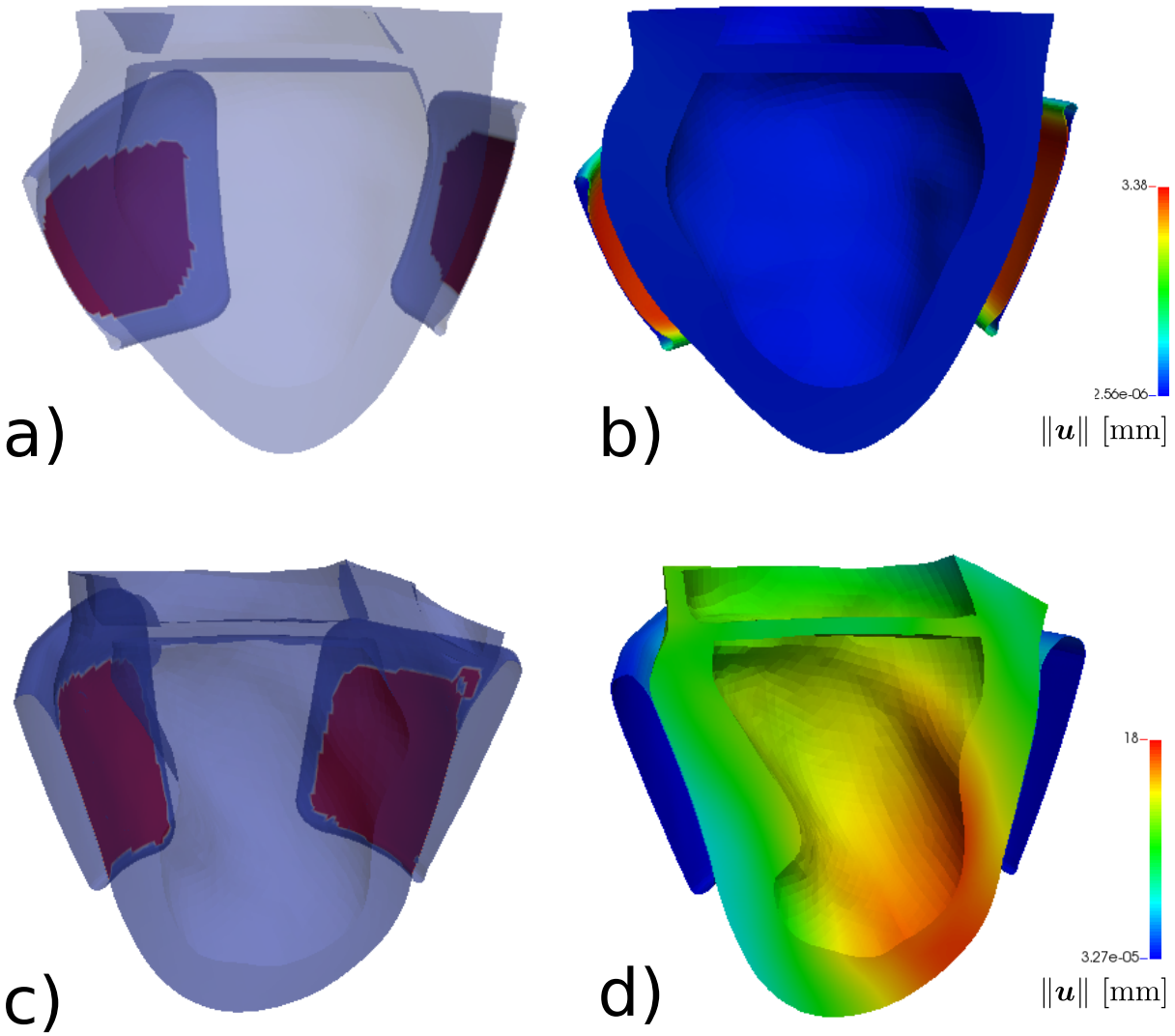

Figure 3.21.: Exemplary snap-shots of contact conditions: Active contact elements at the end of the deflation period of two EUs around the left ventricle are colored in red in the sagittal cut view a) while the rest is semi-transparent. The displacement of the same view is shown in b). The figure c) visualizes active contact elements at the end of the inflation process, when contact between heart and the EUs is established. The corresponding displacement is depicted in d).

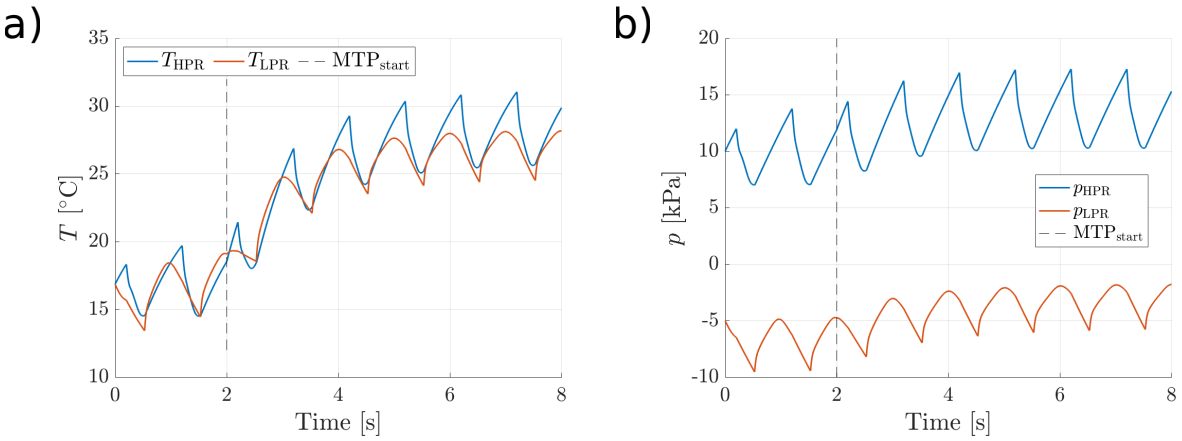

Figure 3.22.: Exemplary results for the reservoir temperature evolution, as result of the mean temperature prediction by the MTP model in a). Its effects on the reservoir pressures are depicted in b). In this example, the MTP model is executed initially after cycle two ($t = 2$ s) and for poor initial temperature guesses for better presentability. Normally, it is executed after every cycle, including the first one.

MTP The effects of the MTP reservoir temperature prediction are visualized in figure 3.22. HPR and LPR temperatures are plotted in a), where the MTP model was added after the second supported heart beat. Normally it is executed after each cycle, including the first. A small kink in both temperature curves marks this event, followed by a subsequent temperature rise of roughly 10 °C. The initial temperatures were knowingly reduced in order to show the adaptation process. Its influence on the corresponding reservoir pressures can be found in b).

3.6. Discussion

A mixed-dimensional multi-physics model of a novel BiVAD is proposed and coupled to an equally mixed-dimensional CVS model. The resulting system allows for analyzing the biological and technical behavior as well as their reciprocal interaction. The BiVAD components and their control as well as the heart geometry and the medical conditions can specifically be tuned to mimic the actual BiVAD on a real patient. This allows its usage in the context of BiVAD design and patient treatment planning. To date, no other combined model with BiVAD-supported specific CVS was presented, with the BiVAD being a 0D yet fully functional, stand-alone system. It allows for the computation of all essential physical signals that are needed to answer engineering questions, especially those, which cannot easily be obtained in bench testing, as e.g. dynamic temperature or flow measurements. Temperature sensors are relatively thermally inert, due to their casing and mass. Both need to be heated first before reliable temperatures can be measured. Time constants of fast, affordable and small temperature sensors are usually greater than 0.5 s. Hence, fast temperature changes < 1 s are not easily measured. Flow signals can be measured more dynamically, however, the flow sensors need to be placed in series, thereby changing the system and introducing inaccuracies. The BiVAD model can further be attached to the MTP model and thereby run at heated temperatures as they are established only after long pe-

riods of operation. The MTP model is in addition a valuable tool to meet normative requirements, as medical devices of that kind are required to not exceed certain temperature limits. Also, many of the electrical and mechanical components of the BiVAD are specified for specific temperature ranges, which need to be complied with. A major advantage of the presented BiVAD model over others with rather generic CVS support is the interchangeability of the single components. Their individual submodels can be adapted in order to test for new or re-worked parts. Eventually, the support outcome is the result of the component interaction and some boundary conditions.

Figures 3.16 to 3.22 present exemplary results of the BiVAD and coupled SCVS model. They are discussed in the following.

Reservoir and pump The reservoir related signals of one supported heart beat can be found in figure 3.16. Pressures and temperatures are plotted in a). The HPR pressure p_{HPR} rises between the end of the previous heart beat $t_{\text{ec},z-1}$ and the end-diastolic time point $t_{\text{ed},z}$ due to the pump inflow g_{PP}. Connected inlet valves are opened at $t_{\text{ed},z}$, connecting HPR and EUs and resulting in a pressure drop due to air flow through the inlet valves. Roughly two slopes can be observed in this example, which stem from the two inflation valve openings $y_{\text{inlet,1}}$ and $y_{\text{inlet,2}}$. Note, that the pressure may already increase before $t_{\text{es},z}$ when $g_{\text{PP}} > \sum g_{\text{V,in}}$, which depends on the boundary conditions. The inlet valve flow eventually increases implant pressures, represented in a) by p^1_{V} and p^1_{EU}, which decreases the pressure difference over the valve and consequently reduces the valve flow. Inlet valves are closed after $t_{\text{es},z}$ and the HPR is recharged such that $p_{\text{HPR}}(t{=}t_{\text{ec},z}) = p_{\text{HPR}}(t{=}t_{\text{ec},z-1})$. The HPR temperature T_{HPR} qualitatively follows the HPR pressure. The LPR pressure p_{LPR} decreases between $t_{\text{ec},z-1}$ and the end-diastolic time point $t_{\text{ed},z}$ together with the implant pressures since open outflow valves connect EUs and LPR and the pump permanently sucks air. Outlet valves are closed between $t_{\text{ed},z}$ and $t_{\text{es},z}$, i.e. during the systole and inflation period. When they are re-opened at $t_{\text{es},z}$, the LPR pressure rises rapidly until it equalizes with the implant pressures. LPR temperature T_{LPR} qualitatively follows p_{LPR}. The LPR signal bulges at $t_{\text{ed},z}$ are caused by a very short period, where inlet valves are opening and outlet valves are not yet fully closed, resulting in a waste flow from HPR to LPR. This flow can directly be observed in figure 3.17 b). The pump flow, depicted in figure 3.16 b), is mainly governed by the control value y_{PP} and the pressure difference over the pump, hence $\Delta p_{\text{Res}} = p_{\text{HPR}} - p_{\text{LPR}}$. While variations of y_{PP} shift the entire flow curve up or down, its form directly relates to that pressure difference. The smaller Δp_{Res}, the more flow can be generated and vice versa. In this example, generated flows vary by roughly 10 % within one heart beat.

Valves and valve control Valve related signals are depicted in figure 3.17. The valve openings and hence their flow coefficients $kv^1_{\text{in,out}}$ are shown together with the resulting flows in b). The outlet valve is open in $t_{\text{ec},z-1} < t < t_{\text{ed},z}$ and $t_{\text{es},z} < t < t_{\text{ec},z}$. Initially, only small flows through the outlet valves prevail, since the LPR and implant pressures are equilibrated. At $t_{\text{ed},z}$, inlet valves are opened and outlet valves are closed. However, due to their inertance, the process takes about 20 ms. In addition, the outlet valves are subject to hysteresis, prolonging the closing process. As a result, inlet and outlet valves are both open for a short period of time, resulting in a waste flow from HPR to LPR, visible in figure 3.17 b)(*). A similar effect can be observed at $t_{\text{es},z}$, where the implant pressure decrease provokes an extra inlet flow due to a not yet fully

closed inlet valve. The corresponding control signals can be seen in a). The inflation phase in $t_{\text{ed},z} < t < t_{\text{es},z}$ is governed by two control signals $y_{\text{inlet},1}$, $y_{\text{inlet},2}$ and consequently by two flow coefficients during this stage. However, due to hysteresis, the second control value $y_{\text{inlet},2}$ does not directly translate to a kv-value. In this example, the two control values $y_{\text{inlet},1} = 0.6$ and $y_{\text{inlet},2} = 0.2$ result in

$$kv^1_{\text{V},1} = kv_{\text{max}} \cdot y^1_{\text{inlet},1} = 3.1 \cdot 0.6 = 1.86\ \text{mm}^2,$$
$$kv^1_{\text{V},2} = kv_{\text{max}} \cdot \left(y^1_{\text{inlet},2} + H_{\text{V}} \cdot y^1_{\text{V,in,max,z}}\right) = 3.1 \cdot (0.2 + 0.043 \cdot 1.86) = 0.7\ \text{mm}^2.$$

The relation between control value and flow coefficient is plotted in c). Due to a difference in the maximum control values during inflation and deflation, $\max\{y^1_{\text{inlet},1}, y^1_{\text{inlet},2}\}$ and y^1_{outlet}, the hysteretic flow coefficients differ, because they depend on the maximum control value. Here, the gap between the two signal legs is smaller during deflation (violet dashed line) than during inflation (blue solid line).

Tubes and connector The tube and connector related pressures, temperatures and flows are depicted in 3.18. Pressures and temperatures are both plotted in a). Here, the pressures mutually follow the LPR pressure before the inflation starts at $t_{\text{ed},z}$. The pressure p^1_{V}, assigned to the location after the valve and before the tube, rises with the steepest slope and to the highest value, followed by the mid-tube and end-tube pressures p^1_{T} and p^1_{EU}, respectively. Their differences result from the pressure drops caused by connector and tube segments. The pressure loss over the first segment $p^1_{\text{V}} - p^1_{\text{T}}$ (connector and half tube) is distinctly greater than the one over the second segment $p^1_{\text{T}} - p^1_{\text{EU}}$ (second half tube). Hence, the connector exerts greater influence than the tube itself. The pressure head losses directly relate to the respective flows, which are depicted in b). Moreover, pressure oscillations diminish continuously along the observed line. Peaks appearing in p^1_{V} are reduced in p^1_{T} and have vanished in p^1_{EU}. It can further be observed, that the modeled gas inertance and the tube compliance provoke a signal delay along the streamline. The close-up in a) (*) allows for better distinction and shows, that p^1_{V} and p^1_{EU} are increasingly delayed, respectively. The same signal lag can be observed at $t_{\text{es},z}$. The temperature at the tube end T^1_{TE} is equal to T^1_{EU} during deflation. It differs only during systole, since temperature calculation in the model for T^k_{V} and T^k_{TE} is dependent on the flow direction, cf. with equations (3.25) and (3.45). Furthermore, T^k_{T} is simply modeled as the mean value between T^k_{V} and T^k_{TE}, cf. with equation (3.46). The latter explains, why pressure drops and temperature drops in a) (*) are disproportional. However, this does not effect the more interesting signals T^k_{V} and T^k_{TE}. The switch between inflation and deflation at $t_{\text{es},z}$ causes the mutual temperature spike, since T^1_{TE} is suddenly equal to T^1_{EU}. Since the EU temperatures T^k_{EU} trend towards the environmental body temperature $T_{\text{body}} = 36.85\ °\text{C}$, the tube end temperature T^k_{TE} follow this balancing process during diastole and consequently T^k_{T} and T^k_{V} likewise, but with pressure drop caused offsets. Flows passing through the connector and tube model are plotted in b). Inlet and outlet valve flows, $g^1_{\text{V,in}}$ and $g^1_{\text{V,out}}$, are defined to be positive when they leave the HPR and enter the LPR, respectively. In contrast, g^1_{EU} can also adopt negative values. Flow oscillations are reversed along the streamline as compared to the pressure signals: g^1_{EU} forms more ripples than $g^1_{\text{V,in}}$ or $g^1_{\text{V,out}}$. This observation can be explained by the fact, that the gas inertance directly contributes to the pressure loss (cf. equation (3.35)), while the flows relate to each other over the compliant tube volume (cf. equation (3.44)). Valve flows in this

example adopt values of more than three times the pump flow. Finally, the Reynolds number is plotted in b). It is the flow pattern determining signal of the corresponding pressure drop model. It can be seen, that it passes laminar, transition and turbulent value ranges ($Re_{\text{crit, connector}} = 700$, $Re_{\text{crit, tube}} = 2900$) and hence the full model functionality is tested here.

EU and CVS coupling Exemplary pressure and temperature development within one EU as well as its boundary air flow are plotted in figure 3.19 a). The EU pressure p^1_{EU} is initially at decreasing LPR level, before it detaches and rises with the beginning of the systole at $t_{\text{ed},z}$. During the first inflation phase, governed by a larger valve control value $y^1_{\text{inlet},1}$, pressure builds up rapidly. A subsequent decline due to the myocardial contraction and the transition to $y^1_{\text{inlet},2}$ can be observed, prior to a further increase. The interplay between the timing of valve opening and heart contraction as well as the HPR-EU gauge pressure regulates the curve during the systole. These parameters can be altered to find an optimal curve for the intended support and the present CVS. With the beginning of the diastole, the deflation is started by opening the outlet valves and closing the inlet valves and the EU pressure drops steeply towards zero gauge pressure, which is the equilibrium point of the EU. The further curve approaches slowly to this equilibrium until the unloaded volume of the specific EU is reached. This point is indicated by a black dashed line in 3.19 a) and b). The moment is further accompanied by zero energy $W^1_{\text{EU,int}} = 0$ stored in the elastic material. The deflation proceeds until EU and LPR pressures are equalized. Since the LPR pressure decreases further, the EU volume decreases beyond its equilibrium point, causing increasing material strain with an ongoing internal energy increase until the end of the cycle. The EU temperature is subject to heat transfer over its boundaries with the surrounding tissue, which is at body temperature $T_{\text{body}} = 36.85\ °\text{C}$. Whenever inflow and outflow are low, heat exchange dominates and the temperature trends towards T_{body}, as it is the case prior to $t_{\text{ed},z}$ and again at the end of the heart cycle. For high flow rates however, it is superimposed by material bound heat inflow and pressure driven alterations. The former is especially observable right after $t_{\text{ed},z}$: Air from the HPR expands from high HPR pressures to initially low EU pressures, driving the concurrent temperature decrease of the incoming air according to (2.19). Additionally, volume change, pressure development and the stored energy in the material elasticity contribute to the temperature development as modeled in (3.58). The temperature peak at the inflation beginning is caused by a delayed volume increase with respect to the flow and pressure signals. Hence, initially incoming air rapidly increases pressure and consequently the temperature, until the volume increase becomes notable.

The volume lags the pressure during inflation and deflation. The differing pV relation during both phases results in a closed pV curve with non-zero area and constitutes the EU work done on its environment. The resulting pV curve of both, EU and heart, are plotted in figure 3.20 a). Here, pV^{ℓ}_{v} and pV^{r}_{v} depict left and right pV curves, while pV^1_{EU} represents the pV loop of EU^1, located at the anterior LV wall. This graph shows the significant difference in done work: For the ventricles it sums to 0.923 J whereas the three EUs combined reach 0.084 J. In figure 3.20 b), the pressure and volume information of LV and EU^1 is plotted over time, allowing one to draw further conclusions concerning the reciprocal interaction. The shape of the EU pressure curve is directly influenced by the heart contraction. The dotted line (*) indicates the opening point of

the aortic valve, which represents the beginning of the blood ejection phase with concomitant heart volume reduction. This process provokes a kink in the EU pressure signal at the same time instant. The second dotted line (**) signals the start of the minor second valve control value $y^1_{\text{inlet},2}$. However, it is primarily the sudden cardiac ejection phase that causes the pressure level to drop. This observation can be confirmed when the EU volume signal V^1_{EU} is analyzed, which increases continuously until the end of systole. Only an attenuation of its rate of change due to the reduction in valve opening to $y^1_{\text{inlet},2}$ is notable as a slight kink. The pressure further declines until the blood ejection rate of the LV slows down, which manifests as a flattening volume curve $V^\ell_{\text{v,CVS}}$. Thereafter, the EU pressure rises again until the end of the systole $t_{\text{es},z}$. It can further be observed, that the depressurization of the EUs takes less time than the isovolumetric relaxation phase of the heart. It is the period between $t_{\text{es},z}$ and the reincrease of ventricular volume V^ℓ_{v}. It can also be seen, that the aortic valve opening is about 10 ms earlier with BiVAD support $(\bullet)_{\text{S}}$ than without $(\bullet)_0$. Likewise, the heart filling phase starts about the same time earlier. The comparison in b) further reveals, that the end-systolic volume is a little decreased, while the LV pressure remains unaltered. The blood ejection rate, which is the slope of V^ℓ_{v} after $t_{\text{ed},z}$, is slightly higher under support. The cardiac stroke volume increase due to BiVAD support is small in this example. More investigations on reciprocal interaction of BiVAD and CVS are carried out in chapter 6.

A more visually obvious presentation is given in figure 3.21 a) and b) for an end-diastolic time point as well as in c) and d) during inflation. They represent sectional views onto the LV with EU^1 and EU^2, placed on its anterior and posterior wall, respectively. The left graphs a) and c) depict the active contact elements in red, while the right graphs b) and d) visualize the displacement field $\boldsymbol{u}$. In b), the displacement is relatively large on the EUs front walls in a deflated state compared to the heart. The opposite is true in an inflated state. The transition from the deflated state, with the EU front and back wall in contact, to the EU exerting force onto the heart surface is characterized by snap-trough phenomena. They demand small time step sizes ($\leq$ 2 ms) and advanced techniques to prevent non-convergence of the Newton-type solution process as described in (3.118). The fully-coupled system is solved monolithically as stated in section 3.3.4. The strategy results in a reduced number of needed system solves and may reduce computational cost. However, it requires a global strategy and the solution process cannot be tailored to the specific subsystems at hand.

MTP model The MTP model was introduced to allow simulations of one or several supported heart beats at realistic drive unit temperatures. Their consideration is essential for many engineering problems of the BiVAD, as e.g normative requirements and component specification compliance. The presented model is a simple yet effective way to predict long term heating effects based on the electrical power consumption of the device minus the pV work leaving the system. Since transient terms are not considered, it exclusively allows the computation of a steady state excess temperature, given an unaltered system until then. On one hand, the system changes from heart beat to heart beat prior to an established periodicity, causing the MTP predictions to be outdated. On the other hand, the computation of the desired SCVS periodic state requires the simulation of several subsequent supported heart beats anyway. Therefore, the repeated, serial

execution of SCVS and MTP model, with mutual exchange of updated solutions, introduces an efficient combination. Moreover, good initial temperature guesses reduce the number of needed MTP executions. The detailed combination strategy is presented in chapter 6. The given example in figure 3.22 a) shows the development of HPR and LPR pressures over eight consecutive supported heart beats, with the MTP model being executed after cycle two for the first time (indicated by $\text{MTP}_{\text{start}}$ in the graph). Here, the initial temperatures were intentionally guessed poorly (about 10 °C too low), causing a strong SCVS model response after the first mean temperature update at $t = 2$ s. This point is characterized by kinks in the respective signals, which is not the case during the following cycles. The solution increment, namely the temperature difference from the current solution to the last, diminishes rapidly after the initial mean temperature predication. With unaltered MTP parameters, this increment typically vanishes after two to three cycles. The influence of MTP predictions on the BiVAD pressure signals is depicted in 3.22 b). Mainly HPR and LPR pressure are affected and their signals are shifted towards higher values, which conforms with the ideal gas law (2.3).

3.7. Limitations

A model is a simplified representation of reality. Its usefulness depends on the intended purpose and the quality of the model. The latter can be assessed in a validation, which is carried out in chapter 4 of the present work. However, many aspects of the real BiVAD as applied to a patient are explicitly not incorporated into the presented models. Besides the assumptions stated in 3.1.1, the presented model is subject to the following limitations:

- The flow coefficient kv is flow dependent, as jet and other restrictive effects depend upon the fluid velocity and its flow regime. This dependency has been considered in the tube model, where the friction factor is a function of the flow driven Reynolds number, but it is not modeled for the variable valve restriction. For larger flow ranges, as they may occur at extreme conditions in the BiVAD or in other applications, ignoring this dependency may lead to increasing erroneous results. The accuracy for the prevailing conditions is assessed in the validation chapter 4.

- Pressure drops caused by inflow into the EU are not modeled. First of all, the physical adapter connecting tube and EU is a flow resistance and causes losses. It could be included into the model by determining an additional loss coefficient ζ, as it was done for the connector. However, the effect is small compared to valve, connector and tube resistances. A second phenomenon, which is not modeled, is a significant pressure head loss due to the initial flow against the deflated EU wall. It is only relevant until the wall has been moved away from the EU inlet.

- The presented control strategy is able to fully mimic the BiVAD behavior at a particular working point, however, proactive control of EU pressures as a combined reaction of pump speed and valve openings to the previously generated pressures is not realized. Hence, pump speed or valve opening curves are not adapted from one supported heart beat to another. It would require an external control model, similar to the MTP model.

- Owing to the 0D character of the BiVAD model, information about thermodynamic states is only available at the network nodal points, shown in figure 3.2. They are further assumed to be homogeneously distributed within the related volume or section, as stated in 3.1.1. Especially engineering questions regarding the temperature distribution within the drive unit cannot be answered accurately with the network approach. The assumption of homogeneous temperatures within each reservoir may be sufficient to assess the global BiVAD behavior regarding heart support, but constitutes a strong simplification. The temperature field changes continuously in each direction with distance from each of the major electrical consumer loads to the BiVAD casing and only their mean values are estimated by the introduced MTP model. In contrast, the assumption of a homogeneous pressure distribution within the reservoirs holds very well.
- The implant design may be subject to ongoing research, resulting in changes in size, form and composition and hence in a differing mechanical response. In order to obtain meaningful results, the model should be updated to its physical counterpart. This is particular of importance if solid mechanical solutions are analyzed. Within this work, the implant model introduced by Hirschvogel [43] was only expanded by considering contact between the inner EU front and back walls to allow the EUs to completely deflate. The real implant's EUs are placed on a shell-like structure, which covers the ventricles of the patient's heart, as it can be seen in the picture in figure 3.1. This shell was replaced by suitable Robin boundary conditions in [43] to hold the EUs in space[5]. This reduced set-up was likewise used in this work. However, the spring-dashpot conditions of both EUs and heart, represent a general simplification. They are identical for all patients in a supposed patient-specific model.
- The coupled CVS model does not include regulations of the body as response to external events, as e.g. adaptations of the heart rate, systemic vessel resistances or other more complex physiological reactions. Hence, these long term adjustments of the body as a complex control unit are not considered and the results of the SCVS have to be understood as the body's short term response.

3.8. Summary

In this chapter, two 0D models were presented, namely the biventricular assist device (BiVAD) and the mean temperature prediction (MTP) model. The former allows for the computation of pressure and temperature developments at distinct points of the BiVAD as well as resulting flows in between. The component submodels combine physical fundamentals with empirically derived parameters and can be adapted in case of a component exchange or drive unit re-design. The electrical components cause the system to slowly warm up and the MTP model was introduced to obtain reasonable estimations of the heated drive unit state, such that the inflation and deflation occur at meaningful temperatures. Ambient pressure and temperature can easily be adapted.

[5] Hirschvogel have introduced both model versions: A solid mechanical model of the shell, which itself is hold in space by spring-dashpot boundary conditions and the mentioned reduced model, where shell and its Robin boundary conditions are replaced by a different set of Robin boundary conditions.

MTP and BiVAD model can be used independently or in coupled fashion, depending of the questions to be answered. The BiVAD is further coupled to a 3D representation of the implant, which provides volume information of the EUs, as a response to the currently prevailing EU pressure. The implant is placed around a 3D, patient-specific heart, which again is coupled to a 0D and patient-specific circulatory system, completing the SCVS model. Contact is enforced between EUs and heart to allow for cardiac support, but also between the EU front and back wall to allow for physically representative and complete deflation. A monolithic solution strategy for the fully coupled problem was introduced and a convergence study performed. Furthermore, exemplary results were given to indicate the potential of the combined model. A validation and sensitivity analysis of BiVAD and MTP model is given in the subsequent chapters 4 and 5, respectively. Additionally, the SCVS model is applied to various patients, HF conditions and diseases in chapter 6.

4. Validation

The validation of the BiVAD model is performed stepwise for all submodels, while heart and circulatory models are decoupled to avoid any influences thereof. The general procedure is to measure the response of the submodel's principle quantity to a reproducable input signal. The same set up with identical input signal is then simulated and the responses are qualitatively and quantitatively compared. The MTP model is separately validated by estimating undetermined parameters in an optimization problem. Figure 4.1 shows the experimental settings for the validation of the reservoirs and the pump in a), valve in b), EU model in c) and tube and connector in d). The equipment used is detailed in appendix A.I.4. Herein after, a pressure sensor is referred to as PS, a temperature and flow sensor as TS and FS, respectively, followed by a roman numeral. Except for the MTP model validation, the sampling rate of any measured signal was 250 Hz. Ambient conditions were measured using pressure and temperature sensors of type PS-II and TS-II, respectively.

4.1. Methods

Most of the submodels predict a pressure or flow curve, which is eventually compared to experimental data. The data is plotted to allow visual assessment of the model quality. However, a quantitative error measure is also derived in order to allow for direct comparison and to assess improvements. Therefore, the mean unsigned absolute and the relative error measures, $\hat{\mathrm{E}}$ and $\hat{\mathrm{e}}$, of a signal $\tilde{\mathrm{S}}$ are deduced from experimental and simulated data sets according to

$$\hat{\mathrm{E}}(\tilde{\mathrm{S}}) = \frac{1}{\Delta t}\int_{t_{\text{start}}}^{t_{\text{end}}} |\mathrm{E}(\tilde{\mathrm{S}},t)|\,\mathrm{d}t \quad \text{with} \tag{4.1}$$

$$\mathrm{E}(\tilde{\mathrm{S}},t) = \tilde{\mathrm{S}}_{\text{exp}}(t) - \tilde{\mathrm{S}}_{\text{sim}}(t) \quad \text{and} \tag{4.2}$$

$$\hat{\mathrm{e}}(\tilde{\mathrm{S}}) = \frac{1}{\Delta t}\int_{t_{\text{start}}}^{t_{\text{end}}} |\mathrm{e}(\tilde{\mathrm{S}},t)|\,\mathrm{d}t \quad \text{with} \tag{4.3}$$

$$\mathrm{e}(\tilde{\mathrm{S}},t) = \frac{\tilde{\mathrm{S}}_{\text{exp}}(t) - \tilde{\mathrm{S}}_{\text{sim}}(t)}{\tilde{\mathrm{S}}_{\text{exp}}(t)}. \tag{4.4}$$

Here, $\hat{\mathrm{E}}(\tilde{\mathrm{S}})$ and $\hat{\mathrm{e}}(\tilde{\mathrm{S}})$ are scalar values and $\Delta t = t_{\text{end}} - t_{\text{start}}$. The absolute values in both, equation (4.1) and (4.3), are utilized to avoid error canceling effects due to the error sign. However, sign information can be extracted from the corresponding graphs.

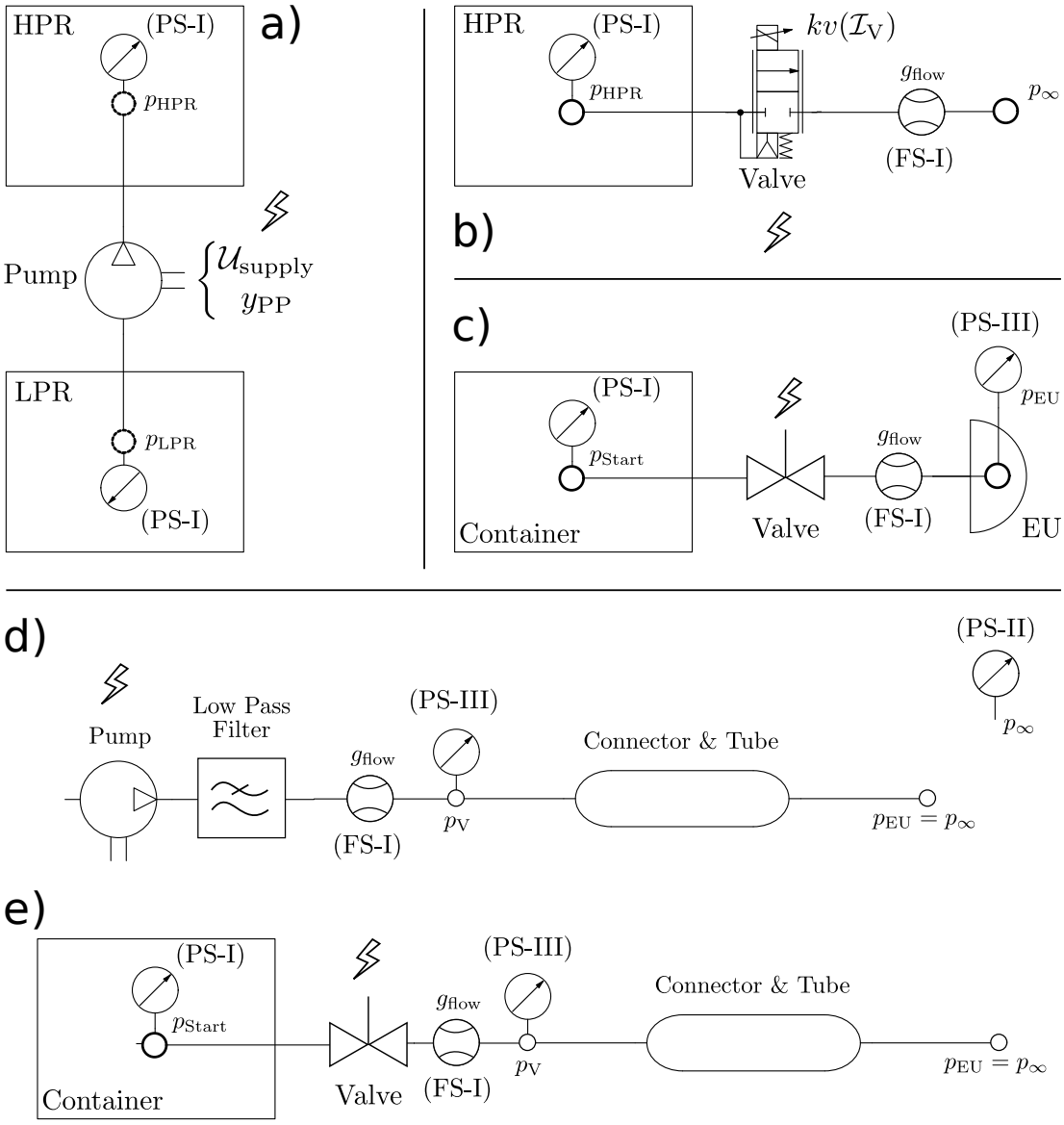

Figure 4.1.: Experimental settings for reservoir and pump in a), reservoir and valve in b) and EU model in c). For tube and connector, two setups are used: Steady state flows with the setup shown in d) and dynamic flows with the setting depicted in e).

4.1.1. Reservoirs and pump

To assess the quality of the reservoir and pump models, a combined validation was performed, comparing simulation to experimental data. The experimental set up is shown in figure 4.1 a) and represents the two reservoirs with pump of the drive unit. The pump can be supplied by the supply voltage $\mathcal{U}_{\text{supply}}$ and the control voltage $y_{\text{PP}} \in [0, 1]$. The pump was started at zero load, thus with zero gauge pressure in the reservoirs, and ran for 12 seconds. Pressure was measured in the reservoirs using pressure sensors of type PS-I. The pressure evolution was compared to simulated data, with the exact same input, namely ambient conditions ($T_\infty <= 25.0$ °C, $p_\infty = 958.5$ hPa), supply voltages $\mathcal{U}_{\text{supply}} \in \{12, 15, 17\}$ V and control signals $y_{\text{PP}} \in \{0.3, 0.6, 1.0\}$ and time. For each combination of supply voltage and control signal, two experimental runs were carried out with different drive units. In addition, the polytropic exponent was chosen to be $n \in \{1.0, 1.4\}$ in the simulations, corresponding to an isothermal and an isentropic process. The error between the pressure predictions and measurements are computed according to (4.1) and (4.3), with Δt being the total time period of 12 s. Results are given in 4.2.1.

4.1.2. Reservoirs and valve

The validation of the presented model was performed as depicted in figure 4.1 b), with an initially charged reservoir at ambient temperature. The valve was then energized and the pressure drop in the HPR due to outflow of air through the valve was measured with sensor type PS-I as well as the mass flow rate using FS-I. Both signals were used as reference signals for validation. The kv-values in the simulation were set according to the applied current in the experiment and the $kv(\mathcal{I}_{\text{V}})$ relation plotted in figure 3.6. Three different initial pressures, $p_{\text{HPR}}(t{=}t_0) \in \{10, 15, 30\}$ kPa and four different currents, $\mathcal{I}_{\text{V}} \in \{0.2, 0.14, 0.12, 0.09\}$ A, were selected for the tests. The currents were set by the laboratory power supply (LPS-I) and verified by a digital multimeter (DMM-I) previously to each individual run. Each configuration was run with two different drive units, resulting in a total of 24 runs. Again, isothermal and isentropic exponents were tested. The mean deviation of each run was determined using (4.1) and (4.3), with $t_{\text{start}} = 0$ s and t_{end} dependent on the time needed for the equalization of pressures. Therefore, the threshold values of $\Delta p_{\text{HPR}} = 0.2$ kPa HPR gauge pressure and $g_{\text{V,in}} = 0.01 \frac{\text{mg}}{\text{ms}}$ valve flow where chosen to define t_{end}.

4.1.3. Tubes and connector

The validation confirms the model pressure response to steady and transient flow input and compares the results with experimental data. The steady flow comparison distinguishes pure tube and tube-connector analysis. For both, a pump was connected in series with a pneumatic low pass filter to cancel out pressure oscillations due to single pump strokes. The set-up can be seen in figure 4.1 d). The pump generated four different flows for at least 20 s and the pressure drop along the test specimen was measured using PS-III. Three different tube lengths were tested, namely 0.6, 0.9 and 1.3 m, all with a diameter of 3 mm. All lengths were tested as a tube only and in combination with the attached connector. Results can be found in figure 4.7. To numerically assess the quality of the model response to steady flow input, the pressure drops at every

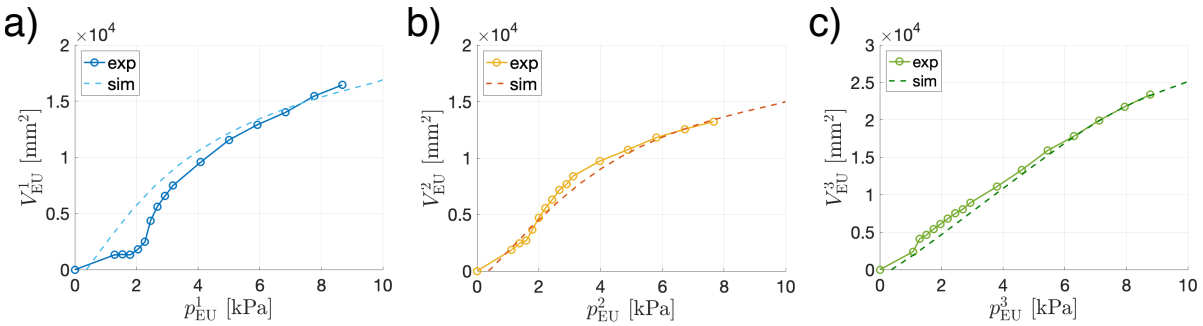

Figure 4.2.: Best match between of the pressure-volume curves of available digital and physical implants.

flow plateau where averaged and compared to the corresponding prediction of the simulation. Hence, the errors are signed. However, averaged values are unsigned in the appertaining tables for tube-connector and tube-only results 4.5. To test for the dynamic characteristics, i.e. the gas inertance stemming from equation (3.35) and the tube compliance and air compressibility in equation (3.44), the response to transient flow input was analyzed, as sketched in figure 4.1 e). A charged container with initial pressures $p(t{=}t_0) \in \{10, 15, 30\}$ kPa was connected to a flow sensor FS-I and the tube-connector specimen. The air was suddenly released by opening a valve. The measured flow served as an input for the simulation and the recorded pressure drop PS-III was used as reference signal for comparison to simulation results. For each initial pressure, the experiment was run two times with different drive units. Again, unsigned absolute and relative errors are computed according to (4.1) and (4.3). Similar to the valve model validation, start and end times were defined to be the extreme time points where pressure data is greater than a threshold value of 0.2 kPa.

4.1.4. Expandable units

To assess the pressure evolution in the EUs, a physical implant with approximately the same pressure-volume characteristics as one of the digital models was identified by comparison of their pV curves, as shown in the graphs 4.2 a) to c) for EU^1 to EU^3, respectively. A charged container was directly connected to the EU to be tested and the air was released into the EU by opening a valve, as it is depicted in the schematic in figure 4.1 c). The flow was measured using sensor FS-I and used as input signal in the simulation. The valve opening was timed, such that an inflation at the heart rates $f_{\mathrm{Heart}} \in \{60, 90\}$ was mimicked. Also, the opening was different in the two runs. While in the run at $f_{\mathrm{Heart}} = 60$ min^{-1}, the valve opening was higher in EU^1 and equal in EU^2 and EU^3, it was the opposite in the run at $f_{\mathrm{Heart}} = 90$ min^{-1}. Here, the valve opening was larger in EU^3 and similar in EU^1 and EU^2. Experimental and simulated pressure curves are plotted in the result section 4.2.4 and are discussed in 4.3.

4.1.5. MTP model

Experimental data of the heating process was used to validate the MTP model. Therefore, the heat transfer parameters α_{HPR}, α_{LPR} and α_{∞}, as well as the reservoir housing thicknesses $\hat{d}_{\text{HPR}}$ and $\hat{d}_{\text{LPR}}$ were estimated based on experimental temperature measurements. The drive unit with the connected implant was placed into a controllable laboratory oven, which was used to set defined and constant ambient temperatures. Once the drive unit's internal temperature sensors reached these ambient values, the drive unit was started and distinct support levels were applied by the controller. Pressure within the implant's EUs was directly measured and allowed to exactly determine the actually achieved pV work (3.121) of each EU due to the knowledge of the individual pV curves. Valve and pump control signals as well as the temperatures at three different points (1x TS-I, 2x TS-II) within each reservoir were also recorded for 2.5 hours, before the drive unit was cooled down for the subsequent run. Two different ambient temperatures $T_{\infty} \in \{35, 40\}$ ° C and seven different support levels were set, resulting in a total of 11 runs. The exact combination of conditions can be found in table 4.1. All other MTP model parameter

Ambient temperature [° C]	Average pressure-volume work per EU [mJ]
35	47, 90, 96, 142
40	26, 43, 66, 92, 118, 129, 134

Table 4.1.: Conditions of experimental heating runs used to validate the MTP model.

were set according to table 3.6. The cycle time was set to $\Delta t_{\text{cylce}} = 0.667$ s, representing a heart rate of 90 bpm. The pneumatic power was computed from the values in 4.1, divided by that cycle time. As inputs for pump and valve power equations (3.71)-(3.75), the averaged pump and valve control signals of the experimental runs were utilized. The model parameter vector to be estimated reads

$$\boldsymbol{\xi} = \begin{bmatrix} \alpha_{\infty} & \alpha_{\text{LPR}} & \hat{d}_{\text{LPR}} & \alpha_{\text{HPR}} & \hat{d}_{\text{HPR}} \end{bmatrix}^T. \tag{4.5}$$

The experimental data results in two reference vectors of size 11, $\tilde{\boldsymbol{T}}_{\text{HPR}}$ and $\tilde{\boldsymbol{T}}_{\text{LPR}}$, containing the steady state temperatures after 2.5 hours as the mean value of the three sensors in each reservoir

$$\tilde{\boldsymbol{T}}_{\text{Res}} = \begin{bmatrix} \Delta\tilde{T}^1_{\text{Res}} ... \Delta\tilde{T}^{11}_{\text{Res}} \end{bmatrix}^{\text{T}}, \tag{4.6}$$

with $\text{Res} \in \{\text{HPR, LPR}\}$. The resulting unconstrained optimization problem reads

$$\min_{\boldsymbol{\xi}} \|f(\boldsymbol{\xi})\|_2^2 = \min_{\boldsymbol{\xi}} \left((\hat{\boldsymbol{T}}_{\text{HPR}}(\boldsymbol{\xi}) - \tilde{\boldsymbol{T}}_{\text{HPR}})^2 + (\hat{\boldsymbol{T}}_{\text{LPR}}(\boldsymbol{\xi}) - \tilde{\boldsymbol{T}}_{\text{LPR}})^2 \right). \tag{4.7}$$

This nonlinear least squares problem is solved using the MATLAB function *lsqnonlin* with a *Trust region* algorithm, both part of the optimization toolbox (MATLAB, The MathWorks Inc., Natick, MA, USA).

4.2. Results

4.2.1. Reservoirs and pump

Figure 4.3 shows the comparison between experimental and simulation results for the two control voltages and polytropic exponents. Experimental data is marked with circles $y_{\text{PP}} = 1.0$ and diamonds $y_{\text{PP}} = 0.3$ in the graphs a) to c). The plots in d) to f) represent pressure curves for the control signal of $y_{\text{PP}} = 0.6$. The figure columns represent different supply voltages $\mathcal{U}_{\text{supply}} \in \{12, 15, 17\}$ V. Dotted lines represent polytropic exponents of $n = 1.4$ and non-dotted lines $n = 1.0$. Negative curves illustrate LPR pressure, while positive values represent pressure evolution in the HPR. Scalar pressure prediction errors are summarized for HPR and LPR in tables 4.2 and 4.3 respectively, each for isothermal $n_{\text{PP}} = 1.0$ and isentropic conditions $n_{\text{PP}} = 1.4$.

Parameter (n_{PP}=1.0)	$\hat{\text{E}}(p_{\text{HPR}})$ [kPa], ($\hat{\text{e}}(p_{\text{HPR}})$ [%])			Mean error [kPa,(%)]
y_{PP} [/] \ $\mathcal{U}_{\text{supply}}$ [V]	12	15	17	
0.3	3.76 (9.86)	0.94 (2.05)	0.75 (2.98)	1.82 (4.96)
0.6	5.81 (11.90)	2.93 (5.41)	2.64 (4.50)	3.79 (7.27)
1.0	1.82 (3.71)	1.53 (3.24)	1.06 (2.17)	1.47 (3.04)
Mean error [kPa,(%)]	3.80 (8.49)	1.80 (3.57)	1.48 (3.22)	2.36 (5.09)

Parameter (n_{PP}=1.4)	$\hat{\text{E}}(p_{\text{HPR}})$ [kPa], ($\hat{\text{e}}(p_{\text{HPR}})$ [%])			Mean error [kPa,(%)]
y_{PP} [/] \ $\mathcal{U}_{\text{supply}}$ [V]	12	15	17	
0.3	2.61 (6.96)	0.46 (1.59)	2.15 (6.63)	1.74 (5.06)
0.6	4.03 (8.46)	1.22 (2.13)	1.93 (3.67)	2.39 (4.75)
1.0	2.69 (6.05)	2.13 (5.06)	2.05 (4.43)	2.29 (5.18)
Mean error [kPa,(%)]	3.11 (7.16)	1.27 (2.93)	2.14 (5.00)	2.17 (5.01)

Table 4.2.: Reservoir and pump validation: Error of HPR pressure curve prediction relative to mean experimental pressure data for $n_{\text{PP}} = 1.0$ and $n_{\text{PP}} = 1.4$ in the upper and lower table, respectively and according to (4.1) and (4.3). Mean errors in the last rows and last columns summarize supply voltage and control signal results. The grayed boxes are the overall mean errors.

4.2.2. Reservoirs and valve

Results of the outflow runs can be seen in figure 4.4 as pressure drops within the reservoir and as flow curves in figure 4.5, both for the currents $\mathcal{I} \in \{0.2, 0.14, 0.12, 0.09\}$ A in a) to d), respectively. Isothermal conditions are plotted only for the highest and lowest pressure levels of the two extreme current conditions. An amplification of the flow predictions for low values

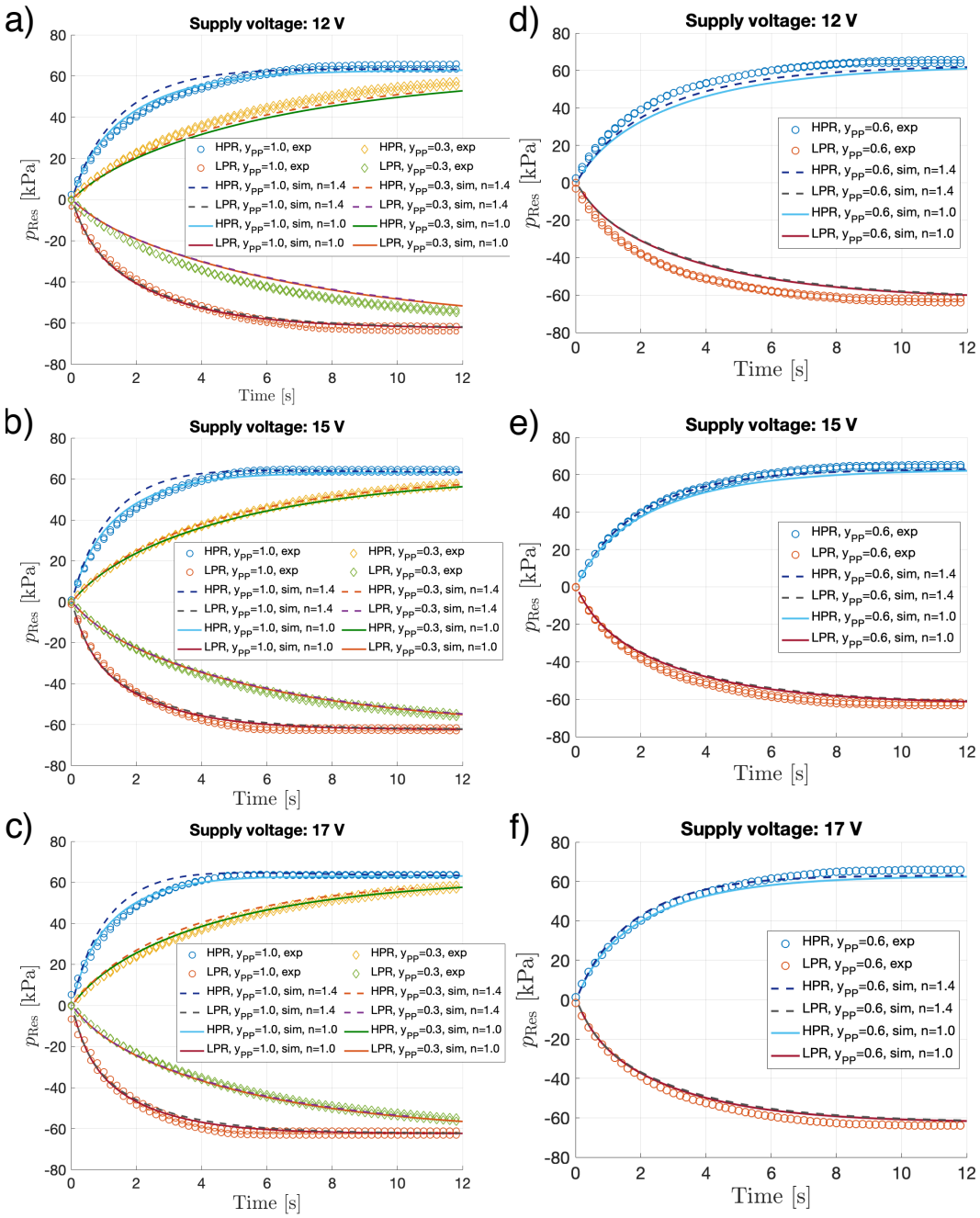

Figure 4.3.: Reservoir and pump validation: Comparison of experimental (lines with markers) and simulated data (no markers) to check the validity of reservoir and pump model. The three different supply voltages are represented by the columns and the rows show in a) to c) control signals of 100 % and 30 % duty cycle, from d) to f) control signals of 60 % duty cycle. Curves of the HPR are positive, while the LPR pressure evolution is negative. Simulation results for the a polytropic exponents of $n = 1.0$ are indicated as non-dashed lines, whereas those of $n = 1.4$ are dashed.

Parameter (n_{PP}=1.0)	$\hat{\text{E}}(p_{\text{LPR}})$ [kPa], ($\hat{\text{e}}(p_{\text{LPR}})$ [%])			Mean error [kPa,(%)]
$\mathcal{U}_{\text{supply}}$ [V] / y_{PP} [/]	12	15	17	
0.3	3.49 (9.82)	0.76 (1.89)	0.83 (2.81)	1.69 (4.84)
0.6	5.66 (12.21)	2.73 (5.44)	2.62 (4.99)	3.67 (7.55)
1.0	1.10 (2.26)	1.03 (2.23)	0.93 (1.74)	1.02 (2.08)
Mean error [kPa,(%)]	3.42 (8.10)	1.51 (3.19)	1.46 (3.18)	2.13 (4.82)

Parameter (n_{PP}=1.4)	$\hat{\text{E}}(p_{\text{LPR}})$ [kPa], ($\hat{\text{e}}(p_{\text{LPR}})$ [%])			Mean error [kPa,(%)]
$\mathcal{U}_{\text{supply}}$ [V] / y_{PP} [/]	12	15	17	
0.3	3.73 (10.40)	1.06 (2.59)	0.51 (2.02)	1.77 (5.00)
0.6	6.12 (13.03)	3.22 (6.39)	3.14 (5.97)	4.16 (8.46)
1.0	1.34 (2.55)	1.43 (2.83)	1.41 (2.53)	1.39 (2.64)
Mean error [kPa,(%)]	3.73 (8.66)	1.90 (3.94)	1.69 (3.51)	2.44 (5.37)

Table 4.3.: Reservoir and pump validation: Error of LPR pressure curve prediction to mean experimental pressure time data for $n_{\text{PP}} = 1.0$ and $n_{\text{PP}} = 1.4$ in the upper and lower table, respectively and according to (4.1) and (4.3). Mean errors in the last rows and last columns summarize supply voltage and control signal results. The grayed boxes are the overall mean relative errors.

is given in figure 4.6. Numerical results are summarized in the tables 4.4 for pressure and flow predictions.

4.2.3. Tubes and connector

The results for steady flow are shown in figure 4.7 a) for the combination of tube and connector and in b) for the tube only. In both graphs for tube lengths of 0.6, 0.9 and 1.3 m and a diameter of 3 mm. The Reynolds numbers are denoted for the distinct flow plateaus. The mutual dynamic responses of tube and connector model are depicted in figure 4.8, with a) showing the input flow signals, here of the 1.3 m tube, as deployed in the simulations. They arise during the equalization process when air from a previously charged container is suddenly released. Figures b), c) and d) show the pressure drop responses to those flow inputs. The two experimental runs, with different drive units, are plotted in the same colors and as lines with circles. Results of the simulations are shown as non-dashed or dashed lines. Absolute and relative deviations of the pressure drop predictions to averaged plateau pressures are computed, resulting in a signed scalar comparison. The values are listed in tables 4.5. Furthermore, the numerical results of the dynamic tube-connector response are summarized in table 4.6. Since a time varying signal is analyzed, equations (4.1) and (4.3) were utilized.

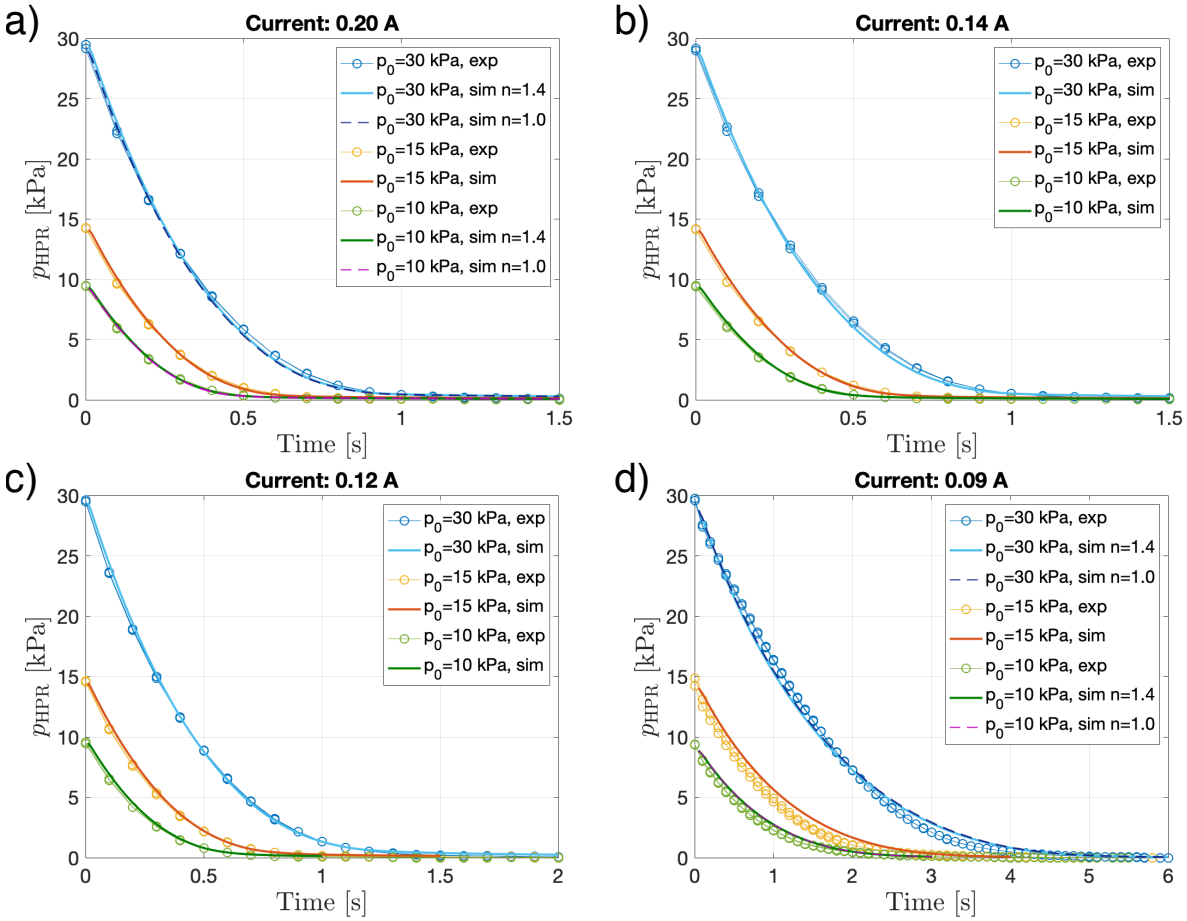

Figure 4.4.: Valve validation: Pressure drop in the HPR due to valve flow for initial pressures $p_{\mathrm{HPR}}(t{=}t_0) \in \{10, 15, 30\}$ kPa and valve currents $\mathcal{I} \in \{0.2, 0.14, 0.12, 0.09\}$ A in a) to d). Experimental data is drawn as lines with circles. For the lowest and highest currents, both isothermal and isentropic results are plotted, which are omitted in all other graphs to enhance legibility.

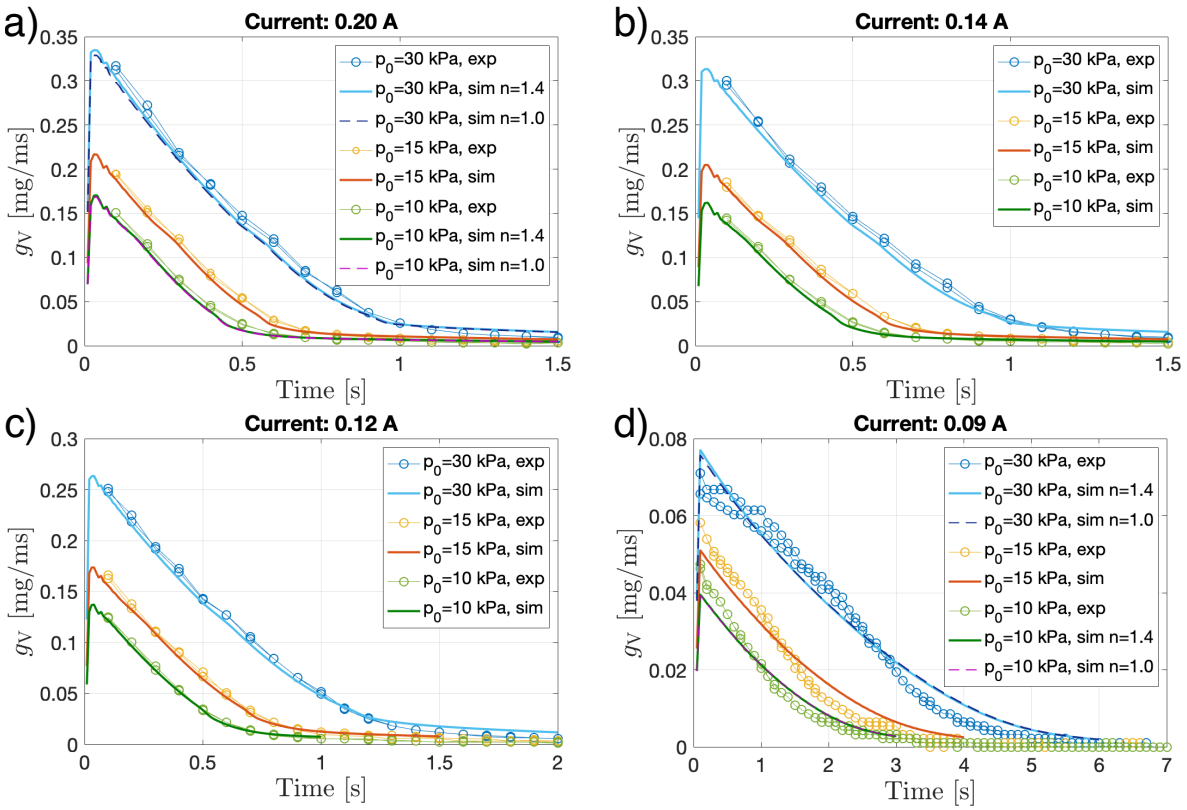

Figure 4.5.: Valve validation: Equalization flow through the valve for initial pressures $p_{\mathrm{HPR}}(t{=}t_0) \in \{10, 15, 30\}$ kPa and valve currents $\mathcal{I}_{\mathrm{V}} \in \{0.09, 0.12, 0.14, 0.2\}$ A. Experimental data is drawn as lines with circles. For the lowest and highest currents, both isothermal and isentropic results are plotted.

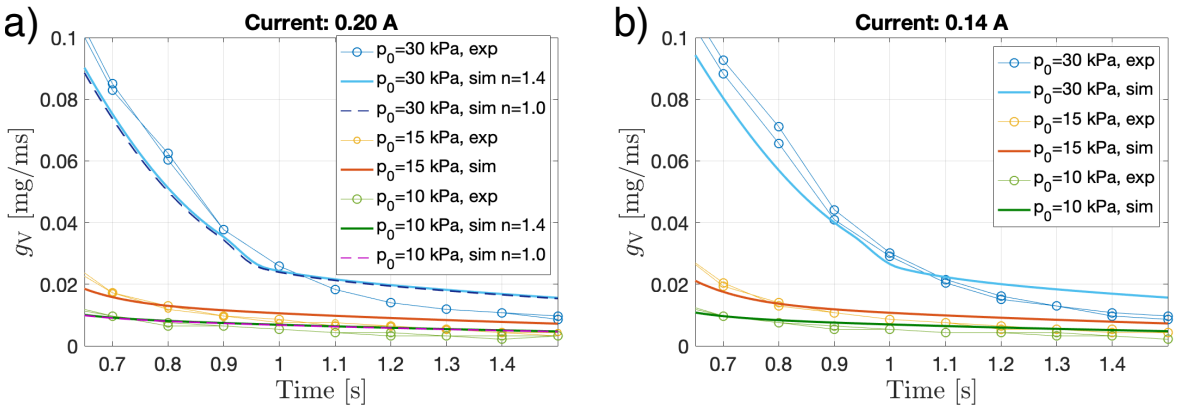

Figure 4.6.: Valve validation: Close ups of figure 4.5 a) and b) at the end of the equalization process.

Parameter	$\hat{\mathrm{E}}(p_{\mathrm{HPR}})$ [kPa], ($\hat{\mathrm{e}}(p_{\mathrm{HPR}})$ [%])			Mean error [kPa,(%)]
$\mathcal{I}_{\mathrm{V}}$ [A] \ $p_{\mathrm{HPR},0}$ [kPa]	10	15	30	
0.09	0.31 (15.52)	0.09 (5.17)	0.12 (6.36)	0.17 (9.02)
0.12	0.19 (8.20)	0.01 (0.55)	0.03 (1.77)	0.08 (3.51)
0.14	0.13 (5.02)	0.02 (0.71)	0.03 (2.02)	0.06 (2.58)
0.20	0.10 (5.22)	0.02 (0.77)	0.06 (3.11)	0.06 (3.03)
Mean error [kPa,(%)]	0.18 (8.49)	0.03 (1.80)	0.06 (3.31)	0.09 (4.53)

Parameter	$\hat{\mathrm{E}}(g_{\mathrm{V}})$ [$\frac{\mathrm{mg}}{\mathrm{ms}}$], ($\hat{\mathrm{e}}(g_{\mathrm{V}})$ [%])			Mean error [$\frac{\mathrm{mg}}{\mathrm{ms}}$, (%)]
$\mathcal{I}_{\mathrm{V}}$ [A] \ $p_{\mathrm{HPR},0}$ [kPa]	10	15	30	
0.09	0.0022 (11.87)	0.0003 (1.44)	0.0006 (2.21)	0.0010 (5.17)
0.12	0.0020 (4.04)	0.0002 (0.41)	0.0007 (1.68)	0.0010 (2.04)
0.14	0.0041 (9.65)	0.0005 (1.03)	0.0010 (2.17)	0.0019 (4.28)
0.20	0.0057 (12.81)	0.0006 (1.08)	0.0019 (4.39)	0.0034 (6.09)
Mean error [$\frac{\mathrm{mg}}{\mathrm{ms}}$, (%)]	0.0035 (9.59)	0.0004 (0.99)	0.0013 (2.61)	0.0018 (4.40)

Table 4.4.: Valve validation: Error of pressure and valve flow predictions in the upper and lower table, respectively, for $n_{\mathrm{V}} = 1.4$ and according to (4.1) and (4.3). Mean errors in the last rows and last columns summarize initial pressure and valve current results. The grayed boxes represent the overall mean error for the valve model.

4.2.4. Expandable units

The generated pressure curves in the EUs due to the applied flows are shown in figure 4.9. Experimental data is again plotted as lines with circles, whereas simulated pressure signals are represented as straight lines.

4.2.5. MTP model

The optimal parameter set as a result of the optimization problem (4.7) is listed in table 4.7. Subsequent forward simulations of all eleven experimental data sets where carried out. Figure 4.10 a) and b) show the computational solutions compared to experimental data for HPR and LPR, respectively. The absolute error is shown in c) for both reservoirs. The relative error in d) is calculated with respect to the temperature change and hence with respect to the ambient temperature in the laboratory oven T_{∞}.

The thus obtained absolute and relative error values for the predicted mean temperatures are listed in table 4.8. They are also used in the dynamic model in equation (3.8) for the respective reservoir.

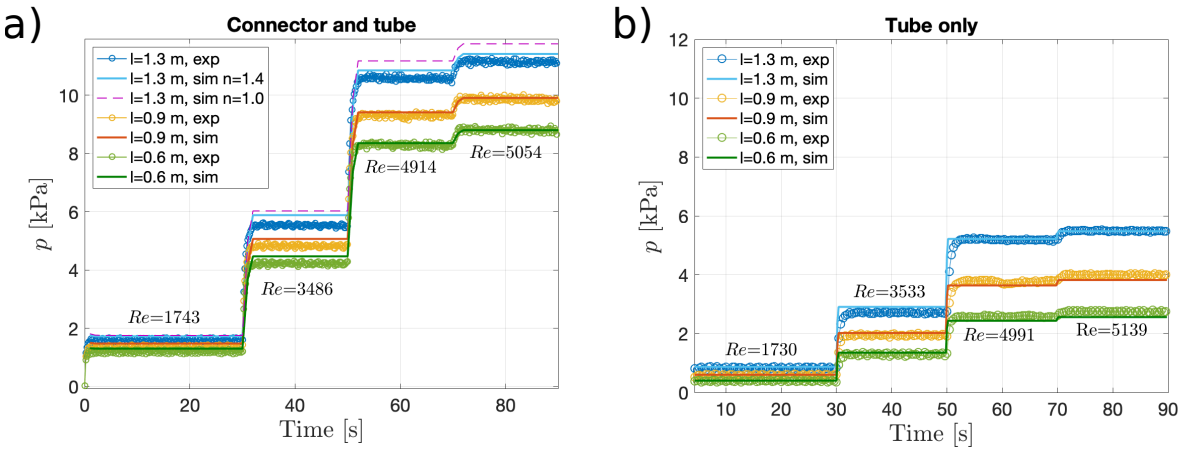

Figure 4.7.: Tube validation: Comparison between measurements and simulations for a) connector and tube in series and b) tube only at various Reynolds numbers. The stepwise increase of the tube flow rate at $t \in \{30, 50, 70\}$ s translates to a stepwise increase in pressure loss along the tube (and connector). This pressure loss is plotted in the graphs as gains in difference pressure.

4.3. Discussion

Air velocities up to roughly 110-120 m/s are generally treated as incompressible flows as the density changes range below 5 %. Confer with section 2.2.1.1 in chapter 2. Among all validation runs, the highest flow rate was measured with approximately 0.35 mg/ms, when air was suddenly released from the HPR through a fully opened valve (cf. figure 4.5 a)). The initial HPR pressure in this run of 30 kPa is among the higher typical reservoir pressures. Assuming a low air density of 1.1 kg/m^3, which favors high velocities, this flow rate can be converted to an average velocity through a tube of 3 mm diameter of $v \approx 45$ m/s according to (2.24). This is less than half of the stated threshold velocity and incompressible fluid behavior can consequently be assumed in this application.

Reservoir and pump model The simulated pressure curves are in good agreement with experimental data. Especially the end pressure difference, previously described as the zero flow point at maximum pressure load in figure 3.4, with its adaptability to a changing HPR pressure, matches the measured data. This can be observed for the $y_{\mathrm{PP}} \in \{0.6, 1.0\}$ runs, where the pressures reach saturation levels. The strongest deviations can be observed for the 12 V runs, depicted in a) and d), which is confirmed by the numerical error data in the table 4.2 and 4.3. A varying polytropic exponent n_{PP} does not significantly alter the overall error: $\hat{\mathrm{e}}(p_{\mathrm{HPR}}, n_{\mathrm{PP}}{=}1.0) = 5.09$ % versus $\hat{\mathrm{e}}(p_{\mathrm{HPR}}, n_{\mathrm{PP}}{=}1.4) = 5.01$ % and $\hat{\mathrm{e}}(p_{\mathrm{LPR}}, n_{\mathrm{PP}}{=}1.0) = 4.82$ % versus $\hat{\mathrm{e}}(p_{\mathrm{LPR}}, n_{\mathrm{PP}}{=}1.4) = 5.37$ %. However, in the graphs, its influence on the HPR pressure is especially notable prior to reaching the saturation levels. Here, the isentropic approach overestimates the pressure evolution. All runs considered, the isothermal approach with $n_{\mathrm{PP}} = 1.0$ is judged to be superior. The observed deviations of the isentropic approach before the end pressure levels is reached, is ranked worse than the deviations of the leveled final pressures. The inaccuracies of the model

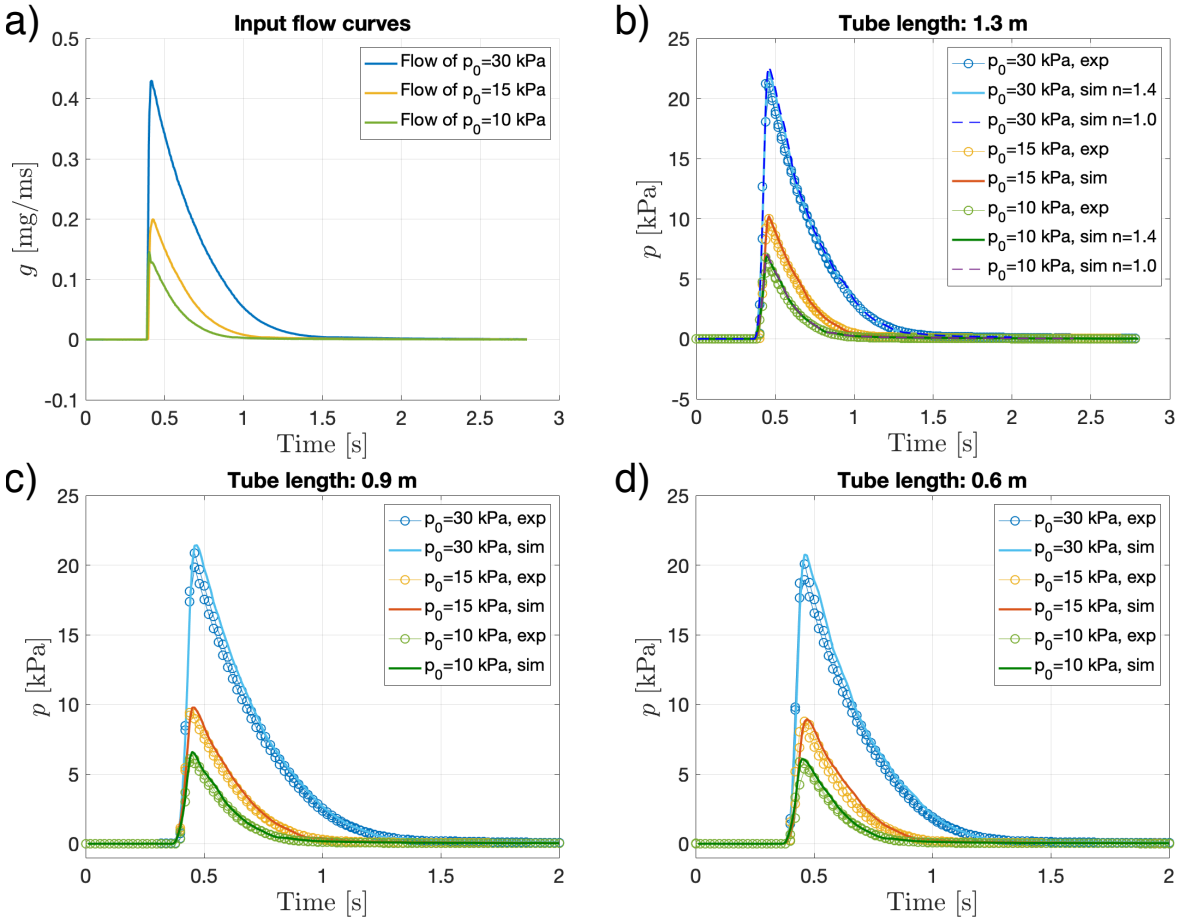

Figure 4.8.: Tube validation: Response of the connector-tube model to unsteady flow. The graphs in b), c) and d) show responses for tube lengths of 1.3, 0.9 and 0.6 m. For each length, air was suddenly released from a charged container by opening a check valve, creating a flow pattern as in a). The three initial pressures of the container were 30, 15 and 10 kPa.

Parameter	Absolute and relative error [kPa,(%)]			Mean error [kPa,(%)]
Re_{mean} [/] \ L_{T} [m]	0.6	0.9	1.3	
1743	-0.10 (-8.41)	-0.19 (-8.90)	-0.12 (-7.45)	0.14 (8.25)
3486	-0.25 (-5.82)	-0.24 (-5.02)	-0.35 (-6.33)	0.28 (5.72)
4914	-0.07 (-0.85)	-0.10 (-1.09)	-0.27 (-2.55)	0.15 (1.50)
5054	$\sim$ 0.00 ($\sim$ 0.00)	-0.05 (-0.50)	-0.27 (-2.45)	0.11 (0.98)
Mean error [kPa,(%)]	0.11 (3.77)	0.15 (3.88)	0.25 (4.69)	0.17 (4.11)

Parameter	Absolute and relative error [kPa,(%)]			Mean error [kPa,(%)]
Re_{mean} [/] \ L_{T} [m]	0.6	0.9	1.3	
1730	-0.01 (-1.36)	-0.03 (-5.29)	-0.04 (-5.44)	0.03 (4.03)
3533	-0.05 (-4.14)	-0.07 (-3.69)	-0.20 (-7.22)	0.11 (5.02)
4991	0.15 (5.69)	0.13 (3.39)	-0.03 (-0.5)	0.10 (3.19)
5139	0.19 (6.96)	0.18 (4.47)	0.01 (0.14)	0.13 (3.86)
Mean error [kPa,(%)]	0.10 (4.54)	0.10 (4.21)	0.07 (3.21)	0.09 (4.01)

Table 4.5.: Tube validation: Mean error for the combination of tube and connector in the upper table and for the tube only in the lower table. Both for tube lengths $L_{\text{T}} \in \{0.6, 0.9, 1.3\}$ m. Note that the total mean errors in the last row and column are unsigned.

Parameter	$\hat{\text{E}}(p_{\text{V}})$ [kPa], ($\hat{\text{e}}(p_{\text{V}})$ [%])			Mean error [kPa,(%)]
$p_{\text{HPR,0}}$ [kPa] \ L_{T} [m]	0.6	0.9	1.3	
10	0.22 (11.91)	0.15 (12.67)	0.21 (13.40)	0.19 (12.66)
15	0.22 (11.96)	0.24 (10.77)	0.22 (9.77)	0.23 (10.83)
30	0.45 (9.24)	0.36 (9.40)	0.31 (8.22)	0.37 (8.95)
Mean error [kPa,(%)]	0.30 (11.04)	0.25 (10.95)	0.25 (10.46)	0.26 (10.81)

Table 4.6.: Tube validation: Deviations of dynamic pressure predictions of the tube model when compared to experimental data. Again, average values in the last column are generated from each initial pressure over all tube lengths as well as from each of the tube lengths over all initial pressures summarized in the last row of the table.

may stem from variations of the individual pump flow generation. Experimental data in a), d) and especially the LPR pressure for $y_{\text{PP}} = 1.0$ in c) show differences of the individual pumps

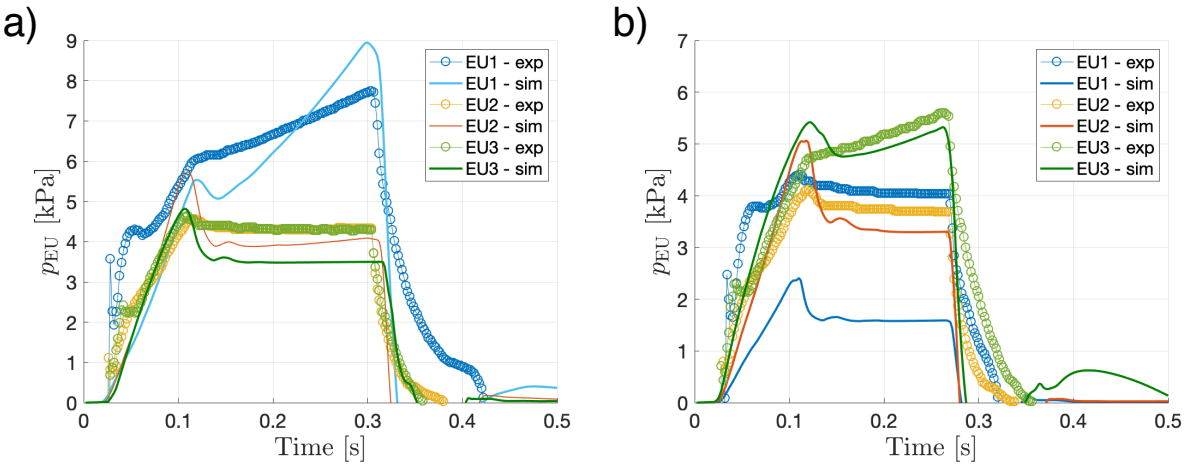

Figure 4.9.: Comparison of the pressure response in the EUs to prescribed flow between experimental and simulated data. Graph a) depicts the run at $f_{\text{Heart}} = 60$ min^{-1} with a higher valve opening in EU[1]. The faster heart rate run at $f_{\text{Heart}} = 90$ min^{-1} is shown in b). Here, the valve opening was the highest in EU[3].

Parameter		Unit	Value
Outer heat transfer coefficient	α_∞	W/m^{2}K	1.5170
LPR inner heat transfer coefficient	α_{LPR}	W/m^{2}K	3.7874
LPR effective wall thickness	$\hat{d}_{\text{LPR}}$	m	0.0090
HPR inner heat transfer coefficient	α_{HPR}	W/m^{2}K	3.0458
HPR effective wall thickness	$\hat{d}_{\text{HPR}}$	m	0.0071

Table 4.7.: MTP validation: Estimated parameter of the MTP model.

Reservoir	Absolute error [°C]		Relative error [%]	
	Median	IQR	Median	IQR
HPR	0.27	1.98	1.55	8.41
LPR	-0.38	2.40	-2.61	20.82

Table 4.8.: MTP validation: Remaining errors of reservoir mean temperature prediction after parameter estimation.

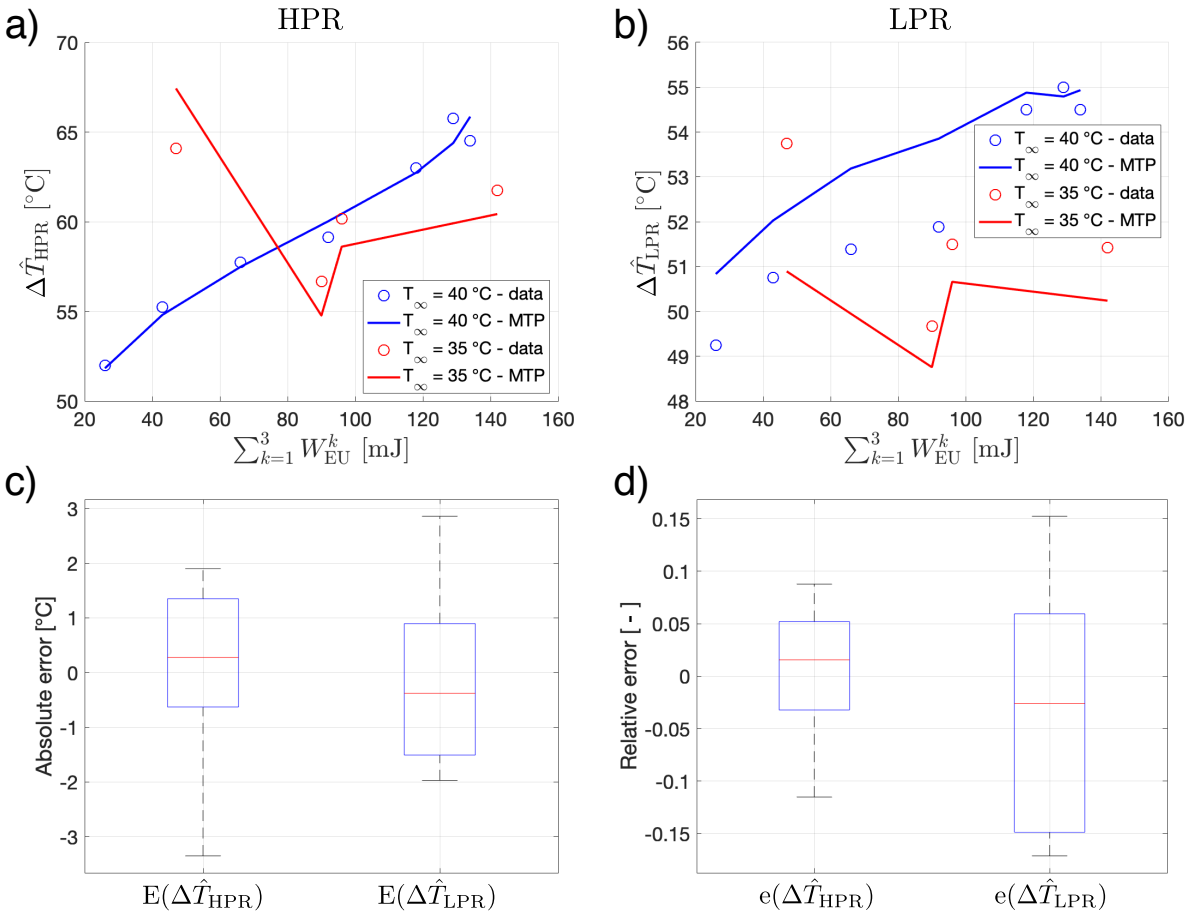

Figure 4.10.: MTP validation: Results of the mean temperature prediction model for varying support levels and two distinct ambient temperatures for the HPR in a) and the LPR in b). The experimental steady mean temperatures were reached after approximately 2.5 hours of operation. The remaining absolute and relative errors are visualized in c) and d) respectively. The error in d) is computed from the over temperature with respect to ambient conditions, e.g. $\mathrm{E} = \Delta\hat{T}_{\mathrm{HPR,data}} - \Delta\hat{T}_{\mathrm{HPR,MTP}}$.

of the two specimen[1]. Also, the lack of heating and cooling of the casing material or stored deformation energy of the latter – neither phenomenon is modeled here – contribute to erroneous temperature predictions and subsequently inaccurate pressure curves. However, an individual or a statistical investigation of the flow curve to replace the current relation is believed to improve predictions.
The reservoir volumes were experimentally determined using a validated volumetric measuring apparatus. Any other method, e.g. from CAD data, failed to provide correct values and compliance as a function of the reservoir pressure $V(p)$ would have required further computational models, e.g. FE models.

Valves The simulated equalization processes after valve opening produce flow signals that superpose the experimental data with very little deviation. The mean relative deviation from measured data is below 5.0 %, leading to the conlcusion, that the valve model, based on the Bernoulli equation for incompressible flows and with averaged density, allows robust valve flow predictions for the low pressure system at hand. Furthermore, the matching pressure curves in the reservoir due to that flow further consolidate the properness of valve and reservoir model. Generally, the predictions are poorer for small valve openings and small initial pressure potentials, resulting in longer lasting equalization flows and consequently a greater relevance of heat transfer effects. Furthermore, the basic $kv(\mathcal{I})$ relation, as shown in 3.6, is not perfectly linear near the valve opening point. In contrast, the relative pressure and flow errors of the two higher initial pressures never exeed 3.31 %. However, the predicted flows for all valve currents above 0.09 A are persistantly below experimental curves, at least for higher flow rates. Even if this deviation is small, it indicates a systematic shortcoming of the model. In addition, in the slow flow ranges, e.g. at the end of an equalization flow or for small valve openings as can be seen in 4.6 a) and b), a more distinct discrepancy can be observed. The simulated flow signal features a kink and leads to a flow overestimation thereafter. It is caused by the absence of a correction for laminar flow, which is predominant for these slow flows. Standardized valve flow equations differ between turbulent and laminar flow patterns and recommend to use correction terms when laminar flow occurs [23], [4]. However, the underlying equations introduce several more valve specific parameters which are to be determined experimentally and a so-called *valve Reynolds number* needs to be calculated. These measurements would introduce further sources of uncertainty. Since the results are generally in good agreement with the experimental data, this additional complexity was avoided. Also, no significant differences between the isothermal and the isentropic approach are observed. The polytropic exponent n_V only occurs in the equation to predict the temperature behind the inflow valve T_V and is computed with respect to the HPR temperature, which drops during each inflow process. Furthermore, the average of both temperatures is utilized to calculate the valve flow. This reciprocal dependency together with small pressure quotients $\frac{p_\mathrm{V}}{p_\mathrm{HPR}}$ in the system at hand and the use of the mean temperature value, result in a low sensitivity of the model with respect to this parameter (cf. figure 5.1).

[1] As explained in 4.1.1, each supply voltage and control value pair was run twice, with different drive units and hence different pumps. That is why each experimental pressure curve consists of the data of two runs.

Connector and tube model The accurate simulation of the pressure drop over the tube and additional restrictions such as the connector are crucial, as it has great influence on the inflation and deflation dynamics. The presented model is in good agreement with experimental data. The polytropic exponent does not exert strong influence. Significant discrepancies can only be observed for higher constant flows and accompanied larger pressure drops. This behavior can be explained similarly to the polytropic exponent of the valve: Low absolute pressure drops lead to small temperature changes and the impact of n_T is further attenuated by averaging the temperatures of the tube segment ends. Due to the obtained results, the polytropic exponent of the tube and connector model is set to $n_\mathrm{T} = 1.4$. Consequently, simulation results with isothermal approach are only shown for the longest tube length tested, hence for 1.3 m. They are plotted as dotted lines in figures 4.7 and 4.8. The results were qualitatively equal or worse for shorter tubes and their representation in the graphs was omitted. The steady flow results show the highest discrepancy near the transition range, in particular around $Re = 3500$. The second plateau from the left in a) in figures 4.7 lays within the transition range of the tube model. The lowest flow levels in a) and b) are in the turbulent range of the connector but in the laminar section of the tube model. The two highest levels are in the turbulent ranges of both models. Both flow patterns can be considered somewhat unstable near this transition range. Changes in thermodynamic conditions, variations in the duct geometry due to manufacturing tolerances and external disturbances, such as vibrations, may cause sudden switchovers from laminar to turbulent flow and vice versa. However, the greatest deviation within the steady flow tests was 0.35 kPa and the mean errors are distinctly below 5.0 %. The flow restriction introduced by the present connector is of greater importance as it produces a greater pressure drop. The mean error of the tube-connector model response to dynamic input is 0.26 kPa, which is low compared to the initial reservoir pressures or typical support pressures. Nevertheless, the mean relative error just exceeds the 10 %. Owing to the low threshold value of $p_\mathrm{V} = 0.2$ kPa, which defines the data range for the error calculation, the elevated relative error is reasonable.

Within this validation, no tube diameter variation was performed to check validity for other values. However, the sensitivity of the diameter was quantified in section 5.2.

EUs The simulated pressure curves strongly differ from the experimental data for EU^1, due to the dissimilarity of the physical implant and its digital counterpart. The EU geometry and their spatial orientation, together with the applied boundary conditions, lead to very specific pressure-volume relationships. Owing to the discrepancies of their pV curves, as shown in figure 4.2 a) to c), the results in 4.9 are not surprising. For EU^2 and EU^3, the pV curves are in better agreement, leading to more accurate simulation results. It is seen as one of the major future work packages to develop processes to quickly and robustly digitize heart specific implants, capable of reproducing the real pV curves in-silico. However, generic implant models can be used to answer engineering questions.

Mean temperature prediction model The MTP allows good predictions of the mean reservoir temperature, subject to long term heating processes with varying input parameters. The absolute error range of both reservoirs is approximately 5°C over the entire data set, which is close to the absolute accuracy of the used temperature sensors, TS-I and TS-II, listed in appendix

A.I.4. The median absolute error for HPR and LPR are 0.27 and -0.38 °C. The relative error is computed from the over temperature with respect to ambient conditions, e.g. $\Delta T = T - T_\infty$, which leads to higher error values. However, median relative errors are 1.55 % and -2.61 %. Nevertheless, variations in the prediction quality can be observed: While the mean temperature prediction in the HPR at an ambient temperature of $T_\infty = 40$°C is almost exact, it is less accurate when the ambient temperature is lowered to $T_\infty = 35$°C. Also, LPR mean temperature predictions are in general poorer than those for the HPR. This may be due to the higher complexity of the valve power consumption model, which contributes to LPR heating. However, the measured temperature values varied strongly over the single sensors within each reservoir: The mean standard deviation over all 11 runs for HPR and LPR are 2.95 and 5.86 °C, respectively. The poorer MTP outcome in the LPR reflects this greater experimental standard deviation in the LPR. Nonetheless, the MTP is a necessary and valuable prediction tool to compute meaningful mean temperature values for the dynamic BiVAD model.

4.4. Summary

In this chapter, BiVAD and MTP model were both validated by the use of experimental data. The mean relative errors are below or equal to 5 % for all relevant comparisons, except for the dynamic tube validation, where it is around 10 %. However, this is only due to the fact, that the processed signal itself approaches zero, which leads mathematically to an increase of the relative error measure. The BiVAD model validation has been carried out by analyzing the discrepancy between measured and simulated signals under a great variation of boundary conditions. All components were at least tested once separately, to avoid influences of other components or, in case of the reservoir, included into more than one test. Also, they were all tested under dynamic conditions. Tube and connector were additionally validated under steady conditions to tune the Reynolds numbers and obtain meaningful results for all flow regimes. Two error measures were introduced, an absolute (4.1) and relative (4.3) description of the discrepancy of two time-dependent signals. Thereby, each moment of the dynamic test phase contributes equally to the errors. In order to cover the full continuous working space of the drive unit in this validation, a large set of representative boundary conditions was tested:

- For reservoir and pump, three supply voltages $\mathcal{U}_{\text{supply}} \in \{12, 15, 17\}$ V and three pump control values $y_{\text{PP}} \in \{0.3, 0.6, 1.0\}$ were experimentally tested with two drive units, resulting in 18 runs under nine conditions. Furthermore, the two benchmark polytropic exponents $n_{\text{PP}} \in \{1.0, 1.4\}$ were tested in the related simulations. Since they do not significantly alter the validation results, $n_{\text{PP}} = 1.0$ is chosen for all following simulations.
- For reservoir and valve, three initial HPR pressures $p_{\text{HPR}} \in \{10, 15, 30\}$ kPa and four different valve openings at $\mathcal{I}_{\text{V}} \in \{0.09, 0.12, 0.14, 0.2\}$ A were chosen and run with two different drive units. Hence, 24 runs at 12 conditions were utilized.
- For tube and connector, two different validations were carried out:
  - Stationary flows at four different flow levels and Reynolds numbers in the laminar, turbulent, transition and mixed flow regime, each for three tube length $L_{\text{T}} \in$

$\{0.6, 0.9, 1.3\}$ m. These tests were further performed for the tube only and the tube-connector configuration, resulting in 24 tested boundary conditions.

  - Dynamic flow response was tested, stemming from three different initial pressures $p_{\text{HPR}} \in \{10, 15, 30\}$ kPa over the connector-tube model with three differing tube lengths $L_{\text{T}} \in \{0.6, 0.9, 1.3\}$ m. It was again tested with two different drive units, connectors and tubes. Thereby, a total of 18 runs was performed.

- For the EUs, one physical implant with comparable pV characteristics could be obtained. It was experimentally inflated at two distinct virtual heart frequencies and reproduced in-silico using the same inflow signal.
- A total of 11 boundary conditions were used to record the heating and the resulting mean reservoir temperatures, which were used to validate the MTP model. These runs split into four support levels at 35 °C ambient temperature and seven support levels for the $T_\infty = 40$ °C. In contrast to the BiVAD model, the validation approach for the MTP model differed, as an optimal set of parameters was estimated in an unconstrained optimization problem to line up experimental and computational results. The parameter set consisted of the unknown heat transfer coefficients and the average material thicknesses of the drive unit housing. The determined optimal setting is physically meaningful for both types of estimated parameters.

This chapter proves, that BiVAD and MTP model allow reliable investigations within the wide range of tested boundary conditions. They are subsequently subject to a parameter sensitivity analysis in chapter 5 and are further applied to a set of cardiovascular conditions in chapter 6.

5. Sensitivity analysis

A local sensitivity analysis is carried out for two major purposes. Firstly, the estimated model parameters introduce uncertainties due to erroneous measurements, idealized assumptions and manufacturing tolerances of the used specimen. The influence of these uncertainties on the prediction quality of BiVAD and MTP model are quantified. Secondly, the found parameter sensitivities may indicate reasonable improvement potential for the BiVAD, as formulated in the the research objectives in 1.7.

5.1. Methods

The local sensitivity analysis is performed by comparing the normalized partial derivatives of the considered model solution with respect to the model parameters [112]. The partial derivatives are approximated using forward finite differences with a small variation $\epsilon = 0.1$ % [122]. For the BiVAD model, the investigated parameters are listed in (5.2)-(5.7) and the solution is defined as the pV work (3.121) done during the systole. For the MTP model, the considered parameters are listed in equation 5.8 and the solution are the estimated mean reservoir temperatures $\Delta\hat{T}_{\text{HPR}}$ and $\Delta\hat{T}_{\text{LPR}}$. The dimensionless sensitivity $\mathcal{S}_j$ is expressed as the change of the solution with respect to one particular parameter ξ_j, subject to that small perturbation ϵ. For the EU pV work, it is defined as

$$\mathcal{S}_j(\xi_j) = \frac{1}{W(\xi_j)} \frac{\partial W(\xi_j)}{\partial \xi_j} \approx \frac{1}{W(\xi_j)} \frac{W(\xi_j + \epsilon \cdot \xi_j) - W(\xi_j)}{\epsilon} \tag{5.1}$$

and adapted to the estimated mean reservoir temperatures when analyzing the MTP sensitivities. The following vectors contain the analyzed parameters of both models.

$$\begin{aligned}
\boldsymbol{\xi}^{\text{AD}} = \Big[& V_{\text{HPR}} \quad C_{\text{HPR}} \quad \Delta\hat{T}_{\text{HPR}} \quad k_{\text{th,HPR}} A_{\text{HPR}} \quad k_{\text{th,W}} A_{\text{W}} \quad \dots && \text{HPR} && (5.2)\\
& V_{\text{LPR}} \quad C_{\text{LPR}} \quad \Delta\hat{T}_{\text{LPR}} \quad k_{\text{th,LPR}} A_{\text{LPR}} \quad \dots && \text{LPR} && (5.3)\\
& C_{\text{PP}} \quad g_{\text{PP,max}} \quad n_{\text{PP}} \quad \dots && \text{Pump} && (5.4)\\
& kv_{\text{max}} \quad \text{H}_{\text{V}} \quad n_{\text{V}} \dots && \text{Valve} && (5.5)\\
& [a_\lambda, b_\lambda]^T \quad [a_\zeta, b_\zeta]^T \quad C_{\text{T}} \quad L_{\text{T}} \quad D_{\text{T}} \quad Re_{\text{crit},\lambda} \quad Re_{\text{crit},\zeta} \quad n_{\text{T}} \quad \dots && \text{Tube} && (5.6)\\
& k_{\text{th,EU}} \quad p_\infty \Big]^T && \text{EU} && (5.7)
\end{aligned}$$

$$\boldsymbol{\xi}^{\text{MTP}} = [T_\infty \quad \mathcal{U}_{\text{source}} \quad k_{\text{th,HPR/LPR}} \quad A_{\text{W}} \quad A_{\text{HPR}} \quad A_{\text{LPR}} \quad y_{\text{PP}} \quad \Lambda_{\text{th,V}} \quad a_{\mathcal{R}} \quad b_{\mathcal{R}}]^T \tag{5.8}$$

The standard parameter sets of the 0D drive unit model and the temperature model, as given in the tables 3.5, 3.9 and 3.6, are utilized. The pump control value was set to $y_{\text{PP}} = 0.35$.

5.2. Results

The sensitivities (5.1) can be understood as the change of the system's output to a change in the system's local input. More precisely, a variation ϵ_{in} of a single parameter in the input results in an alteration $\epsilon_{\text{in}} \cdot \mathcal{S}_j$ in the output.

5.2.1. SCVS model

The results of the sensitivity analysis are depicted in figure 5.1, showing the individual parameter sensitivities in descending order and for each EU. Note that the EUs have differing control values assigned, with significant lower values for EU[3] (cf. table 3.9). A magnified view of the parameters with sensitivities below 0.05 was inserted to enhance visibility, marked as *close-up* in the figure.

5.2.2. MTP model

The sensitivity analysis results of the MTP model are depicted in figure 5.2. The variation of each individual parameter alters the mean predicted temperatures in both reservoirs, HPR and LPR, whose sensitivity values are plotted as blue and red bars, respectively.

5.3. Discussion

BiVAD model The sensitivity of a parameter differs for the different EUs, as differing control values were assigned and their individual pressure-volume curves are distinct. The sensitivity pattern for the three EUs reflect this difference for most parameters, either directly, with the greatest sensitivity of the EU being observed for the highest valve openings, or inversely, with the most pressurized EU showing the lowest sensitivity. The former, the direct mapping, is the case for the three most influencing parameters: ambient pressure, reservoir volume and reservoir mean temperature. The greatest influence on the pV work stems from ambient pressure value and can be explained by its presence in every pressure or density dependent equation within the system. Ambient pressure is not exerted onto the 3D implant. Hence, the EUs are in vacuum space and their internal pressure p^k_{EU} is a relative pressure, with $p^k_{\text{EU}} = 0$ kPa in the equilibrium state. However, owing to thermodynamic relations require absolute pressures, e.g. in the ideal gas law or to compute densities, an ambient pressure has to be introduced and consequently has great influence on the simulation output. Lower ambient pressures favor higher EU work, but changes within the meteorological range are very normal and no design recommendations can be made regarding $\mathcal{S}(p_\infty)$. As the HPR volume is the parameter with the second highest sensitivity, the sophisticated determination of the reservoir volumes, as it was carried out within this thesis in appendix A.I.1, is justified. The volume influences the pressure curve during charging and discharging and thus reciprocally the pressure driven valve and tube flow. Note that during inflation of the EUs, the only influence of the LPR is of indirect nature over the pump flow, which depends on LPR conditions. Sensitivities of HPR and LPR volume are assumed to switch positions within the diagram 5.1 during deflation, as their equations do not differ. It stands to

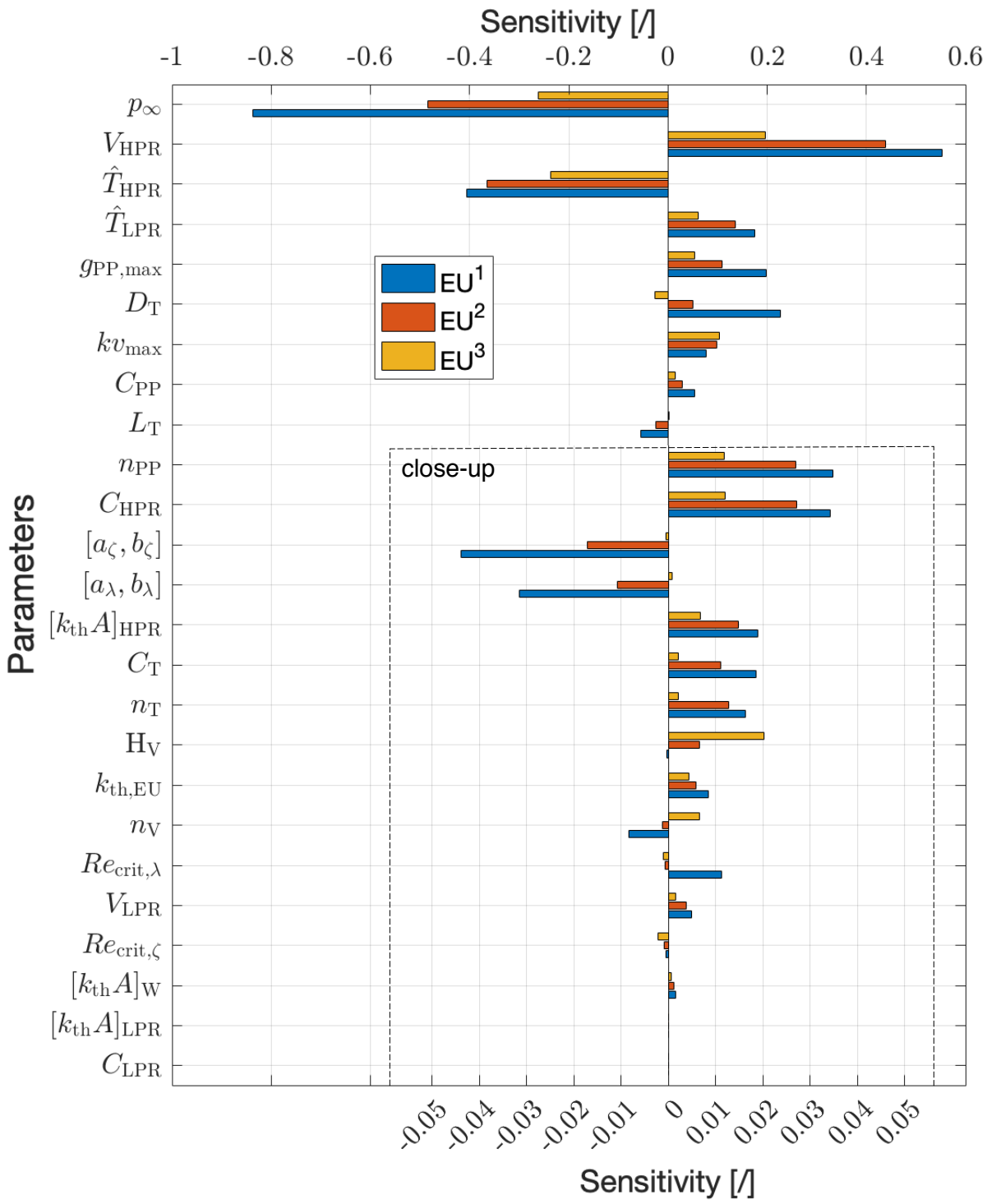

Figure 5.1.: Sensitivities of the drive unit model with respect to parameter variations in descending order for all three EUs. The unaltered parameters where set to their standard values, listed in table 3.5. Note that the valve control values of each EU differed. A magnification view is inserted for values below 0.05 and denoted as *close-up*.

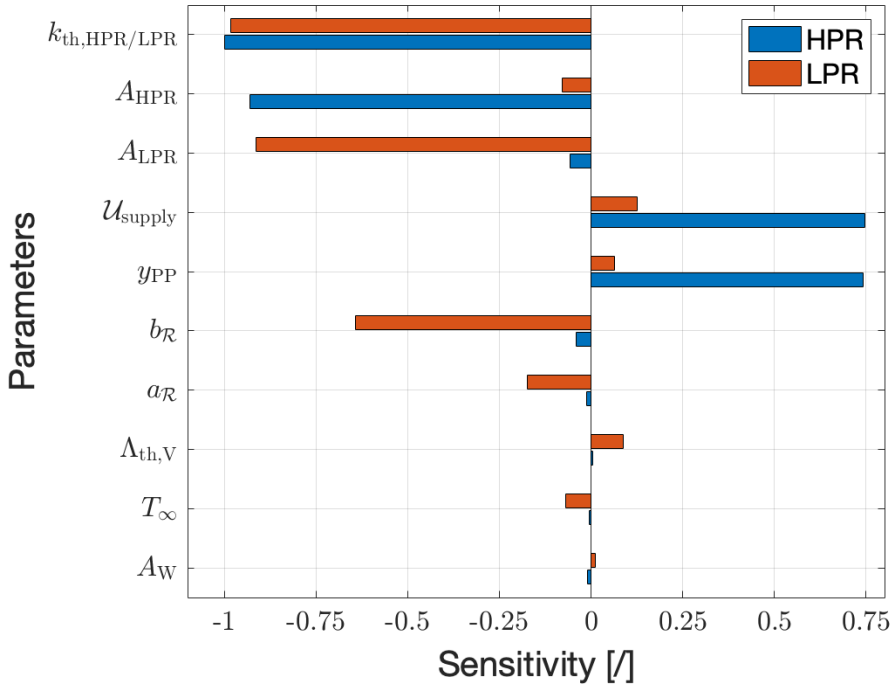

Figure 5.2.: Sensitivities of the mean temperature prediction model with respect to its parameters as listed in 5.8.

reason that an increase of the reservoir volumes in future BiVAD designs would significantly increase the EU work and the drive unit efficiency and is recommended. Both mean reservoir temperatures commonly exert high influence during the inflation of the EUs. The air cools down while expanding from the HPR into the EUs, but its temperature is proportional to the reservoir temperatures for equal pressure conditions according to (2.19). The importance of meaningful mean temperatures is emphasized and the introduction of the MTP model in section 3.2 justified. Design measures to cool the HPR would beneficially influence the work outcome of the BiVAD. Practical recommendations can be deduced from the MTP parameter sensitivity analysis later in this chapter. The pump free-flow (no load) $g_{\mathrm{PP,max}}$ is the most sensitive pump parameter, followed by the compression ratio C_{PP}. These pump parameters are not independently influenceable as a greater free-flow or pressure ratio is typically accompanied by an increased power consumption. Whether the beneficial effects outweigh the negative ones, must be tested specifically with the modified pumps. The parameter kv_{max} introduces the highest sensitivity within the valve model. The other valve parameter, namely hysteresis $\mathrm{H_V}$ and polytropic exponent n_{V}, have very little influence. For the latter, this was already observed during model validation (cf. 4.1.2). The small hysteresis sensitivity, however, may be explained by the fact that hysteresis only plays a role for a fraction of the inflation period. It comes exclusively into play after the control value drop from $y^k_{\mathrm{inlet,1}}$ to $y^k_{\mathrm{inlet,2}}$, that occurs roughly after 1/3 of the inflation period. This first third however is the highly dynamic phase, what can easily be verified by considering the flow curve in figure 3.17. Hysteresis may take a more important role in other control strategies, as e.g. closed-loop control, when it applies within this high-flow phase. The selection of high-flow valves with great

$kv_{\max}$ values is endorsed, as they help to increase the EU output work. For the tube, the diameter is the only parameter with a prominent influence on the model outcome and an increase of D_{T} is reasonable, if possible. Tube length and the friction model parameters for tube and connector lay close to or within the 0.05 range. All other tube and heat exchange related parameters only weakly influence the model outcome. Note that changes of conditions in the simulation can significantly alter the diagram 5.1. In this analysis, only the inflow process was checked, which leads to low sensitivities of LPR related parameters by default. Also, changes in the valce control values and higher or lower initial pressures or temperature would lead to other values and a different sensitivity ranking. However, since the standard parameter set (cf. table 3.5) was used, which is close to a typical heart support scenario, figure 5.1 is a good representation of the parameter sensitivities of the BiVAD. Note that the sensitivities of individual parameters may be different when their effect on the submodel outcome is judged decoupled of the full model.

MTP model The sensitivities relative to the individual MTP model parameters are more direct, as parameters related to components of one of the two reservoirs almost exclusively contribute to the temperature of this specific reservoir. Consequently, the valve coil resistance parameters $a_{\mathcal{R}}$, $b_{\mathcal{R}}$ and $\Lambda_{\mathrm{th,V}}$ predominately alter the LPR temperature, while the pump control signal almost exclusively effects HPR temperature. The supply voltage influences both, but the pump, as the greater electrical load, transforms more electrical energy into heat. However, the greatest influence is exerted by the heat exchange parameters heat transmittance and their corresponding areas. The magnitudes of both are about the same, as they appear as a product in the equations. These parameters offer great potential to lower the mean reservoir temperatures. Larger surface areas would be concomitant features when increasing the reservoirs volumes, which is recommended to gain the pV^k_{EU} work. However, it could further be enlarged by structuring the inner or outer reservoir wall with ribs. Moreover, the heat transmittance can be increased by choosing reservoir materials with a higher thermal conductivity or by lowering the material thickness. Additionally, component level improvements to reduce the supply voltage and the pump control value can lower the resulting temperatures.

5.4. Summary

In this chapter, the introduced BiVAD and MTP models have been analyzed with respect to the sensitivity of their parameters. None of the involved parameters were found to be extremely sensitive to change, as their sensitivity values are below one. However, this observation is only valid in case of single-parameter variation. Any multi-parameter changes are unpredictable with the used method and may alter the solution. However, the local sensitivity analysis results summarize some essential findings regarding the modeling in chapter 3 and the underlying real system:

- Ambient pressure should carefully be adapted to the scenario of interest. It may be advantageous to test for the two extreme boundary values and for an expected average ambient pressure.

- The reservoir volume determination is crucial and the efforts made in this thesis to obtain accurate values are endorsed. Any change of design should involve a re-calibration of the volumes. Their compliances can be seen as less critical parameters for the conditions prevailing during the sensitivity analysis. However, they gain importance for higher reservoir pressures.
- The introduction of the MTP model is justified as its output, namely $\Delta\hat{T}_{\text{HPR}}$ and $\Delta\hat{T}_{\text{LPR}}$, exerts relatively strong influence on the solution. Any reliable SCVS analysis should therefore include MTP model temperature updates.
- The key parameters for the submodels pump, valve and tube are $\{g_{\text{PP,max}}, C_{\text{PP}}\}$, $\{kv_{\text{max}}\}$ and $\{D_{\text{T}}\}$, respectively. Great efforts to adapt the remaining parameters only need to be considered in case of substantial changes.
- The effect of valve hysteresis plays a minor role in combination with the presented valve control approach. However, as stated in 5.3, its relevance may significantly increase for other control strategies.
- Thermal transmittance of the BiVAD casing and the individual reservoir surfaces must precisely be determined as this predominately influences MTP model outcome and thereby the SCVS simulation results.

As outlined in the research objectives of this thesis in 1.7, the system should be analyzed for optimization potential. The sensitivities allow for promising device design improvements, which are listed in the following.

- A reservoir volume increase would have a number of beneficial effects: It would increase the amount of energy delivered to the heart and consequently enhance the support effect. The device efficiency would also be elevated, since the power consumption is either unaltered or even decreased. Moreover, a larger reservoir volume is accompanied by greater reservoir surface areas, which improves heat transfer and leads to lower device temperatures. As can be seen in the results, lower temperatures would again increase the support efficacy and efficiency. Hence, the advantageous effects are self-reinforcing.
- The reservoir surface areas can be increased independently of the reservoir volume, which may be restricted to a certain size. Therefore, structured inner and outer surfaces, e.g. with ribs, are possible. By virtue of the beneficial consequences of an area increase, this measure is separately stated.
- Measures to increase the heat transmittance would decrease the device temperature. Therefore, a reservoir material with a higher thermal conductivity and or thinner reservoir walls can be chosen.
- Increasing the tube diameter would increase the pV work and improve inflation and deflation dynamics. The effect of a reduced tube length is comparably small and not necessarily recommended.
- Improvements concerning the pump or valves, e.g. increasing kv or $g_{\text{PP,max}}$, seem straightforward but are typically limited by the range of commercially available products and the

accompanied increase in power consumption. However, custom-made parts may increase the efficiency in this particular application.

6. Application

The SCVS model of a supported cardiovascular system is applied to a set of medically relevant cases. Since the effect of varying support pressures on the CVS has been studied by Jagschies [54] and Hirschvogel [43] it will not be the focus of this work. Here, in contrast, the implications of medical conditions and their impact on the BiVAD are of interest. They are assumed to vary in both manner and intensity with changing CVS conditions, due the coupled nature of the model. A confirmation of this assumption would support the possibility of patient and hence disease specific treatment. It would further raise the question as to what degree the BiVAD enables the assessment of physiological and pathological changes.

6.1. Methods

6.1.1. Medical cases

The CVS model allows for mimicking various systemic conditions of heart related diseases. To do so, parameters of the 0D circulatory system and of the 3D heart model are set such that they represent complex pathological conditions, e.g. different types of HF. Other diseases may occur suddenly, like myocardial infarction, or develop over time as e.g. aortic valve stenosis. Their occurances are expected to influence not only the physiology but also the technical system.

6.1.1.1. Specific patients

The BiVAD is intended to be used within all eligible patients, hence allowing support of hearts of different sizes and in different conditions. In this context, the 3D heart of the CVS model is not an arbitrary geometry, but stems from actual porcine data, which was first used by Jagschies et al. [54]. They applied an early prototype of the BiVAD in pigs and assessed the support effects. In this study, CT scans were taken from three of the animals and have been used to build FE models. The process from medical imaging to a sophisticated computational model, including the individual 3D expandable units (EU) is described by Hirschvogel et al. [43]. Also, CVS parameters were measured during the animal trials in [54] and used by [45] in a parameter estimation to mimic patient specific CVS behavior of the three animals in-silico. The same three geometries and appertaining CVS model parameter sets, herein after referred to as patients $p1$, $p2$ and $p3$, are utilized in the present work. These specific SCVS models are extended by inner EU contact (cf. 3.3) to allow complete deflation. The FE models with EUs are depicted with additional volume information in figure 6.1. Patient $p1$ has the largest heart volume, while $p2$ and $p3$

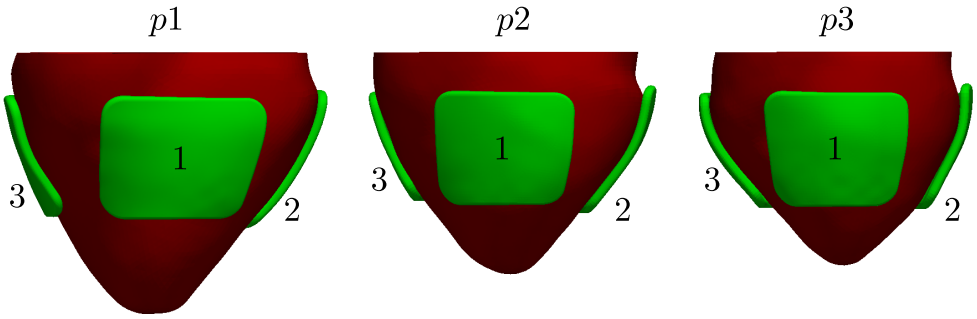

$p1$	$p2$	$p3$
$V_{\mathrm{v}}^{\ell} = 95.70$ ml	$V_{\mathrm{v}}^{\ell} = 90.95$ ml	$V_{\mathrm{v}}^{\ell} = 54.74$ ml
$V_{\mathrm{v}}^{r} = 73.25$ ml	$V_{\mathrm{v}}^{r} = 90.20$ ml	$V_{\mathrm{v}}^{r} = 54.62$ ml
$V_{\mathrm{EU}}^{1} = 7.25$ ml	$V_{\mathrm{EU}}^{1} = 7.03$ ml	$V_{\mathrm{EU}}^{1} = 7.08$ ml
$V_{\mathrm{EU}}^{2} = 7.19$ ml	$V_{\mathrm{EU}}^{2} = 7.13$ ml	$V_{\mathrm{EU}}^{2} = 7.25$ ml
$V_{\mathrm{EU}}^{3} = 7.86$ ml	$V_{\mathrm{EU}}^{3} = 7.67$ ml	$V_{\mathrm{EU}}^{3} = 7.36$ ml

Figure 6.1.: Specific patient geometries $p1$, $p2$ and $p3$ with their proper EUs (green), all visualized in the same scale at 80 % of the heart cycle period, hence near the end-diastolic time point. A further size quantity is given by the left and right, blood-containing ventricular volumes V_{v}^{ℓ} and V_{v}^{r}, respectively. The BiVAD EUs, numbered 1, 2, 3, with EU^1 being placed on the anterior wall of the LV, EU^2 on the posterior wall of the LV and EU^3 on the lateral RV wall. Their initial cavity volumes $V_{\mathrm{EU}}^{k}(t_0)$ with $k \in \{1, 2, 3\}$ are also given.

are comparable. However, the ventricular volumes are similar in $p1$ and $p2$, but are considerably smaller in $p3$. In contrast, EU volumes are comparable over all three patients.

6.1.1.2. Heart failure conditions

The intended use of the BiVAD is to support the CVS of patients suffering from HF. A description of this disease and the resulting symptoms can be found in 1.3. Consequently, the CVS model should allow for valid HF representations in order to assess the SCVS model in a relevant condition. Therefore, the following conditions are considered:

- Low-afterload HF (LA-HF): created by infusion of beta blocker (β_1 blockade), which dilates arteries and reduces vascular resistance. Furthermore, heart rate and myocardial contractility are reduced, eventually leading to poor cardiac output [96].
- High-afterload HF (HA-HF): provoked by injection of phenylephrine, which constricts arteries and veins and consequently increases vascular resistance [107]. It leads to high blood pressure and reduces the heart rate.
- Absence of HF (NO-HF): reference case without explicit HF condition.

A parameter set of the CVS model was chosen and its values were estimated by [45] such that simulated left ventricular pressures and ejection fractions coincide with measurements taken

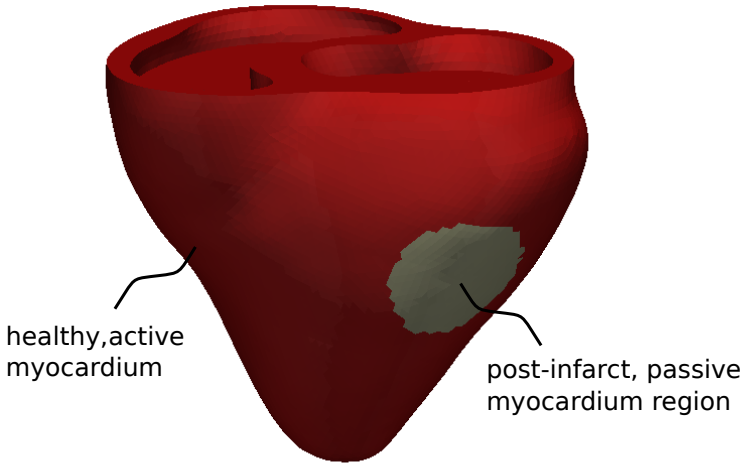

Figure 6.2.: Patient heart $p1$ with predefined post-infarct region (gray) of approximately 30 mm in diameter. The region spans the entire wall thickness and is characterized by purely passive material behavior.

during the study of [54]. The parameter set included heart contractility (cf. 3.3.1), upstroke and relaxation rates of the heart's active stress, left atrial elastance and systemic vascular resistance. The parameter estimation was carried out for the LA-HF and HA-HF condition, for each of the patients $p1$, $p2$ and $p3$. They are consequently representations of specific HF patients. In addition to the HF cases, a generic parameter set, denoted as NO-HF, is used with the same literature-based parameters in all patients. The resulting heart frequencies of the cases are in $[48.8, 61.2]$ 1/min. Other parameter values for all different cases can be found in [43].

6.1.1.3. Myocardial infarction

Myocardial infarction (MI) occurs when coronary arteries or their branches occlude and thereby restrict or event prevent blood flow to corresponding heart muscle regions such that the respective myocardial cells are damaged. MI may lead to HF due to remodeling processes which can take years. However, MI can occur in HF patients [19] as the underlying causes for HF have not completely vanished during treatment, but rather been intensified due to the advancing character of HF and the related worsening of the patient's vascular condition.

MI can be simulated by setting the myocardial contractility to zero within a predefined region. The active stress term in (3.89) vanishes and the material is purely passive. Figure 6.2 shows an infarct region in the left ventricular myocardium of patient $p1$. The diameter is approximately 30 mm. However, this approach is limited as it leaves changing material properties unconsidered.

6.1.1.4. Valvular heart diseases

Valvular heart diseases (VHD) include valvular stenosis, which is a narrowing of the valve's opening, and valvular insufficiency or regurgitation, which is synonymous with valve leakage. Many HF patients have concurrent VHD [114]. HF may result from valvular insufficiency [51] or be the cause for VHD, as myocardial dilatation and remodeling processes may lead to reduced leaflet closure [94]. The study of [70] quantifies the prevalence of aortic stenosis, aortic regurgitation, mitral stenosis and mitral regurgitation to 10%, 8.4%, 1%, and 12.5%, respectively, within a cohort of suspected HF patients. However, due to the enclosing nature of the BiVAD (cf. figure 1.7), it is more likely to induce a mitral regurgitation after implantation and during support, due to a potential re-shaping of the ventricles[1]. Consequently, the present work analyses all of the mentioned VHD except for mitral stenosis with insignificant prevalence in HF patients. Furthermore, mitral regurgitation is a focus due to its importance in BiVAD support. Stenosis and regurgitation are both modeled by varying the flow resistance of the respective heart valve. It is increased in the open state for a stenosis, while it is decreased in the closed state for a regurgitation. The exact values can be found in [43].

6.1.2. Computation process

CVS and BiVAD model are closed dynamical systems. They will consequently approach an homeostatic (CVS model) and periodic (BiVAD model) state, which depend on the initial and boundary conditions[2]. Any reliable analysis should therefore be conducted at such state of periodicity. In order to simulate the full coupled system, various steps are subsequently performed. The computation of a homeostatic cardiovascular condition is performed in a first separate step, before including the BiVAD model. A periodic state of the coupled SCVS is computed thereafter. Lastly, a specific medical case, as described in 6.1.1, can be provoked with a subsequent computation of the new, diseased periodic state. This procedure is depicted in figure 6.3 and will be explained precisely in the following.

Cardiovascular homeostasis The computation of the homeostasis is the first phase of the general procedure applied in the present work and marked as phase A in figure 6.3. Here, only the CVS model, consisting of the 3D heart and 0D circulatory system are used. The homeostatic state needs to be computed for every specific heart geometry with one of the HF conditions in 6.1.1.2. The heart is prestressed (cf. 3.3.3) to the initial ventricular pressures and active stresses prior to the execution of a transient simulation of the heart beat. The resulting end-cycle values are reutilized as initial values in the next heart beat. Prestressing and forward simulation are repeatedly executed on the initial geometry until the maximum relative error $\mathrm{E}_{\mathrm{cycle}}^{\mathrm{CVS}}$ of all monitored CVS

[1] The leaflets of the mitral and tricuspid valve are attached to the papillary muscle over fibrous cords (lat. chordae tendineae). Deforming the heart muscle may alter the distance between papillary muscle and valvular plane, resulting in a changed leaflet position. A direct influence of the BiVAD on the leaflets is likewise conceivable.

[2] Note that the term *homeostatic* and *periodic* refer to the same condition of a dynamic system, namely that its signals repeat identically after a constant time period. However, the former term is predominately used for biological (and social) systems, while the latter is rather utilized for technical systems. In this work, the combined bio-technical SCVS model is attributed with *periodic* when the mentioned case applies.

variables reaches a threshold ϵ_{cycle}. These variables are $p_{\text{ar}}^{\text{sys}}$, $p_{\text{ar}}^{\text{pul}}$, $p_{\text{ven}}^{\text{sys}}$, $p_{\text{ven}}^{\text{pul}}$, V_{V}^{ℓ}, V_{V}^{r} as well as the ventricular stroke volumes SV^{ℓ}, SV^{r}. Refer to figure 3.13 for their location within the CVS model. The individual error is computed by relating the difference between start and end cycle value to the start value, for example

$$\text{E} = \left| \frac{p_{\text{ar}}^{\text{sys}}(t_{\text{ec},z}) - p_{\text{ar}}^{\text{sys}}(t_{\text{ec},z-1})}{p_{\text{ar}}^{\text{sys}}(t_{\text{ec},z-1})} \right|, \tag{6.1}$$

where $t_{\text{ec},z-1}$ is the beginning of the z-th cycle and $t_{\text{ec},z}$ its end time. The relative error computation differs for the stroke volume, where the difference between both ventricles is related to the stroke volume of the left ventricle. Once the relative error reaches an acceptable value

$$\text{E}_{\text{cycle}} \leq \epsilon_{\text{cycle}}, \tag{6.2}$$

the CVS model's end-cycle variables of that heart beat are stored and can be utilized as homeostatic initial conditions in subsequent simulations.

Cardiovascular support with heated BiVAD The SCVS model utilizes previously computed homeostatic conditions as initial values for the BiVAD supported phase B in figure 6.3. The implant as well as BiVAD model are added to complete the system, as it is described in 3.3. The heart is prestressed to the actual initial ventricular pressures and actives stresses of the previously computed homeostatic state prior to the dynamic computation of a supported heart cycle. After every transient simulation, new mean reservoir temperatures are predicted in order to consider large time-scale heating processes. Therefore, the BiVAD state variables of the last heart beat p_z^{AD} are passed to the MTP model. It computes the new mean reservoir temperatures $\Delta\hat{\boldsymbol{T}}_{z+1}^{\text{MTP}} = \left[\Delta\hat{T}_{\text{HPR}}, \Delta\hat{T}_{\text{LPR}}\right]_{z+1}^{T}$. These improved estimates are further utilized as initial conditions of the subsequent heart cycle computation on the small time scale. This iterative procedure is stopped when a maximum error threshold is reached. The previously introduced maximum error $\text{E}_{\text{cycle}}^{\text{CVS}}$ is extended by the BiVAD pressures p_{EU}^{k}, p_{V}^{k}, p_{T}^{k}, p_{HPR}, p_{LPR} and reservoir temperatures T_{HPR}, T_{LPR} as well as implant volumes V_{EU}^{k}. The overall maximum error then reads

$$\text{E}_{\text{cycle}}^{\text{SCVS}} = \max \Bigg\{ \quad \text{E}_{\text{cycle}}^{\text{CVS}}, \tag{6.3}$$

$$\left| \frac{p_{\text{EU}}^{k}(t_{\text{ec},z}) - p_{\text{EU}}^{k}(t_{\text{ec},z-1})}{p_{\text{EU}}^{k}(t_{\text{ec},z-1})} \right|, \left| \frac{p_{\text{V}}^{k}(t_{\text{ec},z}) - p_{\text{V}}^{k}(t_{\text{ec},z-1})}{p_{\text{V}}^{k}(t_{\text{ec},z-1})} \right|, \tag{6.4}$$

$$\left| \frac{p_{\text{T}}^{k}(t_{\text{ec},z}) - p_{\text{T}}^{k}(t_{\text{ec},z-1})}{p_{\text{T}}^{k}(t_{\text{ec},z-1})} \right|, \left| \frac{p_{\text{Res}}(t_{\text{ec},z}) - p_{\text{Res}}(t_{\text{ec},z-1})}{p_{\text{Res}}(t_{\text{ec},z-1})} \right|, \tag{6.5}$$

$$\left| \frac{T_{\text{Res}}(t_{\text{ec},z}) - T_{\text{Res}}(t_{\text{ec},z-1})}{T_{\text{Res}}(t_{\text{ec},z-1})} \right|, \left| \frac{V_{\text{EU}}^{k}(t_{\text{ec},z}) - V_{\text{EU}}^{k}(t_{\text{ec},z-1})}{V_{\text{EU}}^{k}(t_{\text{ec},z-1})} \right| \Bigg\}, \tag{6.6}$$

with Res $\in \{\text{HPR, LPR}\}$ and $k \in \{1, 2, 3\}$. The SCVS model is considered to be in a periodic state, when

$$\text{E}_{\text{cycle}}^{\text{SCVS}} \leq \epsilon_{\text{cycle}}^{\text{SCVS}}, \tag{6.7}$$

with $\epsilon_{\text{cycle}}^{\text{SCVS}} = 0.05$. Note that the relative error of pressures and temperatures in (6.4) to (6.6) are calculated from relative values (= gauge pressure and temperature in °C), which results in higher errors but consequently in a more accurate prediction of the periodic state.

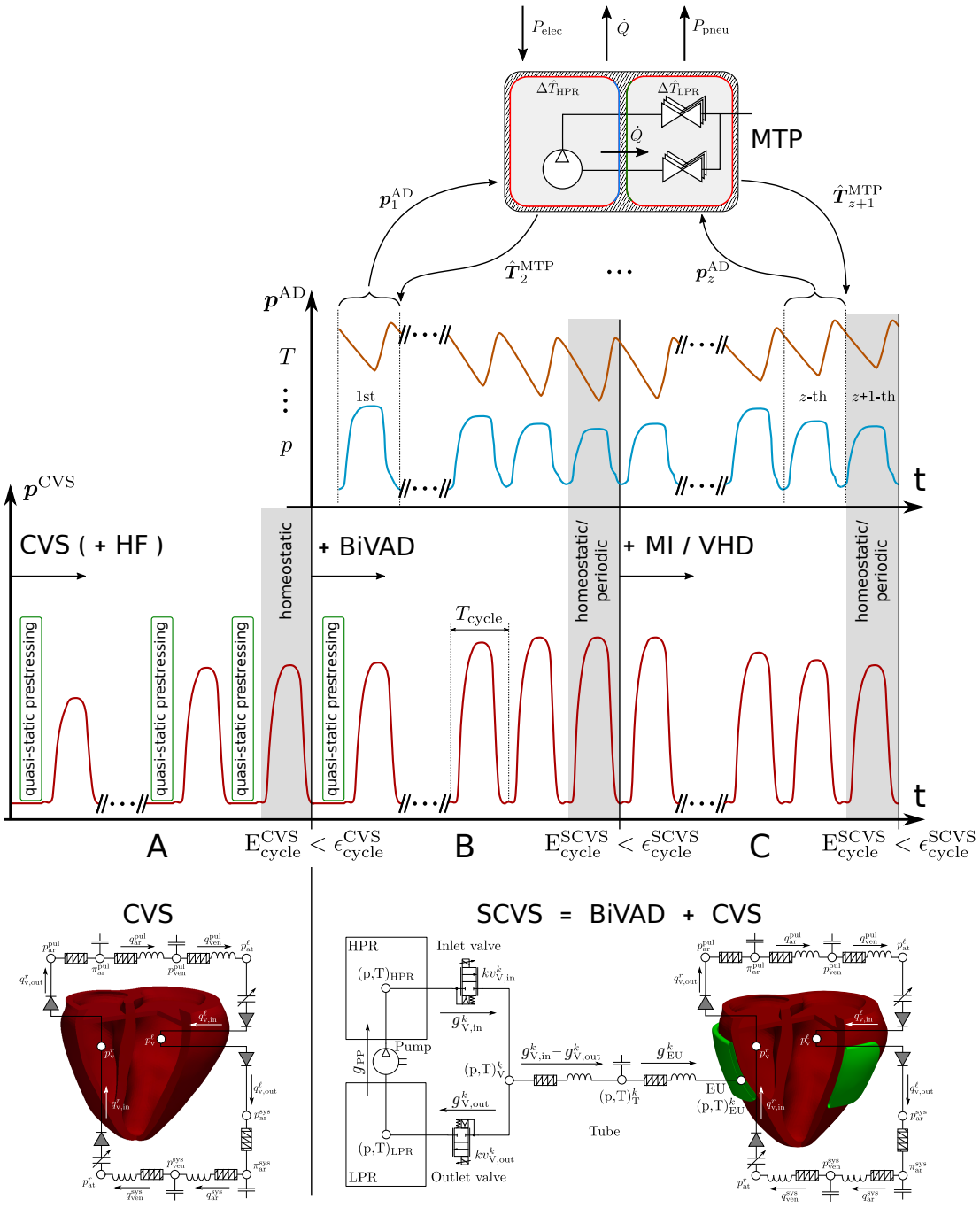

Figure 6.3.: Schematic of the general procedure: In a first phase A, the homeostatic state of the CVS model is computed, prior to the simulation of BiVAD supported heart beats in phase B and the occurrence of an additional myocardial infarction or a valvular heart disease in phase C. Depending on the boundary conditions of the patient and the related condition, it takes several heart cycles before periodicity is eventually established in each phase $\in$ A,B,C. The MTP model is called after each supported heart beat and computes new mean reservoir temperatures based on the results of the last heart cycle. This information then updates the SCVS model for the subsequent heart beat.

Additional infarction or valvular heart disease Myocardial infarction or valvular heart diseases can be mimicked as described in 6.1.1.3 and 6.1.1.4. The diseases are introduced in a last step, represented by phase C in figure 6.3. An earlier event occurrence is possible and would lead to the same periodic result. However, it would omit the possibility of comparing the supported diseased and supported undiseased heart cycle at valid periodic states. Consecutive heart beats are simulated until the maximum error drops below the defined threshold, as in (6.7).

6.1.3. Case study

A case study is carried out in order to apply the introduced models in a meaningful context. Therefore, the three presented patient geometries and corresponding HF conditions as well as additional diseases (MI, VHD) are applied within the SCVS model according to the scheme presented in the previous section 6.1.2.

The primary goal of the case study is to investigate the influence of differing, clinically relevant cases on the technical BiVAD. This is important for two reasons: Firstly, engineering questions regarding the impact of e.g. heart size or HF condition on the device performance need to be answered. Secondly, the knowledge of the BiVAD response to differing patient conditions may allow for better patient selection or pharmaceutical adjustment prior to BiVAD support. A systematic investigation of the effects of differing support intensities on the CVS system is not a focus here, as it has previously been studied by [54] and [43].

Besides the influence of CVS changes on the BiVAD, the case study may demonstrate the robustness of the presented model. By extensively varying the heart geometry and patient condition, the pressure-volume (pV) relation of both CVS and EU can drastically be altered. Thereby contact conditions and snap-through phenomena can be changed, both challenging the solution process. However, under the assumption of many more patient cases to be simulated in the future, robustness regarding changing geometries and CVS conditions is key.

Cases Any combination of patient geometry, HF condition, MI and considered VHD is possible. A relevant selection of these possible combinations is chosen and analyzed. Table 6.1 gives an overview of the simulated cases. They are analyzed according to the following scheme:

1. Specific HF patients: The indication of the BiVAD is to support patients suffering from HF. Therefore, the three available patients $p1$, $p2$ and $p3$, each with a specific heart geometry and three different conditions, NO-HF, LA-HF and HA-HF, are supported with similarly sized EUs (cf. 6.1.1).

2. Mitral valve regurgitation: Mitral valve regurgitation (MR), which is synonymous with valve insufficiency, has one of the highest incidences among VHD in HF patients and is a more likely adverse event, stemming directly from mechanical heart support (cf. 6.1.1.4). Hence, MR is focused on within the considered VHD. Its effect on the SCVS is analyzed by systematically comparing all patients under LA-HF as well as all HF conditions in patient $p1$ subject to this additional burden.

Patient	HF condition		Additional diseases			
		NO	MI	AS	AR	MR
$p1$	NO-HF	✓	✓	✓	✓	✓
	LA-HF	✓				✓
	HA-HF	✓				✓
$p2$	NO-HF	✓				
	LA-HF	✓			✓	✓
	HA-HF	✓				
$p3$	NO-HF	✓				
	LA-HF	✓				✓
	HA-HF	✓	✓	✓		

Table 6.1.: Overview on the studied cases. The diseases are abbreviated as follows: AS=aortic stenosis, AR=aortic regurgitation, MR=mitral regurgitation and MI=myocardial infarction. The case without additional disease (only with one of the HF conditions) is denoted with NO.

3. Other diseases: Further cases are investigated, namely myocardial infarction (MI) and aortic stenosis (AS) in patient $p1$ and $p3$ with NO-HF and HA-HF, respectively, as well as aortic regurgitation (AR) in $p1$ and $p2$ with NO-HF and LA-HF, respectively. Even if these cases are less important in the context of BiVAD support, they may occur in HF patients as stated in 6.1.1.3 and 6.1.1.4. Note that mitral stenosis (MS) is not considered due to the low incidence within the group of HF patients.

Evaluation Among all possible results (cf. section 3.5), a reasonable set is chosen to analyze the coupled response of the investigated cases.

Depictions of ventricular and EU pV loops contain much of the relevant information and are therefore given for each of the cases. Their areas represent the cardiac stroke work SW_{Heart} and EU work W^k_{EU}. SW_{Heart} may be any of $\{SW^\ell + SW^r, SW^\ell, SW^r\}$, depending on the considered system. Their changes ΔSW_{Heart} due to BiVAD support are obtained by subtracting the areas of these pV loops with and without cardiac support:

$$\Delta SW_{\text{Heart}} = SW_{\text{Heart,+BiVAD}} - SW_{\text{Heart}}, \tag{6.8}$$

where $SW_{\text{Heart}} \in \{SW^\ell + SW^r, SW^\ell, SW^r\}$. In the case of an additional MI or VHD, equation (6.8) changes to

$$\Delta SW_{\text{Heart,disease}} = SW_{\text{Heart,+BiVAD+disease}} - SW_{\text{Heart,+BiVAD}}, \tag{6.9}$$

with the disease $\in \{\text{MI}, \text{AS}, \text{AR}, \text{MR}\}$. Note that the equation (6.9) reflects the change in stroke work due to the disease, not due to the BiVAD support. In order to compute the EU work, equation (3.121) is utilized. The total of all three EUs or the fractions related to either the LV or RV are considered. In accordance with the EUs' geometrical arrangement (cf. figure 6.1), $W^1_{\text{EU}} + W^2_{\text{EU}}$ are assigned to the LV, W^3_{EU} to the RV. A change can be quantified by subtracting

EU	Valve opening [-]		
	$y_{\text{inlet,1}}$	$y_{\text{inlet,2}}$	y_{outlet}
1	0.6	0.2	0.5
2	0.7	0.15	0.5
3	0.4	0.1	0.4

Table 6.2.: Utilized valve control values in the case study.

the non-diseased from the diseased EU work value

$$\Delta W_{\text{EU}}^{k} = W_{\text{EU+disease}}^{k} - W_{\text{EU}}^{k}. \tag{6.10}$$

In addition, the efficiency of BiVAD-CVS energy transmission is derived. It relates the change in stroke work to the sum of all EU work according to

$$\eta_{\text{BiVAD-CVS}} = \frac{SW_{\text{Heart}}}{\sum_{k=1}^{3} W_{\text{EU}}^{k}}. \tag{6.11}$$

Likewise, the power supply efficiency of the BiVAD is assessed by computing the ratio of the output to the input power within the BiVAD only. It reads

$$\eta_{\text{BiVAD}} = \frac{\sum P_{\text{EU}}}{P_{\text{logic}} + P_{\text{PP}} + \sum P_{\text{V}}}. \tag{6.12}$$

The total electrical power consumption and the individual component contributions of pump, valves and logical unit within the BiVAD are further depicted and quantified. They are closely related to the attained mean reservoir temperatures $\Delta\hat{T}_{\text{HPR}}$ and $\Delta\hat{T}_{\text{LPR}}$, which are additionally presented.

Parameters Standard parameters of the BiVAD model, as listen in table 3.5, are utilized. If not otherwise stated, the control parameters in table 3.4 are used. The valve control value signals are the same for all cases and listed in table 6.2. The pump control value in patient $p1$ is set to $y_{\text{PP}}(p1) = 0.35$, which is slightly above the corresponding values of the smaller patients $p2$ and $p3$: $y_{\text{PP}}(p2) = y_{\text{PP}}(p3) = 0.33$. This variation allows both the comparison at equal and differing control values. CVS related parameters (cf. 3.3) remain unaltered, except those of the medical cases, addressed in 6.1.1.

Solution Heart and EU geometries are discretized as outlined in section 2.3.1. Tetrahedral elements with an approximate edge length of 2 mm are utilized to represent the heart. For the EUs, 1 mm hexahedral elements with F-BAR technology [20] are used. Table 6.3 summarizes the number of unknowns for each of the applied combinations. The work load of each simulation is distributed to a number of cores in the range $\text{n}_{\text{cores}} \in [15, 47]$, depending on availability. One heart cycle is calculated in a varying number of steps, which span the range of $\text{n}_{\text{steps}} \in [200, 1000]$. The low core and step numbers are typically used to compute the homeostatic state of the CVS, prior

Name		Patients		
		$p1$	$p2$	$p3$
3D	Heart	126102	110670	101178
	Implant	107004	105690	104904
	$\sum$	233106	216360	206082
0D	Circulation	16		
	Assist device	43		
	$\sum$	59		
3D-0D	$\sum$	233165	216419	206141

Table 6.3.: Number of unknowns for patients $p1$, $p2$ and $p3$ under cardiac assist, separated into structural (3D) and 0D degrees of freedom. The 0D unknowns equally apply in all patients.

to a BiVAD supported CVS simulation (cf. phase A in figure 6.3). However, due to a variation of time step sizes, the exact number of steps varies. First of all, a predefined time step size course is utilized, as presented in section 3.4.1.1. Here, the typical fine time step size is set to $\Delta t_{\text{fine}} = 1.0$ ms and the time step factor to $f_{\Delta t} = 4.0$. Secondly, time step size adaption is allowed in the case of non-convergence, which may result from contact or snapping phenomena. Pseudo-transient continuation [31], as introduced in section 3.3.4, is utilized for the same reasons and the initial value in (3.118) is set to $k_{\text{PTC}}^{i=1} = 0.1$.

6.2. Results

This section presents the case study results. It is organized in accordance with the case groups, formulated in 6.1.3: First, the coupled SCVS response to a variation of specific HF patients is presented in section 6.2.1, followed by the results of the considered MR cases in 6.2.2. The influence of other additional diseases is presented in section 6.2.3. All results presented here refer to the solution in its periodic state, hence to the end of phase A, B or C in figure 6.3.

6.2.1. Specific HF patients

Three different conditions are systematically compared for all available patients $p1$, $p2$ and $p3$. The results are given in this section. The first three figures 6.4, 6.5 and 6.6 present pV curves as well as cardiac stroke work changes and EU work done on the heart for the patients $p1$, $p2$ and $p3$, respectively. The following explanation holds for all of them: The graphs a), b) and c) each show the unsupported and the supported ventricular pV curves, where the latter is denoted with $(\bullet)_{\text{+BiVAD}}$, for the HF conditions NO-HF, LA-HF and HA-HF, respectively, along with those of the EUs. The bar charts d), e) and f) represent the corresponding work. For the CVS, they are given as change in cardiac stroke work due to BiVAD support, hence comparing the unsupported and supported configuration according to (6.8). In contrast, the BiVAD work is given as actual area under the EU pV curves. The bar plots d), e) and f) depict the work done on LV+RV as well

as of LV and RV alone. The assignment of the EU is in accordance with the geometrical arrangement. It is also given particularly for the EU work in d) of each of the figures. The indicated bar values are additionally given as a number on top or below the bars. Likewise, the relative change of the cardiac stroke work is noted in percent and relative to the unsupported condition. For better comparability, the pV curves of the implant's EU^2, located at the posterior LV wall, are depicted in figure 6.7 for the patients $p1$, $p2$ and $p3$ in the studied conditions.

Figure 6.8 visualizes the derived efficiencies of the system: a) to c) show the support efficiency as in (6.11), thus the ratio of cardiac stroke work change to the summed work of all EUs. It is given for the heart as well as individually for the two ventricles. The indicated values are again given above or below the bars. The bar charts d), e) and f) present the technical efficiency of the BiVAD as it translates the electrical input power to an output support power according to (6.12) and its values are explicitly given above the bars in percent.

Figure 6.9 summarizes the results related to power consumption and consequent BiVAD heating. The bar charts a), b) and c) visualize the component specific power consumption for the patients $p1$, $p2$ and $p3$. Their values are noted above the individual bars in watts. The sum of all electrical powers is further given for each of the HF conditions, NO-HF, LA-HF and HA-HF. The resulting mean reservoir temperatures, $\Delta\hat{T}_{\mathrm{HPR}}$ and $\Delta\hat{T}_{\mathrm{LPR}}$, as they are computed in the MTP model, are depicted on the right in d), e) and f).

6.2.2. Mitral valve regurgitation

The results of the systematic investigation on MR effects on the SCVS are given in this section. Among all possible combinations, MR was added to all HF conditions of patient $p1$ and to all patients subject to LA-HF condition.

Figure 6.10 presents the pV curves for patient $p1$ in the three considered HF conditions NO-HF, LA-HF and HA-HF in a), b) and c), respectively. Here, the supported pV curves with and without additional MR are drawn. For the EU, only the pV loops with MR are displayed for visibility reasons. The right bar charts show absolute and relative changes of system-related work in reference to the supported configuration without MR.

Figure 6.11 shows the results for the LA-HF condition in all three patients $p1$, $p2$ and $p3$ in the same fashion as explained for figure 6.10. Note that the graphs b) and e) in figure 6.11 are the same as a) and d) in 6.10.

BiVAD efficiency η_{BiVAD}, power consumption and resulting mean reservoir temperatures are depicted in figure 6.12 a), b) and c) for patient $p1$ and in d), e) and f) for the LA-HF condition. Owing to the systematic selection of cases, the LA-HF case in the left column is identical to the $p1$ results in the right column.

Another insight in the BiVAD response to altering CVS conditions, here by occurrence of MR, is given in figure 6.13, which depicts the pressure difference between HPR and LPR, $\Delta p_{\mathrm{Res}} =$

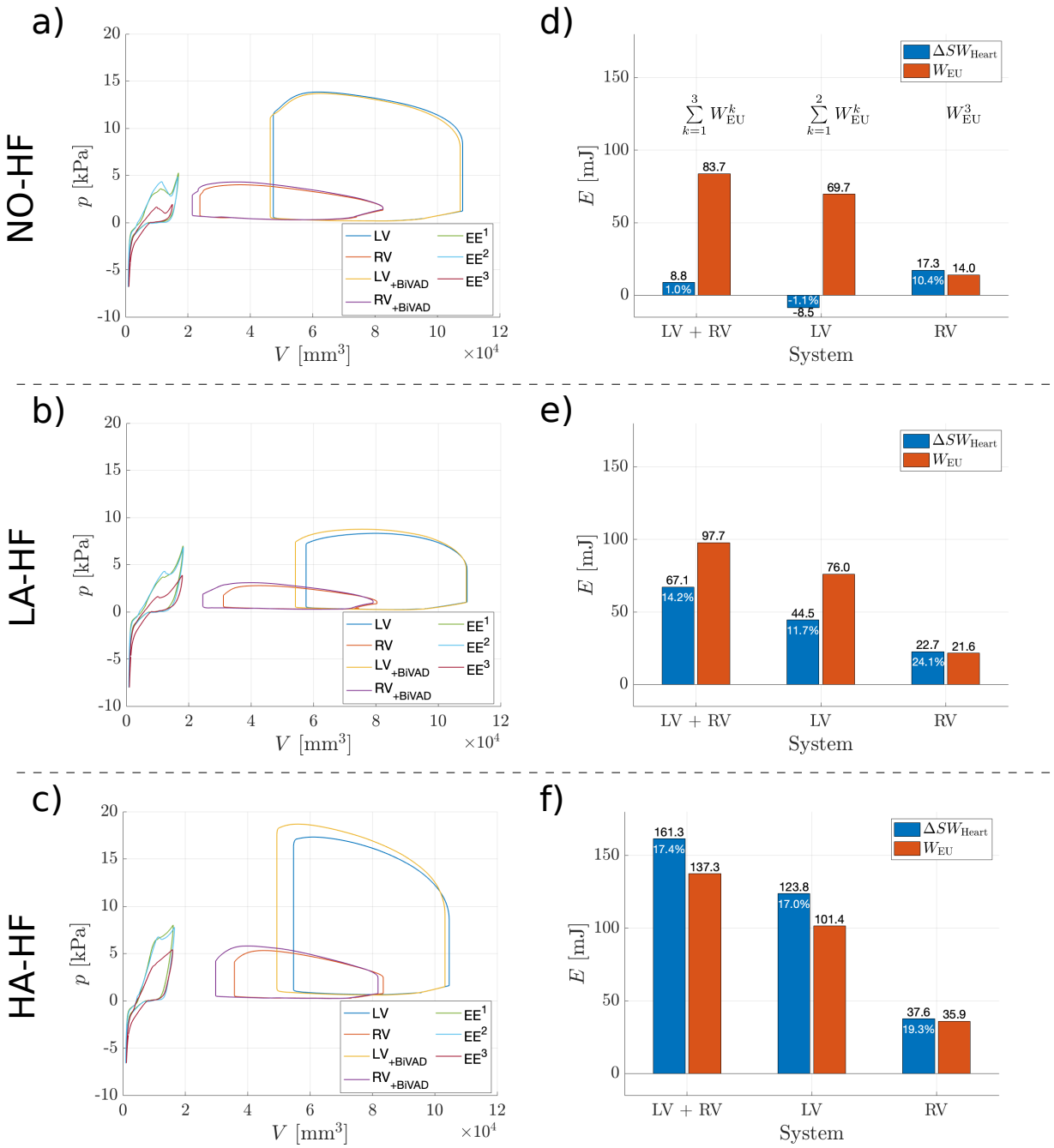

Figure 6.4.: Patient $p1$: Pressure volume loops of heart and EUs are shown in a) to c) for the unsupported and the supported $(\bullet)_{\text{+BiVAD}}$ configuration and for each of the HF cases. The cardiac stroke work increase ΔSW_{Heart} under support and the applied EU work W_{EU} are visualized in d) to f) for the total system as well as for each of the ventricles specifically and again for all HF cases. The work differences as well as the relative changes in the CVS system are numerically displayed at the bars' top. In accordance with the geometrical arrangement (cf. figure 6.1), EU^1 and EU^2 are related to the LV and EU^3 corresponds to the RV. Note that the scales are identical for all graphs of a kind to enhance comparability.

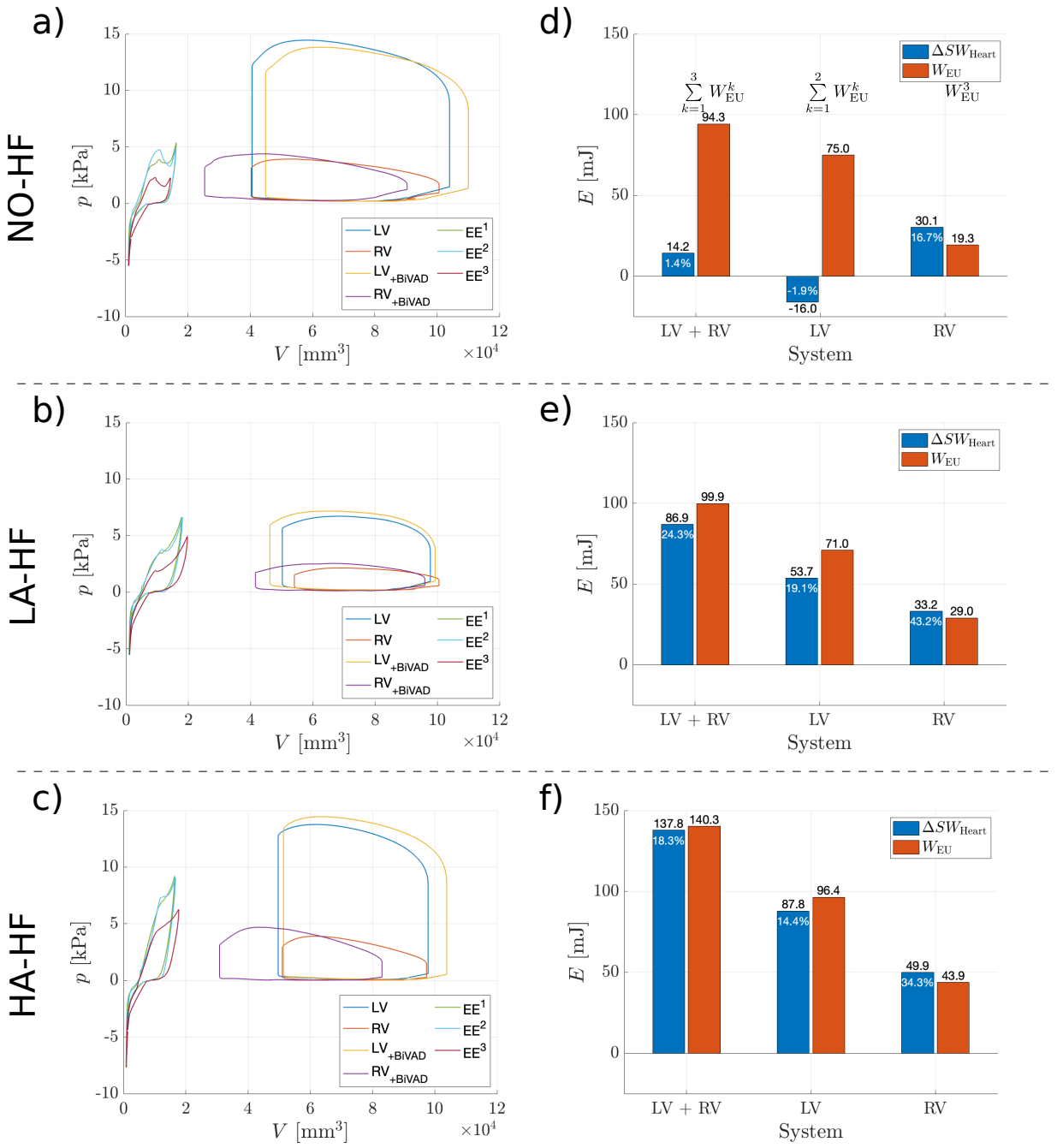

Figure 6.5.: Patient $p2$: Pressure volume loops of heart and EUs are shown in a) to c) for the unsupported and the supported $(\bullet)_{\text{+BiVAD}}$ configuration and for each of the HF cases. The cardiac stroke work increase ΔSW_{Heart} under support and the applied EU work W_{EU} are visualized in d) to f) for the total system as well as for each of the ventricles specifically and again for all HF cases. The work differences as well as the relative changes in the CVS system are numerically displayed at the top of the bars. In accordance with the geometrical arrangement (cf. figure 6.1), EU^1 and EU^2 are related to the LV and EU^3 corresponds to the RV. Again, the scales are identical for all similar graphs to enhance comparability.

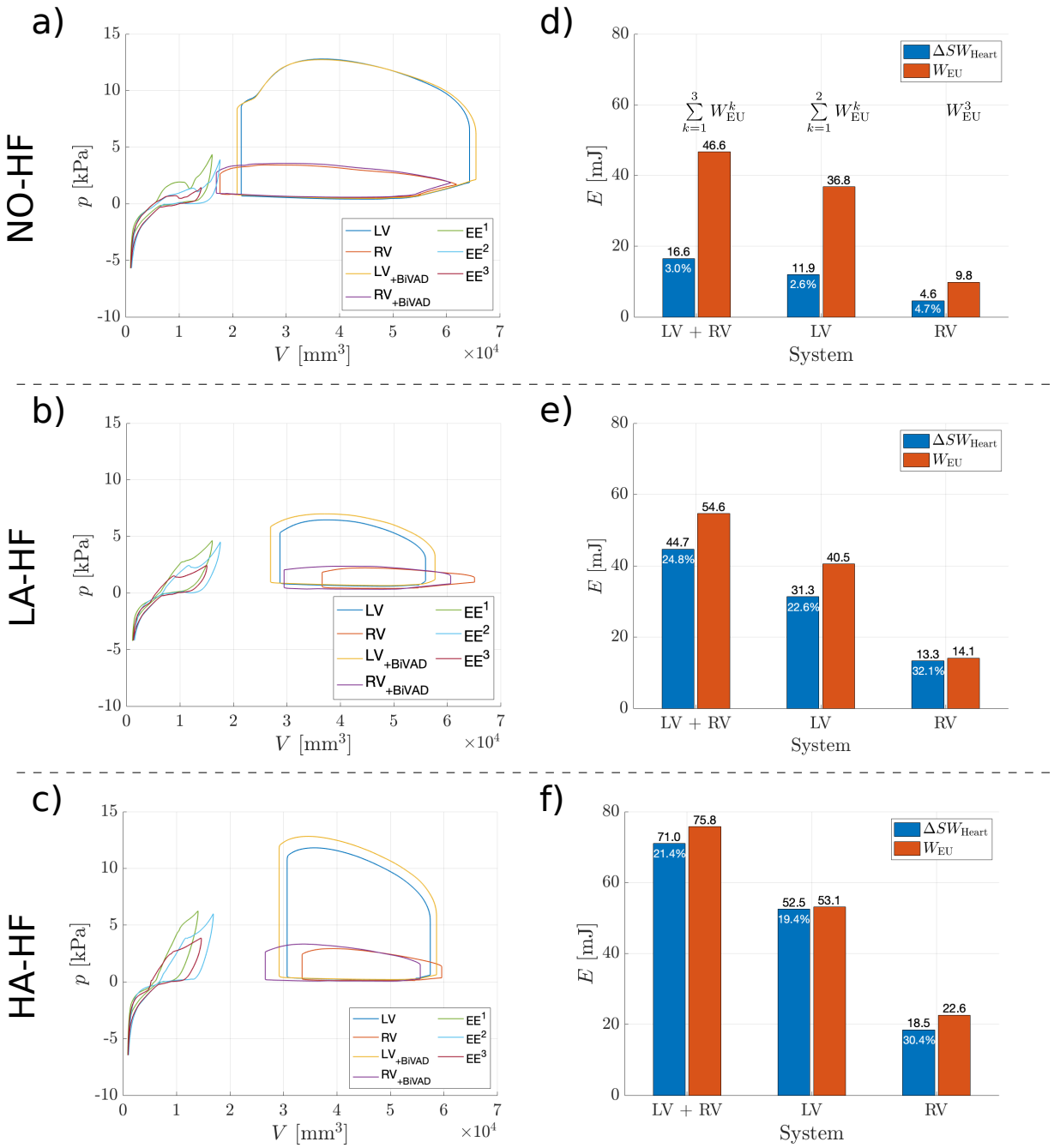

Figure 6.6.: Patient $p3$: Pressure volume loops of heart and EUs are shown in a) to c) for the unsupported and the supported $(\bullet)_{\text{+BiVAD}}$ configuration and for each of the HF cases. The cardiac stroke work increase ΔSW_{Heart} under support and the applied EU work W_{EU} are visualized in d) to f) for the total system as well as for each of the ventricles specifically and again for all HF cases. The work differences as well as the relative changes in the CVS system are numerically displayed at the bars' top. In accordance with the geometrical arrangement (cf. figure 6.1), EU^1 and EU^2 are related to the LV and EU^3 corresponds to the RV. The scales are identical for all similar graphs to enhance comparability.

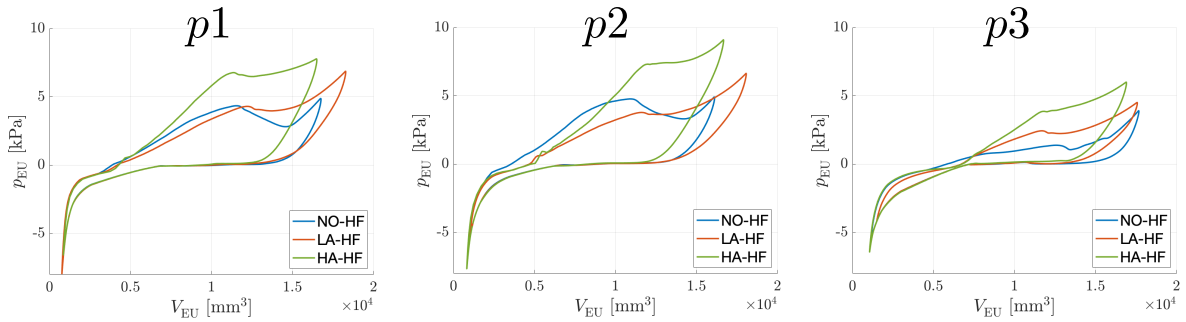

Figure 6.7.: pV curves of EU[2], located on the posterior LV wall, of the specific HF patients $p1$, $p2$ and $p3$ for the three HF conditions under BiVAD support. The EU inflation is represented by the upper side of the pV loop, running from the bottom left to the top right point. The following deflation follows the lower side of the loop back to the initial point.

Patient	HF condition	BiVAD efficiencies for cases			
		NO	MI	AS	AR
$p1$	NO-HF	1.02	1.0	1.33	1.0
$p2$	LA-HF	1.07			0.87
$p3$	HA-HF	0.95	0.90	0.97	

Table 6.4.: BiVAD efficiencies as a ratio of pV power delivered to the body and the sum of all input electrical powers for the three additional diseases MI, AS and AR.

$p_{HPR} - p_{LPR}$. It is the property that drives the pump power consumption. The relation can be reviewed in figure 3.4 in the preceding chapter 3.

6.2.3. Other diseases

The results of the remaining cases are given in this section. Figure 6.14, 6.15, 6.16 depict the conditions myocardial infarction, aortic stenosis and aortic regurgitation, respectively. The explanation of the graphs is identical to the MR result description. In figure 6.17, only power consumption and reservoir temperatures are shown. The corresponding BiVAD efficiencies are given in table 6.4. The reservoir pressure difference with and without additional diseases is depicted in figure 6.18.

6.3. Discussion

The results presented in 6.2 are discussed in this section, which is subdivided as follows: The results of the specific HF patients are examined in 6.3.1, followed by those with MR in 6.3.2. The results of the remaining additional diseases are discussed in 6.3.3. An overall conclusion of the findings is given in section 6.4.

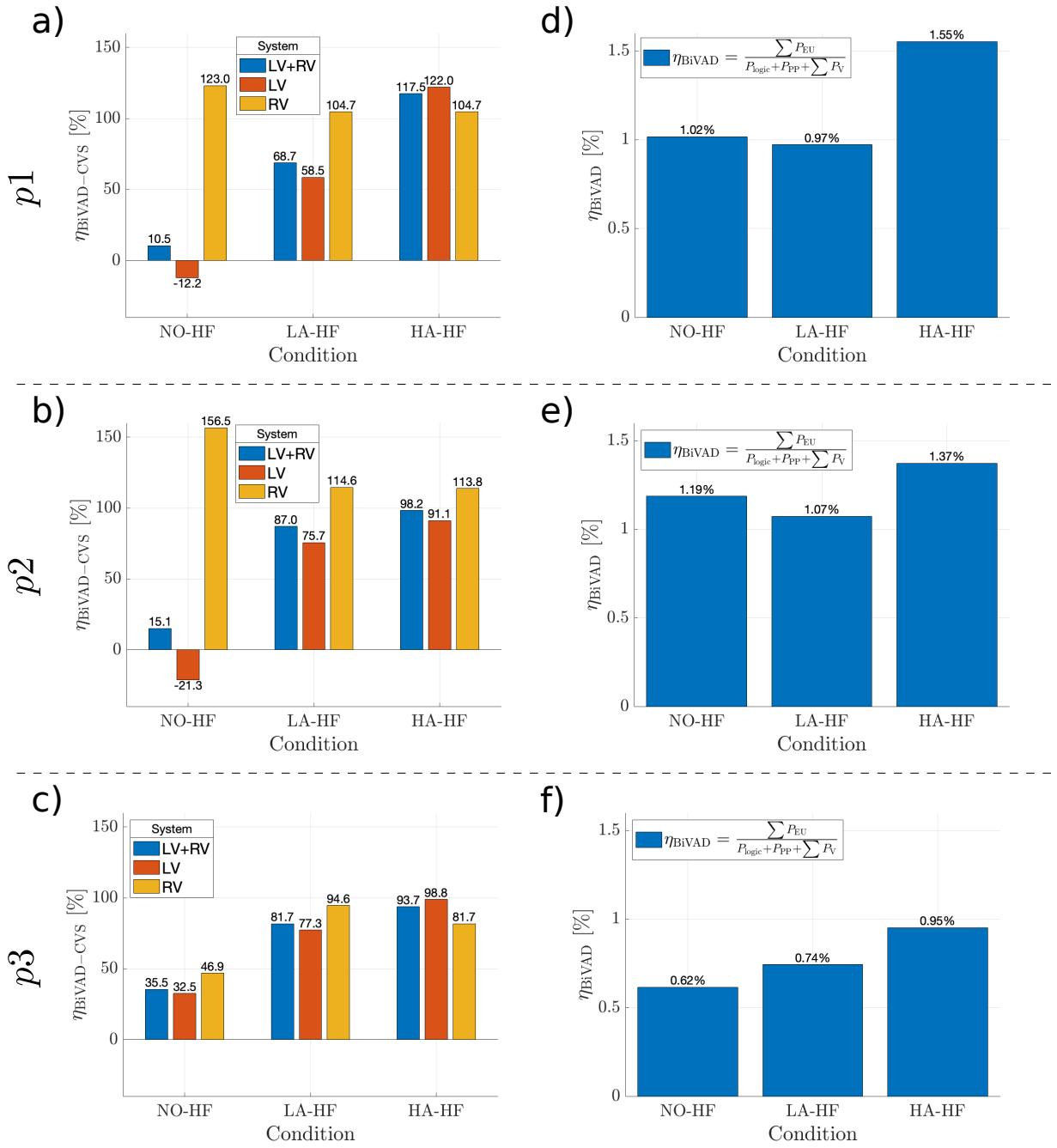

Figure 6.8.: The system's efficiencies are given for all patients and HF conditions: For the support interface in a) to c), relating the increase in cardiac stroke work to the sum of EU work for the three patients. In addition to the total efficiency, the ventricular-specific efficiencies are given. In accordance with the geometrical arrangement (cf. figure 6.1), EU^1 and EU^2 are related to the LV and EU^3 corresponds to the RV. The BiVAD internal efficiency is plotted in d) to f), relating the totally EU output power to the total consumed electrical input power. Scales are identical for all graphs of a kind to enhance comparability.

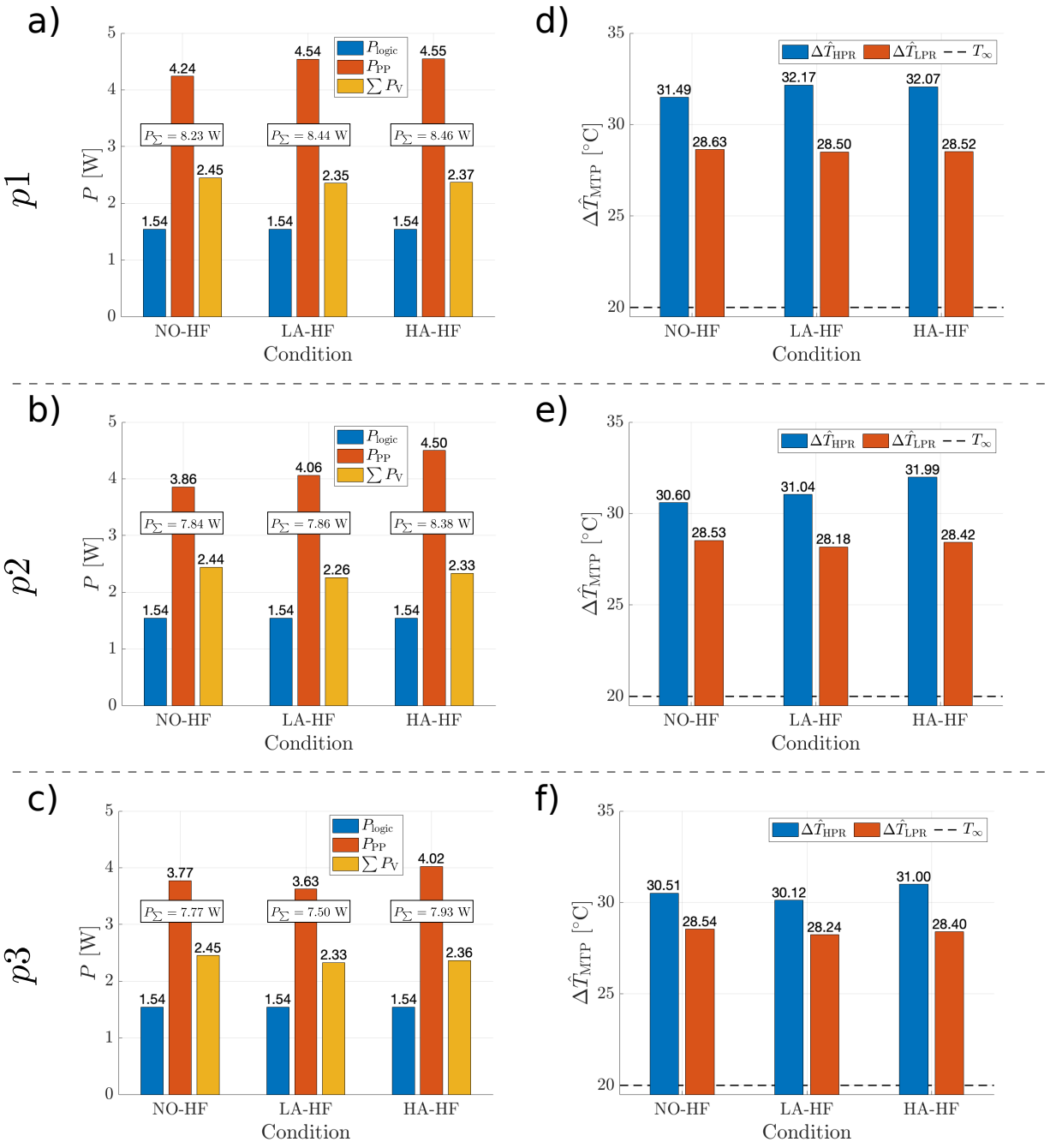

Figure 6.9.: The system's electrical power contributions and resulting mean reservoir temperatures are given for all patients and HF cases: Power contributions in a) to c) with absolute values in watt. A power sum $P_\sum$ is additionally displayed for each of the cases. The final mean temperatures for both reservoirs are presented in d) to f) as excess over the environmental temperature T_∞. The scales are identical for all similar graphs to enhance comparability.

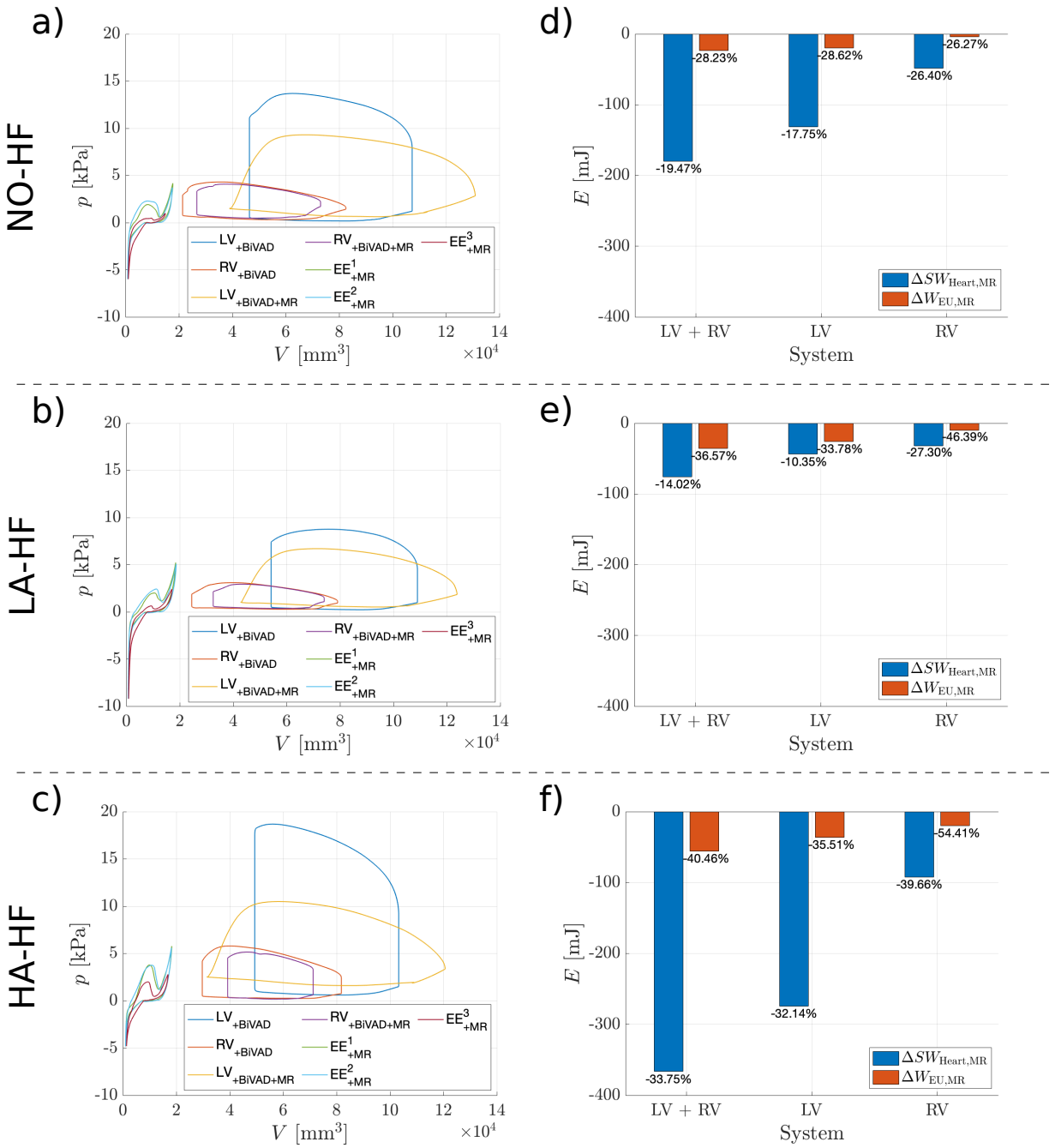

Figure 6.10.: MR in patient $p1$ for all HF conditions: Pressure volume loops of heart and EUs are shown in a) to c) for the supported $(\bullet)_{\text{+BiVAD}}$ and the supported CVS with MR $(\bullet)_{\text{+BiVAD+MR}}$. The relative cardiac stroke work change $\Delta SW_{\text{Heart,MR}}$ after MR occurrence and the change in EU work $\Delta W_{\text{EU,MR}}$ due to MR are visualized in d) to f) for the total system as well as for each of the ventricles specifically. The relative changes are numerically displayed below the bars and refer to the supported condition without MR. In accordance with the geometrical arrangement (cf. figure 6.1), EU^1 and EU^2 are related to the LV and EU^3 corresponds to the RV. The scales are identical for all similar graphs to enhance comparability.

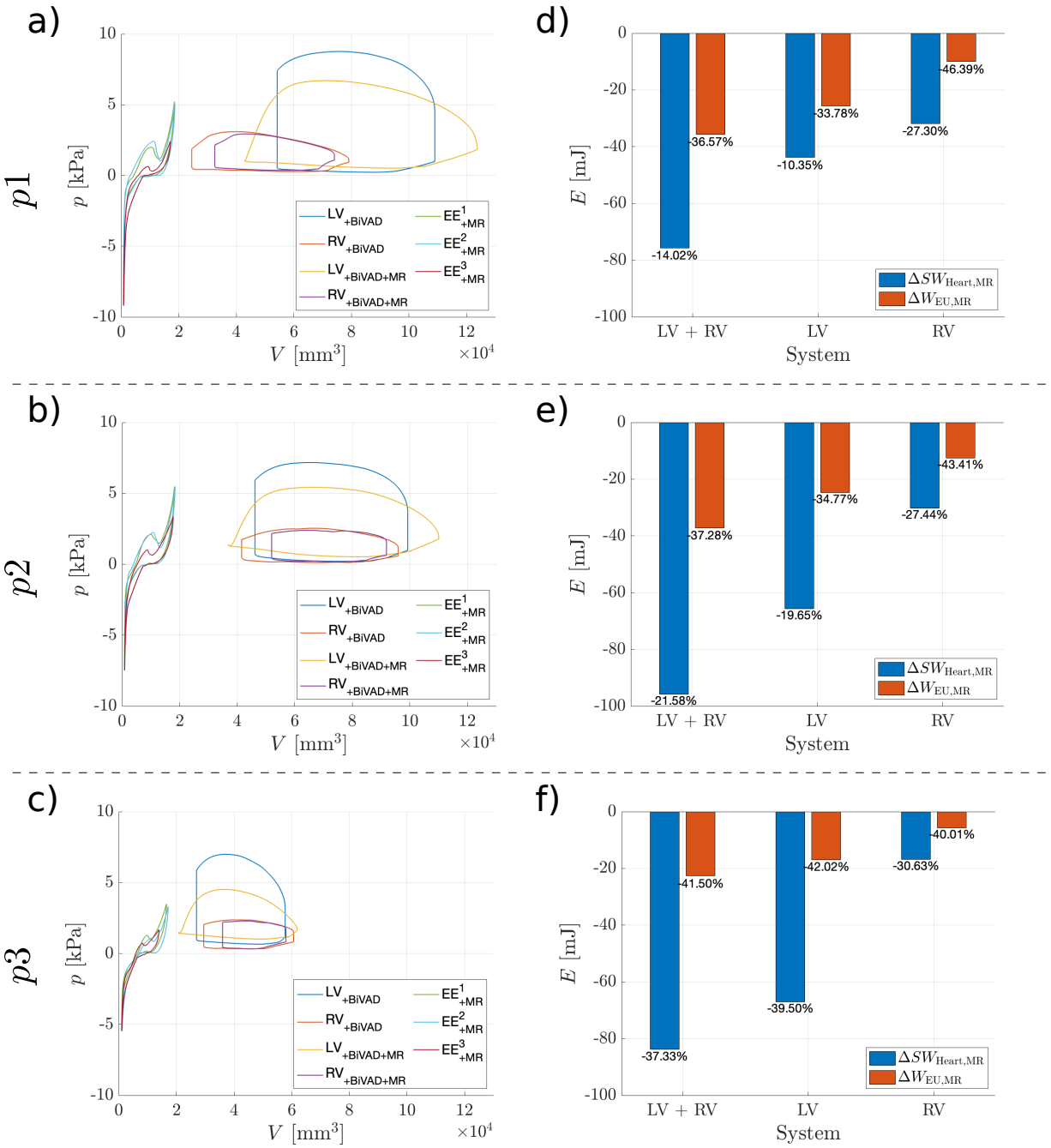

Figure 6.11.: MR with LA-HF condition for all patients: Pressure volume loops of heart and EUs are shown in a) to c) for the supported $(\bullet)_{\text{+BiVAD}}$ and the supported CVS with MR $(\bullet)_{\text{+BiVAD+MR}}$. The relative cardiac stroke work change $\Delta SW_{\text{Heart,MR}}$ after MR occurrence and the change in EU work $\Delta W_{\text{EU,MR}}$ due to MR are visualized in d) to f) for the total system as well as for each of the ventricles specifically. The relative changes are numerically displayed below the bars and refer to the supported condition without MR. In accordance with the geometrical arrangement (cf. figure 6.1), EU^1 and EU^2 are related to the LV and EU^3 corresponds to the RV. The scales are identical for all similar graphs to enhance comparability.

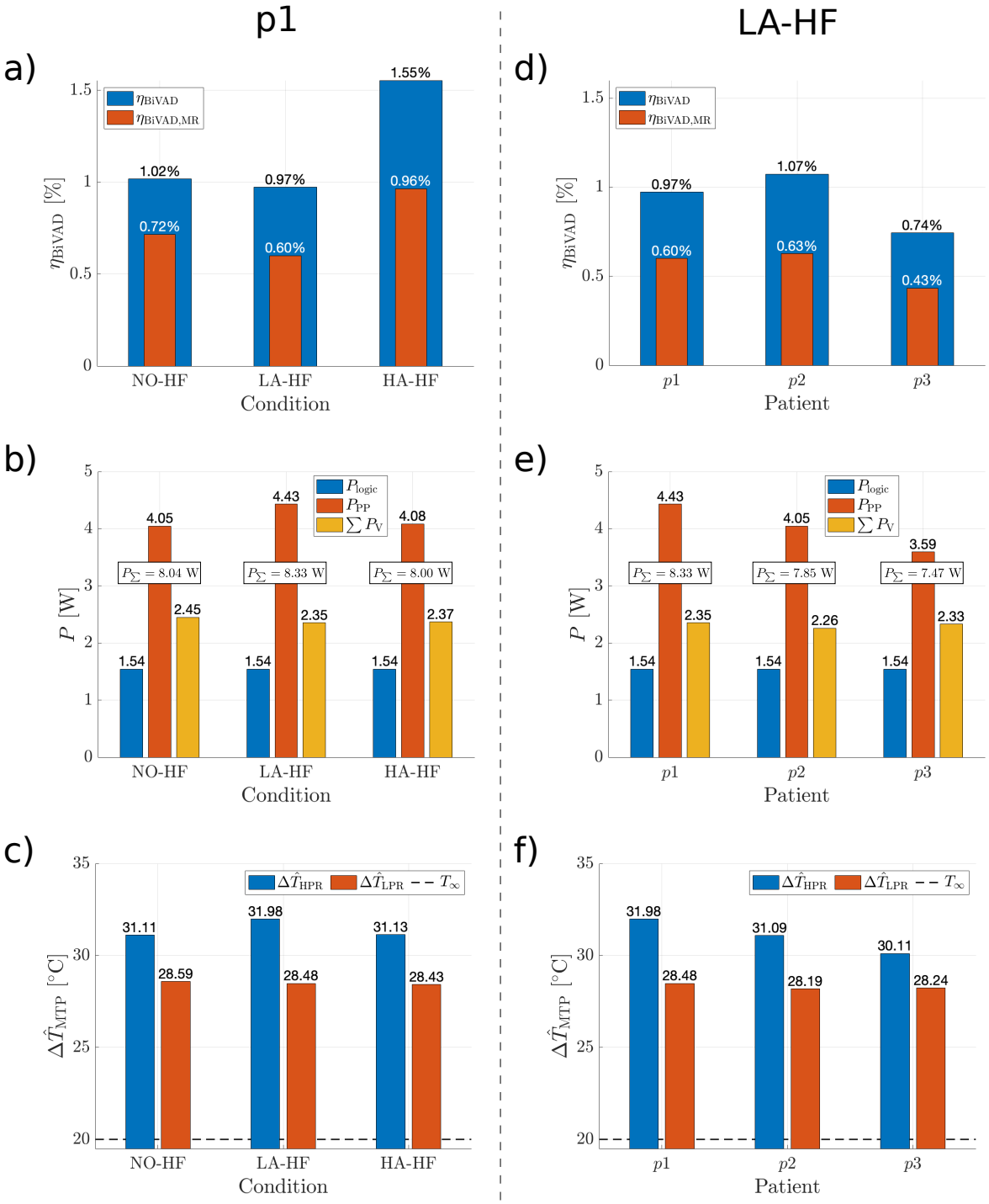

Figure 6.12.: MR and its effects on the BiVAD: The results for patient $p1$ under all HF conditions are given in a) to c), while those of the LA-HF condition for all patients are depicted in d) to f). For both columns, the BiVAD efficiency is plotted with and without MR and the respective values are noted above the bars. Component power contributions and the case specific power sum are given in b) and e). Likewise, the resulting mean reservoir temperatures are plotted in c) and f).

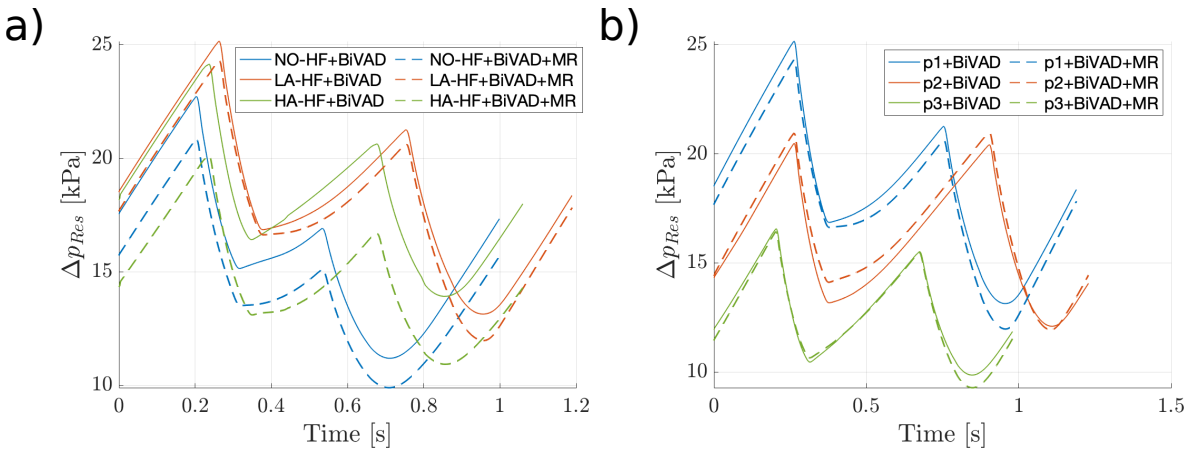

Figure 6.13.: MR effect on difference reservoir pressure $\Delta p_{\text{Res}} = p_{\text{HPR}} - p_{\text{LPR}}$ for patient $p1$ in the three conditions NO-HF, LA-HF and HA-HF in a) as well as for the LA-HF condition in patients $p1$, $p2$ and $p3$ in b). Δp_{Res} is given for the supported cases without MR (+BiVAD) as a non-dashed line and with additional MR (+BiVAD+MR) as a dashed line.

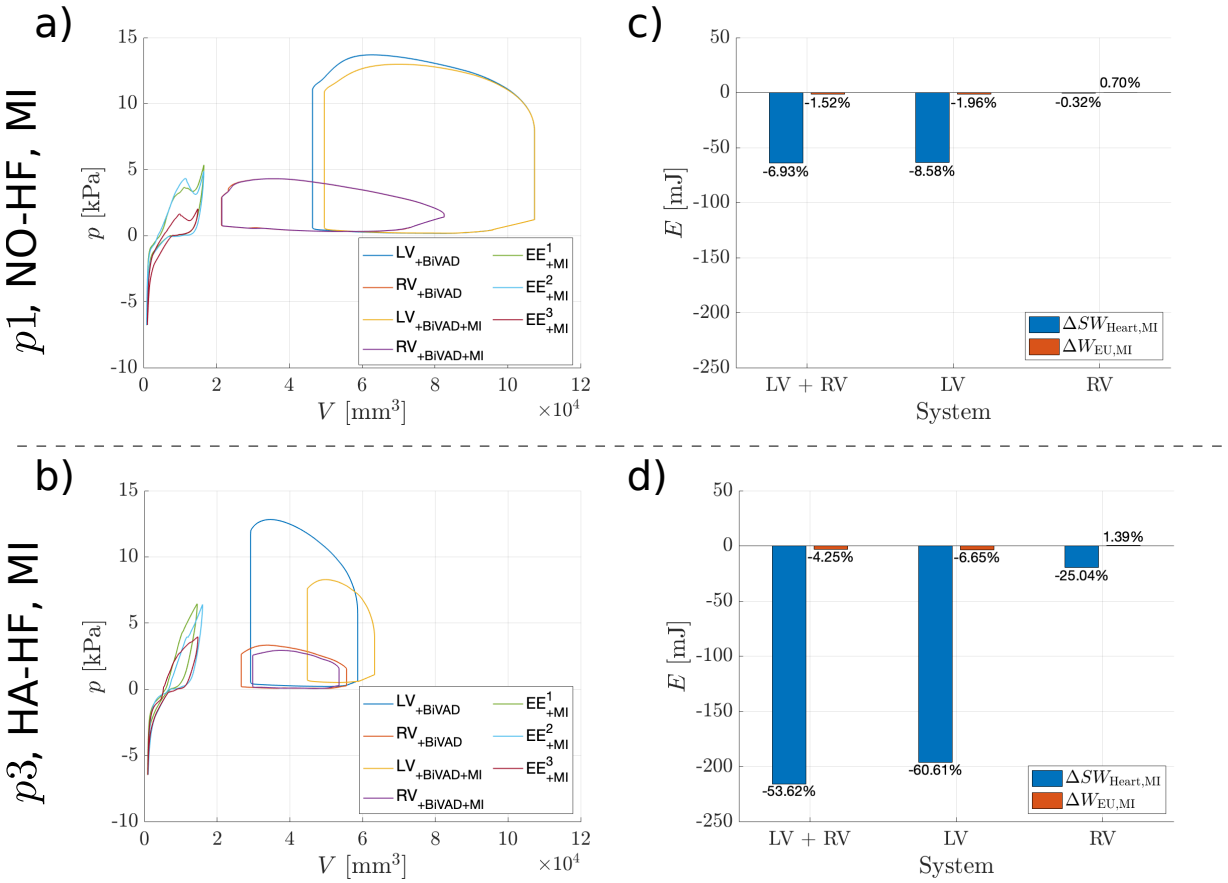

Figure 6.14.: Infarct pV curves in a) for patient $p1$ in NO-HF condition and for patient $p3$ in HA-HF condition in b). The respective changes in cardiac stroke work and EU work are depicted in c) and d).

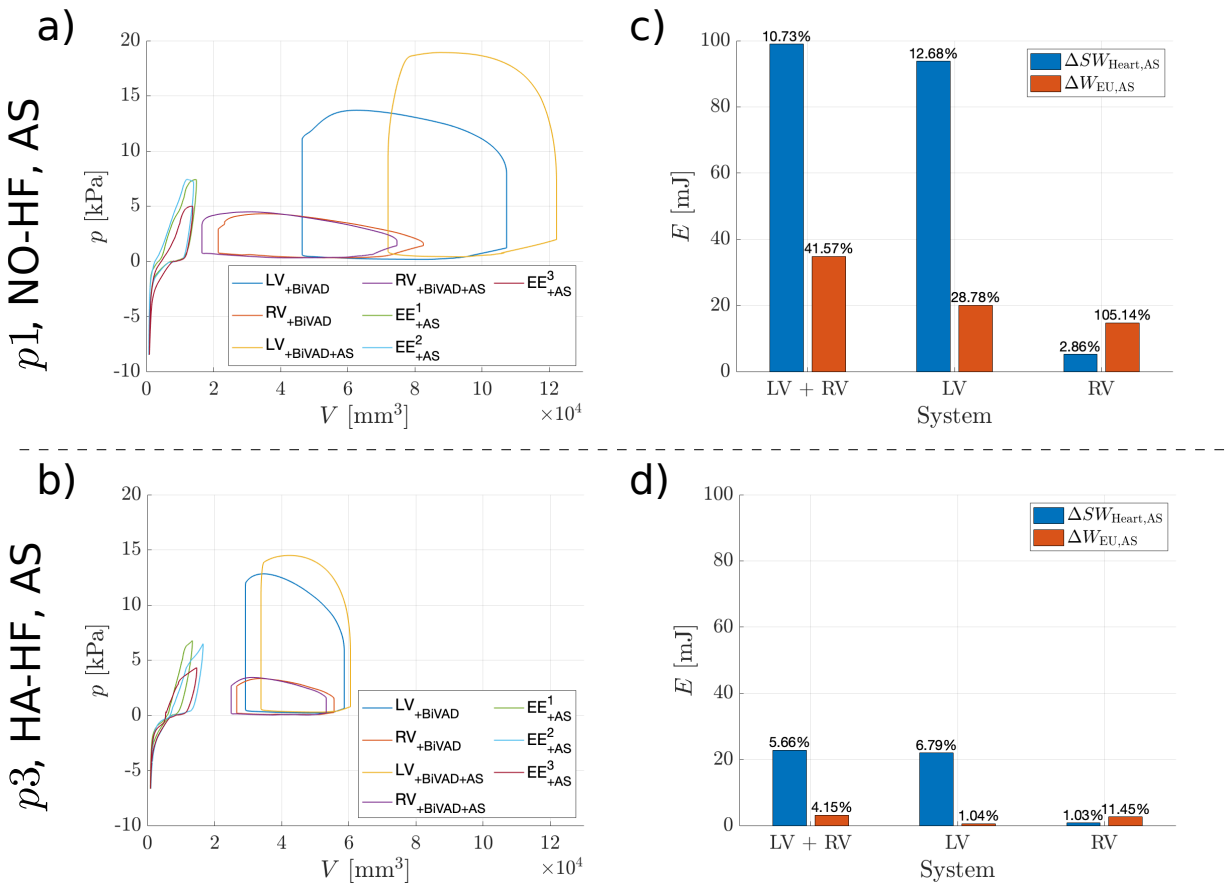

Figure 6.15.: Aortic stenosis pV curves in a) for patient $p1$ in NO-HF condition and for patient $p3$ in HA-HF condition in b). The respective changes in cardiac stroke work and EU work are depicted in c) and d).

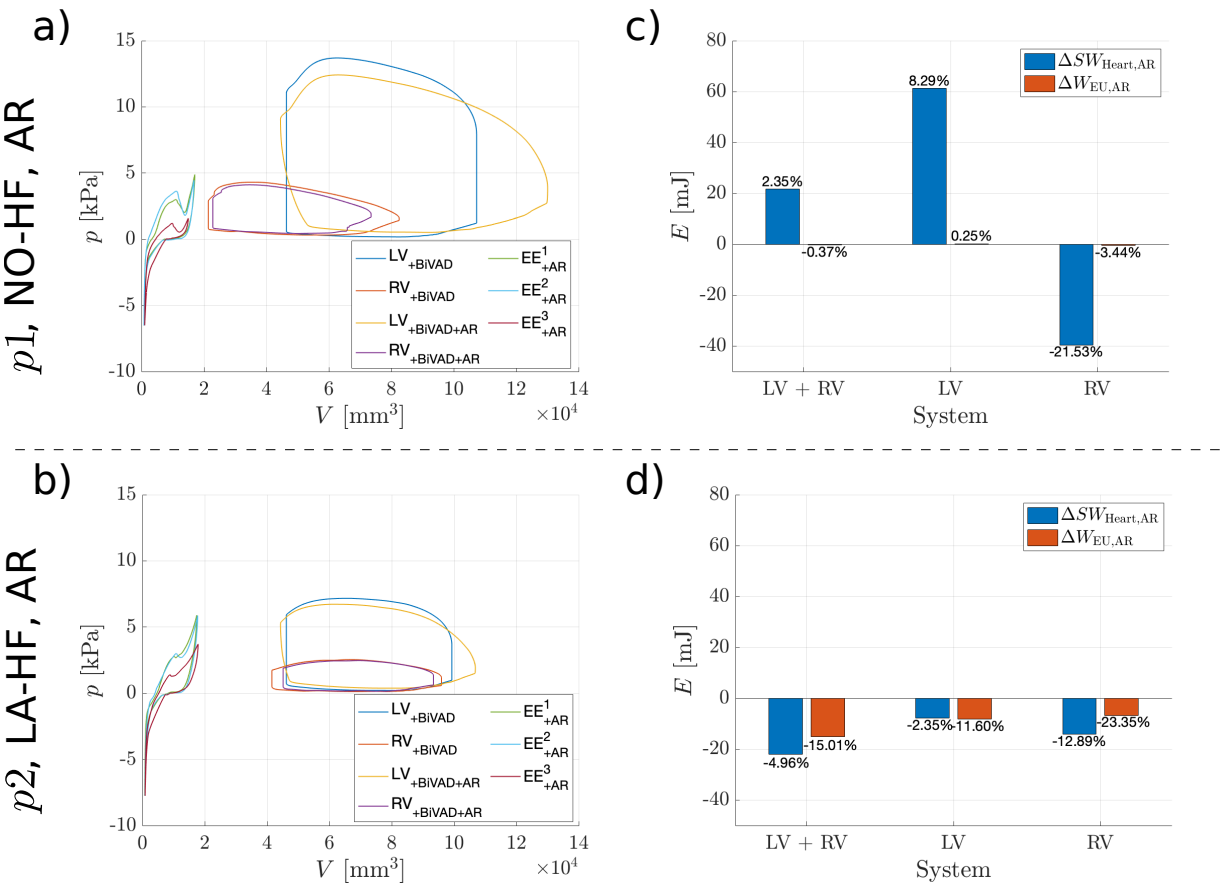

Figure 6.16.: Aortic regurgitation pV curves in a) for patient $p1$ in NO-HF condition and for patient $p2$ in LA-HF condition in b). The respective changes in cardiac stroke work and EU work are depicted in c) and d).

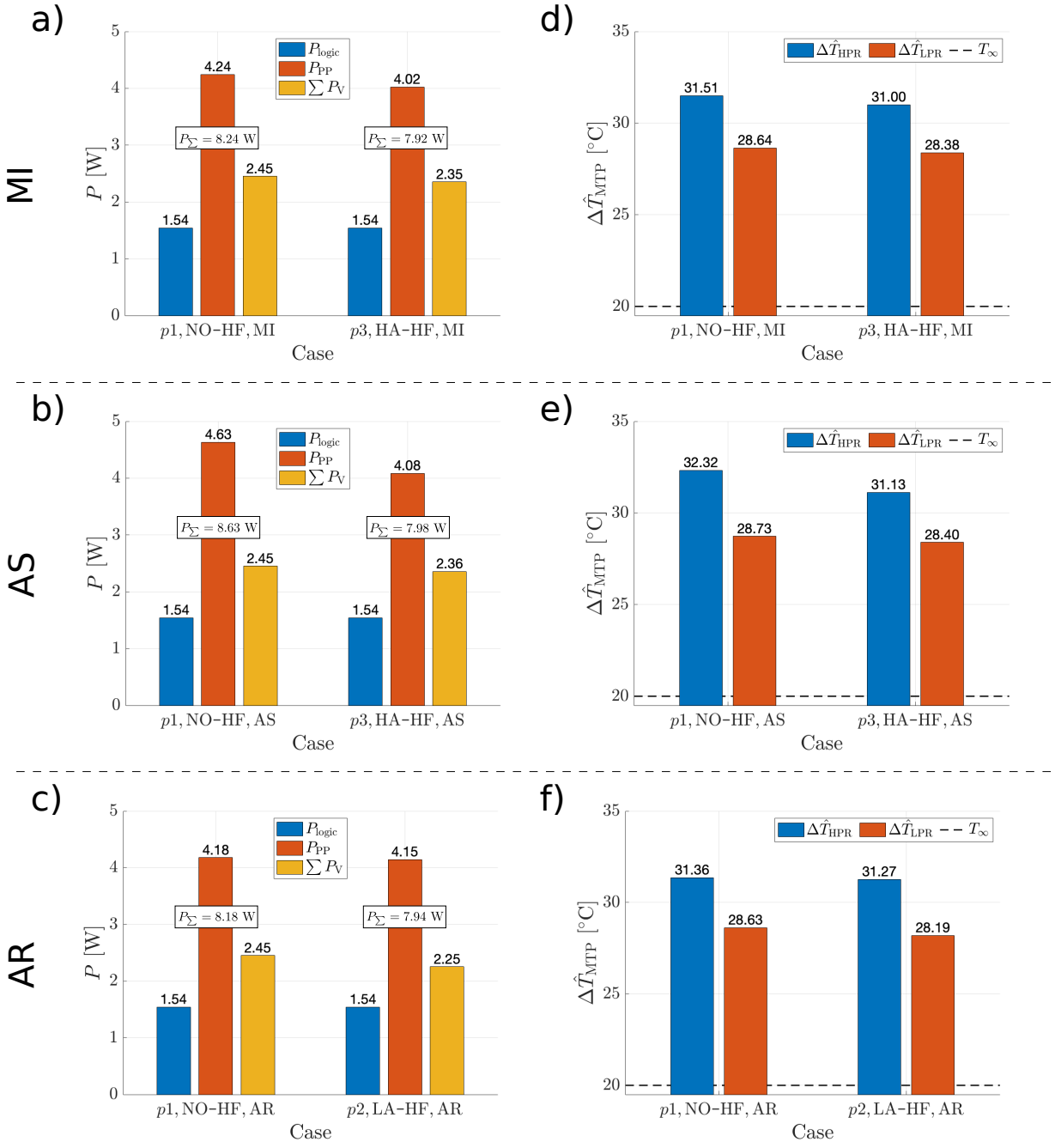

Figure 6.17.: Electrical power contributions for the MI, AS and AR conditions in a) to c). A power sum $P_\sum$ is additionally given for each case. The final mean temperatures for both reservoirs are presented in d) to f) for the same cases with respect to the environmental temperature T_∞.

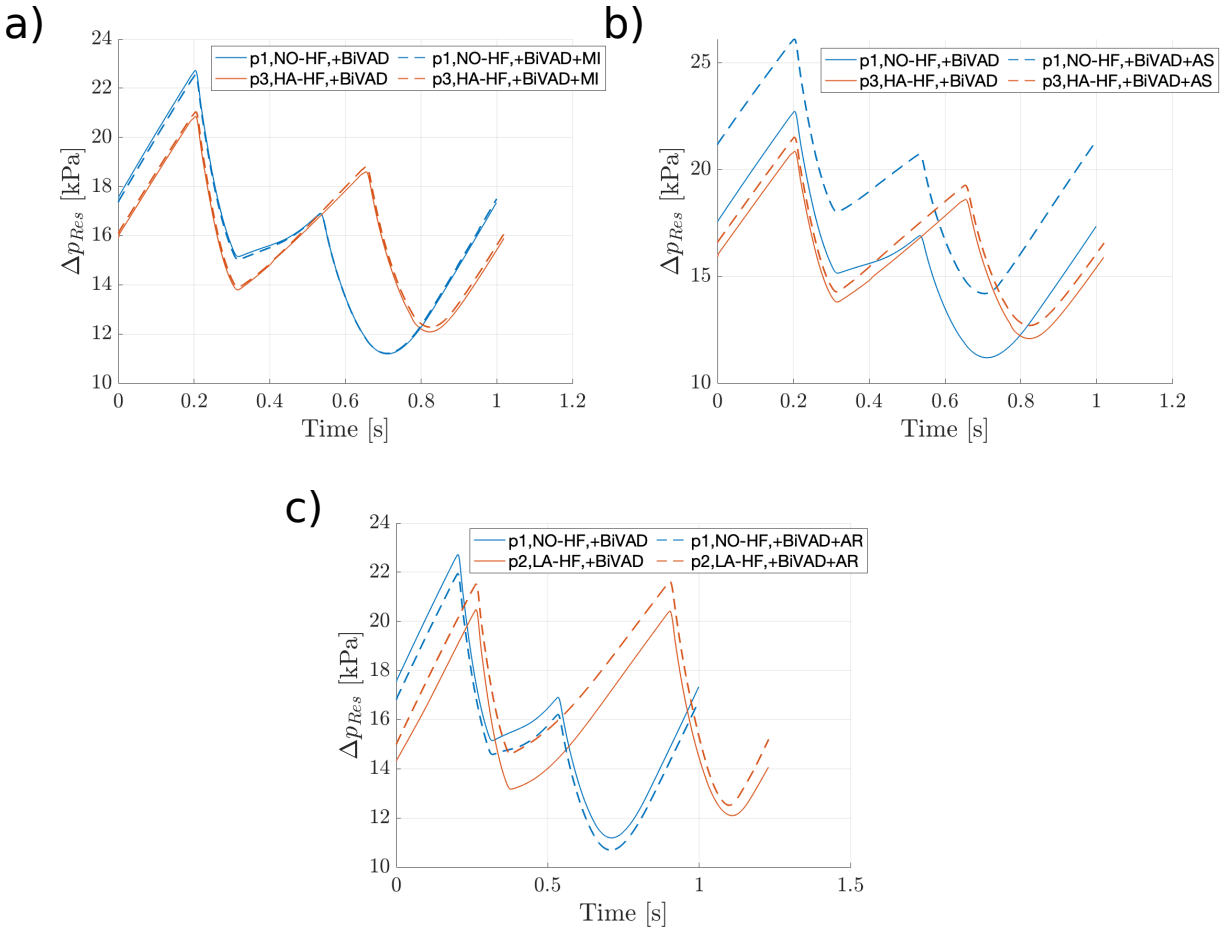

Figure 6.18.: The difference reservoir pressure curves and their changes due to the previous MI in a), AS in b) and AR in c). Each of the graphs depicts the supported case without the respective disease as a non-dashed line and diseased as a dashed line. The corresponding patients and HF conditions are further given in the legends.

The case study was designed to allow for comparison between the available medical cases with a focus on the BiVAD response. Therefore, most of the BiVAD parameters were kept constant and hence only a small range of the possible working range was used. An alternative would have been to vary the support level of the BiVAD and check the CVS response. This however, would drastially have increased the amount of cases to be computed or would have limited the examination to fewer patients and conditions. Also, the effects of varying support intensities have previously been presented in [54] and [43]. Comparing the available medical cases under the same BiVAD conditions is thus a reasonable approach, especially when the BiVAD engineering is focused.

A general limitation (cf. section 3.7) of the SCVS model as it is presented here, is the instantaneous response character. More complex, long-term adaptations of the CVS as e.g. heart rate or afterload adaptions, structural changes as they occur in growth and remodeling processes, aggravations of VHD or healing effects are not considered in the cases dealt with here. However, some of the mentioned physiological or pathological processes have previously been incorporated by Hirschvogel [43] and can in principle be added to the models of the present work.

6.3.1. Specific HF patients

The results presented in 6.3.1 are discussed systematically in this section: The pV curves and done works of the figures 6.4, 6.5 and 6.6 are examined firstly regarding the HF conditions and secondly regarding the individual patients, before single peculiarities are pointed out. Thereafter, support and technical efficiency, presented in figure 6.8 are discussed. Lastly, the component individual and total power consumption is focused and related to the heating of the BiVAD. Both can be found in figure 6.9.

The overall effects of the three HF conditions on the CVS pV loops are qualitatively similar in all patients, showing that HF of a certain kind manifests itself comparably in patients with differing heart sizes. However, the shift direction of the pV curves differs. The form of the EU pV loops changes also similarly over the conditions in all patients. Those of the non-diseased condition (NO-HF) case are characterized by a kink. It stems from the higher contractility of the non-diseased condition NO-HF and altered upstroke and relaxation rates of the diseased conditions, LA-HF and HA-HF. From NO-HF to HA-HF, higher pressures are obtained at smaller volumes, resulting in more bloated pV loops and consequently in greater work.

The smallest support effect can be seen for the NO-HF condition in all patients, which is directly observable in the corresponding pV loops and is reflected in the absolute and relative SW changes in the corresponding bar charts in the figures 6.4, 6.5 and 6.6. The archived total (=LV+RV) elevation of SW_{Heart} increases from NO-HF over LA-HF to HA-HF in all three patients. The relative SW_{Heart} increase develops in the same manner for the patient $p1$ but not strictly in the patients $p2$ and $p3$, where the relative increase is greater in the LA-HF than in the HA-HF condition for all, the total and the individual LV and RV systems. However, the support efficiencies, depicted in figure 6.8 a) to c), increase strictly in the order NO-HF, LA-HF, HA-HF

for all patients. This is also the case for the LV but not for the RV subsystem.

The support related changes of cardiac stroke work ΔSW_{Heart} are greater, but not size-proportional, in the larger patients $p1$ and $p2$ for the LA-HF and HA-HF, but not for the NO-HF case. The relative ΔSW_{Heart} increase is the highest for the RV. It profits indirectly from the LV supporting EUs. Also, due to the smaller initial stroke work, the percentage change is elevated. The patient $p3$ with smaller ventricles exhibits positive support efficiencies in the NO-HF condition. The comparison of the patients regarding the support efficiency does not allow for further conclusions. The EU work done on the heart, $\sum_{k=1}^{3} W_{\text{EU}}^{k}$, is maximal for the HA-HF cases within the examined patients group, as can be seen exemplary for EU^2 in figure 6.7. Also, the delivered W_{EU}^{k} in $p1$ and $p2$ are comparable, but are roughly 50 % lesser in $p3$ over all conditions. The ventricular volumes of $p3$ measure only 60 to 65 % the sizes of $p1$ and $p2$ (cf. figure 6.1). In the HA-HF condition in patient $p1$, ΔSW_{Heart} is greater than the total pV work brought into the CVS by the EUs, resulting in a total support efficiency above 100 % in figure 6.8 a). The heart, as central circulation organ, is an independent energy source and is characterized by its own (unknown) characteristic curve, which may be highly non-linear. Mechanical support can shift the actual working point along that curve, such that the energy output is disproportionately high. The heart parameters remained unaltered. In real patients, the body is likely to respond to any energy input via a multitude of physiological reactions, as e.g. the adaption of heart rate, inotropy and vascular resistances. These possible adaptations occur on a larger time scale of several minutes and are not part of the CVS model. The knowledge of the heart's characteristic curve would be of great assistance in identifying such beneficial working points for the individual patients. The total ΔSW_{Heart} change is persistently positive for all patients and HF conditions. However, it is found to be negative in the LV sub system for the NO-HF condition in patients $p1$ and $p2$, with relative values $\in [-1.9 - 1.1]$ %. It could be argued that the working point is shifted to a more unfavorable condition. However, in contrast to the $p1$ HA-HF case, the total support efficiencies are far below 100 %, namely at $\eta_{\text{+BiVAD}}(p1) = 10.5$ % and $\eta_{\text{+BiVAD}}(p1) = 15.1$ %. It stands to reason, that the single EU energy contributions cannot simply be assigned to the LV or RV, but will partly be transferred to the opposite ventricle. The distribution of the EU energy to one or the other ventricle is, among others, dependent upon the mechanical properties of the myocardial tissue and their changes during one heart beat, the systole and diastole timings and the time dependent conditions in the RV and LV connected circulatory systems, namely the pulmonary and systemic system, respectively.

The BiVAD efficiency is highest for the HA-HF condition within each of the patients. Furthermore the patient comparison shows, that greater delivered energy by the BiVAD in the patients with larger ventricles $p1$ and $p2$ results in a greater BiVAD efficiency of the drive unit. The power contributions in figure 6.9 a) to c) show, that the electrical valve power consumption only varies by 0.19 W, with $2.26\ \text{W} \leq \sum \text{P}_{\text{V}} \leq 2.45\ \text{W}$. However, this variation stems purely from differing patients and HF conditions, as the valve control values were strictly identical in all cases. The valve contributions in the NO-HF condition are significantly above those for the LA-HF and HA-HF conditions in all patients. The pump power consumption varies by 0.92 W, with $3.63\ \text{W} \leq \sum \text{P}_{\text{PP}} \leq 4.55\ \text{W}$. The pump control value was elevated in $p1$ ($y_{\text{PP}}(p1) = 0.35$ versus $y_{\text{PP}}(p2, p3) = 0.33$), but a difference in power consumption is observable in the mean values

between all patients: $\overline{\sum P}(p1) = 8.38$ W, $\overline{\sum P}(p2) = 8.03$ W, $\overline{\sum P}(p3) = 7.73$ W. Hence, the elevated pump control value is not the only cause for a higher power consumption.

6.3.2. Mitral valve regurgitation

In this section, the results of the investigation related to HF patients with additional MR are discussed. It comprises the analysis of patient $p1$ under all HF conditions and the LA-HF condition for all three patients.

The cardiac pV curve deformation is similar in all MR cases in a) to c) of both figures 6.10 and 6.11: The LV SV is increased along with a lowered systolic pressure. Due to the mitral valve insufficiency, the isovolumetric phases lack in the pV loops. In contrast, the RV SV is decreased while the systolic pressure remains unaltered. However, both individual ventricular work and total cardiac work are reduced. The amount of MR induced change differs within the HF conditions of patient $p1$ and over all patients in LA-HF condition. The corresponding EU pV curves exhibit similar shapes. The altered LV pV curve translate to the EUs, which results in a strong pressures decrease. Subject to the present parameter set, the BiVAD is unable to supply sufficient flow to sustain the initially built up pressure.

Within patient $p1$, the SW reductions are qualitatively similar for the three conditions, which can be seen in d) to f) of the same figures. The absolute SW decrease is greater in the LV, but relatively more important in the RV. However, within the HF conditions, the values strongly differ. The greatest percentage decrease of one third is observed in the HA-HF case. The EU work sum is even stronger reduced, by more than 40 % in the HA-HF case. It is followed by the NO-HF and LA-HF condition, respectively. Within the LA-HF condition, the SW reductions are qualitatively similar for the three patients. The relative decrease of SW is most prominent in patient $p3$, followed by $p2$ and $p1$. The absolute changes however, are not as spread out as for the case of patient $p1$ under varying HF conditions. Hence, the patient's HF conditions has greater impact than the heart geometry under MR within the examined cases.

Computing a support efficiency only makes sense, if the unsupported condition with MR could be used as reference, which was not computed in the present work. Therefore, $\eta_{\text{+BiVAD}}$ is not given for the MR related cases nor for any other additional diseases. The BiVAD efficiency is strongly reduced for all MR cases, in the range of $[-60, -30[$ percentage points. As previously stated, the MR induced CVS changes translate to the EUs, resulting in a reduced pV work W^k_{EU}. Since the control parameters remained unaltered, their power consumption changes exclusively due to the differing pressures and temperatures which establish in the reservoirs (cf. figure 6.13). However, they do not decrease as much as W^k_{EU} or even increase and consequently, the BiVAD efficiency as ratio between EU work and electrical power drops. The change of power consumption within patient $p1$ with MR quantifies to -0.19, -0.10 and -0.46 W for NO-HF, LA-HF and HA-HF respectively[3]. It stems purely from an altered pump power consumption, as those of the valves remain the same. The most prominent power reduction of -0.46 W can be observed in the same condition that also provokes the greatest decrease of W^k_{EU}, namely the HA-HF condition. In

[3] By comparing the summed power values of figure 6.9 a) and those in figure 6.12 b).

the comparison of LA-HF patients, the reduction is small for the patients $p2$ and $p3$, namely -0.01 and -0.03 W and -0.10 for $p1$. Again, the valve power consumption is constant. In patient $p1$ and $p2$, the absolute and relative reductions of W_{EU}^{k} are similar (cf. figure 6.11 d), e)), but they do not translate proportionally to a reduction in power consumption, which differ by one order of magnitude. The reservoir pressure difference curves, which govern the pump power consumption, can be found in figure 6.13. They reveal, how diverse the changes of W_{EU}^{k} can manifest in the drive unit. While Δp_{Res} is shifted downwards for $p1$, it is lifted up for $p2$ and remains almost unaltered for $p3$ in a). Also, the virtual means are located on different levels, even though the very initial conditions, including pressure, temperature and hence air mass, were equal in all three patients (cf. values in table 3.5). Within the conditions in patient $p1$ in b) however, the greatest pressure drop of Δp_{Res} can be observed in HA-HF condition, followed by NO-HF and LA-HF. This order agrees qualitatively with the decrease of W_{EU}^{k} in figure 6.10 d) to f). The different signal lengths and the differing starts and ends of the inflation and deflation phases are caused by the patient individual ECGs. Hence, the effects of CVS changes upon the BiVAD depend on the individual working point and the working point shifts due to these changes. The mean reservoir temperatures follow the pattern of power consumption as can be seen in figure 6.12 c) and f).

6.3.3. Other diseases

The results with additional diseases are discussed in this section. It is subdivided into MI, AS and AR, which each occurred in two patients with differing HF condition. The examination of these diseases in the present case study does not allow any systematic classification of the observations. However, the results may consolidate previous interpretations or add new aspects.

The MI scenario mimics the post-infarction condition after some time but before growth and remodeling effects have occurred. Depending on the affected area, the systemic condition of a person during an infarction and immediately after can be strongly altered due its potentially traumatic nature. This period is not addressed here. In both patients, $p1$ and $p3$, the infarction results in a reduced cardiac output. However, the extent differs extremely: While the overall SW reduction in the larger $p1$ is below 7 %, it is reduced by almost 54 % in the smallest patient $p3$. The absolute reductions behave similarly. The result is not surprising, since the infarcted myocardial area was the same in both patients (cf. figure 6.2) and consequently effects relatively more muscle tissue in $p3$. Moreover, the infarction occurred in the LV wall and hence has less influence on the RV SW in both patients. In contrast, W_{EU}^{k} is only weakly altered, with LV related reduction less than 2 and 7 % in $p1$ and $p3$, respectively. The RV related EUs even exhibit slight increases around 1 %. Due to the weak MI effects on W_{EU}^{k}, the power consumption and consequently the temperature development are not significantly changed compared to the patients without MI (cf. figure 6.9). This can also be concluded from figure 6.18 a), which shows that the reservoir pressure differences $\Delta p_{\mathrm{Res}} = p_{\mathrm{HPR}} - p_{\mathrm{LPR}}$ are almost unaltered for both MI cases. Likewise, the BiVAD efficienties remain almost equal, as can be seen by comparing figure 6.8 and table 6.4.

The CVS and BiVAD response to AS are similar in $p1$ and $p2$ as can be seen in figure 6.15. SVs are decreased, while reached pressures are increased in the LV. The loops are also shifted to the

right. In contrast, the RV pV curves are moved to the left, towards smaller volumes, while the pressures remain unaltered. SW and W_{EU}^k are increased in both patients. In $p3$ with HA-HF, the SW increase is near 7 % in the LV and negligible in the RV, while they are close to 13 % and 3 % in the LV and RV, respectively, in patient $p1$ with NO-HF. The effect is hence opposed to the MI cases, where the effects were stronger in $p3$. The increases of W_{EU}^k are more prominent in the RV related EU. The rise of W_{EU}^k is especially remarkable in $p1$: The overall pV work is increased by over 41 %, with an relative gain near 105 % in the RV EU. In contrast, $\sum_{k=1}^{3} W_{\text{EU}}^k$ increases only by less than 5 % in $p3$. The changes in W_{EU}^k are reflected by the related change in power consumption, which increases by 0.4 W ($\approx$ 5 %) in $p1$ and by 0.05 W ($\approx$ 0.6 %) in $p3$. The changes stem purely from an altered pump power consumption, which depends exclusively upon the difference reservoir pressure depicted in figure 6.18 b). For $p1$, it is shifted upwards by roughly 4 kPa ($\approx$ 22 %). On the contrary, Δp_{Res} increases only weakly in the $p3$ related case. Consequently, the temperature difference with and without AS in (HPR, LPR) are (0.83,0.1) °C in $p1$ and (0.13, 0) °C in $p3$. The increase of W_{EU}^k is also reflected in the BiVAD efficiency, which is increased by 30 % in $p1$ and negligible in $p3$, when comparing figure 6.8 and table 6.4.

In the first instance, the AR effects on the pV curves in figure 6.16 seem similar in both patients. Especially the cardiac pV loops are qualitatively comparable. However, the consequences of AR are very different for the two considered patients $p1$ with NO-HF and $p2$ with LA-HF: The LV SW increases by near 8 %, while it decreases by more than 21 % in the RV in $p1$. The accompanying changes in W_{EU}^k are negligible. In $p2$ in contrast, both SW and W_{EU}^k decrease significantly as can be seen in figure 6.16 d). The change in power consumption amounts to -0.05 and 0.08 W for $p1$ and $p2$, respectively, which relates directly to the shift directions of Δp_{Res} in figure 6.18 c). The mean reservoir temperatures develop accordingly.

6.4. Summary

This section summarizes the conclusions that can be deduced from the results and the corresponding discussions.

- HF Conditions: Within the considered HF conditions, HA-HF leads to an optimal support performance, as SW and W_{EU}^k are maximized. It is characterized by an increased vascular resistance and enables early pressure build up in the implant and hence bloated pV loops, even if EU volumes are typically reduced. However, whether high afterload HF patients are more eligible for BiVAD support or whether clinicians can and want to adjust patients pharmaceutically towards this condition is questionable. In general and including the MR cases, the HF condition has a greater influence on the BiVAD support effectiveness than the patient-specific geometry and heart size.
- Patients: The absolute increase of cardiac stroke work ΔSW_{Heart} is higher in larger patients ($p1$, $p2$ compared to $p3$) in the specific HF states LA-HF and HA-HF. The opposite was observed in the generic NO-HF condition. Since the CVS parameter of the latter are based on literature data, they are not patient specific (cf. section 6.1.1.2) and hence do not represent real cases. Owing to this observation within this study, it is generally expectable to achieve higher stroke works in larger patients. The greater relative ΔSW_{Heart} increases

in the smaller patient $p3$ in all HF conditions can be mathematically explained by smaller initial values. The amount of delivered pV work during BiVAD support (absence of VHD or MI) depended on the size of the patient's ventricular volumes. Values of the combined implant pV work, $\sum_{k=1}^{3} W_{\mathrm{EU}}^{k}$, in the smaller patient $p3$ ($V^{\ell+r}(p3) \approx 109$ ml) only reached values between $[49, 56]$ % of those in the bigger and more evenly sized patients $p1$ and $p2$ ($V^{\ell+r}(p1) \approx 169$ ml, $V^{\ell+r}(p2) \approx 181$ ml), even though boundary conditions were equal (only the pump control value was elevated by 2 % points in $p1$) and the combined implant volumes are very similar with $\sum_{k=1}^{3} V_{\mathrm{EU}}^{k} \in \{22.3, 21.8, 21.7\}$ ml for $p1$, $p2$ and $p3$, respectively.

- EU assignment: The single EU work contributions cannot generally be assigned to either the systemic (LV) or pulmonary (RV) circulatory system. They always effect the entire heart as their related forces translate through the myocardium, whose mechanical properties change strongly during one heart beat. In the examined cases, the strongest relative SW gain can consistently be observed in the RV. However, the EU located on the RV wall, EU^3, was persistently the least inflated EU.

- The greatest support efficiency can be observed in the HA-HF condition. In $p1$, a value above 117 % is observed and interpreted as a support induced shift to a more beneficial CVS working point. Here, the heart, with an unchanged myocardial contractility and as an independent source of energy, is exposed to boundary conditions that result in a higher stroke work.

- A high BiVAD efficiency correlates with high EU pV work and thus is greater for the HA-HF condition and for the larger patients $p1$ and $p2$. The power contributions vary moderately within a 0.2 W range for the valves (< 9 % of P_{V}) and strongly for the pump, with $3.59 \leq P_{\mathrm{PP}} \leq 4.63$ W over all cases in this chapter (including MI, VHD). The span of 1.04 W represents 22 to 29 % of P_{PP}. When only $p2$ and $p3$ with identical pump control values are considered, the resulting span of 0.91 W still represents 20 to 25 % of P_{PP}. The pump power consumption is a direct consequence of the difference reservoir pressure Δp_{Res}, which is determined by the prevailing CVS condition. However, neither the shift direction nor the values of Δp_{Res} behave consistently with regard to $\Delta \sum_{k=3}^{3} W_{\mathrm{EU}}^{k}$. Hence, if not actively controlled, the BiVAD working point establishes as individual response to the present CVS. In contrast, the mean reservoir temperatures are directly driven by the power consumption. The mean HPR temperature correlates strongly with P_{PP} throughout all examined cases.

- MR leads to a reduced cardiac SW and to a distinctive decrease of implant pV work. The effect is very similar for all patients and conditions, but most prominent in the HA-HF condition. Also, most of the other examined diseases provoke significant changes in the BiVAD signals. Under the active support level control, the BiVAD would react to a reduction (elevation) of W_{EU}^{k} by increasing (decreasing) the pump and valve control values over the heart cycles, trying to reestablish the former intensity of cardiac assist. Also, MR, or any of the other examined diseases other than MI, typically progresses over larger time spans than a few heart beats. However, whether CVS changes occur suddenly or creeping, it stands to reason that changes of W_{EU}^{k} or of the control values can be detected by appropriate algorithms and reported to the clinician.

- The SCVS model and the presented solution strategy has proven to be robust. It was applied to three different patients, with individual heart and implant geometries. Each of the patients was examined in three differing HF conditions, whereof two were patient-specific. An additional set of four diverse diseases was applied to these patients and HF conditions, resulting in altered cardiac dynamics. Thereby, a total of 20 differing supported periodic states of the SCVS model were computed, not including the preceding computations of homeostatic CVS model states. This sums to 96 simulated heart cycles under BiVAD support and results in an average of 4.8 heart cycles per periodic state calculation.
- The degree of coupling between the models, especially the BiVAD and CVS model is strong. Changes in one or the other initiate a transient phase, which eventually ceases in an altered periodic state of all degrees of freedom. The onset of biventricular support has been shown to be strong and has had the intended impact on the patient CVS, with an average support efficiency of 91 % in the patient specific cases (LA-HF, HA-HF). Vice versa, the prevailing HF condition or the occurrence of further diseases provoked significant changes in the BiVAD power consumption and temperature development. The variation of power consumption within the cases of one patient was in average 0.56 W or 7 % and resulted in a an average temperature alteration of 1.2 °C. Note that these changes were purely passive, as no controller actions were carried out, e.g. to reestablish disease caused SW break-ins.

7. Summary and outlook

This chapter provides a recapitulation of the presented work and lists reasonable further research and improvements for the future.

7.1. Summary

For the first time, a mixed-dimensional multi-physics model of a novel, pneumatically driven BiVAD has been presented and has been coupled to patient-specific heart and circulatory systems in various physiological and pathological conditions. It allows the computation of both, long-term device heating as well as highly dynamic flow processes on a small time scale. Besides the fundamental pressure and volume evolution in implant and heart, it considers electrical, thermal and control aspects. Thereby, holistic questions regarding BiVAD engineering can be answered. By accelerating the BiVAD engineering process and by assessing the individual patient therapy suitability, the present work can contribute in the fight against the HF pandemic.

The BiVAD components, namely air reservoirs, pump, valves, tubes and the expandable units were specifically designed to mimic their real-life counterparts, but are at the same time exchangable with physically equivalent alternatives if needed. Therefore, physical and empirical approaches were combined and methodologies to determine empirical component parameters were utilized or introduced. The prevailing thermodynamics and fluid mechanics relations were tailored to the system at hand. The BiVAD was represented as lumped-parameter model and at least the two state defining properties pressure and temperature were computed for each model node, with fluid flow in between. Thereby, each component was defined by one to three nodal points. The 0D assist device model was then coupled to an existing cardiovascular system model, featuring 3D representations of the implant's expandable units and an actively beating, patient-specific 3D heart with coupled 0D circulatory model. Calibrated parameter sets of heart and circulatory system were used to reproduce patient-specific cardiovascular dynamics. Long-lasting heating effects of the BiVAD, resulting from non-ideal electrical components, were considered by estimating the steady state mean reservoir temperatures. Therefore, the MTP model was introduced and coupled to the BiVAD model. Dynamic simulation of a supported heart beat and mean reservoir temperature estimation update each other iteratively over time. After a supported heart beat, results of the SCVS model are passed to the MTP model, which computes new mean temperature estimates for the reservoirs, to be used in the next supported heart beat. The SCVS, in contrast, is solved monolithically, hence the solution of the 3D solid mechanics problem is computed mutually with the 0D solutions of BiVAD and CVS.

In order to check the model validity, the assist device component models were individually compared to experimental measurements. This approach allows for locating the origin of inaccuracies in contrast to an integral validation. Therefore, the experimental set-ups and boundary conditions were reproduced in-silico and results were compared to the measurements. Many boundary conditions were varied, e.g. supply voltages, pump control values, reservoir pressures, polytropic exponents, valve currents or tube lengths. Thereby, the components were found to accurately simulate the BiVAD dynamics. The MTP model was validated by calibrating the reservoir heat transfer coefficients and mean reservoir material thicknesses such that the error between simulated and measured temperature data was minimized.

A sensitivity analysis with respect to the parameter variations of both, BiVAD and MTP model, was carried out. The results point to an accurate specification of the system's ambient pressure and to carefully determine the reservoir volumes. The importance of accurate mean reservoir temperatures is further emphasized, justifying the introduction of the MTP model. The reservoir's thermal transmittance and surface areas have the highest sensitivity among the MTP model parameters. Thereby, the calibration process is endorsed, since the thermal transmittance is computed from the calibrated parameters. These high-sensitivity parameters allow for design improvements: Larger reservoir volumes and areas as well as materials with a better thermal conductivity improve the BiVAD efficacy and efficiency.

The introduced models were then utilized to simulate the BiVAD support of three different patients with CT based heart geometries and individually calibrated CVS parameters to mimic three different HF conditions in each patient. In addition, myocardial infarction, mitral regurgitation as well as aortic stenosis and regurgitation were provoked in these HF patients by altering their CVS parameters. The applied computational procedure allowed for comparison of homeostatic states of the unsupported and the supported CVS. The BiVAD support parameters were the same in almost all cases, assessing particularly the periodic BiVAD response to varying patients and conditions. Indications were found, that larger patient hearts allow a higher energy to be transferred to the body. However, more than the heart geometry, the patient condition strongly influences the amount of work done on the heart. Any change in the biological system alters the amount of delivered BiVAD work to the heart. Changes in the delivered work, in turn, modified the reservoir pressure curves, which govern the pump power consumption and affect the BiVAD heating process. This cascade however, was not found to be directionally consistent as a reduction in delivered support energy led to both decreasing and increasing power consumption, endorsing the need for case individual assessment.

7.2. Outlook

This section gives an outlook on reasonable future work concerning the presented models and their application. It is split into the description of model improvements and extensions in 7.2.1 and a listing of suggested model applications in 7.2.2.

7.2.1. Model improvements and extensions

The presented coupled models are a valid representation of the real BiVAD system. However, many improvements and extensions can be conceived of, whereof the most important are mentioned in the following.

Firstly, a computational model of a device under development, as it is the case in this thesis, requires continuous model maintenance to match the latest design changes. While the progress made in the drive unit was fully updated in the model to date, the 3D implant representation needs revision. Size and form of the expandable units as well as the adhesion of the implant to the surrounding tissue has undergone significant changes in real-life. For reliable analysis, these advancements should be analyzed with respect to their importance in mimicking the implant dynamics and then be incorporated into the presented model if needed.

Secondly, the claim of easy component exchangeability is not consistent with the tube evaluation point $(\bullet)_{\mathrm{T}}$ being placed in the middle of the tube. It should be moved somewhere between connector and tube to obtain two independent parts, connector and tube, to allow for exclusive exchange of one or the other.

Thirdly, the actuator control values within the BiVAD remain unchanged over the simulated supported heart beats. An essential continuation of this work should enable the controlled adaptation of pump and valve control values in between two cycles. Therefore, the BiVAD must quantify the error between a set support intensity, expressed e.g. as support pressure or EU work, and the actually prevailing values. It can then react by setting new pump speeds and valve openings to minimize the control error over consecutive supported heart beats. Preliminary work thereof can be found in the master's thesis of [25]. Moreover, new control strategies could be implemented and tested, as e.g. closed-loop control.

Fourthly, the presented BiVAD should be connected to existing, more sophisticated representations of the CVS. Here, the utilized heart is a two chamber representation and the circulatory system model comprises the arterial and venous compartments of the organism. Hirschvogel [43] however, has introduced more advanced CVS models to simulate long term disease progression. These advancements are a four chamber heart with additional actively contracting atria, circulatory system models, including the systemic and pulmonary capillary network as well as oxygen and carbon dioxide transport and dissociation. Furthermore, he has developed a multiscale model to mimic myocardial growth (dilated and hypertrophic) and remodeling. Combining the introduced BiVAD with these advancements is an important step to predict support outcome in specific patient cases.

Fifthly, a major challenge regarding repeated simulations of the SCVS model is to reduce the computational costs as they certainly limit the above stated ideas. Order reduction techniques have also been introduced by Hirschvogel, but were not considered here. However, in order to perform system optimization at a reasonable cost, these methods should further be investigated and utilized in the solution procedure of the coupled SCVS.

7.2.2. Model usages

The presented models should be used in future research to increase the understanding of CVS support and eventually increase the support efficiency.

Firstly, the presented model should be extended to the more sophisticated heart and circulatory models of Hirschvogel [43], to simulate supported heart beats of diseased patients. They further include growth and remodeling phenomena as well as gas transport and dissociation. The patient-specific influence of BiVAD support on heart failure progression and on the important target parameter of oxygen saturation at distal body points could be studied. However, such model lack further adaptations of the body to cope with the prevailing diseases. These include, among others, adaptation of heart rate and (position dependent) systemic peripheral resistances, changes in blood volume, oxygen consumption and activity level. Including all or some of these mechanisms is a challenging task but can eventually allow for reliable and clinically relevant risk-benefit analysis prior to surgery.

Secondly, the sensitive BiVAD response to CVS changes found in this thesis suggests the additional BiVAD usage as a diagnostic tool. Data exploration techniques can be used to identify patterns in BiVAD support in differing patient or disease groups. In order to build large data sets, CVS parameters can be altered in a fully-automated fashion in-silico and be correlated to changes in the BiVAD signals. However, it will take some years until the device is implanted in a significant number of patients to obtain larger clinical data sets for validation.

Thirdly, the coupled SCVS model can be utilized in the context of an optimization, with several conceivable objectives. One could be to maximize the delivered PV work to the heart while minimizing the power consumption by defining a weighted objective function. Depending on the applied control strategy, design variables could be the control values of pump and valves, the valve control time points and the initial reservoir pressures. Other sets of design variables are possible. Furthermore, the energy that is temporarily stored in the EU material $W_{\mathrm{EU,int}}$ does not contribute to pressure or volume increase in the EU and can be minimized by varying the EU design.

A. Appendix

A.I. Bench tests

A.I.1. Volume and compliance

The test bench was built using the method presented by Riedl and Neumann [89], where a larger reference container (RC) with an exact known volume is pneumatically connected to the hollow structure to be tested, the test container (TC), but the pneumatic connection is initially blocked. A pressure sensor is connected to the RC, allowing to observe the pressure value as it changes. In a first step, the RC is pressurized to p_1. After equalization of temperature between RC and environment, the pressurized air in RC is released into TC by clearing the connection blockage. After temperature equalization, a final pressure p_2 is measured in the combined volume of RC and TC. The law of Boyle and Mariotte (cf. section 2.1.1) is used to compute the unknown volume V_{TC}

$$V_{TC} = \frac{p_\infty V_T + p_1 V_{RC} - p_2(V_{RC} - V_T)}{p_2 - p_\infty}, \tag{A.1}$$

with V_T being the volume of the connecting tubes. According to Riedl and Neumann [89], the condition $p_1 \geq 1.5\, p_\infty$ must be satisfied to reach relative errors below 1 %.
Repeating the method for different equalized pressures p_2, allows an estimation of the pressure volume relation of the test specimen. Consequently, a compliance, as the slope of $V(p)$, and an unloaded volume can be determined.

A.I.2. Heat transmittance

The heat transmittance was determined based on the method presented by Carneiro and Almeida [14]. A syringe was used to inflate the tested EUs with a known volume of air at atmospheric conditions. A pressure sensor was connected to the EU volume, recording the pressure evolution. Once the volume was injected, the supply tube was clamped. Measurement was stopped, when the pressure decrease due to heat transfer was converged to a fixed value. The equation

$$p(t) = p_0 + \Delta p \exp(-t/\tau) \tag{A.2}$$

was used to fit the recorded pressure curve and the thermal time constant τ could eventually be determined. In analogy to the electrical time constant, which is defined as ohmic resistance times capacity, the thermal time constant can be expressed as thermal capacity times thermal resistance $m \cdot c_{\text{th}}$, or, as adapted here, the thermal insulance $1/(k_{\text{th}} A)$. When this relation is rearranged, the thermal transmittance can be determined to

$$k_{\text{th}} = \frac{c_v p V}{\tau R T A}. \tag{A.3}$$

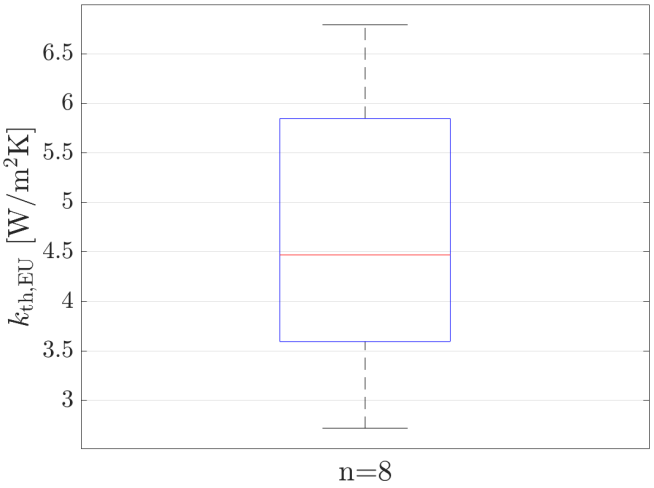

Figure A.1.: Deduced thermal transmittance of EUs.

The value for k_{th} was determined to 4.47 $\frac{\mathrm{W}}{\mathrm{m^2K}}$. The data is visualized in figure A.1.

A.I.3. Flow coefficient

The flow coefficient kv, as a function of the solenoid current $\mathcal{I}_{\mathrm{V}}$, was derived using the experimental setup shown in figure A.2, which is build on the basis of normative guidelines [23], [4]. The laboratory power supply (LPS-I) was used to power the proportional valves and the digital multimeter (DMM-I) was utilized to check the exact applied current. The LPS-I was also used to set varying pump speeds. The pressure difference was measure by two PS-I sensors and the valve flow was recorded with FS-I. The ambient temperature, which roughly prevails in the large aluminum container, was measured using TS-I and used to calculate the fluid's density. A total of four valves were used to derive the $kv(\mathcal{I}_{\mathrm{V}})$ relation. In order to compute the flow coefficient kv, the sampled data was then inserted into

$$kv(\mathcal{I}_{\mathrm{V}}) = \frac{g_{\mathrm{V}}}{\sqrt{\Delta p \rho_{1,2}}} = \frac{g_{\mathrm{V}}}{\sqrt{(p_1 - p_2)\frac{p_1+p_2}{2RT_\infty}}}. \tag{A.4}$$

A.I.4. Equipment

This section lists the used equipment, especially the sensor technology, which was used within the present thesis.

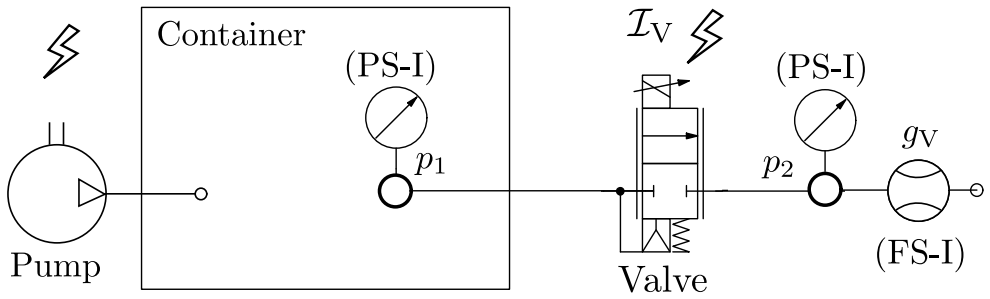

Figure A.2.: Schematic of the experimental setup to deduce the current dependent flow coefficient kv: Flow and pressure difference are directly measured. Valve current and pump speed were varied to obtain sufficient data points to derive a $kv(\mathcal{I}_V)$ relation.

Sensor/Equipment	Reference
PS-I	All Sensors DLV-005D
PS-II	Greisinger GMSD 2BA with GDUSB 1000
PS-III	Greisinger GMSD 350MR with GDUSB 1000
TS-I	Measurement Specialties MS8607-02BA01
TS-II	Greisinger GMH 3750 with probe GTF 401 ME
TS-III	Conrad Pico data logger TC-08 121847 with RS PRO thermocouples of Type K
FS-I	First Sensor WTAL020DUP
LPS-I	BK Precision 1762-ND
DMM-I	Voltcraft VC 290

Table A.1.: Utilized sensors and equipment.

A.II. Supporting documents

A.II.1. Neglecting kinetic energy

Two verifications were made to check the assumption of negligible kinetic energy contributions in the energy equation used during BiVAD modeling. First, by comparing the thermal energy inflow, namely the enthalpy flow $\dot{H} = gh$, to the contribution of the kinetic energy $\dot{E}_{kin} = g\frac{v^2}{2}$. The specific enthalpy can be replaced by $h = c_p T$ and $c_p = \frac{\kappa R}{\kappa - 1}$, yielding

$$\dot{H} = gh = gc_p T = \frac{\kappa}{\kappa - 1} gRT. \tag{A.5}$$

Expressing the velocity v with the mass flow using (2.24) and replacing the density by (2.4), the kinetic term reads

$$\frac{g^3}{2\rho^2 A^2} = \frac{g^3 R^2 T^2}{2p^2 A^2}. \tag{A.6}$$

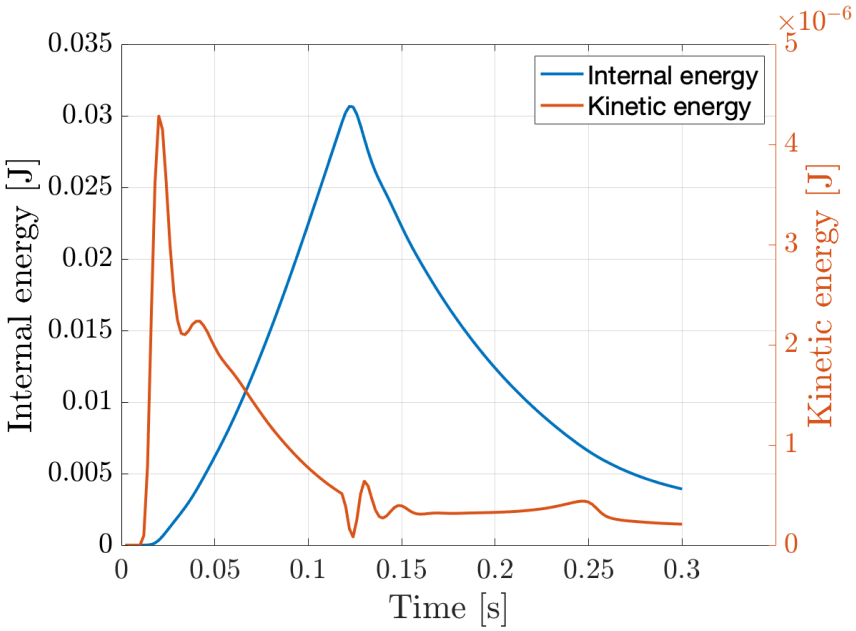

Figure A.3.: Comparison of total internal and kinetic energy during inflation and deflation of three EUs. The orders of magnitude differ by 10^4.

Both equations are divided by gRT. Inserting $p = 9 \cdot 10^4$ Pa, $R = 287 \frac{\text{J}}{\text{KgK}}$, $T = 310$ K, $A = 0.25\pi 0.003^2$ m^2 and $g = 1e^{-4} \frac{\text{kg}}{\text{s}}$ in (A.6), which are realistic values of the system at hand favoring high kinetic energies, the comparison between (A.6) and (A.5) yields

$$\frac{g^2 RT}{2p^2 A^2} = 8.62 \cdot 10^{-4} \ll 3.5 = \frac{\kappa}{\kappa - 1}. \tag{A.7}$$

Secondly, kinetic and internal energies were compared after a typical EU inflation and deflation and plotted over time in figure A.3. The orders of magnitude differ by 10^4.

A.II.2. Model parameter

A.II.3. Robin boundary conditions

Parameter	α_b $[\frac{\text{kPa}}{\text{mm}}]$	$\alpha_{b,\perp}$ $[\frac{\text{kPa}}{\text{mm}}]$	α_e $[\frac{\text{kPa}}{\text{mm}}]$	β_b $[\frac{\text{kPa·s}}{\text{mm}}]$	$\beta_{b,\perp}$ $[\frac{\text{kPa·s}}{\text{mm}}]$	β_e $[\frac{\text{kPa·s}}{\text{mm}}]$	α_p $[\frac{\text{kPa}}{\text{mm}}]$	β_p $[\frac{\text{kPa·s}}{\text{mm}}]$
Value	0.25	1.25	0.075	0.0005	0.0005	0005	1e^4	0.0

Table A.2.: Parameters of the Robin spring dashpot boundary conditions at heart basis and epicardium as well as EUs backface.

Parameter	a_0 [kPa]	a_f [kPa]	a_s [kPa]	a_{fs} [kPa]	κ_{H} [kPa]
Value	0.059	18.472	2.481	0.216	10^3
Parameter	b_0 [/]	b_f [/]	b_s [/]	b_{fs} [/]	$\rho_{0,\mathrm{H}}$ $[\frac{\mathrm{kg}}{\mathrm{mm}^3}]$
Value	8.023	16.026	11.120	11.436	10^{-6}

Table A.3.: Parameters of passive myocardial material according to [47]. The density $\rho_{0,\mathrm{H}}$ matches that of water.

Parameter	μ_{EU} [kPa]	κ_{EU} [kPa]	$\rho_{0,\mathrm{EU}}$ $[\frac{\mathrm{kg}}{\mathrm{mm}^3}]$
Value	9346	$233.65{\cdot}10^3$	$1.2{\cdot}10^{-6}$

Table A.4.: Material parameters of the implant.

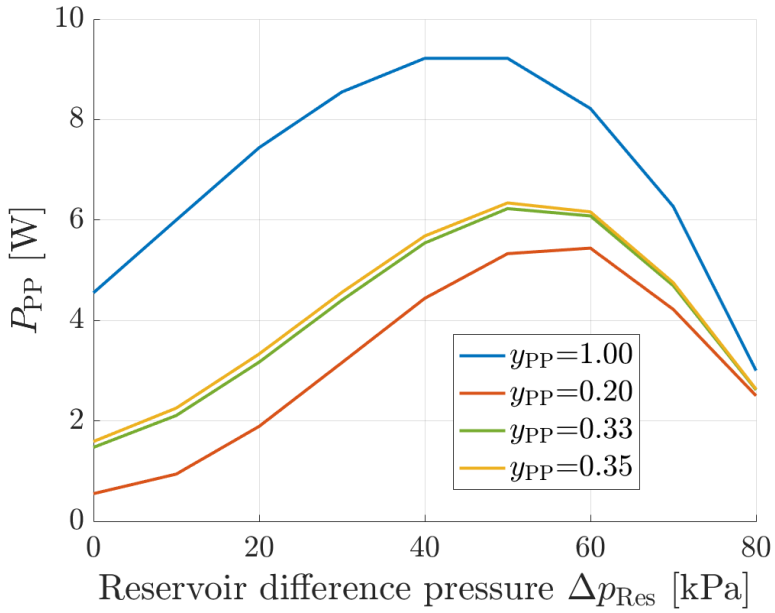

Figure A.4.: Pump power consumption as a function over the reservoir pressure difference. The curves at $y_{\mathrm{PP}} = 1.00$ and $y_{\mathrm{PP}} = 0.20$ are extracted from the manufacturer's data sheet. Any other curve is generated by linear interpolation (and extrapolation for $y_{\mathrm{PP}} < 0.20$) as e.g. the curves for $y_{\mathrm{PP}} = 0.33$ and $y_{\mathrm{PP}} = 0.35$ used in the application chapter.

A.II.4. Material parameter

A.II.5. Pump power curve

A.II.6. The BiVAD model stiffness matrix

The residual has a size of $n_{\text{DOF}}^{\text{AD}} = k \cdot n_{\text{DOF}}^{\text{AD,var}} + n_{\text{DOF}}^{\text{AD,fix}} = 3 \cdot 14 + 7$, with $n_{\text{DOF}}^{\text{AD,var}}$ being the DOF set for one of the three EUs, k, and $n_{\text{DOF}}^{\text{AD,fix}}$ the DOFs of reservoirs and pump. All non-zero entries of $\boldsymbol{K}^{\text{AD}} = \frac{\partial \boldsymbol{r}^{\text{AD}}}{\partial \boldsymbol{p}^{\text{AD}}}\Big|_{n+1}^{i}$ are listed in the following using r_j^{AD} to represent the j-th entry, where $r_j^{\text{AD}} \widehat{=} r^{\text{AD}}_{[j+(k-1)\cdot n_{\text{DOF}}^{\text{AD,var}}]}$, with $k = 3$. Fixed DOF entries have indices in the range $(\bullet)_{+1}$ to $(\bullet)_{+7}$. The residual $\boldsymbol{r}^{\text{AD}}$ can be found in equation (3.103), the DOF vector $\boldsymbol{p}^{\text{AD}}$ in (3.102). If the stiffness matrix entry differs for inflation and deflation, both terms are given, separated by a semicolon.

$$
\begin{aligned}
\partial r_1^{\text{AD}}/\partial p_1^{\text{AD}} &= \frac{1}{\Delta t} + \theta \left(\frac{q_{\text{EU}}^k}{V_{\text{EU}}^k} - \frac{\tau_{\text{EU}}^k}{T_{\text{EU}}^k} \right)_{n+1} \\
\partial r_1^{\text{AD}}/\partial p_2^{\text{AD}} &= \theta \left(\frac{p_{\text{EU}}^k}{V_{\text{EU}}^k} \right)_{n+1} \\
\partial r_1^{\text{AD}}/\partial p_3^{\text{AD}} &= -\theta \left(\frac{p_{\text{EU}}^k}{T_{\text{EU}}^k} \right)_{n+1} \\
\partial r_1^{\text{AD}}/\partial p_4^{\text{AD}} &= \theta \left(\frac{p_{\text{EU}}^k \tau_{\text{EU}}^k}{T_{\text{EU}}^{k\,2}} - \frac{g_{\text{EU}}^k R}{V_{\text{EU}}^k} \right)_{n+1} \\
\partial r_1^{\text{AD}}/\partial p_8^{\text{AD}} &= -\theta \left(\frac{R T_{\text{EU}}^k}{V_{\text{EU}}^k} \right)_{n+1} \\
\partial r_2^{\text{AD}}/\partial p_2^{\text{AD}} &= -\theta \\
\partial r_3^{\text{AD}}/\partial p_3^{\text{AD}} &= -\theta \\
\partial r_3^{\text{AD}}/\partial p_4^{\text{AD}} &= \frac{1}{\Delta t} \\
\partial r_4^{\text{AD}}/\partial p_1^{\text{AD}} &= \theta \left(\frac{\tau_{\text{EU}}^k V_{\text{EU}}^k}{T_{\text{EU}}^k(\kappa-1)} + q_{\text{EU}}^k \right)_{n+1} \\
\partial r_4^{\text{AD}}/\partial p_2^{\text{AD}} &= \theta p_{\text{EU},n+1}^k \\
\partial r_4^{\text{AD}}/\partial p_3^{\text{AD}} &= \theta \left(\frac{p_{\text{EU}}^k V_{\text{EU}}^k}{T_{\text{EU}}^k(\kappa-1)} \right)_{n+1} \\
\partial r_4^{\text{AD}}/\partial p_4^{\text{AD}} &= \theta \left(k_{\text{th,EU}} A_{\text{EU}}^k - \frac{p_{\text{EU}}^k V_{\text{EU}}^k}{(\kappa-1)(T_{\text{EU}}^k)^2} \tau_{\text{EU}}^k + g_{\text{EU,in}}^k \frac{R}{\kappa-1} - g_{\text{EU,out}}^k R \right)_{n+1} \\
\partial r_4^{\text{AD}}/\partial p_5^{\text{AD}} &= -\theta R \frac{\kappa}{\kappa-1} g_{\text{EU,in},n+1}^k ; 0 \\
\partial r_4^{\text{AD}}/\partial p_8^{\text{AD}} &= -\theta \frac{R}{\kappa-1} \left(\kappa T_{\text{TE}}^k - T_{\text{EU}}^k \right)_{n+1} ; -\theta R T_{\text{EU},n+1}^k
\end{aligned}
\tag{A.8}
$$

$$
\begin{aligned}
\partial r_5^{\mathrm{AD}}/\partial p_1^{\mathrm{AD}} &= -\theta \left(\frac{(n_{\mathrm{T}}-1)T_{\mathrm{V}}^k \left(\frac{p_{\mathrm{EU}}^k}{p_{\mathrm{V}}^k}\right)^{\frac{n_{\mathrm{T}}-1}{n_{\mathrm{T}}}}}{n_{\mathrm{T}} p_{\mathrm{EU}}^k} \right)_{n+1} ; 0 \\
\partial r_5^{\mathrm{AD}}/\partial p_4^{\mathrm{AD}} &= 0; -\theta \\
\partial r_5^{\mathrm{AD}}/\partial p_5^{\mathrm{AD}} &= \theta \\
\partial r_5^{\mathrm{AD}}/\partial p_6^{\mathrm{AD}} &= \theta \left(\frac{(n_{\mathrm{T}}-1)T_{\mathrm{V}}^k \left(\frac{p_{\mathrm{EU}}^k}{p_{\mathrm{V}}^k}\right)^{\frac{n_{\mathrm{T}}-1}{n_{\mathrm{T}}}}}{n_{\mathrm{T}} p_{\mathrm{V}}^k} \right)_{n+1} ; 0 \\
\partial r_5^{\mathrm{AD}}/\partial p_7^{\mathrm{AD}} &= -\theta \left(\frac{p_{\mathrm{EU}}^k}{p_{\mathrm{V}}^k}\right)_{n+1}^{\frac{n_{\mathrm{T}}-1}{n_{\mathrm{T}}}} ; 0 \\
\partial r_6^{\mathrm{AD}}/\partial p_6^{\mathrm{AD}} &= -\theta \left(\frac{\mathrm{f}_{\mathrm{T},1}\left(g_{\mathrm{V,in}}^k - g_{\mathrm{V,out}}^k\right) + \mathrm{f}_{\mathrm{T},2}\left(g_{\mathrm{V,in}}^k - g_{\mathrm{V,out}}^k\right)^2 R}{T_{\mathrm{V}}^k \left(\frac{p_{\mathrm{V}}^k}{T_{\mathrm{V}}^k} + \frac{p_{\mathrm{T}}^k}{T_{\mathrm{T}}^k}\right)^2} + 1 \right)_{n+1} \\
\partial r_6^{\mathrm{AD}}/\partial p_7^{\mathrm{AD}} &= \theta \left(\frac{\mathrm{f}_{\mathrm{T},1}\left(g_{\mathrm{V,in}}^k - g_{\mathrm{V,out}}^k\right) + \mathrm{f}_{\mathrm{T},2}\left(g_{\mathrm{V,in}}^k - g_{\mathrm{V,out}}^k\right)^2 R\, p_{\mathrm{V}}^k}{(T_{\mathrm{V}}^k)^2 \left(\frac{p_{\mathrm{V}}^k}{T_{\mathrm{V}}^k} + \frac{p_{\mathrm{T}}^k}{T_{\mathrm{T}}^k}\right)^2} \right)_{n+1} \\
\partial r_6^{\mathrm{AD}}/\partial p_9^{\mathrm{AD}} &= \theta \mathrm{f}_{\mathrm{T,3},n+1}^k \left[2(g_{\mathrm{V,in}}^k - g_{\mathrm{V,out}}^k)\mathrm{f}_{\mathrm{T},2} + \mathrm{f}_{\mathrm{T},1}\right]_{n+1} + \frac{L_{\mathrm{T}}}{2A_{\mathrm{T}}\Delta t} \\
\partial r_6^{\mathrm{AD}}/\partial p_{10}^{\mathrm{AD}} &= -\theta \mathrm{f}_{\mathrm{T,3},n+1}^k \left[2(g_{\mathrm{V,in}}^k - g_{\mathrm{V,out}}^k)\mathrm{f}_{\mathrm{T},2} + \mathrm{f}_{\mathrm{T},1}\right]_{n+1} - \frac{L_{\mathrm{T}}}{2A_{\mathrm{T}}\Delta t} \\
\partial r_6^{\mathrm{AD}}/\partial p_{11}^{\mathrm{AD}} &= \theta \left(1 - \frac{\mathrm{f}_{\mathrm{T},1}\left(g_{\mathrm{V,in}}^k - g_{\mathrm{V,out}}^k\right) + \mathrm{f}_{\mathrm{T},2}\left(g_{\mathrm{V,in}}^k - g_{\mathrm{V,out}}^k\right)^2 R}{T_{\mathrm{T}}^k \left(\frac{p_{\mathrm{V}}^k}{T_{\mathrm{V}}^k} + \frac{p_{\mathrm{T}}^k}{T_{\mathrm{T}}^k}\right)^2} \right)_{n+1} \\
\partial r_6^{\mathrm{AD}}/\partial p_{12}^{\mathrm{AD}} &= \theta \left(\frac{\mathrm{f}_{\mathrm{T},1}\left(g_{\mathrm{V,in}}^k - g_{\mathrm{V,out}}^k\right) + \mathrm{f}_{\mathrm{T},2}\left(g_{\mathrm{V,in}}^k - g_{\mathrm{V,out}}^k\right)^2 R\, p_{\mathrm{T}}^k}{(T_{\mathrm{T}}^k)^2 \left(\frac{p_{\mathrm{V}}^k}{T_{\mathrm{V}}^k} + \frac{p_{\mathrm{T}}^k}{T_{\mathrm{T}}^k}\right)^2} \right)_{n+1} \\
\partial r_7^{\mathrm{AD}}/\partial p_1^{\mathrm{AD}} &= 0; \theta \left(\frac{(n_{\mathrm{T}}-1)T_{\mathrm{TE}}^k \left(\frac{p_{\mathrm{V}}^k}{p_{\mathrm{EU}}^k}\right)^{\frac{n_{\mathrm{T}}-1}{n_{\mathrm{T}}}}}{n_{\mathrm{T}} p_{\mathrm{EU}}^k} \right)_{n+1} \\
\partial r_7^{\mathrm{AD}}/\partial p_4^{\mathrm{AD}} &= 0; -\theta \left(\frac{p_{\mathrm{V}}^k}{p_{\mathrm{EU}}^k}\right)_{n+1}^{\frac{n_{\mathrm{T}}-1}{n_{\mathrm{T}}}} \\
\partial r_7^{\mathrm{AD}}/\partial p_6^{\mathrm{AD}} &= -\theta \left(\frac{(n_{\mathrm{V}}-1)T_{\mathrm{HPR}} \left(\frac{p_{\mathrm{V}}^k}{p_{\mathrm{HPR}}}\right)^{\frac{n_{\mathrm{V}}-1}{n_{\mathrm{V}}}}}{n_{\mathrm{V}} p_{\mathrm{V}}^k} \right)_{n+1} \\
\partial r_7^{\mathrm{AD}}/\partial p_7^{\mathrm{AD}} &= \theta \\
\partial r_7^{\mathrm{AD}}/\partial p_{+1}^{\mathrm{AD}} &= \theta \left(\frac{(n_{\mathrm{V}}-1)T_{\mathrm{HPR}} \left(\frac{p_{\mathrm{V}}^k}{p_{\mathrm{HPR}}}\right)^{\frac{n_{\mathrm{V}}-1}{n_{\mathrm{V}}}}}{n_{\mathrm{V}} p_{\mathrm{HPR}}} \right)_{n+1} ; 0 \\
\partial r_7^{\mathrm{AD}}/\partial p_{+2}^{\mathrm{AD}} &= -\theta \left(\frac{p_{\mathrm{V}}^k}{p_{\mathrm{HPR}}}\right)_{n+1}^{\frac{n_{\mathrm{V}}-1}{n_{\mathrm{V}}}} ; 0
\end{aligned}
\tag{A.9}
$$

$$
\begin{aligned}
\partial r_8^{\mathrm{AD}}/\partial p_8^{\mathrm{AD}} &= \theta \left(\frac{RT_{\mathrm{T}}^k}{p_{\mathrm{T}}^k C_{\mathrm{T}} + \frac{V_{\mathrm{T}}}{n_{\mathrm{T}}}} \right)_{n+1} \\
\partial r_8^{\mathrm{AD}}/\partial p_9^{\mathrm{AD}} &= -\theta \left(\frac{RT_{\mathrm{T}}^k}{p_{\mathrm{T}}^k C_{\mathrm{T}} + \frac{V_{\mathrm{T}}}{n_{\mathrm{T}}}} \right)_{n+1} \\
\partial r_8^{\mathrm{AD}}/\partial p_{10}^{\mathrm{AD}} &= \theta \left(\frac{RT_{\mathrm{T}}^k}{p_{\mathrm{T}}^k C_{\mathrm{T}} + \frac{V_{\mathrm{T}}}{n_{\mathrm{T}}}} \right)_{n+1} \\
\partial r_8^{\mathrm{AD}}/\partial p_{11}^{\mathrm{AD}} &= \frac{1}{\Delta t} + \theta \left(\frac{(g_{\mathrm{V,in}}^k - g_{\mathrm{V,out}}^k - g_{\mathrm{EU}}^k) R T_{\mathrm{T}}^k C_{\mathrm{T}}}{\left(p_{\mathrm{T}}^k C_{\mathrm{T}} + \frac{V_{\mathrm{T}}}{n_{\mathrm{T}}} \right)^2} \right)_{n+1} \\
\partial r_8^{\mathrm{AD}}/\partial p_{12}^{\mathrm{AD}} &= -\theta \left(\frac{(g_{\mathrm{V,in}}^k - g_{\mathrm{V,out}}^k - g_{\mathrm{EU}}^k) R}{p_{\mathrm{T}}^k C_{\mathrm{T}} + \frac{V_{\mathrm{T}}}{n_{\mathrm{T}}}} \right)_{n+1} \\
\partial r_9^{\mathrm{AD}}/\partial p_6^{\mathrm{AD}} &= \frac{\theta}{2} \left(\frac{k v_{\mathrm{V,in}} \left(2T_{\mathrm{HPR}} p_{\mathrm{V}}^k + p_{\mathrm{HPR}} T_{\mathrm{V}}^k - p_{\mathrm{HPR}} T_{\mathrm{HPR}} \right)}{\sqrt{(p_{\mathrm{HPR}} - p_{\mathrm{V}}^k)\left(p_{\mathrm{HPR}} T_{\mathrm{V}}^k + p_{\mathrm{V}}^k T_{\mathrm{HPR}} \right)}} \right)_{n+1} \\
\partial r_9^{\mathrm{AD}}/\partial p_7^{\mathrm{AD}} &= \theta \left(\frac{T_{\mathrm{HPR}} R g_{\mathrm{V,in}}^k}{\sqrt{2T_{\mathrm{HPR}} T_{\mathrm{V}}^k R}} - \frac{k v_{\mathrm{V,in}} \left(p_{\mathrm{HPR}}^2 - p_{\mathrm{HPR}} p_{\mathrm{V}}^k \right)}{2\sqrt{(p_{\mathrm{HPR}} - p_{\mathrm{V}}^k)\left(p_{\mathrm{HPR}} T_{\mathrm{V}}^k + p_{\mathrm{V}}^k T_{\mathrm{HPR}} \right)}} \right)_{n+1} \\
\partial r_9^{\mathrm{AD}}/\partial p_9^{\mathrm{AD}} &= \theta \sqrt{2T_{\mathrm{HPR}} T_{\mathrm{V}}^k R}_{n+1} \\
\partial r_9^{\mathrm{AD}}/\partial p_{+1=}^{\mathrm{AD}} &= -\frac{\theta}{2} \left(\frac{k v_{\mathrm{V,in}} \left(2T_{\mathrm{V}}^k p_{\mathrm{HPR}} + p_{\mathrm{V}}^k T_{\mathrm{HPR}} - p_{\mathrm{V}}^k T_{\mathrm{V}}^k \right)}{\sqrt{(p_{\mathrm{HPR}} - p_{\mathrm{V}}^k)\left(p_{\mathrm{HPR}} T_{\mathrm{V}}^k + p_{\mathrm{V}}^k T_{\mathrm{HPR}} \right)}} \right)_{n+1} \\
\partial r_9^{\mathrm{AD}}/\partial p_{+2}^{\mathrm{AD}} &= \theta \left(\frac{T_{\mathrm{V}}^k R g_{\mathrm{V,in}}^k}{\sqrt{2T_{\mathrm{HPR}} T_{\mathrm{V}}^k R}} - \frac{k v_{\mathrm{V,in}} \left(p_{\mathrm{HPR}} p_{\mathrm{V}}^k - {p_{\mathrm{V}}^k}^2 \right)}{2\sqrt{(p_{\mathrm{HPR}} - p_{\mathrm{V}}^k)\left(p_{\mathrm{HPR}} T_{\mathrm{V}}^k + p_{\mathrm{V}}^k T_{\mathrm{HPR}} \right)}} \right)_{n+1} \\
\partial r_{10}^{\mathrm{AD}}/\partial p_6^{\mathrm{AD}} &= -\frac{\theta}{2} \left(\frac{k v_{\mathrm{V,out}} \left(2T_{\mathrm{LPR}} p_{\mathrm{V}}^k + p_{\mathrm{LPR}} T_{\mathrm{V}}^k - p_{\mathrm{LPR}} T_{\mathrm{LPR}} \right)}{\sqrt{(p_{\mathrm{V}}^k - p_{\mathrm{LPR}})\left(p_{\mathrm{LPR}} T_{\mathrm{V}}^k + p_{\mathrm{V}}^k T_{\mathrm{LPR}} \right)}} \right)_{n+1} \\
\partial r_{10}^{\mathrm{AD}}/\partial p_7^{\mathrm{AD}} &= \theta \left(\frac{T_{\mathrm{LPR}} R g_{\mathrm{V,out}}^k}{\sqrt{2T_{\mathrm{LPR}} T_{\mathrm{V}}^k R}} - \frac{k v_{\mathrm{V,out}} \left(p_{\mathrm{LPR}} p_{\mathrm{V}}^k - p_{\mathrm{LPR}}^2 \right)}{2\sqrt{(p_{\mathrm{V}}^k - p_{\mathrm{LPR}})\left(p_{\mathrm{LPR}} T_{\mathrm{V}}^k + p_{\mathrm{V}}^k T_{\mathrm{LPR}} \right)}} \right)_{n+1} \\
\partial r_{10}^{\mathrm{AD}}/\partial p_{10}^{\mathrm{AD}} &= \theta \sqrt{2T_{\mathrm{LPR}} T_{\mathrm{V}}^k R}_{n+1} \\
\partial r_{10}^{\mathrm{AD}}/\partial p_{+3}^{\mathrm{AD}} &= \frac{\theta}{2} \left(\frac{k v_{\mathrm{V,out}} \left(2T_{\mathrm{V}}^k p_{\mathrm{LPR}} + p_{\mathrm{V}}^k T_{\mathrm{LPR}} - p_{\mathrm{V}}^k T_{\mathrm{V}}^k \right)}{\sqrt{(p_{\mathrm{V}}^k - p_{\mathrm{LPR}})\left(p_{\mathrm{LPR}} T_{\mathrm{V}}^k + p_{\mathrm{V}}^k T_{\mathrm{LPR}} \right)}} \right)_{n+1} \\
\partial r_{10}^{\mathrm{AD}}/\partial p_{+4}^{\mathrm{AD}} &= \theta \left(\frac{T_{\mathrm{V}}^k R g_{\mathrm{V,out}}^k}{\sqrt{2T_{\mathrm{LPR}} T_{\mathrm{V}}^k R}} - \frac{k v_{\mathrm{V,out}} \left({p_{\mathrm{V}}^k}^2 - p_{\mathrm{LPR}} p_{\mathrm{V}}^k \right)}{2\sqrt{(p_{\mathrm{V}}^k - p_{\mathrm{LPR}})\left(p_{\mathrm{LPR}} T_{\mathrm{V}}^k + p_{\mathrm{V}}^k T_{\mathrm{LPR}} \right)}} \right)_{n+1}
\end{aligned}
\tag{A.10}
$$

$$
\begin{aligned}
\partial r_{11}^{\mathrm{AD}}/\partial p_{1}^{\mathrm{AD}} &= \theta\left(1-\frac{\mathrm{f}_{\mathrm{T},4}g_{\mathrm{EU}}^{k}+\mathrm{f}_{\mathrm{T},5}g_{\mathrm{EU}}^{k^2}R}{T_{\mathrm{TE}}^{k}\left(\frac{p_{\mathrm{T}}^{k}}{T_{\mathrm{T}}^{k}}+\frac{p_{\mathrm{EU}}^{k}}{T_{\mathrm{TE}}^{k}}\right)^{2}}\right)_{n+1}\\
\partial r_{11}^{\mathrm{AD}}/\partial p_{5}^{\mathrm{AD}} &= \theta\left(\frac{\mathrm{f}_{\mathrm{T},4}g_{\mathrm{EU}}^{k}+\mathrm{f}_{\mathrm{T},5}g_{\mathrm{EU}}^{k^2}R\;p_{\mathrm{EU}}^{k}}{(T_{\mathrm{TE}}^{k})^{2}\left(\frac{p_{\mathrm{EU}}^{k}}{T_{\mathrm{TE}}^{k}}+\frac{p_{\mathrm{T}}^{k}}{T_{\mathrm{T}}^{k}}\right)^{2}}\right)_{n+1}\\
\partial r_{11}^{\mathrm{AD}}/\partial p_{8}^{\mathrm{AD}} &= \theta\mathrm{f}_{\mathrm{T},6}\left(2g_{\mathrm{EU}}^{k}\mathrm{f}_{\mathrm{T},5}+\mathrm{f}_{\mathrm{T},4}\right)_{n+1}+\frac{L_{\mathrm{T}}}{2A_{\mathrm{T}}\Delta t}\\
\partial r_{11}^{\mathrm{AD}}/\partial p_{11}^{\mathrm{AD}} &= -\theta\left(\frac{\mathrm{f}_{\mathrm{T},4}g_{\mathrm{EU}}^{k}+\mathrm{f}_{\mathrm{T},5}g_{\mathrm{EU}}^{k^2}R}{T_{\mathrm{T}}^{k}\left(\frac{p_{\mathrm{T}}^{k}}{T_{\mathrm{T}}^{k}}+\frac{p_{\mathrm{EU}}^{k}}{T_{\mathrm{TE}}^{k}}\right)^{2}}+1\right)_{n+1}\\
\partial r_{11}^{\mathrm{AD}}/\partial p_{12}^{\mathrm{AD}} &= \theta\left(\frac{\mathrm{f}_{\mathrm{T},4}g_{\mathrm{EU}}^{k}+\mathrm{f}_{\mathrm{T},5}g_{\mathrm{EU}}^{k^2}R\;p_{\mathrm{T}}^{k}}{(T_{\mathrm{T}}^{k})^{2}\left(\frac{p_{\mathrm{EU}}^{k}}{T_{\mathrm{TE}}^{k}}+\frac{p_{\mathrm{T}}^{k}}{T_{\mathrm{T}}^{k}}\right)^{2}}\right)_{n+1}\\
\partial r_{12}^{\mathrm{AD}}/\partial p_{5}^{\mathrm{AD}} &= -\tfrac{1}{2}\theta\\
\partial r_{12}^{\mathrm{AD}}/\partial p_{7}^{\mathrm{AD}} &= -\tfrac{1}{2}\theta\\
\partial r_{12}^{\mathrm{AD}}/\partial p_{12}^{\mathrm{AD}} &= \theta\\
\partial r_{+1}^{\mathrm{AD}}/\partial p_{9}^{\mathrm{AD}} &= \theta\left(\frac{RT_{\mathrm{HPR}}}{V_{\mathrm{HPR}}+p_{\mathrm{HPR}}C_{\mathrm{HPR}}}\right)_{n+1}\\
\partial r_{+1}^{\mathrm{AD}}/\partial p_{+1}^{\mathrm{AD}} &= \tfrac{1}{\Delta t}-\theta\left(\frac{V_{\mathrm{HPR}}^{2}\tau_{\mathrm{HPR}}+RT_{\mathrm{HPR}}^{2}(\sum_{k=1}^{3}g_{\mathrm{V,in}}^{k}-g_{\mathrm{PP}})C_{\mathrm{HPR}}}{T_{\mathrm{HPR}}(V_{\mathrm{HPR}}+p_{\mathrm{HPR}}C_{\mathrm{HPR}})^{2}}\right)_{n+1}\\
\partial r_{+1}^{\mathrm{AD}}/\partial p_{+2}^{\mathrm{AD}} &= -\theta\left(\frac{R(g_{\mathrm{PP}}-\sum_{k=1}^{3}g_{\mathrm{V,in}}^{k})-\frac{p_{\mathrm{HPR}}V_{\mathrm{HPR}}}{T_{\mathrm{HPR}}^{2}}\tau_{\mathrm{HPR}}}{V_{\mathrm{HPR}}+p_{\mathrm{HPR}}C_{\mathrm{HPR}}}\right)_{n+1}\\
\partial r_{+1}^{\mathrm{AD}}/\partial p_{+5}^{\mathrm{AD}} &= -\theta\left(\frac{RT_{\mathrm{HPR}}}{V_{\mathrm{HPR}}+p_{\mathrm{HPR}}C_{\mathrm{HPR}}}\right)_{n+1}\\
\partial r_{+1}^{\mathrm{AD}}/\partial p_{+6}^{\mathrm{AD}} &= -\theta\left(\frac{p_{\mathrm{HPR}}V_{\mathrm{HPR}}}{T_{\mathrm{HPR}}(V_{\mathrm{HPR}}+p_{\mathrm{HPR}}C_{\mathrm{HPR}})}\right)_{n+1}
\end{aligned}
\tag{A.11}
$$

$$
\begin{aligned}
\partial r^{\mathrm{AD}}_{+2}/\partial p^{\mathrm{AD}}_{9} &= \theta \frac{T^2_{\mathrm{HPR}}}{p_{\mathrm{HPR}}}(1-\kappa) \\
\partial r^{\mathrm{AD}}_{+2}/\partial p^{\mathrm{AD}}_{+1} &= \theta \frac{T_{\mathrm{HPR}}\left[g_{\mathrm{PP}}\kappa T_{\mathrm{LPR}}\left(\frac{p_{\mathrm{HPR}}}{p_{\mathrm{LPR}}}\right)^{\frac{n_{\mathrm{PP}}-1}{n_{\mathrm{PP}}}} + (\kappa-1)n_{\mathrm{PP}}\dot{Q}_{\mathrm{HPR}} + \left(\sum_{k=1}^{3} g^k_{\mathrm{V,in}}(1-\kappa) - g_{\mathrm{PP}}\right)n_{\mathrm{PP}}T_{\mathrm{HPR}}\right]}{n_{\mathrm{PP}}p^2_{\mathrm{HPR}}} \\
\partial r^{\mathrm{AD}}_{+2}/\partial p^{\mathrm{AD}}_{+2} &= \frac{V_{\mathrm{HPR}}}{R}\frac{1}{\Delta t} + \frac{\theta}{p_{\mathrm{HPR}}}\Big[-\Upsilon_{\mathrm{HPR}}\frac{\kappa-1}{R} + 2T_{\mathrm{HPR}}\left(\sum_{k=1}^{3} g^k_{\mathrm{V,in}}(\kappa-1) + g_{\mathrm{PP}}\right) - \\
&\quad -\kappa g_{\mathrm{PP}}T_{\mathrm{LPR}}\left(\frac{p_{\mathrm{HPR}}}{p_{\mathrm{LPR}}}\right)^{\frac{n_{\mathrm{PP}}-1}{n_{\mathrm{PP}}}} + T_{\mathrm{HPR}}(\kappa-1)(k_{\mathrm{th,W}}A_{\mathrm{W}} + k_{\mathrm{th,HPR}}A_{\mathrm{HPR}})\Big] \\
\partial r^{\mathrm{AD}}_{+2}/\partial p^{\mathrm{AD}}_{+3} &= \theta \frac{g_{\mathrm{PP}}\kappa(n_{\mathrm{PP}}-1)T_{\mathrm{LPR}}T_{\mathrm{HPR}}\left(\frac{p_{\mathrm{HPR}}}{p_{\mathrm{LPR}}}\right)^{\frac{n_{\mathrm{PP}}-1}{n_{\mathrm{PP}}}}}{n_{\mathrm{PP}}p_{\mathrm{HPR}}p_{\mathrm{LPR}}} \\
\partial r^{\mathrm{AD}}_{+2}/\partial p^{\mathrm{AD}}_{+4} &= -\theta\frac{T_{\mathrm{HPR}}}{p_{\mathrm{HPR}}}\left(\frac{k_{\mathrm{th,W}}A_{\mathrm{W}}(\kappa-1)}{R} + g_{\mathrm{PP}}\kappa\left(\frac{p_{\mathrm{HPR}}}{p_{\mathrm{LPR}}}\right)^{\frac{n_{\mathrm{PP}}-1}{n_{\mathrm{PP}}}}\right) \\
\partial r^{\mathrm{AD}}_{+2}/\partial p^{\mathrm{AD}}_{+5} &= -\theta\kappa\frac{T_{\mathrm{HPR}}}{p_{\mathrm{HPR}}}T_{\mathrm{LPR}}\left(\frac{p_{\mathrm{HPR}}}{p_{\mathrm{LPR}}}\right)^{\frac{n_{\mathrm{PP}}-1}{n_{\mathrm{PP}}}} \\
\partial r^{\mathrm{AD}}_{+3}/\partial p^{\mathrm{AD}}_{10} &= -\theta\left(\frac{RT_{\mathrm{LPR}}}{V_{\mathrm{LPR}}+p_{\mathrm{LPR}}C_{\mathrm{LPR}}}\right)_{n+1} \\
\partial r^{\mathrm{AD}}_{+3}/\partial p^{\mathrm{AD}}_{+3} &= \frac{1}{\Delta t} - \theta\left(\frac{V^2_{\mathrm{LPR}}\tau_{\mathrm{LPR}} + RT^2_{\mathrm{LPR}}(g_{\mathrm{PP}} - \sum_{k=1}^{3} g^k_{\mathrm{V,out}})C_{\mathrm{LPR}}}{T_{\mathrm{LPR}}(V_{\mathrm{LPR}}+p_{\mathrm{LPR}}C_{\mathrm{LPR}})^2}\right)_{n+1} \\
\partial r^{\mathrm{AD}}_{+3}/\partial p^{\mathrm{AD}}_{+4} &= -\theta\left(\frac{R(\sum_{k=1}^{3} g^k_{\mathrm{V,out}} - g_{\mathrm{PP}}) - \frac{p_{\mathrm{LPR}}V_{\mathrm{LPR}}}{T^2_{\mathrm{LPR}}}\tau_{\mathrm{LPR}}}{V_{\mathrm{LPR}}+p_{\mathrm{LPR}}C_{\mathrm{LPR}}}\right)_{n+1} \\
\partial r^{\mathrm{AD}}_{+3}/\partial p^{\mathrm{AD}}_{+5} &= \theta\left(\frac{RT_{\mathrm{LPR}}}{V_{\mathrm{LPR}}+p_{\mathrm{LPR}}C_{\mathrm{LPR}}}\right)_{n+1} \\
\partial r^{\mathrm{AD}}_{+3}/\partial p^{\mathrm{AD}}_{+7} &= -\theta\left(\frac{p_{\mathrm{LPR}}V_{\mathrm{LPR}}}{T_{\mathrm{LPR}}(V_{\mathrm{LPR}}+p_{\mathrm{LPR}}C_{\mathrm{LPR}})}\right)_{n+1} \\
\partial r^{\mathrm{AD}}_{+4}/\partial p^{\mathrm{AD}}_{7} &= -\theta\frac{T_{\mathrm{LPR}}}{p_{\mathrm{LPR}}}\kappa\sum_{k=1}^{3} g^k_{\mathrm{V,out}} \\
\partial r^{\mathrm{AD}}_{+4}/\partial p^{\mathrm{AD}}_{10} &= -\theta\frac{T_{\mathrm{LPR}}}{p_{\mathrm{LPR}}}\kappa T_{\mathrm{V}} \\
\partial r^{\mathrm{AD}}_{+4}/\partial p^{\mathrm{AD}}_{+2} &= -\theta\frac{T_{\mathrm{LPR}}}{p_{\mathrm{LPR}}}\frac{\kappa-1}{R}k_{\mathrm{th,W}}A_{\mathrm{W}} \\
\partial r^{\mathrm{AD}}_{+4}/\partial p^{\mathrm{AD}}_{+3} &= \theta\left[\Upsilon_{\mathrm{LPR}}\frac{\kappa-1}{R} + \kappa T_{\mathrm{V}}\sum_{k=1}^{3} g^k_{\mathrm{V,out}} - \kappa g_{\mathrm{PP}}T_{\mathrm{LPR}} - \left(\sum_{k=1}^{3} g^k_{\mathrm{V,out}} - g_{\mathrm{PP}}\right)T_{\mathrm{LPR}}\right]\frac{T_{\mathrm{LPR}}}{p^2_{\mathrm{LPR}}} \\
\partial r^{\mathrm{AD}}_{+4}/\partial p^{\mathrm{AD}}_{+4} &= \frac{V_{\mathrm{LPR}}}{R}\frac{1}{\Delta t} + \frac{\theta}{p_{\mathrm{LPR}}}\Big[2T_{\mathrm{LPR}}\left(g_{\mathrm{PP}}(\kappa-1) + \sum_{k=1}^{3} g^k_{\mathrm{V,out}}\right) + \\
&\quad + \frac{\kappa-1}{R}\left(\Upsilon_{\mathrm{LPR}} + T_{\mathrm{LPR}}(k_{\mathrm{th,W}}A_{\mathrm{W}} + k_{\mathrm{th,LPR}}A_{\mathrm{LPR}})\right) - \kappa T_{\mathrm{V}}\sum_{k=1}^{3} g^k_{\mathrm{V,out}}\Big] \\
\partial r^{\mathrm{AD}}_{+4}/\partial p^{\mathrm{AD}}_{+5} &= \theta\frac{T^2_{\mathrm{LPR}}}{p_{\mathrm{LPR}}}(\kappa-1)
\end{aligned}
\tag{A.12}
$$

$$
\begin{aligned}
\partial r^{\mathrm{AD}}_{+5}/\partial p^{\mathrm{AD}}_{+1} &= -\theta \left(\tfrac{g_{\mathrm{PP,max}} y_{\mathrm{PP}} T_{\mathrm{norm}}}{C_{\mathrm{PP}}-1} \right)_{n+1} \\
\partial r^{\mathrm{AD}}_{+5}/\partial p^{\mathrm{AD}}_{+3} &= -\theta \left(g_{\mathrm{PP,max}} y_{\mathrm{PP}} T_{\mathrm{norm}} \left(1 + \tfrac{1}{C_{\mathrm{PP}}-1} \right) \right)_{n+1} \\
\partial r^{\mathrm{AD}}_{+5}/\partial p^{\mathrm{AD}}_{+4} &= \theta g_{\mathrm{PP}} p_{\mathrm{norm}} \\
\partial r^{\mathrm{AD}}_{+5}/\partial p^{\mathrm{AD}}_{+5} &= \theta T_{\mathrm{LPR}} p_{\mathrm{norm}} \\
\partial r^{\mathrm{AD}}_{+6}/\partial p^{\mathrm{AD}}_{+2} &= \tfrac{1}{\Delta t} \\
\partial r^{\mathrm{AD}}_{+6}/\partial p^{\mathrm{AD}}_{+6} &= -\theta \\
\partial r^{\mathrm{AD}}_{+7}/\partial p^{\mathrm{AD}}_{+4} &= \tfrac{1}{\Delta t} \\
\partial r^{\mathrm{AD}}_{+7}/\partial p^{\mathrm{AD}}_{+7} &= -\theta
\end{aligned}
\tag{A.13}
$$

Bibliography

[1] E. E. Adams and M. L. Wrightson, Quality of life with an LVAD: A misunderstood concept, *Heart & Lung* **47**, 177–183, 2018.

[2] S. A. Akhter, A. Badami, M. Murray, T. Kohmoto, L. Lozonschi, S. Osaki, and E. B. Lushaj, Hospital readmissions after continuous-flow left ventricular assist device implantation: Incidence, causes, and cost analysis, *The Annals of Thoracic Surgery* **100**, 884 – 889, 2015.

[3] A. P. Ambrosy, G. C. Fonarow, J. Butler, O. Chioncel, S. J. Greene, M. Vaduganathan, S. Nodari, C. S. Lam, N. Sato, A. N. Shah, and M. Gheorghiade, The global health and economic burden of hospitalizations for heart failure, *Journal of the American College of Cardiology* **63**, 1123–1133, 2014.

[4] ANSI/ISA-S75.01-1985 (R1995), Flow equations for sizing control valves, Standard, Instrument Society of America, Durham, USA, 1995.

[5] G. L. Anstadt, P. Schiff, and A. E. Baue, Prolonged circulatory support by direct mechanical ventricular assistance, *ASAIO Journal* **12**, 72–79, 1966.

[6] G. L. Anstadt. Heart massage apperatus, U.S. Patent 5 119 804, Jun. 1992.

[7] H. D. Baehr and K. Stephan, *Wärme- und Stoffübertragung*, Springer-Vieweg GmbH Deutschland, 2019.

[8] G. Barclay, D. Griffiths, and D. Higham, Theta method dynamics, *LMS Journal of Computation and Mathematics* **3**, 27–43, 2000.

[9] E. J. Benjamin, M. J. Blaha, S. E. Chiuve, M. Cushman, S. R. Das, R. Deo, S. D. de Ferranti, J. Floyd, M. Fornage, C. Gillespie, C. R. Isasi, M. C. Jiménez, L. C. Jordan, S. E. Judd, D. Lackland, J. H. Lichtman, L. Lisabeth, S. Liu, C. T. Longenecker, R. H. Mackey, K. Matsushita, D. Mozaffarian, M. E. Mussolino, K. Nasir, R. W. Neumar, L. Palaniappan, D. K. Pandey, R. R. Thiagarajan, M. J. Reeves, M. Ritchey, C. J. Rodriguez, G. A. Roth, W. D. Rosamond, C. Sasson, A. Towfighi, C. W. Tsao, M. B. Turner, S. S. Virani, J. H. Voeks, J. Z. Willey, J. T. Wilkins, J. H. Wu, H. M. Alger, S. S. Wong, and P. Muntner, Heart disease and stroke statistics - 2017 update: A report from the american heart association, *Circulation* **135**, e146–e603, 2017.

[10] J. Bestel, F. Clément, and M. Sorine, A biomechanical model of muscle contraction, In *Medical Image Computing and Computer-Assisted Intervention – MICCAI 2001*, Volume 2208, pages 1159–1161, Berlin, 2001, Springer-Verlag Berlin Heidelberg.

[11] U. Boeken, A. Assmann, F. Born, S. Klotz, and C. Schmid, *Mechanische Herz-Kreislaufunterstützung*, Springer-Verlag, Berlin Heidelberg, 2017.

[12] L. Böswirth and S. Bschorer, *Technische Strömungslehre*, Springer Fachmedien Wiesbaden, 2014.

[13] J. F. Carneiro and F. G. de Almeida, Reduced-order thermodynamic models for servo-pneumatic actuator chambers, *Proceedings of the Institution of Mechanical Engineers, Part I: Journal of Systems and Control Engineering* **220**, 301–314, 2006.

[14] J. F. Carneiro and F. G. de Almeida, Heat transfer evaluation of industrial pneumatic cylinders, *Proceedings of the Institution of Mechanical Engineers, Part I: Journal of Systems and Control Engineering* **221**, 119–128, 2007.

[15] J. Chung and G. M. Hulbert, A time integration algorithm for structural dynamics with improved numerical dissipation: The generalized-α method, *Journal of Applied Mechanics* **60**, 371–375, 1993.

[16] T. D. Cordeiro, D. L. Sousa, I. A. Cestari, and A. M. N. Lima, Controlling the cardiovascular response under synchronized ventricular assist device support, In *2016 IEEE International Conference on Automatica (ICA-ACCA)*, pages 1–6, 2016.

[17] Covestro AG. Desmopan 385 S, data sheet, 12/2018.

[18] J. C. Criscione, L. D. Harrison, M. R. Moreno, C. M. Bolch, D. I. Robbins, S. Biswas, and B. Leschinsky. Cardiac conpression device having passive and active chambers, U.S. Patent 2017/0080137, Mar. 2017.

[19] J. W. Cunningham, M. Vaduganathan, B. L. Claggett, J. E. John, A. S. Desai, E. F. Lewis, M. R. Zile, P. Carson, P. S. Jhund, L. Kober, B. Pitt, S. J. Shah, K. Swedberg, I. S. Anand, S. Yusuf, J. J. V. McMurray, M. A. Pfeffer, and S. D. Solomon, Myocardial infarction in heart failure with preserved ejection fraction: Pooled analysis of 3 clinical trials, *JACC Heart Fail* **8**, 618–626, 2020.

[20] E. de Souza Neto, D. Perić, M. Dutko, and D. Owen, Design of simple low order finite elements for large strain analysis of nearly incompressible solids, *International Journal of Solids and Structures* **33**, 3277 – 3296, 1996.

[21] R. DeSilva, *Heart Disease*, Biographies of Disease, Greenwood, 2013.

[22] DIN 1343:1990-01, Referenzzustand, Normzustand, Normvolumen; Begriffe und Werte, Norm, Deutsche Institut für Normung e. V., Berlin, Germany, 1990.

[23] DIN EN 60534-2-1:2011, Stellventile für die Prozessregelung - Teil 2-1: Durchflusskapazität - Bemessungsgleichungen für Fluide unter Betriebsbedingungen, Norm, Deutsche Institut für Normung e. V., Berlin, Germany, 2012.

[24] J. C. Dutton and E. R. Covergirl, Experiments to study the gaseous discharge and filling of vessels, *Int. J. Engng. Ed.* **13**, 123–134, 1997.

[25] T. Egger, *Entwicklung einer robusten Mehrgrößenregelung für ein pneumatisches Herzunterstützungssystem*, Master's thesis, Technische Universität München, 2018.

[26] H. Elman, V. Howle, J. Shadid, R. Shuttleworth, and R. Tuminaro, A taxonomy and comparison of parallel block preconditioners for the incompressible Navier Stokes equations, *Journal of Computational Physics* **227**, 1790–1808, 2008.

[27] Ensinger GmbH. TECAFORM AH black - Halbzeuge (Rundstäbe, Platten, Hohlstäbe), data sheet, 02/2018.

[28] Fluid Automation Systems s.a. FAS 16 mm FLATPROP EQP High flow pressure compensated proportional valve, data sheet, 01/2016.

[29] I. French and C. Cox, Modelling, design and control of a modern electropneumatic actuator, *Control Theory and Applications, IEE Proceedings D* **137**, 145 – 156, 1990.

[30] J. Funk and T. Robe, Transients in pneumatic transmission lines subjected to large pressure changes, *International Journal of Mechanical Sciences* **12**, 245 – 257, 1970.

[31] M. Gee, C. Kelley, and R. Lehoucq, Pseudo-transient continuation for nonlinear transient elasticity, *International Journal for Numerical Methods in Engineering* **78**, 1209 – 1219, 2009.

[32] M. Gee, C. Förster, and W. Wall, A computational strategy for prestressing patient-specific biomechanical problems under finite deformation, *International Journal for Numerical Methods in Biomedical Engineering* **26**, 52–72, 2010.

[33] W. Geller, *Thermodynamik für Maschinenbauer*, Springer-Verlag Berlin Heidelberg, 2015.

[34] G. A. Giridharan, M. Skliar, D. B. Olsen, and G. M. Pantalos, Modeling and control of a brushless DC axial flow ventricular assist device, *ASAIO Journal* **48**, 272–289, 2002.

[35] B. Glueck, *Hydrodynamische und gasdynamische Rohrströmung - Druckverluste*, VEB Verlag für Bauwesen, 1988.

[36] B. Goldstein, L. Thomas, J. Zaroff, J. Nguyen, R. Menza, and K. Khush, Assessment of heart transplant waitlist time and pre- and post-transplant failure, *Epidemiology* **27**, 469–476, 2016.

[37] I. Gosev, K. Wood, B. Ayers, B. Barrus, P. Knight, J. D. Alexis, H. Vidula, H. Lander, J. Wyrobek, C. Cheyne, I. Goldenberg, S. McNitt, and S. Prasad, Implantation of a fully magnetically levitated left ventricular assist device using a sternal-sparing surgical technique, *The Journal of Heart and Lung Transplantation* **39**, 37–44, 2020.

[38] A. Groenewegen, F. H. Rutten, A. Mosterd, and A. W. Hoes, Epidemiology of heart failure, *European Journal of Heart Failure* **22**, 1342–1356, 2020.

[39] S. E. Haaland, Simple and explicit formulas for the friction factor in turbulent pipe flow, *Journal of Fluids Engineering* **105**, 89–90, 1983.

[40] B. Hanson, R. Richardson, G. Davies, K. Watterson, M. Levesley, and P. Walker, Control of a non-blood contacting cardiac assist device, In *Proceedings of the 3rd IASTED International Conference on Biomedical Engineering 2005*, pages 679–684, 2005.

[41] K. H. Haugh and J. Salyer, Needs of patients and families during the wait for a donor heart, *Heart & Lung* **36**, 319 – 329, 2007.

[42] J. L. Hermsen, K. K. Stout, A. Stempien-Otero, E. D. Verrier, and N. A. Mokadam, Long-term right ventricular assist device therapy in an adult with pulmonary atresia/intact ventricular septum, *ASAIO Journal* **64**, e72–e74, 2018.

[43] M. Hirschvogel, *Computational modeling of patient-specific cardiac mechanics with model reduction-based parameter estimation and applications to novel heart assist technologies*, PhD thesis, Technische Universität München, 2018.

[44] M. Hirschvogel, M. Bassilious, L. Jagschies, S. M. Wildhirt, and M. W. Gee, A monolithic 3D-0D coupled closed-loop model of the heart and the vascular system: Experiment-based parameter estimation for patient-specific cardiac mechanics, *International Journal for Numerical Methods in Biomedical Engineering* **33**, e2842, 2017.

[45] M. Hirschvogel, L. Jagschies, A. Maier, S. M. Wildhirt, and M. W. Gee, An in-silico twin for epicardial augmentation of the failing heart, *International Journal for Numerical Methods in Biomedical Engineering* **35**, e3233, 2019.

[46] G. A. Holzapfel, *Nonlinear Solid Mechanics for Engineers - A Continuum Approach for Engineering*, John Wiley & Sons, 2000.

[47] G. A. Holzapfel and R. W. Ogden, Constitutive modelling of passive myocardium: A structurally based framework for material characterization, *Phil. Trans. R. Soc. A.* **367**, 3445–3475, 2009.

[48] E. C. Hord, C. M. Bolch, E. Tuzun, W. E. Cohn, B. Leschinsky, and J. C. Criscione, Evaluation of the CorInnova heart assist device in an acute heart failure model, *Journal of Cardiovascular Translational Research* **12**, 155–163, 2019.

[49] E. M. Hsich, Matching the market for heart transplantation, *Circulation: Heart Failure* **9**, e002679, 2016.

[50] S. N. Hunyor and Y. Huang. An implantable direct cardiac compression device and system, World Intellectual Property Organization Patent 2005/014082, Feb. 2005.

[51] P. A. Iaizzo, *Handbook of Cardiac Anatomy, Physiology and Devices*, Springer International Publishing Switzerland, 2015.

[52] F. Ikhouane and J. Rodellar, *Systems with Hysteresis: Analysis, Identification and Control Using the Bouc-Wen Model*, John Wiley & Sons, 2007.

[53] L. Jagschies, *Biventricular epicardial augmentation of the failing heart - Investigation of a novel technology in a drug induced porcine failing heart model and using computational modeling*, PhD thesis, Technische Universität München, 2018.

[54] L. Jagschies, M. Hirschvogel, J. Matallo, A. Maier, K. Mild, H. Brunner, R. Hinkel, M. W. Gee, P. Radermacher, S. M. Wildhirt, and S. Hafner, Individualized biventricular epicardial augmentation technology in a drug-induced porcine failing heart model, *ASAIO Journal* **64**, 480–488, 2017.

[55] D. C. Jiles and D. L. Atherton, Theory of ferromagnetic hysteresis (invited), *Journal of Applied Physics* **55**, 2115–2120, 1984.

[56] Z. Kamiński, Mathematical modeling of pneumatic pipes in a simulation of heterogeneous engineering systems, *Journal of Fluids Engineering* **133**, 121401, 2011.

[57] Z. Kamiński, A simplified lumped parameter model for pneumatic tubes, *Mathematical and Computer Modelling of Dynamical Systems* **23**, 523–535, 2017.

[58] R. C. P. Kerckhoffs, M. L. Neal, Q. Gu, J. H. Bassingthwaighte, J. H. Omens, and A. D. McCulloch, Coupling of a 3D finite element model of cardiac ventricular mechanics to lumped systems models of the systemic and pulmonic circulation, *Annals of Biomedical Engineering* **35**, 1–18, 2007.

[59] M. Khorsandi, J. Schroder, M. Daneshmand, M. Bishawi, O. Bouamra, P. Winterton, A. Y. Choi, C. Patel, J. Rogers, J. M. D. Rio, and C. Milano, Outcomes after extracorporeal right ventricular assist device combined with durable left ventricular assist device support, *The Annals of Thoracic Surgery* **107**, 1768 – 1774, 2019.

[60] J. K. Kirklin, F. D. Pagani, R. L. Kormos, L. W. Stevenson, E. D. Blume, S. L. Myers, M. A. Miller, J. T. Baldwin, J. B. Young, and D. C. Naftel, Eighth annual intermacs report: Special focus on framing the impact of adverse events, *The Journal of Heart and Lung Transplantation* **36**, 1080 – 1086, 2017.

[61] J. K. Kirklin, R. Xie, J. Cowger, T. M. M. H. de By, T. Nakatani, S. Schueler, R. Taylor, J. Lannon, P. Mohacsi, J. Gummert, D. J. Goldstein, K. Caliskan, and M. M. Hannan, Second annual report from the ISHLT mechanically assisted circulatory support registry, *Journal of Heart and Lung Transplantation* **37**, 685–691, 2018.

[62] S. Klotz, U. Boeken, and A. Assmann, *Leben mit einem Kunstherz - Ein Ratgeber für Betroffene, Angehörige und Interessierte*, Deutsche Herzstiftung, 2016.

[63] KNF DAC GmbH. NMS030.1.2 SERIES MICRO DIAPHRAGM GAS PUMPS, data sheet, 01/2019.

[64] M. A. Konstam, D. G. Kramer, A. R. Patel, M. S. Maron, and J. E. Udelson, Left ventricular remodeling in heart failure: Current concepts in clinical significance and assessment, *JACC: Cardiovascular Imaging* **4**, 98 – 108, 2011.

[65] R. L. Kormos, J. Cowger, F. D. Pagani, J. J. Teuteberg, D. J. Goldstein, J. P. Jacobs, R. S. Higgins, L. W. Stevenson, J. Stehlik, P. Atluri, K. L. Grady, and J. K. Kirklin, The society of thoracic surgeons intermacs database annual report: Evolving indications, outcomes, and scientific partnerships, *The Journal of Heart and Lung Transplantation* **38**, 114 – 126, 2019.

[66] R. T. Kung and M. Rosenberg, Heart booster: a pericardial support device, *The Annals of Thoracic Surgery* **68**, 764 – 767, 1999.

[67] B. Long, J. Robertson, A. Koyfman, and W. Brady, Left ventricular assist devices and their complications: A review for emergency clinicians, *The American Journal of Emergency Medicine* **37**, 1562–1570, 2019.

[68] J. MacIver and H. J. Ross, Quality of life and left ventricular assist device support, *Circulation* **126**, 866–874, 2012.

[69] A. Maier, *Computational Modeling of Rupture Risk in Abdominal Aortic Aneurysms*, PhD thesis, Technische Universität München, 2012.

[70] A. Marciniak, K. Glover, and R. Sharma, Cohort profile: prevalence of valvular heart disease in community patients with suspected heart failure in UK, *BMJ Open* **7**, e012240, 2017.

[71] J. Mau, S. Menzie, Y. Huang, M. Ward, and S. Hunyor, Nonsurround, nonuniform, biventricular-capable direct cardiac compression provides frank-starling recruitment independent of left ventricular septal damage, *The Journal of Thoracic and Cardiovascular Surgery* **142**, 209 – 215, 2011.

[72] E. McGee, M. Danter, M. Strueber, C. Mahr, N. A. Mokadam, G. Wieselthaler, L. Klein, S. Lee, T. Boeve, S. Maltais, G. V. Pretorius, E. Adler, T. Vassiliades, and A. Cheung, Evaluation of a lateral thoracotomy implant approach for a centrifugal-flow left ventricular assist device: The LATERAL clinical trial, *The Journal of Heart and Lung Transplantation* **38**, 344–351, 2019.

[73] M. Mehra, N. Uriel, Y. Naka, J. Cleveland, M. Yuzefpolskaya, C. Salerno, M. Walsh, C. Milano, C. Patel, S. Hutchins, J. Ransom, G. Ewald, A. Itoh, N. Raval, S. Silvestry, R. Cogswell, R. John, A. Bhimaraj, B. Bruckner, and D. Goldstein, A fully magnetically levitated left ventricular assist device - final report, *New England Journal of Medicine* **380**, 1618–1627, 2019.

[74] L. Miller, E. Birks, M. Guglin, H. Lamba, and O. Frazier, Use of ventricular assist devices and heart transplantation for advanced heart failure, *Circulation Research* **124**, 1658–1678, 2019.

[75] E. Molina, P. Shah, M. Kiernan, W. Cornwell, H. Copeland, K. Takeda, F. Fernandez, V. Badhwar, R. Habib, J. Jacobs, D. Koehl, J. Kirklin, F. Pagani, and J. Cowger, The Society of Thoracic Surgeons Intermacs 2020 Annual Report, *The Annals of Thoracic Surgery* **111**, 778–792, 2021.

[76] M. R. Moreno, S. Biswas, L. D. Harrison, G. Pernelle, M. W. Miller, T. W. Fossum, D. A. Nelson, and J. C. Criscione, Assessment of Minimally Invasive Device That Provides Simultaneous Adjustable Cardiac Support and Active Synchronous Assist in an Acute Heart Failure Model, *Journal of Medical Devices* **5**, 041008, 2011.

[77] M. R. Moreno, S. Biswas, L. D. Harrison, G. Pernelle, M. W. Miller, T. W. Fossum, D. A. Nelson, and J. C. Criscione, Development of a non-blood contacting cardiac assist and support device: An in vivo proof of concept study, *Journal of Medical Devices* **5**, 041007, 2011.

[78] K. Nadeem, B. Ng, E. Lim, S. Gregory, R. Salamonsen, M. Stevens, M. Mubin, and N. Lovell, Numerical simulation of a biventricular assist device with fixed right outflow cannula banding during pulmonary hypertension, *Annals of Biomedical Engineering* **44**, 1008–1018, 2016.

[79] M. Naveed, L. Han, G. J. Khan, S. Yasmeen, R. Mikrani, M. Abbas, L. Cunyu, and Z. Xiaohui, Cardio-supportive devices (VRD & DCC device) and patches for advanced heart failure: A review, summary of state of the art and future directions, *Biomedicine & Pharmacotherapy* **102**, 41 – 54, 2018.

[80] N. M. Newmark, A method of computation for structural dynamics, *ASCE Journal of the Engineering Mechnaics Devision* **85**, 67–94, 1959.

[81] C. J. Payne, I. Wamala, C. Abah, T. Thalhofer, M. Saeed, D. Bautista-Salinas, M. A. Horvath, N. V. Vasilyev, E. T. Roche, F. A. Pigula, and C. J. Walsh, An implantable extracardiac soft robotic device for the failing heart: Mechanical coupling and synchronization, *Soft Robotics* **4**, 241–250, 2017.

[82] K. Pekkan, D. Frakes, D. de Zelicourt, C. W. Lucas, W. J. Parks, and A. P. Yoganathan, Coupling pediatric ventricle assist devices to the fontan circulation: Simulations with a lumped-parameter model, *ASAIO Journal* **51**, 618–628, 2005.

[83] P. Ponikowski, S. D. Anker, K. F. AlHabib, M. R. Cowie, T. L. Force, S. Hu, T. Jaarsma, H. Krum, V. Rastogi, L. E. Rohde, U. C. Samal, H. Shimokawa, B. Budi Siswanto, K. Sliwa, and G. Filippatos, Heart failure: preventing disease and death worldwide, *ESC Heart Failure* **1**, 4–25, 2014.

[84] P. Ponikowski, A. A. Voors, S. D. Anker, H. Bueno, J. G. F. Cleland, A. J. S. Coats, V. Falk, J. R. GonzÃ¡lez-Juanatey, V.-P. Harjola, E. A. Jankowska, M. Jessup, C. Linde, P. Nihoyannopoulos, J. T. Parissis, B. Pieske, J. P. Riley, G. M. C. Rosano, L. M. Ruilope, F. Ruschitzka, F. H. Rutten, P. van der Meer, and E. S. D. Group, 2016 ESC guidelines for the diagnosis and treatment of acute and chronic heart failurethe task force for the diagnosis and treatment of acute and chronic heart failure of the european society of cardiology (ESC) developed with the special contribution of the heart failure association (HFA) of the ESC, *European Heart Journal* **37**, 2129–2200, 2016.

[85] A. Popp, *Mortar Methods for Computational Contact Mechanics and General Interface Problems*, PhD thesis, Technische Universität München, 2012.

[86] A. Popp, M. W. Gee, and W. A. Wall, A finite deformation mortar contact formulation using a primal-dual active set strategy, *International Journal for Numerical Methods in Engineering* **79**, 1354–1391, 2009.

[87] A. Popp, M. Gitterle, M. W. Gee, and W. A. Wall, A dual mortar approach for 3D finite deformation contact with consistent linearization, *International Journal for Numerical Methods in Engineering* **83**, 1428–1465, 2010.

[88] Rahmel, A. and Biet, T. Jahresbericht Organspende und Transplantation in Deutschland 2017. Deutsche Stiftung Organtransplantation, 2017.

[89] J. Riedel and J. Neumann, Pneumatische Bestimmung von Behältervolumina mit Hilfe kleiner Druckdifferenzen, *tm - Technisches Messen* **78**, 327–333, 2011.

[90] E. T. Roche, R. Wohlfarth, J. T. B. Overvelde, N. V. Vasilyev, F. A. Pigula, D. J. Mooney, K. Bertoldi, and C. J. Walsh, A bioinspired soft actuated material, *Advanced Materials* **26**, 1200–1206, 2014.

[91] E. T. Roche, M. A. Horvath, I. Wamala, A. Alazmani, S.-E. Song, W. Whyte, Z. Machaidze, C. J. Payne, J. C. Weaver, G. Fishbein, J. Kuebler, N. V. Vasilyev, D. J. Mooney, F. A. Pigula, and C. J. Walsh, Soft robotic sleeve supports heart function, *Science Translational Medicine* **9**, 2017.

[92] E. T. Roche, S. Obiajulu, C. J. Walsh, D. J. Mooney, and F. A. Pigula. Biometic actuation device and system, and methods for controlling a biometic actuation device and system, U.S. Patent 10 058 647, Aug. 2018.

[93] J. Rogers, F. Pagani, A. Tatooles, G. Bhat, M. Slaughter, E. Birks, S. Boyce, S. Najjar, V. Jeevanandam, A. Anderson, I. Gregoric, H. Mallidi, K. Leadley, K. Aaronson, O. Frazier, and C. Milano, Intrapericardial left ventricular assist device for advanced heart failure, *New England Journal of Medicine* **376**, 451–460, 2017.

[94] G. Rosano, Valvular heart disease in heart failure, *International Cardiovascular Forum Journal* **10**, 70–72, 2017.

[95] M. Rosenberg and R. T. V. Kung. Extra cardiac ventricular assist device, U.S. Patent 5 713 954, Feb. 1998.

[96] C. Rosendorff, Beta-blocking agents with vasodilator activity, *J Hypertens Suppl* **11**, 37–40, 1993.

[97] Y. Saad and M. H. Schultz, GMRES: A generalized minimal residual algorithm for solving nonsymmetric linear systems, *SIAM Journal on Scientific and Statistical Computing* **7**, 856–869, 1986.

[98] G. Savarese and L. H. Lund, Global public health burden of heart failure, *Cardiac Failure Review* **3**, 7–11, 2017.

[99] A. Schmidt, *Technical Thermodynamics for Engineers*, Springer Nature Switzerland, 2019.

[100] S. Schueler, C. Bowles, R. Hinkel, J. Fischer, R. Wohlfarth, S. Wildhirt, H. Smail, and U. Stock, A novel intra-pericardial pulsatile device for individualized, biventricular circulatory support without direct blood contact - the impact of precise electro-mechanical synchronization on haemodynamic performance, *Journal of Thoracic and Cardiovascular Surgery*, (forthcoming).

[101] P. C. Schulze, S. Kitada, K. Clerkin, Z. Jin, and D. M. Mancini, Regional differences in recipient waitlist time and pre- and post-transplant mortality after the 2006 united network for organ sharing policy changes in the donor heart allocation algorithm, *JACC: Heart Failure* **2**, 166–177, 2014.

[102] K. Shekar, S. Gregory, and J. Fraser, Mechanical circulatory support in the new era: An overview, *Critical Care* **20**, 2016.

[103] A. Sievert, A. Arndt, W. Drewelow, B. Lampe, and O. Simanski, A control oriented model design of heart assistant devices, *IFAC Proceedings Volumes* **44**, 5007 – 5011, 2011.

[104] A. Sievert, C. Wiesener, A. Arndt, W. Drewelow, and O. Simanski, Control of an extracorporeal heart assist device, In *2012 IEEE International Conference on Control Applications*, pages 63–68, 2012.

[105] A. Sievert, W. Drewelow, T. Jeinsch, and O. Simanski, Modeling and control of an extracorporeal heart assist device, *IFAC Proceedings Volumes* **47**, 6581 – 6586, 2014.

[106] H. Sigloch, *Technische Fluidmechanik*, Springer-Verlag Berlin Heidelberg, 2014.

[107] D. G. Silverman, A. B. Jotkowitz, M. Freemer, V. Gutter, T. Z. O'Connor, and I. M. Braverman, Peripheral assessment of phenylephrine-induced vasoconstriction by laser doppler flowmetry and its potential relevance to homeostatic mechanisms, *Circulation* **90**, 23–26, 1994.

[108] Statistisches Bundesamt (Destatis). Todesursachen in Deutschland 2015, 2017.

[109] J. Steffel and T. Lüscher, *Herz-Kreislauf*, Springer-Verlag Berlin Heidelberg, 2014.

[110] D. D. Streeter, H. M. Spotnitz, D. P. Patel, J. Ross, and E. H. Sonnenblick, Fiber orientation in the canine left ventricle during diastole and systole, *Circulation Research* **24**, 339–347, 1969.

[111] L.-B. Tan, S. Williams, D. Tan, and A. Cohen-Solal, So many definitions of heart failure: Are they all universally valid? A critical appraisal, *Expert Review of Cardiovascular Therapy* **8**, 217–228, 2010.

[112] M. Thon, *Multiphysics Modeling and Quantification of Early Atherosclerosis*, Phd thesis, Technische Universität München, München, 2018.

[113] N. Vaiana, S. Sessa, F. Marmo, and L. Rosati, An accurate and computationally efficient uniaxial phenomenological model for steel and fiber reinforced elastomeric bearings, *Composite Structures* **211**, 196 – 212, 2019.

[114] T. S. Wang, A. F. Hernandez, G. M. Felker, C. A. Milano, J. G. Rogers, and C. B. Patel, Valvular heart disease in patients supported with left ventricular assist devices, *Circulation: Heart Failure* **7**, 215–222, 2014.

[115] H. Weber, *Herzinsuffizienz: Vom Symptom zum Therapie-Erfolg*, 2008.

[116] F. M. White, *Fluid Mechanics*, McGraw-Hill, 2011.

[117] M. J. Wilhelm, Long-term outcome following heart transplantation: current perspective, *Journal of Thoracic Disease* **7**, 549–551, 2015.

[118] J. M. Willenbring and M. A. Heroux. Trilinos users guide, 2003.

[119] R. Wohlfarth, *Beschreibung und Modellierung der pneumatischen Komponenten des AdjuCor-Herzunterstützungssystems für Herzinsuffizienzpatienten*, Diploma thesis, Technische Universität München, 2014.

[120] P. Wriggers, *Computational Contact Mechanics*, Springer Verlag Berlin Heidelberg, 2006.

[121] Y. Wu, P. Allaire, G. Tao, and D. Olsen, Modeling, estimation, and control of human circulatory system with a left ventricular assist device, *IEEE Transactions on Control Systems Technology* **15**, 754 – 767, 2007.

[122] Z. Zi, Sensitivity analysis approaches applied to systems biology models, *IET Systems Biology* **5**, 336–346, 2011.

[123] B. Ziaeian and G. Fonarow, Epidemiology and aetiology of heart failure, *Nature Reviews Cardiology* **13**, 368–378, 2016.

[124] O. Zienkiewicz and R. Taylor, *Finite Element Method for Solid and Structural Mechanics*, Elsevier Butterworth-Heinemann, 2005.

[125] H. Zobel and J. Kruschik, *Strömung durch Rohre und Ventile*, Springer-Verlag Wien New York, 1982.